# An investigation into vibrational dynamics in organic semiconductors

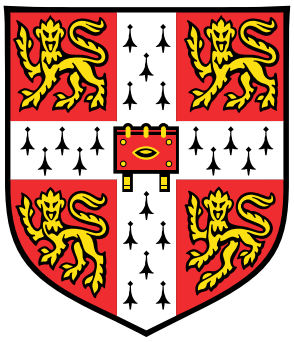

**Mateusz Aleksander Zelazny**

Cavendish Laboratory

University of Cambridge

This dissertation is submitted for the degree of

*Doctor of Philosophy*

Churchill College

October 2018

# Abstract

## An investigation into vibrational dynamics in organic semiconductors

Mateusz Aleksander Zelazny

This thesis is concerned with study of vibrational dynamics and their effect on charge transport in thin films of organic semiconductors. Two classes of organic semiconductors are investigated- crystalline small molecules and conjugated polymers. Although device performance of both classes of materials has greatly improved over last two decades, detailed understanding of relationship between structure and transport properties is still missing- so far development of organic semiconductors has mostly been based on experimental approach, with theoretical models providing post factum justification rather than guiding rational design of novel compounds. In this thesis I establish methodology to investigate both inter- and intramolecular vibrational modes by combining latest computational techniques with experimental pressure-dependent Raman spectroscopy.

The dominant factor limiting charge delocalization in crystalline small molecules are low frequency, large amplitude intermolecular modes. However theoretical modeling of these modes require use of periodic boundary conditions increasing computational cost by orders of magnitude when compared to commonly used vacuum phase simulations. I report comparative study of two implementations (CRYSTAL09 and CASTEP) of density functional theory (DFT) and dispersion correction (Grimme and Tkatchenko-Scheffler) and evaluate their applicability to predict low frequency vibrational modes in 2,7-Dioctyl[1]benzothieno[3,2-b][1]benzothiophene (C8-BTBT) and 2,8-Difluoro-5,11-bis(triethylsilylethynyl)anthradithiophene (dif-TES-ADT).

Charge transport in conjugated polymers is strongly affected by energetic disorder arising from spatial variations in backbone conformation. I combine vacuum phase DFT simulations of intramolecular vibrational modes with pressure-dependent

Raman spectroscopy to study planarity and torsional backbone disorder of 2,5-bis(3-alkylthiophene-2-yl)thieno[3,2-b]thiophene (pBTTT), indacenodithiophene-co-benzothiadiazole (IDT-BT), diketopyrrolopyrrole-benzotriazole (DPP-BTZ) and naphtalene-bithiophene (NDI-T2) at pressures up to 3.9 GPa. It is shown that Raman spectra of pBTTT and NDI-T2 demonstrate dependence of mode intensities on hydrostatic pressure, whereas spectra of IDT-BT and DPP-BTZ exhibit lack of dependence. Simulations of theoretical spectra performed as a function of backbone torsion indicate that pBTTT undergoes deplanarization of already non-planar backbone and that NDI-T2 backbone is planarized, whereas backbones of IDT-BT and DPP-BTZ are resilient to changes of conformation.

Finally, I perform large scale molecular dynamics simulations of crystalline, semi-crystalline and disordered phases of IDT-BT and DPP-BT in order to investigate effect of disorder on backbone conformation. Both compounds were previously reported to exhibit extremely low degree of energetic disorder- I assign this phenomenon to their surprisingly strong resilience to side chain disorder. In both systems simulations demonstrate novel mechanism of disorder accommodation- their backbones bend rather than twist and retain low degree of torsional variation even in amorphous phase.

*To my loving family.*

# Declaration

I hereby declare that except where specific reference is made to the work of others, the contents of this dissertation are original and have not been submitted in whole or in part for consideration for any other degree or qualification in this, or any other University. This dissertation is the result of my own work and includes nothing which is the outcome of work done in collaboration, except where specifically indicated in the text. This dissertation contains fewer than 60,000 words including appendices, bibliography, footnotes, tables and equations..

Mateusz Aleksander Zelazny
October 2018

# Acknowledgements

This thesis describes work undertaken at the Cavendish Laboratory of the University of Cambridge during the period from October 2012 to January 2015 and carried out under a research scholarship from NanoDTC Cambridge.

I owe my thanks to Professor Henning Sirringhaus for his supervision and invaluable support. Henning offered me guidance through the project and advice when I needed it. My thanks also extend to Professor Graeme Day who was my co-supervisor during his stay at Cambridge and offered me endless support, training and advice on computational techniques. I am very thankful to Dr Vincent Lemaur and Dr Yoann Olivier from University of Mons in Belgium. Significant part of work presented in my thesis is based on close collaboration with Vincent and Yoann- in fact I regard them as my secondary supervisors.

Additionally, I would like to thank Dr Michal Kepa from University of Edinburgh for interesting discussions, advice on design of diamond anvil cell and collaboration, which led to a high profile publication. I am grateful to Dr Tom Kehoe from OE for being an excellent expert on Raman spectroscopy. I thank Professor Jeremy Baumberg and Dr Agnieszka Iwasiewicz-Wabnig from NanoDTC for their advice on choosing research group and writing PhD proposal during my first year training. At this point I would also like to thank Mark Nikolka and Igor Romanov from OE for great scientific and non-scientific discussions making the office a fantastic place to work in. I would also like to thank Dr Radoslav Chakalov and Roger Beadle for being extremely helpful with any technical problems.

Finally, I would like to thank Churchill College for awarding me sports scholarship to support intensive olfactory training while I was a member of Cambridge University varsity team and Blind Wine Tasting Society.

# Contents

# Chapter 1

# Introduction

## 1.1 Organic electronics- a disruptive innovation?

Development of synthetic organic chemistry enabled humankind to access virtually unlimited number of new compounds, many of which improve our standard of living by offering new therapies and consumer goods. Organic materials exhibit a broad range of tunable biological, mechanical and electrical properties. Studies of electrical properties and synthesis of organic semiconductors are relatively novel and less understood branches of science compared to pharmaceuticals and structural plastics. The field was pioneered by Hideki Shirakawa, Alan MacDiarmid and Alan Heeger who reported orders of magnitude increase of conductivity in oxidized iodine-doped polyacetylene in 1977 [1]. Although polyacetylene itself did not find practical applications, they encouraged rapid growth of the field and were awarded the 2000 Nobel Prize in Chemistry "*for the discovery and development of conductive polymers*". Development of organic light emitting diodes (OLEDs) by researchers from Eastman Kodak [2] in 1987 and subsequent discovery of polymers suitable for solution-processed OLEDs reported by researchers from Cavendish Laboratory in 1990 [3] were key milestones towards practical applications of organic semiconductors. Recent decade was a period of intense research towards commercialization of organic photovoltaics (OPVs) and thin film transistors (OFETs) with particular emphasis on solution processing and scalable manufacturing. The promise of using organic materials for devices fabricated using low cost wet printing process is often perceived as being potentially disruptive to established semiconductor industry. It is therefore no surprise that so much effort has been put into process engineering and development of novel materials by both industry and academia.

Up to date organic semiconductors have been successfully commercialized in a

limited number of market segments. In this respect, the use of OLEDs in television screens and mobile phone displays is presumably the most common application of organic semiconductors in consumer electronics. The field was pioneered by Samsung, who developed active-matrix organic light-emitting diode (AMOLED) displays incorporating an array of OLEDs controlled by inorganic FETs. AMOLED displays became commercially viable because they offer unparalleled contrast and reproduction of colour, however they do not explore key potential benefits of organic materials, namely ease of manufacturing and flexibility. In a fact, it is the opposite- OLEDs are deposited on solid backplane in a process that incorporates novel material into established manufacturing routine making the resultant product more expensive than all-inorganic displays. So far this hybrid technology can only be applied in selected markets where customers value specific features of new materials and the key advantage of organic compounds is not fully explored. In contrast, OFETs and OPVs have only seen niche market applications such as low resolution displays for electronic paper or wearable power sources, however these technologies are just beginning to transition to mass market. One of the most promising future applications of organic semiconductors are fully flexible and transparent OLED displays. In order to become commercially viable, such displays require high performance materials with good uniformity and stability. These requirements inevitably impose constraints on the choice of semiconductors, both in terms of their performance and compatibility with other dielectrics, substrates and electrodes. For instance, although small organic molecules are potentially able to deliver required performances in laboratory conditions, their varying degree of crystallinity, fluctuations in performance and processing complexity render these materials insufficient for most of the applications.

On the other hand, conjugated polymers represent good uniformity and ease of processing, but their performance is still inferior compared to small molecules. It is generally acknowledged that improvement of polymer transport properties is more viable route to commercialization than engineering of crystalline order of small molecules. In recent years, a lot of research has been conducted to improve the performance of polymers, with mobilities improved by orders of magnitude over the past three decades. Historical evolution of polymer performance is illustrated in Figure 1.1[1]. Recently, most significant advancements in charge carrier mobilities have been achieved by the class of amorphous donor-acceptor polymers. Some of these new systems have already demonstrated hole and electron mobilities exceeding 1 $cm^2V^{-1}s^{-1}$ [6, 7], al-

[1]Figure 1.1 contains raw numbers as reported in original papers and should be interpreted with dose of skepticism. In scientific community there is an ongoing debate about methodology of mobility extraction and resultant overestimation of device performance [5].

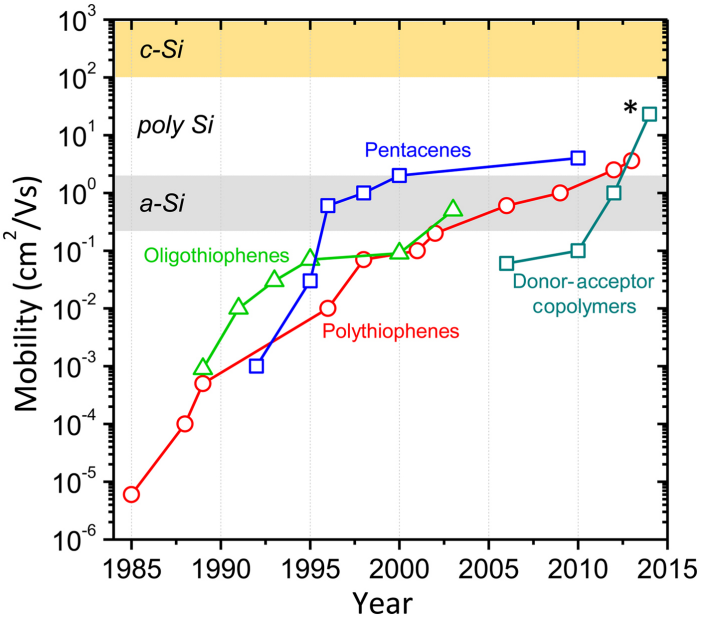


Figure 1.1: Historical evolution of charge carrier mobilities in semiconducting polymers. Mobility has improved by over six orders of magnitude in the last three decades. E-paper displays are the least demanding and can be fabricated using materials with mobilities above 0.1 $cm^2V^{-1}s^{-1}$, whereas OLEDs generally require mobilities between 3 and 10 $cm^2V^{-1}s^{-1}$. Logic applications are the most demanding and require mobilities above 10 $cm^2V^{-1}s^{-1}$. The asterisk denotes materials aligned using a special technique that is not suitable for practical implementation. Figure adapted from [4].

lowing them to exceed performance of amorphous silicon, which is used in many TFT display backplanes that are currently embedded in consumer electronics. Unfortunately, the process of new materials discovery is mostly heuristic and our understanding of charge transport mechanism in these novel materials is rather limited, which constrains intelligent design and predictable, systematic improvement. Furthermore, carrier mobility is not the ultimate benchmark that determines commercial viability- most of the organic semiconductors are vulnerable to gradual degradation of performance and therefore development of materials for prospective plastic electronics is a multidimensional problem.

Organic semiconductors are deficient to silicon in several aspects and, broadly speaking, are not commercially successful. Their performance is less appealing, their chemical stability is a problem, and most importantly consumer products incorporating organic technology are more expensive than their silicon-based equivalents. Yet, many industry experts still perceive organic materials as a potential game-changer in semiconductor industry. In order to understand this apparent contradiction we have to

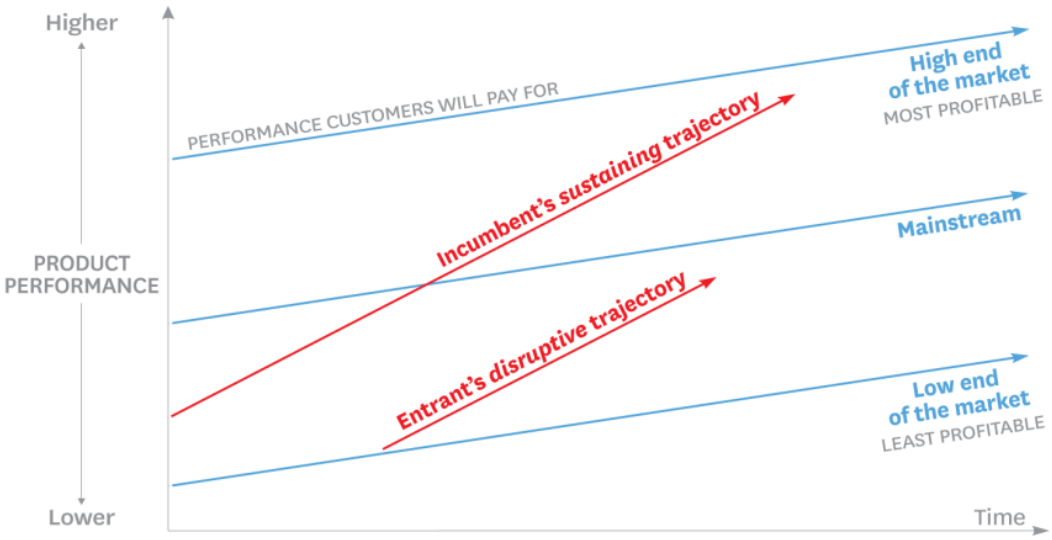


Figure 1.2: Product performance trajectories (red lines showing product improvement over time) are typically growing faster than consumer demand trajectories (blue lines showing customers' willingness to pay for the performance). As incumbent companies introduce higher-quality products (upper red line) to satisfy the high end, most profitable market segment, they overshoot expectations of low-end customers and neglect them. This creates opportunity for new entrants to find footholds in the less profitable market segments. Gradually, disruptive entrants improve the performance of their products and challenge incumbents. Time axis and product performance scale are illustrative, as the steepness of trajectories varies between industries and cannot be generalised. Figure adapted from [9].

refer to the original concept of disruptive innovation [8] that was formulated by Clayton Christensen from Harvard Business School, and is based on analysis of historical innovation paths within hard drive industry. Hard drive industry is a model system used for studies of innovation due to its short product life cycle and fragmented market with no long-standing oligopolies. Contrary to common misunderstanding, disruptive innovation is not any breakthrough that changes industry's competitive patterns. Theory of disruptive innovation is based on two key observations: firstly, trajectory of technological improvement is often steeper than inflation of consumers' expectations and price they are willing to pay, as illustrated in Figure 1.2. As a result, producers gradually migrate towards the most profitable, high end segment of the market. Moreover, consumers are not willing to pay premium price for a product that exceeds their needs- once the functionality is just good enough, they base their choice on other factors such as convenience or price- this phenomenon is called *buying hierarchy* [8]. Over time, incumbents optimise their profits by neglecting or even

exiting least profitable, low end of the market, since their cost structure promotes sales of high performance products. Entrants that provide disruptive products begin by targeting those less profitable market segments, gaining a foothold by delivering affordable products that are less advanced technologically but functional enough to satisfy basic needs. Entrants then move upmarket according to product performance trajectory while preserving the advantages that drove their early success. Secondly, small markets don't solve the growth needs of large companies- to maintain their share prices, successful companies need to continue to grow. As a result, they tend to be risk averse and avoid entering new markets that are highly unpredictable and adopt a strategy of waiting until new markets are "large enough to be interesting". Good examples of such market segments are flexible electronics and wearables. In the case of new market footholds, entrants create markets where none existed by finding a way to turn nonconsumers into consumers and gain first-mover advantage. A disruptive innovation, by definition, starts from one of those footholds- it is either emerging or low-end market. In that sense, Samsung's AMOLED is a sustaining technology- it was introduced as a gradual performance improvement in established, high-end segment of the market, where strategic planning and careful analysis are feasible to perform. Organic OPVs, on the other hand, are completely different case from a business perspective. Their performance trajectory is unlikely to match most efficient cells within near future, however the cost advantage resulting from roll-to-roll processing can make them well-suited for low end market segment. OFET have the highest potential for disruption and least predictable trajectory- they can enter the low-end market as printed large area displays or emerging market as flexible electronics. Both scenarios, however, require simultaneous improvement of both microstructural and charge transfer properties making OFET commercialization a challenge. In summary, organic semiconductors already found their way to the market as sustaining innovations, however they have many attributes of prospective disruptive technologies.

## 1.2 Organic semiconductors

Conductivity in metals and inorganic semiconductors results from the presence of unbound electrons that can freely flow in a periodic potential. The energy of these carriers, also known as conduction band, with respect to the outermost electrons that are too tightly bound to carry electric current determines a material's band bap. Depending on the band gap, materials are classified as insulators, semiconductors, semimetals or metals [10]. In organic semiconductors the origin of conduction is very

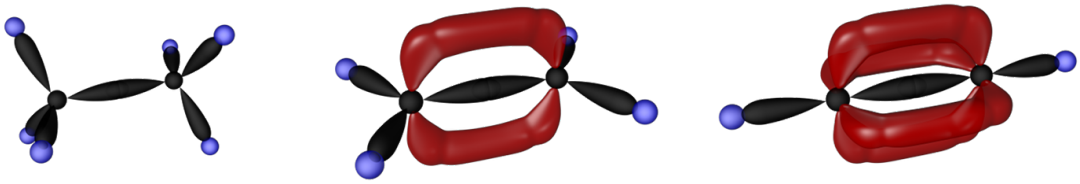

Figure 1.3: Visualization of molecules containing sp hybridized carbon bonds. In ethane (**left**) every carbon is bonded by three $sp^3$ hybridized $\sigma$-bonds. In ethene (**centre**) carbon atoms are $sp^2$ hybridized forming one $\sigma$- and one $\pi$-bond in between, whereas in ethyne (**right**) $sp^1$ hybridized carbon atoms are triple bonded with one $\sigma$- and two $\pi$-bonds. Figure adapted from [11].

different compared to inorganic structures with periodic lattice. The central unit is the carbon atom, which has a ground state electronic configuration of $1s^2 2s^2 2p^2$ with mutually orthogonal p-orbitals. Since the energy difference between 2s and 2p orbitals is relatively small, it is possible to excite the electron from the doubly occupied 2s orbital to the empty 2p orbital producing four simply occupied orbitals in $1s^2 2s^1 2p^3$ configuration. This leads to so-called bond hybridization between 2s and 2p orbitals where either four $sp^3$, three $sp^2$ or two $sp^1$equienergetic orbitals are formed. Bonds formed between two $sp^2$ orbitals, or an s and $sp^2$ orbital, are called $\sigma$-bonds. The remaining $p_z$ electron does not take part in hybridization and occupies an orbital in the plane perpendicular to the hybrid orbitals. Two $p_z$ orbitals on adjacent carbon atoms lead to formation of weakly bound $\pi$-bond with electron density located above and below the molecular plane, as illustrated in Figure 1.3. Strong overlap of $sp^2$ orbitals leads to a large splitting of that orbital into lower energy, occupied $\sigma$ bonding and higher energy, unoccupied $\sigma^*$ anti-bonding orbitals. Similar orbital splitting is present in $\pi$-bond orbital, however the energy difference between $\pi^*$ and $\pi$ orbitals is much smaller due to weak overlap. $\pi$ orbital forms the highest occupied molecular orbital (HOMO), whereas the lowest unoccupied molecular orbital (LUMO) is at $\pi^*$ orbital. Since organic molecules are bound by van der Waals forces, the properties of these systems depend to large extent on the structure of isolated molecules and, at least to some extent, can be engineered in a controlled manner.

Relatively small energy gap between HOMO and LUMO levels can be exploited to design organic compounds with semiconducting properties. The overlap of adjacent orbitals results in further energy splitting, leading to charge delocalisation and formation of "electronic bands" made of filled $\pi$ and unfilled $\pi^*$ states. This effect is well illustrated by benzene molecule, were orbitals of 6 carbon atoms overlap and form

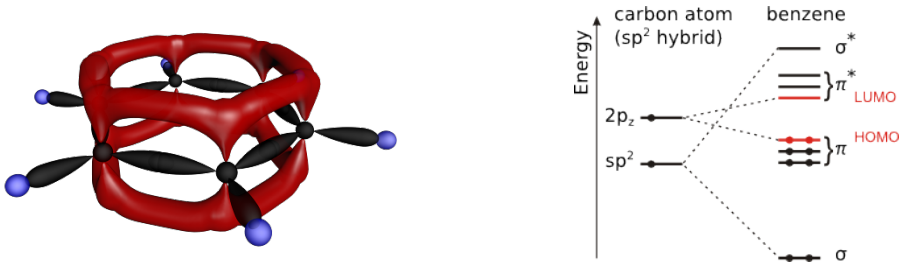


Figure 1.4: Visualization of benzene molecule (**left**) with its $\pi$-electron system delocalised along the complete carbon ring (red). Splitting of $\pi$-bond orbitals (**right**) leads to formation of HOMO and LUMO gap. Figure adapted from [11].

highly delocalised $\pi$-electron system above and below the plane of carbon atoms, as shown in Figure 1.4. As the number of conjugated atoms is increased, carrier delocalisation becomes extended and discrete $\pi$, $\pi^*$ energy levels converge into continuous energy bands as in periodic inorganic systems. In a fact, organic systems are never designed to maximise number of $\pi$-bonds, since $sp^1$ hybridized carbons can only form linear chains and in practice molecules mostly consist of $sp^2$ hybridized carbons with number of $\sigma$-bonds used to establish the molecular framework. Theoretically, the interaction of $\pi$-electrons is most simply described by Hückel Molecular Orbital (MO) theory. In Hückel theory the electronic structure of molecules is approximated by a linear combination of atomic $p_z$ orbitals (LCAO). Only $\pi$ electrons are included because these determine electronic properties of molecules and $\sigma$ electrons are ignored due to orthogonality of $\sigma$ and $\pi$ in planar systems. In its simplest form, the Hamiltonian is constructed by considering only the nearest neighbour atomic orbitals:

$$H = \sum_{i=1}^{N} \epsilon_i \left|\phi_i\right\rangle \left\langle\phi_i\right| + \sum_{i=1}^{N-1} \nu_{ij} \left|\phi_i\right\rangle \left\langle\phi_j\right| \tag{1.1}$$

where $\phi_i$ is the atomic orbital on site $i$, $\epsilon_i$ is the energy of $i$-th orbital and $\nu_{i,j}$ is the energy of pairwise interaction between neighbour orbitals $\phi_i$ and $\phi_j$. In LCAO method, the molecular orbital $\boldsymbol{\psi}$ is expressed in terms of known atomic orbitals:

$$\left|\psi\right\rangle = \sum_{i}^{N} c_i \left|\phi_i\right\rangle \tag{1.2}$$

where $c_i$ are weight coefficient corresponding to atomic orbitals. It is important to note that the Hamiltonian does not contain any explicit electron-electron or electron-

phonon interaction, however they do contribute to $\epsilon_i$ and $\nu_{ij}$ as an effective potential. By solving Schrödinger's equation it is possible to find energy eigenstates and eigenvectors corresponding to molecular orbitals, predicting how many energy levels exist for a given molecule, what is their degeneracy and what are their energies in terms of $\epsilon_i$ and $\upsilon_{ij}$. As an example, let us consider the simple model of benzene ring. Hamiltonian would be simply a $6 \times 6$ matrix and due to symmetry of the system all $\epsilon_i$ and $\upsilon_{ij}$ terms would be the same:

$$H = \begin{bmatrix} \epsilon & \upsilon & 0 & 0 & 0 & \upsilon \\ \upsilon & \epsilon & \upsilon & 0 & 0 & 0 \\ 0 & \upsilon & \epsilon & \upsilon & 0 & 0 \\ 0 & 0 & \upsilon & \epsilon & \upsilon & 0 \\ 0 & 0 & 0 & \upsilon & \epsilon & \upsilon \\ \upsilon & 0 & 0 & 0 & \upsilon & \epsilon \end{bmatrix} \tag{1.3}$$

and by solving eigenvalue problem:

$$det \begin{bmatrix} \epsilon - E & \upsilon & 0 & 0 & 0 & \upsilon \\ \upsilon & \epsilon - E & 0 & 0 & 0 & 0 \\ 0 & \upsilon & \epsilon - E & \upsilon & 0 & 0 \\ 0 & 0 & \upsilon & \epsilon - E & \upsilon & 0 \\ 0 & 0 & 0 & \upsilon & \epsilon - E & \upsilon \\ \upsilon & 0 & 0 & 0 & \upsilon & \epsilon - E \end{bmatrix} = 0 \tag{1.4}$$

one obtain six energy levels such that $E_1 = \epsilon + 2\upsilon$, $E_2 = E_3 = \epsilon + \upsilon$, $E_4 = E_5 = \epsilon - \upsilon$ and $E_6 = \epsilon - 2\upsilon$. As one can see, Molecular Orbitals formalism is a convenient way to study degeneracy in systems where symmetry can be exploited predicting that the number of energy levels increases and energy difference between HOMO and LUMO decreases with increasing number of contributing $p_z$ orbitals.

Organic semiconductors can be broadly classified into two categories: small molecules and conjugated polymers. Small molecules are usually simple oligomers based on benzene or benzothiophene containing less than 10 conjugated rings. They form well-ordered crystalline structures bound together by van der Waals forces. Some of these systems are known to exhibit high bulk mobilities in excess of 100 $cm^2V^{-1}s^{-1}$ at temperatures below 30 K [12, 13] suggesting presence of electronic states delocalised over several molecules and a band-like transport regime similar to that of inorganic semicon-

ductors [14]. The highest room temperature mobility achieved to day[2], 43 $cm^2V^{-1}s^{-1}$, has been reported by Yuan et al. [15] on specially aligned thin films of a polymorph of C8-BTBT and in practice the mobilities are typically less than 10 $cm^2V^{-1}s^{-1}$. There are, however, theoretical calculations predicting that achieving mobilities higher than 50 $cm^2V^{-1}s^{-1}$ in common small molecules, such as pentacene or C12-BTBT, is not impossible with proper crystalline structure [16, 17]. Simulations performed by Bredas et al. [14] suggest that the single most important parameter limiting charge transport are transfer integrals between[3] adjacent chains both in band-like and hopping transport regimes. There is no doubt that crystalline small molecules represent the upper bound of performance and are exciting model systems to understand fundamental physics of organic semiconductors. However, their applications are rather limited due to their mechanical properties and lack of established methods of crystal growth- in practice small molecules are vacuum-deposited forming semi-crystalline layers and do not fully explore their potential performance.

Conjugated polymers are macromolecular chains made up from large number of identical, covalently bonded units called monomers. Compared to small molecules, most[4] conjugated polymers exhibit mobilities lower by orders of magnitude and transport relies mostly on charge delocalisation along the single polymer backbone [14] rather than states extended over large number of molecular units. For this reason, the electronic properties are mostly governed by properties of individual polymer strands rather than long range crystalline order. It is therefore crucial to minimise the number of individual backbone defects, such as torsion or non-linearity, simultaneously maximising the average molecular weight. Since conjugated polymers are solution processed, the backbones are modified with side chains typically made of linearly bonded, $sp^3$ hybridized carbon atoms. Side chains have dual role- they not only increase solubility in organic solvents but also control aggregation and hence microstructure of polymer films. As one will see in latter chapters, the same polymer backbone modified with different kinds of side chains exhibits different transport properties and side

[2]This record-breaking number refers to data collected from a single device in saturation regime and might be overestimated as a consequence of mobility extraction method. In linear regime, the same device demonstrated mobility of 20 $cm^2V^{-1}s^{-1}$ and average saturation mobilities of the batch were reported to be 25 $cm^2V^{-1}s^{-1}$. A more in-depth discussion of mobility extraction and possible causes of mobility overestimation can be found in review paper by Sirringhaus[5].

[3]Transfer integrals are measure of degree of wave function overlap between adjacent molecules and hence are modulated by intermolecular vibrations. Mathematically, transfer integral $t$ between molecules $i$ and $j$ is defined as $t =< \phi_i \mid H \mid \phi_j >$ where $\phi_i$ and $\phi_j$ denote wave functions localised on adjacent molecules and $H$ is an electronic Hamiltonian.

[4]Although historically true, recent progress in development of conjugated polymers reduced the performance gap to approximately one order of magnitude.

chain engineering is one of the less understood but certainly crucial aspects of molecular design [18]. With exception of pBTTT, all polymers presented in this thesis are classified as so-called donor-acceptor polymers. This class of conjugated polymers comprise alternating sequence of electron rich donor units and electron poor acceptor units along the backbone. Over past years there has been increasing interest in donor-acceptor systems due to their low band gap facilitating injection of both electrons and holes, which is why they have significantly contributed to improvement of ambipolar transport properties of polymer FETs.

In this thesis I am going to discuss two small molecular systems (C8-BTBT and dif-TES-ADT) and five conjugated polymers (pBTTT, IDT-BT, two derivatives of DPP-BTZ and NDIT2). My choice of small molecules is rather standard- I was looking for well understood molecules that could be used as model systems to test my methods development. Similarly, I begin studies of conjugated polymers by testing my instrumentation on pBTTT, which is one of earliest high mobility systems, before proceeding to recently developed IDT-BT and DPP-BTZ. Finally, I use NDIT2 as an example of donor-acceptor system that provides a link between early crystalline and modern amorphous conjugated polymers.

## 1.3 Charge transport and the role of disorder

There is no single, complete theoretical model that fully explains transport properties observed in organic semiconductors. The mechanism of transport is still a matter of debate and models previously developed for inorganic semiconductors can only be applied in a limited scope. Within organic semiconductors there are clear discrepancies in transport characteristics between small molecular systems and conjugated polymers. Furthermore, a single system is likely to exhibit very different characteristics depending on temperature of external field regime and no single model can be used to explain physics of charge transport in a comprehensive manner. Organic semiconductors require a more holistic approach- in the following paragraphs I am going to briefly introduce some transport models, that often coexist and can be used to justify observed transport characteristics in different regimes.

Charge transport in a highly ordered inorganic semiconductor can be explained by phenomenological **band-like transport** model. When atoms are strongly coupled, their individual energy levels overlap and widen forming two continuous energy levels called valence and conduction band corresponding to bonding and anti-bonding states. At zero Kelvin temperature, the valence band is completely filled with electrons

and the conduction is empty. Electrons can be injected into conduction band either thermally, as in intrinsic semiconductors, or through doping process. The electrons that have been injected into conduction band are highly mobile and move in delocalised, extended states. Apart from impurities and defects in lattice, the major cause of scattering are phonons causing mobility to decrease with increasing temperature. Typically, the mobility scales with temperature as inverse power law:

$$\mu \propto T^{-n} \tag{1.5}$$

where $n$ is an empirical constant. Scaling of mobility indicating band-like transport has been reported for several high purity single crystals such as naphtalene and perylene [12, 13]. Observed mobilities exceeding 100 $cm^2V^{-1}s^{-1}$ at temperatures below 30 K indicate that the transport depends on intermolecular charge delocalisation, however inverse power dependence of mobility on temperature does not necessarily imply band-like transport, as was reported by Sakanoue et al [19]. Sakanoue demonstrated that in TIPS-pentacene negative temperature coefficient of the mobility at high fields is not due to extended-state conduction but to localized transport limited by thermal lattice fluctuations- in such transport mobility arises from freezing of low-energy intermolecular vibrations. In practice coupling between adjacent molecules is relatively weak and can easily be broken by lattice disorder and phonons leading to localized states. Furthermore, organic semiconductors typically have a high degree of disorder and grain boundaries that rule out band-like transport in most cases.

The **multiple trapping and release** model accounts for low mobility in materials where highly conducting regions coexist with local structural disorder such as grain boundaries. Originally developed for hydrogenated amorphous silicon (a-Si:H) [20], it assumes existence of a narrow transport band associated with high concentration of trap states, such as impurities or lattice defects, that immobilise charge carriers. These traps can be classified as deep traps, meaning that they are located close to the centre of the band gap, or shallow traps closer to the conduction or valence band. Transport then operates as a sequence of trapping events with trapping probability assumed to be nearly 1, and subsequent releases that are activated thermally. Assuming homogeneous spatial distribution of traps [21], charge mobility exhibits an Arrhenius-like temperature dependence:

$$\mu = \mu_0 \cdot \alpha \cdot exp\Big[-\frac{E_{trap}}{kT}\Big] \tag{1.6}$$

where $E_{trap}$ is energy of the trap state, $\alpha$ is the ratio between the effective density of states at the transport band edge and the density of traps, and $\mu_0$ is the mobility at the band edge. When traps are not distributed uniformly but are localized around lattice defects as in polycrystalline materials, the mobility can become temperature-independent [21] and it is considered that charges are actually able to tunnel across grain boundaries.

In the absence of delocalised states hopping becomes dominant mechanism of charge transport. One of the earliest theoretical descriptions of hopping process is the **Miller-Abrahams model**. The model was originally developed to explain temperature dependence of mobility in lightly doped inorganic semiconductors at low temperatures and with an assumption of weak lattice coupling. The model assumes hopping from occupied site with energy $\epsilon_i$ to an unoccupied site with energy $\epsilon_j$ with following rate:

$$\nu_{ij} = \nu_0 \cdot exp(-2\gamma R_{ij}) \cdot \begin{cases} exp\Big[-\frac{\epsilon_j - \epsilon_i}{kT}\Big] & for\ \epsilon_j > \epsilon_i \\ 1 & for\ \epsilon_j < \epsilon_i \end{cases} \tag{1.7}$$

where $\nu_0$ is the attempt hopping frequency, $\gamma$ is the overlap factor and $R_{ij}$ is the separation between sites. The first exponential term accounts for the decay of electronic coupling with distance and tunnelling probability, however it does not incorporate the sensitivity of coupling on the relative orientation of molecules. Second term is energy-dependent Boltzmann factor for a thermally activated jump upward and is equal 1 for a jump downward. The Miller-Abrahams formalism assumes that downward jumps are not accelerated by the electric field and always occur.

Another important hopping model, which in contrast to Miller-Abrahams formalism accounts for electron-phonon interaction, is **Marcus theory** of semi-classical electron transfer rates. It was originally introduced to model inorganic crystals [22] and has later been applied to explain charge transfer in molecular crystals [23] and conjugated polymers [24]. Marcus model is based upon a concept of polaron- a quasi-particle consisting combination of charge carrier and lattice deformation resulting from strong charge-phonon coupling. The transport between adjacent sites with energies $\epsilon_i$ and $\epsilon_j$ is thermally activated and occurs with a following rate:

$$\nu_{ij} = \frac{\pi t^2}{\hbar} \frac{1}{\sqrt{kT\lambda}} \cdot exp\Big[-\frac{(\epsilon_j - \epsilon_i + \lambda)^2}{4\lambda kT}\Big] \tag{1.8}$$

where $t$ denotes transfer integral and $\lambda$ is the total reorganization energy. High rates of charge transfer require large transfer integrals and small reorganization energy. A major implication of Marcus model is that the transfer rate does not keep continuously increasing with energy difference $\epsilon_j - \epsilon_i$. For a given $\lambda$, the transfer rate first increases with the magnitude of $\epsilon_j - \epsilon_i$ reaching maximum when $\epsilon_j - \epsilon_i = \lambda$ and decreases when $\epsilon_j - \epsilon_i > \lambda$ in so-called inverted region. As a consequence, there is a turning point beyond which hopping rate will decrease with increasing electric field. In contrast to Miller-Abrahams model, the Marcus expression is valid for large electron-phonon coupling and high temperatures.

None of the models discussed so far is exhaustive on its own- these microscopic models are limited in scope and restricted to specific ranges of delocalisation lengths, temperatures and phonon coupling constants. A more general understanding is provided by macroscopic models that are valid for arbitrary range of physical parameters. In such models the total mobility can be approximated as a sum of hopping and tunnelling contributions. Tunnelling dominates the transport at low temperatures, whereas hopping is thermally activated. The relative contributions of hopping and tunnelling depend on strength of electron-phonon coupling. In case of weak coupling, the mobility is dominated purely by tunnelling and exhibits a band-like $\mu \sim T^{-n}$ dependence in the whole range of temperatures. For intermediate coupling strengths the mobility is band-like at low temperatures, but displays weaker dependence at higher temperatures. Strong coupling leads to three distinct temperature regimes. At low temperatures band-like transport is again dominant, but as the temperature increases the hopping starts to dominate and mobility increases exhibiting crossover to an incoherent, temperature-activated transport. At high temperatures thermal energy becomes large enough to dissociate polaron and residual electrons are scattered by thermal phonons. As a consequence, mobility decreases again with temperature. One of such macroscopic models is **Holstein model** based on perturbation theory [21]. The mathematical formalism will not be discussed in detail, however in case of weak strength of polaron binding Holstein's formula for hopping rate obeys a standard Arrhenius-type law, and when polaron binding is taken into account one recovers classical Marcus equation for electron transfer rate. Furthermore, the versatility of Holstein model is proven in high temperature regime- when $E_{polaron} \ll kT$, predicted mobility shows $T^{-\frac{3}{2}}$ dependence, which is in agreement with non-perturbative microscopic theories. A more in-depth discussion of micro- and macroscopic models can be found in review article by Coropceanu et al. [21].

Disorder is of central importance for physics of charge transport in organic semiconductors. Theoretical models typically distinguish two kinds of disorder: diagonal and off-diagonal. Diagonal disorder reflects fluctuations in the energies of HOMO and LUMO levels of individual molecules or polymer chain segments and is induced by electrostatic and polarization effects from adjacent molecules, which vary with fluctuations in local packing. In theoretical models this spectrum of HOMO and LUMO energies is generally described as a Gaussian distribution with standard deviation of the order of 50-100 meV in case of conjugated polymers [21]. The off-diagonal disorder is related to fluctuations of relative positions, and hence the strength of interactions, between adjacent molecules. It leads to distribution of electronic couplings within the material and modulation of tunnelling between the adjacent molecules- an important factor in systems where transport depends on intermolecular vibrational modes and thermal fluctuations limiting transfer integrals.

Structural defects are among the main factors suppressing charge delocalisation in both small molecules and conjugated polymers. In small molecules, weak van der Waals coupling results in narrow bands that can easily be disrupted by introducing disorder in the system- in the case of pentacene it was demonstrated that varying deposition conditions can lead to variations in charge mobility by up to 6 orders of magnitude [25]. Although small molecular crystals exhibit band conduction, interactions localized on individual molecules play a dominant role and room-temperature mean free path is comparable to the lattice spacing.

By contrast, conjugated polymers do not exhibit degree of crystallinity comparable to small molecules. In a fact, there is no obvious correlation between structural order at macromolecular level and transport properties- recent studies of IDT-BT prove that there are systems in which near amorphous structure and high charge mobility coexist. In such polymers charge transport is a combination of carrier delocalisation along the backbone and hopping between adjacent polymer strands [26]. As a result, the major contribution to diagonal disorder is conformational freedom leading to a distribution of torsional angles or non-linearity of the backbone. Such structural defects result in variation of local dielectric environment and formation of conjugated segments with different lengths, and therefore different HOMO and LUMO energies. All of these effects contribute to so-called energetic disorder that leads to broadening of the density of states[5]. Effectively, this means that for a given carrier's energy range there will be fewer states available for transfer.

[5]The density of states (DOS) is essentially the number of different states at a particular energy level that electrons are allowed to occupy, i.e. the number of electron states per unit volume per unit energy.

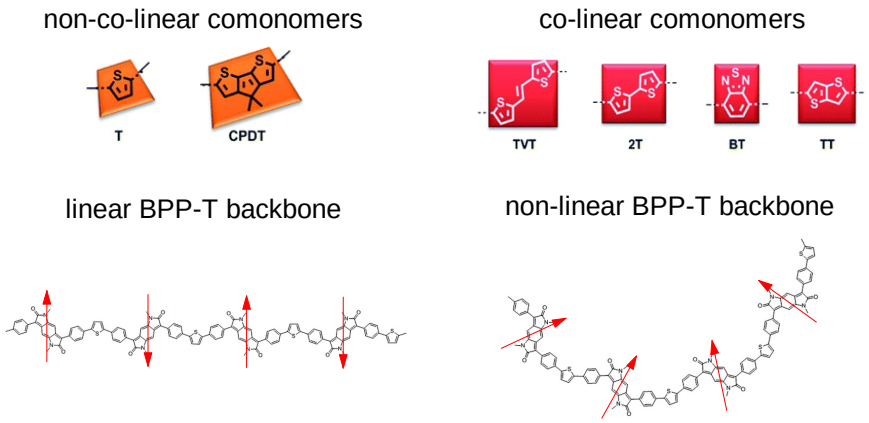


Figure 1.5: Illustration (**top**) of common examples of non-co-linear and co-linear comonomers. Red arrows denote orientation of comonomers so that difference between parallel and anti-parallel configurations is clearly marked. Depending on relative orientation, non-co-linear comonomers can form both linear and non-linear backbones (**bottom**). Figure adapted from [27].

In practice the degree of conformational freedom can be engineered at least to some extent. Figure 1.5 illustrates examples of some common polymer building blocks. These units may broadly be classified into co-linear and non-co-linear comonomers. Six-membered rings or larger units containing even number of five-membered rings typically form co-linear comonomers, whereas units with odd number of five-membered rings are non-co-linear. Polymer backbones made of co-linear comonomers are always linear in the absence of external forces such as steric interactions between side-chains. In contrast, non-co-linear comonomers often result in kinks if two or more adjacent units are in the same orientation $(\cdots \uparrow\uparrow\uparrow \cdots)$[6] and only backbones with every second unit rotated by 180° $(\cdots \downarrow\uparrow\downarrow \cdots)$ are linear as shown in bottom panel of Figure 1.5. Second factor that governs conformational freedom it the torsional potential of dihedrals along the backbone. Highly symmetric and steep torsional potential with energetic minima at 0° and 180° leads to a planar, locally ordered backbone even in the absence of long-range macromolecular order. Similarly, semi-crystalline polymers such as pBTTT exhibit local twists of the backbone, if the positions of torsional potential minima are not 180° apart, or significant variation of dihedral angles in case of gentle curvature of the potential landscape around the minima. A more in-depth discussion of the effects of comonomer non-linearity and shape of torsional potentials on polymer macrostructure is included in latter chapters.

[6] In later chapters I use spin notation denoting $[\cdots \uparrow\uparrow\uparrow \cdots]$ configuration of chain units as parallel and $[\cdots \uparrow\downarrow\uparrow \cdots]$ as anti-parallel.

## 1.4 Aims and open research questions

Organic semiconductors are far from being just scientific curiosity- the research is clearly beyond the stage of fundamental science. As previously discussed, disruptive model of innovation is based upon ability to maintain innovation curve that is steeper than curve of performance demand. At the same time, the nature of organic chemistry provides virtually unlimited number of potential systems of interest that may be synthesized and tested. As a consequence, research efforts are not concentrated and their scope gradually diffuses over time- contrary to what is expected from commercial point of view. Paradoxically, one may argue that the field as a whole became a victim of its own success as there are no low hanging fruits left and one has to continuously scale research capabilities in order to maintain rate of performance growth. In fact, the research is obviously not a trial and error, but it appears to be rather heuristic within some selected classes of materials that are perceived as promising. There do exist design rules based on previous studies, however they are predominantly based on empirical intuition or experience with certain compound families and hence often misleading. For example, the prior knowledge of transport mechanism in crystalline P3HT, once perceived as high performance system, cannot be applied to explain phenomenon of recently discovered near amorphous systems- in many ways our understanding of physics of IDT-BT is in contradiction with previously known design guidelines and theoretical simulations are just post-factum justification.

Scientific community intends to address the problem of molecular design exploiting concepts of structure-property relationship and rational design. Idea of structure-property relationship is based upon assumption that geometrical structure of the system can be related to transport properties in a predictable manner. The correlation is generally true given the strong electron-phonon coupling in organic semiconductors, however the exact causation is not straightforward to understand. In general, rules of design based on previously reported coexistence of certain structural features and transport properties are difficult to implement in practice- existing suggestions are mostly descriptive and qualitative parameters such as length or shape of alkyl chains cannot be quantified as numerical inputs for regression models or other methods of predictive analytics.

Rational design, on the other hand, is a more general concept that emphasizes theoretical prediction of system's properties using computational methods without any a-priori assumptions about structure-property relationships. In practice, rational design is a heuristic way of property prediction based on established simulation methods such as Density Functional Theory or Monte Carlo. In recent years rational design

has gained a lot of momentum as a way to preliminary screen tens to hundreds of molecules and select few for synthesis and experimental characterization.

Key factor fostering computational screening is fact that manual labour and experimental resources are gradually becoming more precious than computational simulations- the performance of computers grows faster than number of PhD scholarships and research grants founded by the government. One of earliest attempts of in silico design approach was published by Blouin [28] and co-workers, who performed series of DFT energy levels calculations on 9 hypothetical derivatives of poly(2,7-Carbazole) (PCDT) to identify compounds suitable for photovoltaic devices. At that time DFT simulations were performed on isolated monomers, however nowadays prediction of HOMO and LUMO levels from first principles is perceived as a standard computational procedure and can be performed on tetramers using typical desktop workstation. A first truly large-scale computational screening is the Harvard Energy Project [29]. Starting from 26 basic building blocks, Hachemann and co-workers constructed a database of 2.3 million potential OPV donor molecular motifs that will be gradually screened. Although the extent of this screening is truly unprecedented, the scope is limited to calculations of HOMO and LUMO levels for isolated molecules in a vacuum phase and so far only vague design guidelines were suggested [30]. A more successful approach has been published by Sokolov et al [31]. Sokolov designed 7 hypothetical derivatives of dinaphtothienothiophene (DNTT), performed structural optimisation and calculated transfer integrals using semi-classical Marcus theory. Two systems were subsequently synthesized and characterized experimentally- the best performing system demonstrated hole mobility as high as 16 $cm^2V^{-1}s^{-1}$ compared to 2.9-3.1 $cm^2V^{-1}s^{-1}$ previously reported for DNTT. To my knowledge, Sokolov's methodology is the most in-depth computational screening procedure published to date, however it is a purely static method that completely neglects effects of lattice vibrations.

In this thesis I attempt to establish a link between lattice vibrations and transport properties by means of computer simulations and experimental spectroscopy. Although Sokolov's publication is an inspiration, I wanted to explore possibility of getting insight into dynamical processes in both small molecules and conjugated polymers hoping that I might be able to establish design rules based on quantitative computational models rather than empirical intuition. To large extent this has never been done before- although all components required for such study have already been developed in different areas of science, I am not aware of any prior attempt to combine them and implement to study organic semiconductors. In my opinion, the cornerstone to understand role of lattice vibrations is ability to address difficulties arising from ex-

perimental techniques that are used to probe vibrational modes. Both IR and Raman spectra provide information about energies of lattice modes but not associated molecular displacements. The loss of information about the system associated with physical measurement of intensity is similar to phase problem in crystallography- there is no method to directly reconstruct vibrational displacements from spectral intensities and in order to make a meaningful conclusion one has to use brute force methods such as guessing a hypothetical geometry that, when used as an input for simulation, results in set of spectra matching experimental data.

In case of small molecular systems I am interested in understanding low frequency intermolecular modes in the region below 100 $cm^{-1}$ that are crucial for modulation of hopping rates. This region of vibrational spectrum is particularly challenging to predict and probe experimentally. Unlike intramolecular modes, which can be calculated using isolated molecules in a vacuum phase, intermolecular modes require use of periodic boundary conditions and tight convergence criteria scaling the computational cost by orders of magnitude- molecules such as C8-BTBT are large by standards of computational quantum chemistry and I had to use latest national supercomputing facilities to complete simulations in a reasonable time-frame. Second degree of computational complexity arises from van der Waals bonding. Current implementations of DFT are a trade-off between efficiency and exactness- it is known that dispersion forces are often difficult to reproduce in accurate manner using pure ab-initio methods [32] and one has to apply semi-empirical correction to account for non-local interactions. Parametrization of dispersion correction is based on set of model systems and hence accuracy depends on "degree of similarity" between benchmark and simulated molecule. A more in-depth discussion of dispersion correction is included in Computational Methods section.

Although bulk structure of conjugated polymers is difficult to predict and quantify due to presence of disorder, studies of vibrational modes are paradoxically less challenging compared to crystalline small molecules. As previously mentioned, charge transport strongly depends on local conformation of the isolated polymer backbone and long range order is of lesser importance. In consequence, I focus on intramolecular modes located in 1200- 1600 $cm^{-1}$ region that typically correspond to various aromatic ring stretching modes. Calculations of those vibrations do not require periodic boundary conditions and can be performed on an isolated molecule in vacuum phase, reducing computational cost by orders of magnitude. It is important to realize that, because of known errors in intensity calculation, simulations performed on an isolated molecule do not provide reliable and quantitative information about the

degree of torsional disorder. However, inaccuracy of computational methods is systematic and although one cannot make a one to one comparison of experimental and simulated spectra, it is possible to correlate qualitative trends in data such as variation of peak intensities as a function of torsional angles. Specifically for that reason I decided to develop a high pressure diamond anvil cell and collect Raman spectra as a function of hydrostatic pressure, since I already knew that in some systems it was demonstrated that planarity of the backbone changes with pressure [33, 34]. High pressure Raman spectra tell us about the compound "stiffness" and resilience of torsional degrees of freedom but not about statistical distribution of torsional angles and nature of disorder. To get a better insight into backbone conformations at local level I had to perform molecular dynamics simulations that account for disorder arising from thermal motion. Unlike DFT, molecular dynamics is a purely Newtonian method that allows simulations of large systems, which are far beyond capabilities of modern supercomputers when treated quantum mechanically. There are, however, several drawbacks and practical implementation of this method is discussed in latter chapters.

The thesis is organized as follows: **Chapter 2** is an overview of computational methods that were adapted and developed during the project. DFT methods that were applied to calculate vibrational spectra of crystalline small molecules are based on previous reports of mode calculations by Li et al. [35] and Parrott et al. [36]- both groups published successful calculations of terahertz spectra for small molecular crystals such as benzoic and malic acids. Sanchez-Carrera demonstrated [37] calculations of phonon frequencies and electron-vibration couplings in oligoacenes such as anthracene and naphtalene making strong case for further studies of $\pi$-conjugated materials using DFT methods, and Civalleri [38] successfully parametrized empirical dispersion correction for simple molecular crystals such as urea and urotropine. Analysis of these publications led me to conclusion that all components required for study of crystalline small molecules are proven to perform well in specific cases, but were never implemented collectively to study large and more demanding systems such as C8-BTBT. In contrast, computational studies of conjugated polymers were performed in collaboration with group from Mons University and were entirely based on previously published methodology based on Newtonian mechanics [39, 40] and unlike systematic DFT it requires some degree of empirical intuition. Computational results were complemented by experimental high pressure Raman spectroscopy, which is introduced in **Chapter 3**. The key component of the setup is a custom made diamond anvil cell and hence major part of the chapter is devoted to high pressure techniques, which are not common in the field of organic semiconductors. Historical evolution and various types

of high pressure instruments are discussed to provide a general context and explain my motivation to modify existing designs of diamond anvil cells. Theory of Raman spectroscopy is introduced only in brief, since standard off-the-shelf spectrometer was used and spectra were acquired in a routine manner.

In **Chapter 4** I report DFT-based methodology developed to predict vibrational modes and Raman spectra of crystalline C8-BTBT and dif-TES-ADT. Both compounds are classified as large in terms of number of atoms per unit cell and hence I carefully evaluated the interplay between computational efficiency and accuracy. Although CRYSTAL09 code was my initial choice due to implementation of Gaussian basis set, I encountered some unforeseen problems and had to switch to plane-wave based CASTEP code. In **Chapters 5** to **8** I report computational and experimental studies of conjugated polymers. My first system of interest is pBTTT- a model compound that was studied to verify my methodology of combined high pressure Raman spectroscopy and DFT simulations. I then proceed to IDT-BT which was at that time completely novel and poorly understood system. From experimental spectra it is evident that the backbone of IDT-BT is resilient to torsional disorder and quantum calculations of torsional potentials suggest energetic minima corresponding to planar configuration. Molecular dynamics simulations of crystal packing revealed coexistence of several distinct packing motifs that have planar backbone and yield similar energies per mole. Inspection of thermally disordered phase led me to conclusion that IDT-BT is capable to accommodate structural disorder in a novel way that preserves backbone planarity- rather than twisting single bonds along the backbone, the polymer chain becomes wavy at a length scale of few monomers. Similar mechanism of disorder accommodation via bending and not twisting has been demonstrated for DPP-BTZ in **Chapter 7**. I examine two DPP-BTZ derivatives with different types of side-chains and hence different packing motifs in ordered, crystalline phase whereas simulations of thermally disordered phases reveal that both compounds exhibit qualitatively similar backbone structures. In **Chapter 8** I report pressure dependence of Raman spectra for two NDIT2 films spun using different solvents. It is known [41] that depending on solvent used, NDIT2 forms two conformers with different crystallographic orientation and charge mobilities. The purpose of my study was to find direct evidence of causation between backbone properties and charge transport within a single system. Finally, in **Chapter 9** I present summary, general conclusions drawn from this work and suggestions for further research and novel design rules based on my studies.

# Chapter 2

# Computational Methods

## 2.1 Density functional theory

### 2.1.1 Elementary quantum chemistry

For most computational quantum chemical methods the ultimate goal is to obtain (approximate) solution of the non-relativistic, time-independent Schrödinger equation:

$$\hat{H}\,\Psi_i(\mathbf{x}_1, ..., \mathbf{x}_N; \mathbf{R}_1, ...\mathbf{R}_\mathrm{M}) = E_i\,\Psi_i(\mathbf{x}_1, ..., \mathbf{x}_N; \mathbf{R}_1, ...\mathbf{R}_\mathrm{M}) \tag{2.1}$$

where $\hat{\mathrm{H}}$ is the Hamiltonian operator for a system defined by wave function $\Psi_i$ and consisting of N electrons with spatial coordinates $\mathbf{x}$ and M nuclei with spatial coordinates $\mathbf{R}$, in the absence of external magnetic or electric fields. The Hamiltonian is a differential operator representing the total energy:

$$\hat{H} = \hat{T}_e + \hat{T}_\mathrm{N} + \hat{V}_\mathrm{Ne} + \hat{V}_\mathrm{NN} + \hat{V}_\mathrm{ee} \tag{2.2}$$

where the first two terms describe the kinetic energy of the electrons and nuclei respectively. The remaining three terms define potential part of the Hamiltonian and represent attractive electrostatic interaction between nuclei and electrons, repulsive interaction between nuclei and repulsive interaction between electrons. The wave function $\Psi_i$ contains all information that can possibly be known about the quantum system at hand. Finally, $E_i$ is the numerical value of the energy of the state described by $\Psi_i$.

As one can see, for a system of many atoms the Schrödinger equation is in a fact a set of coupled differential equations. This can be greatly simplified if we take an advantage of significant differences between masses of nuclei and electrons. In

the *Born-Oppenheimer* approximation it is assumed that nuclei are "clamped" in space. The wave function of the system may be broken into nuclear and electronic components:

$$\Psi = \psi_{\text{electronic}} \times \psi_{\text{nuclear}} \tag{2.3}$$

hence Schrödinger equation becomes separable and one can reduce the Hamiltonian to so-called electronic Hamiltonian:

$$\hat{H}_{\text{elec}} = \hat{T} + \hat{V}_{\text{Ne}} + \hat{V}_{\text{ee}} \tag{2.4}$$

such that

$$\hat{H}_{\text{elec}}\Psi_{\text{elec}} = E_{\text{elec}}\Psi_{\text{elec}} \tag{2.5}$$

and

$$E_{\text{total}} = E_{\text{elec}} + E_{\text{nuc}} \tag{2.6}$$

therefore from a mathematical point of view the *Born-Oppenheimer* approximation effectively reduces dimensionality of the problem. In order to solve equation 2.5 we first have to set up a specific Hamiltonian of the system. By inspecting equation 2.4 one can see that the only information that depends on the actual molecule is the number of electrons in the system and the external potential, however remaining parts representing kinetic energy and electron-electron repulsion are independent of the particular molecule we are looking at. Unfortunately, apart from one trivial exception, the non-linear Coulomb terms result in a non-separable differential equation with entangled eigenfunctions and therefore no strategy to solve Schrödinger equation exactly exists.

The only systematic approach to determine the ground state wave function $\Psi_0$ is the *variational principle*, which holds a prominent place in quantum-chemical calculations. The variational principle states that the energy computed as the expectation value of the Hamiltonian $\hat{H}$ from any guessed wave function $\Psi_{\text{trial}}$ will be the upper bound to the true energy of the ground state, i. e.

$$\left\langle \Psi_{\text{trial}} \middle| \hat{H} \middle| \Psi_{\text{trial}} \right\rangle = E_{\text{trial}} \geq E_0 = \left\langle \Psi_0 \middle| \hat{H} \middle| \Psi_0 \right\rangle \tag{2.7}$$

where the equality holds only if the trial wave function is identical to the true ground state wave function. See [42] for a formal proof of the inequality 2.7. The strategy for finding ground state energy and wave functions is based on minimization of the

functional $E(\Psi)$ by searching through *all acceptable N-electron wave functions*. By acceptable it is meant that the $\Psi_{\text{trial}}$ must make physical sense, i.e. it must be continuous everywhere and be quadratic integrable, otherwise the normalization condition could not be fulfilled.

### 2.1.2 Hartree-Fock approximation

It is impossible to search for $\Psi_{trial}$ through all acceptable N-electron wave functions, therefore one has to define a suitable subset, which offers a reasonable approximation to the exact wave function. In the Hartree-Fock scheme this is realized by constructing an asymmetrical product of N one-electron wave functions $\chi_i(x_i)$, which is usually referred to as a *Slater* determinant:

$$\Psi_0 \approx \frac{1}{\sqrt{N!}} \begin{vmatrix} \chi_1(x_1) & \cdots & \chi_N(x_1) \\ \vdots & \ddots & \vdots \\ \chi_1(x_N) & \cdots & \chi_N(x_N) \end{vmatrix} \tag{2.8}$$

where $\Psi_0$ denotes wave function of N-electron system and single-electron wave functions $\chi_i(x_i)$, called *spin-orbitals*, are composed of spatial wave functions $\phi(\mathbf{r})$ and one of the spin functions, $\alpha$ or $\beta$:

$$\chi(\mathbf{x}) = \phi(\mathbf{r})\sigma(s),\ \sigma = \alpha, \beta \tag{2.9}$$

The next step is to use variational principle to find the best Slater determinant. The spin orbitals $\chi_i(x_i)$ are varied under the constraint that they remain orthonormal such that the energy obtained from the corresponding Slater determinant is minimal. The condition for the "best" spin orbitals is given by *Hartree-Fock equations*:

$$\hat{F}\chi_i = \epsilon_i \chi_i \tag{2.10}$$

where $\epsilon_i$ is a Lagrangian multiplier (physically, this corresponds to orbital energy) and Fock operator $\hat{F}$ is an effective one-electron operator given by

$$\hat{F}_i = \hat{T}_i + \hat{E}_{Ne} + \sum_j^N (\hat{J}_j(x_i) - \hat{K}_j(x_i)) \tag{2.11}$$

where $\hat{J}$ is the Coulomb operator, $\hat{K}$ is so-called exchange operator and the sum in equation 2.11 represents the average repulsive force experienced by the $i^{th}$ electron due to the remaining N-1 electrons and is referred to as the *Hartree-Fock potential* $V_{HF}$.

The derivation of equations 2.10 and 2.11 can be found in a relevant textbook [43].

The wave function of many-electron system must be anti-symmetric under exchange of any two electrons, since they are fermions. The antisymmetry produces a spatial separation between electrons that have the same spin and thus reduces the Coulomb energy of the electronic system. One must realize that the occurrence of exchange term is entirely due to antisymmetry of the Slater determinant. The reduction of the energy of the system is called the *exchange energy*.

It is important to emphasize that the Fock operator is an effective single-electron operator and the final Hamiltonian of the system is simply a sum of all Fock operators. In other words, the Hamiltonian now describes a system of N electrons that no longer interact with each other but experience an effective potential $V_{HF}$. This mean-field approximation provides great simplification of many-body problem that would otherwise be unsolvable. In a typical Hartree-Fock technique, we have to start with a "guessed" set of orbitals with which the Hartree-Fock equations are solved. The resulting set of new orbitals is then used in the next iteration and the process is repeated. This procedure is sometimes called the *self-consistent field* (SCF) method.

### 2.1.3 Kohn-Sham equations and hybrid functionals

In conventional approach to the quantum chemistry the wave function $\Psi$ is used as the key quantity. This is justified by fact that by definition $\Psi$ constraints all information that can be known about the state of the particular system. The Hartree-Fock approximation is a typical example of this approach. There is, however, a severe problem that makes it very difficult to apply such a strategy, especially for large system such as organic molecules. The wave function is a very complicated quantity and, since it is not an observable, cannot be probed experimentally. Moreover, the wave function of N electrons depends on 4N variables (three spatial coordinates and one spin variable), which makes the computational treatment very difficult if not impossible. On the other hand, the Hamiltonian contains only operators that act on at most two particles at a time, independent of the size of the system. Hence, the question is whether the complicated wave function based techniques are really needed for obtaining the energy and other properties of the system or whether the wave function contains irrelevant information and we can get away with a less complicated formalism. This consideration finally resulted in the development of a completely new method of dealing with multi-electron systems, known as the *Density Functional Theory* (DFT).

The Coulomb energy of the system can be reduced below its Hartree-Fock value if electrons that have opposite spins are also spatially separated. In such a case, the

Coulomb energy of the system is reduced at the cost of increasing the kinetic energy of the electrons. The difference between the energy of the electronic system and the energy calculated in the Hartree-Fock approximation is called the *correlation energy.*

The density-functional theory, developed by Kohn and Hohenberg [44] provided a method for describing effects of correlation and exchange in electron gas. Kohn proved that the total energy, including correlation and exchange, is a unique functional (so called Kohn-Sham functional) of the electron density $n(\mathbf{r})$. Thus, all properties of all states are formally determined by the ground state density. The minimum value of the total energy functional is the ground-state energy and the density that yields this minimum is the exact single-particle ground state density. Kohn and Sham [45] then proved that it is possible, formally, to replace the many-body problem by an exactly equivalent set of self-consistent one-electron equations. The set of wave functions $\psi_i$ that minimize the Kohn-Sham functional is given by the self-consistent solutions to the Kohn-Sham equations [45]:

$$\left[\hat{T} + \hat{V}_{\text{ion}}(r) + \hat{V}_{\text{Coulomb}}(r) + \hat{V}_{\text{XC}}(r)\right] \psi_i(r) = \varepsilon_i \psi_i(r) \tag{2.12}$$

where the exchange-correlation potential $V_{\text{XC}}$ is given formally by the exchange-correlation derivative:

$$V_{\text{XC}} = \frac{\delta E_{XC}[n(r)]}{\delta n(r)} \tag{2.13}$$

As for Hartree-Fock method, Kohn-Sham equations represent a mapping of the interacting many-electron system onto a system of non-interacting electrons moving in an effective mean-field potential. If the correlation-exchange functional is known exactly, taking the derivative of the functional with respect to the density would produce an exchange-correlation potential that includes the effects of correlation and exchange exactly (for rigorous proof see[45]). The typical scheme of solving self-consistent field equations is following:

1. Choose a trial density $n(\mathbf{r})$. The electron density is an observable that can be probed with x-ray diffraction, therefore a reasonable guess can be easily made.

2. Calculate the density dependent energy functional $E_{\text{XC}}[n(\mathbf{r})]$ and hence relevant potentials.

3. Solve Kohn-Sham equations 2.12 by diagonalization of the Hamiltonian matrix.

4. Calculate new density $n(\mathbf{r})$ using $\psi_i(\mathbf{r})$ from step 3.

5. Iterate until the difference between $n_{trial}$ and $n_{calculated}$ is below predefined threshold.

The density functional theory is far more efficient than Hartree-Fock approximation, however its accuracy depends on choice of proper exchange-correlation functional. The problem is that, unlike in Hartree-Fock method, the exchange-correlation functional does not follow directly from the initial assumptions and the mathematical formalism. Within the Kohn-Sham formulation, Hartree-Fock theory can be regarded as a special case of density functional theory with exchange functional given by HF exchange functional and zero correlation functional. So far numerous functionals have been proposed. The oldest is the Local Density Approximation (LDA), which has been suggested by Hohenberg and Kohn in their original DFT paper [44] and more recent examples include PW91 (Perdew/Wang 91) [46] and PKZB (Perdew, Kurth, Zupan and Blaha functional) [47], however most of the functionals lack universality, i.e. some of them perform very well in in certain circumstances but fail in others. A compromise between computational efficiency and accuracy is realized via so-called *hybrid functionals*, which incorporate portion of the exact exchange for the Hartree-Fock theory with exchange and correlation form other sources such as classical DFT functionals and even empirical corrections. An example of hybrid functional is B3LYP (Becke, 3-parameter, Lee-Yang-Parr) [48], which was used during this project. A more detailed discussion of various types of functionals and their performance can be found in Chemist's Guide to Density Functional Theory [49].

### 2.1.4 Dispersion correction

Electron dispersion forces play crucial role in determination of properties of molecular crystals such as C8-BTBT and dif-TES-ADT that were subject of research presented in my thesis. Although DFT is in principle exact, an accurate description of electronic forces is challenging and in practice approximations must be made by introduction of so-called exchange-correlation (XC) functional. However, in certain situations approximate form of XC functional results in questionable accuracy of calculations- a prominent example is incorrect handling of long-range electron correlations by standard XC functionals and there is no doubt that the imprecise description of dispersion forces is one of the most significant limitations of modern DFT methods. In the following paragraphs I briefly discuss some of key aspects of dispersion correction including schemes I used, namely Grimme DFT-D2 and Tkatchenko-Scheffler methods that are implemented in CRYSTAL09 and CASTEP codes, respectively. In general, disper-

sion forces can be regarded as an attractive interaction arising from the response of electrons in one region to instantaneous charge density fluctuations in another [32]. The instantaneous dipole- induced dipole interaction gives rise to the $^{-1}/_{r^6}$ term in the decay of interaction energy with the interatomic separation $r$. This decay term is often improperly described by standard XC functionals because they do not consider instantaneous fluctuations of charge density and calculate the XC energy including only local properties of the system.

The key requirement for any DFT-based method of dispersion correction is that it reasonably reproduces $^{-1}/_{r^6}$ asymptote of the interaction energy in the gas phase, were r represents the distance between the particles. This is achieved by adding an additional energy term that accounts for the missing long range interactions so that total energy then reads:

$$E_{\text{total}} = E_{\text{dft}} + E_{\text{dispersion}} \tag{2.14}$$

were $E_{\text{dft}}$ is the total energy computed with a given XC functional and $E_{\text{dispersion}}$ is a correction term accounting for long range interactions. In the most general form $E_{\text{dispersion}}$ may be expressed as follows:

$$E_{\text{dispersion}} = -\sum_{A,B} C_6^{AB}/r_{AB}^6 \tag{2.15}$$

where the dispersion coefficients $C_6^{AB}$ depend on the elemental pairs $A$ and $B$. As one can see, the underlying assumption is that dispersion correction terms are pairwise additive and can be expressed as a sum over all possible pairs of atoms within the system.

The pairwise correction scheme is widely used due to low computational cost and simplicity; nevertheless there are certain shortcomings that limit accuracy of the method. Obviously, the $C_6/r^6$ dependence neglects many-body dispersion effects [50] and faster decaying terms such as $C_8/r^8$ or $C_{10}/r^{10}$. Second, the $C_6/r^6$ function diverges to negative infinity for small r and one has to implement additional method to remove the divergence. In practice this is typically done by introducing some form of "damping" function that depends on the inter-atomic separation. The damped correction is typically expressed in following form:

$$E_{\text{dispersion}} = -\sum_{A,B} f(r_{AB}, A, B) C_6^{AB}/r_{AB}^6 \tag{2.16}$$

where the damping function $f(r_{AB}, A, B)$ is equal to one for large inter-atomic distance

r and decreases to zero for small $r$ [51]. It is important to realize that the shape of resultant binding energy cure depends on both XC functional and damping function; therefore damping function must be adjusted so as to be compatible with each XC functional. The fitting of damping function is also sensitive to the definition of van der Waals radii and must be done carefully; otherwise it can affect the binding energies even more than the $C_6$ coefficients [52].

Finally, it is not entirely clear how to obtain $C_6$ coefficients. Several formulae, often based on experimental input such as ionisation potentials, have been proposed for this. Unfortunately, this reliance on experimental data limits the set of elements that can be treated to those typically present in organic compounds. One of a more widely applicable method is scheme developed by Grimme, often referred to as DFT-D2. In Grimme's approach the dispersion coefficients are calculated from a formula which couples ionization potentials with static polarizabilities of isolated atoms [32] and proportionality constants that were adjusted to reproduce experimental binding energies-for that reason Grimme's scheme is often classified as a semi-empirical method. It is important to emphasize that in DFT-D2 scheme the $C_6$ coefficients are predetermined and kept constant during calculation. Even though such approach to treat dispersion correction seems to be rather simplistic as it completely neglects variations in the environment of the atoms, its applicability to predict vibrational properties of molecular crystals has been demonstrated by several authors [38, 53, 54]. On the practical side, DFT-D2 algorithm is implemented in CRYSTAL09 code and $C_6$ coefficients can be imported from publicly available database [55], although in principle it is possible to fine-tune them using first principles calculation.

A fundamental problem with DFT-D2 scheme is that the $C_6$ coefficients are predetermined and therefore the same coefficient will be assigned to an element regardless its hybridization or oxidation state [32]. In some cases this approximation can lead to significant errors, for example in case of carbon $C_6$ coefficients can differ by more than 30% between the sp and $sp^3$ states [56]. One way to overcome this limitation is to introduce variable $C_6$ coefficients, whose values depend on physical neighbourhood of an atom. An example of such dispersion correction is method proposed by Tkatchenko and Scheffler in 2009 [57], often referred to as TS scheme. In TS method $C_6$ coefficients for pairs of unlike atoms are derived from free-atom polarizabilities and $C_6$ coefficients. Both quantities are derived using calculations from first principles and contrary to DFT-D2 no empirical inputs are necessary. In order to account for environmental dependence of pairwise $C_6$ coefficients in molecule or solid, Tkatchenko and Scheffler introduced concept of effective volume, referenced to the free atom in

vacuum. TS scheme takes advantage of the direct relation between polarizability and volume [58] to determine changes of the dispersion energy. During the calculation electron density of the system is divided using Hirshfeld partitioning scheme [57] and for each atom its corresponding density is computed to derive volume-dependent factors of proportionality that link free-atom and local $C_6$ coefficients.

A somehow similar logic was applied to extension of Grimme's scheme, often referred to as DFT-D3 [55]. In DFT-D3 the environmental dependence of $C_6$ coefficients is captured by considering the number of neighbours each atom has- it is assumed that as the number of neighbours increases, the atom gets squeezed and resultant $C_6$ coefficient decreases. To account for this effect, DFT-D3 makes reference to a database of precalculated $C_6$ coefficients corresponding to various states of hybridisation. During calculation appropriate $C_6$ coefficients are assigned by making a continuous interpolation between the precaculated reference values. Although DFT-D3 scheme is rather simple way of accounting for changes in atomic neighbourhood, it yields pretty accurate results with mean absolute percentage deviation in $C_6$ coefficients of 8.4% [32]. This number indicates somehow lower precision when compared with TS, however it is efficient computationally since the number of neighbours can be derived quickly.

As a final remark I would like to briefly comment on two more sophisticated schemes of dispersion correction: long-range density functionals and methods involving many-body interactions. As mentioned before, standard XC functionals are local and do not account for long-range interactions. Rather than adding separate contribution to total energy as in equation 2.14, one may embed an additional non-local term in the functional and calculate the dispersion interaction directly from electron density without making reference to any predetermined input parameters, such as atomic polarizabilities of free atom $C_6$ coefficients. A notable example of non-local functional is so called van der Waals density functional (vdW-DF) suggested by Dion e al. in 2004 [59] and more recent functionals such as optB88 and optPBE have been shown to yield accurate results for a wide range of systems [60, 61]. Although long-range functionals are very elegant way of addressing dispersion correction, their computational cost is often prohibitive compared to parametrised methods such as DFT-D or TS.

The main reason behind development of many-body methods is fact than in pairwise models the interaction energy of two molecules or atoms remains constant no matter material separates them and collective excitations are not considered [62]. Although these effects do not seem to be crucial in the gas phase, they are important for condensed matter systems where interactions are screened[62]. The range of multibody approaches is quite broad and spans from atom centred interactions to methods

using electron orbitals. A notable example of atom-centred scheme is recent application [63] of Axilrod-Teller-Muto formula to include triple-dipole interactions between three atoms. Another promising method using electron orbitals to calculate correlation energy is based on the adiabatic-connection fluctuation-dissipation theorem (ACFDT) [64]. Methods based on ACFTD have been demonstrated to exhibit consistent accuracy for solids capturing features that the pairwise methods fail to describe [65, 66] in a correct manner. As with non-local functionals, the computational expense is higher than that of Grimme's and Tkatchenko schemes and applicability of both methods is rather limited. A more in-depth discussion of dispersion correction methods can be found in review article published by Klimes et al. [32].

## 2.2 Molecular dynamics

Molecular dynamics has been extensively used to determine possible conformers of conjugated polymers. Examples of possible crystalline, low energy packing motifs that have been published up to date include P3HT [67], pBTTT [68], CDT-BTZ [69], DPP-DTT [70], NDI-T2 [70] and IDT-BT [26]. Molecular dynamics simulations typically predict hypothetical existence of several thermodynamically stable polymorphs. Such studies provide insights into possible interdigitation of side chains, backbone conformations, $\pi$-stacking distance, interchain separation or unit cell parameters and enable interpretation of experimental GIWAXS and X-ray patterns. Several authors [39, 68] used MD simulations to draw a conclusion about link between morphology and charge-carrier transport parameters in crystalline domains. In case of disordered systems crystalline unit cells are used as an input to find semi-crystalline and amorphous phases and determine their properties such as variation of backbone planarity or distribution of density of states [26]. Finally, crystalline structures simulated using molecular dynamics may be used to correlate nucleus independent chemical shift (NICS) maps theory with experimental NMR data, as was demonstrated by Niedzialek [69] and Chaudhari [70].

Quantum-chemical calculations allow for very accurate description of geometric, electronic, and optical properties of relatively small chemical systems. The main drawback is the computational cost that quickly becomes prohibitive when increasing the size of the systems. Molecular dynamics is a versatile and powerful method used to predict possible unit cell packing and mechanical properties of large systems, such as conjugated polymers, that are beyond computational capabilities of DFT based methods. It also allows study of systems that are far from energetic minimum such as

semi-crystalline and amorphous phases. In molecular dynamics the system is treated in a classical, Newtonian manner and the general principle is very simple- assuming that the pairwise potentials are known, one can evaluate the net force acting on every single atom at any given point and hence track evolution of system completely neglecting electrons. Classical approach reduces computing expense by orders of magnitude compared to quantum mechanical methods, however in order to be successful it requires a careful parametrization of pairwise interactions and some prior knowledge or reasonable guess about possible structure. In other words, it enables to overcome computational expense of DFT but it is not systematic and final result will depend on intuition or experience of a researcher. The set of functions that replace quantum interaction with classical potentials is called a force field. Proper choice and parametrization of a force field is presumably the most important part of simulation setup. In the following paragraphs I will introduce methodology that was used to parametrize force field and explore a set of possible unit cell packing motifs.

### 2.2.1 Force fields

Choice of a force field depends on type of chemical system that is subject of simulation- most of the force fields are designed to reproduce specific classes of materials. During this project I decided to use DREIDING [71] force field, since it is known to provide a good representation of organic systems and has previously been successfully applied to predict structures and dynamics of conjugated polymers [39, 40]. The force field parameters are typically derived from experiments or parametrized to reproduce selected features such as electrostatic potentials, experimental bond lengths of crystalline structures. Force field is therefore a semi-empirical technique and the choice of parameters must be carefully verified in order to obtain correct results. In the most general form of a force filed, the potential energy for an arbitrary molecule can be expressed as a superposition of valence (bonded) interactions $E_{val}$ that depend on on the structure and non-bonded interactions $E_{nb}$ that depend only on the distance between atoms. In DREIDING force field the valence interactions consist of two-body bond stretch $E_B$, three-body angle bend $E_A$, four-body dihedral angle torsion $E_T$ and four-body inversion[1] terms $E_I$:

$$E_{val} = E_B + E_A + E_T + E_I \tag{2.17}$$

[1]The inversion term represents the difficulty of forcing all three bonds for atom $i$ bonded to exactly three other atoms $j$, $k$, $l$ into the same plane.

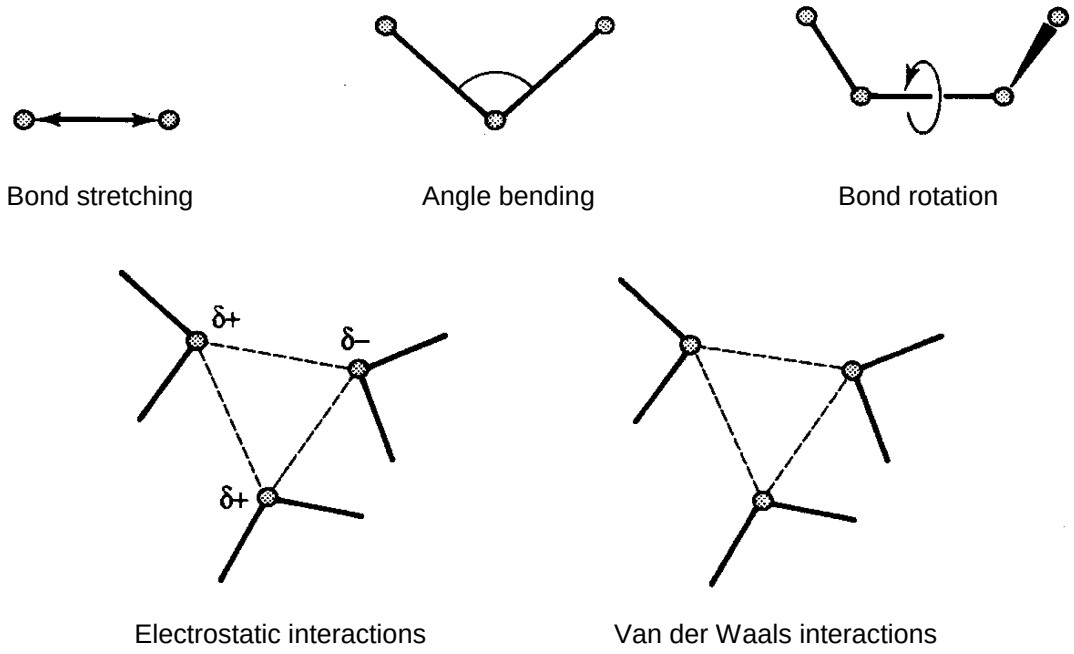


Figure 2.1: Schematic representation of the key contributions to a molecular mechanics force field.

while the nonbonded interactions consist of the electrostatic $E_Q$, van der Waals or dispersion $E_{vdw}$ and explicit hydrogen bonds $E_{hb}$:

$$E_{nb} = E_{vdw} + E_Q + E_{hb} \tag{2.18}$$

The only bonded interactions that were parametrized by us were dihedral angle torsional terms that are expressed as a symmetric Fourier expansion:

$$E_T = \sum_{n=1} B_n(1 - d_n cos(n\varphi)) \tag{2.19}$$

where $B_n$, $d_n$ and $n$ are free parameters adjusted to reproduce positions of minima and energy barriers in torsional potential. In DREIDING force field the expansion is typically parametrized to up to sixth order, but most of torsional potentials used by us were parametrized to fourth ordered[2]. Similarly, the only parameter relevant to parametrization of nonbonded interactions is the fractional charge.

To parametrize the force field, I performed geometry optimisation followed by single point energy calculations for a range of torsional angles in 5° increment and subtracted

[2]Parameters are adjusted by hand using iterated trial and error methods. Expansion up to higher terms is not convenient, since it increases dimensionality of the problem and number of iterations required to correctly parametrize the force field.

the lowest value, so that torsional potentials represent a relative energy difference with respect to the lowest energy configuration as shown in Figure 2.2. The DFT simulations were performed using B3LYP functional with cc-pvtz basis set. Compared to 6-31G(d,p) basis set used for Raman calculations, cc-pvtz is much bigger (in terms of number of wave functions used) and computationally expensive, however energy calculation is relatively quick and my aim was to maximise accuracy of calculations. This procedure was followed by adjustment of $B_n$, $d_n$ and $n$ parameters and calculation of torsional potential using molecular mechanics. Briefly speaking, the goal is to choose DREIDING parameters such that classical mechanics reproduces quantum simulation. One would typically begin with $n = 2$ or $n = 3$ so that there are 6 parameters to adjust ($B_1$ to $B_3$ and $d_1$ to $d_3$). Fitting is done by hand using trial and error method and number of terms in expansion is increased until there is sufficient agreement between calculated and parametrized torsional potentials, which means that the positions of energetic minima and height of potential barrier are correctly reproduced by force field. The fit does not have to follow DFT potential exactly, but it is important to reproduce positions of minima, local gradients of potential and energy barrier height. For example, fit of DPP-T potential shown in Figure 2.2 is an illustration of correctly parametrized force field even though it does not match quantum calculation in the entire domain. The procedure of torsion parametrization has to be performed for dihedral angles along polymer backbone and links with side-chains. The same DFT data was used to assign charge multiplicities to every atom within a monomer so that nonbonded interactions are modelled correctly, while the rest of DREIDING force field parameters remained unchanged. A more in-depth discussion of parameters and mathematical formulation of DREIDING and other force fields can be found in the original paper by Mayo and co-workers [71] and book by Leach [72].

### 2.2.2 Prediction of structure using molecular mechanics

Molecular dynamics is computationally efficient but not necessarily rigorous method of structure prediction. The process begins with a guess of possible input structures based on DFT optimised monomers and empirical data, such as GIWAXS patterns, that provide information about characteristic length scales. There are no formal rules of design and the process depends on intuition and prior experience of a researcher. Typically, one would explore all possible relative orientations of building units within a dimer, packing of dimers within a unit cell and finally structure of alkyl chains including both interdigitated and non-interdigitated cases. Typical input cell was made of 16 monomers, however some configurations of alkyl chains required a supercells

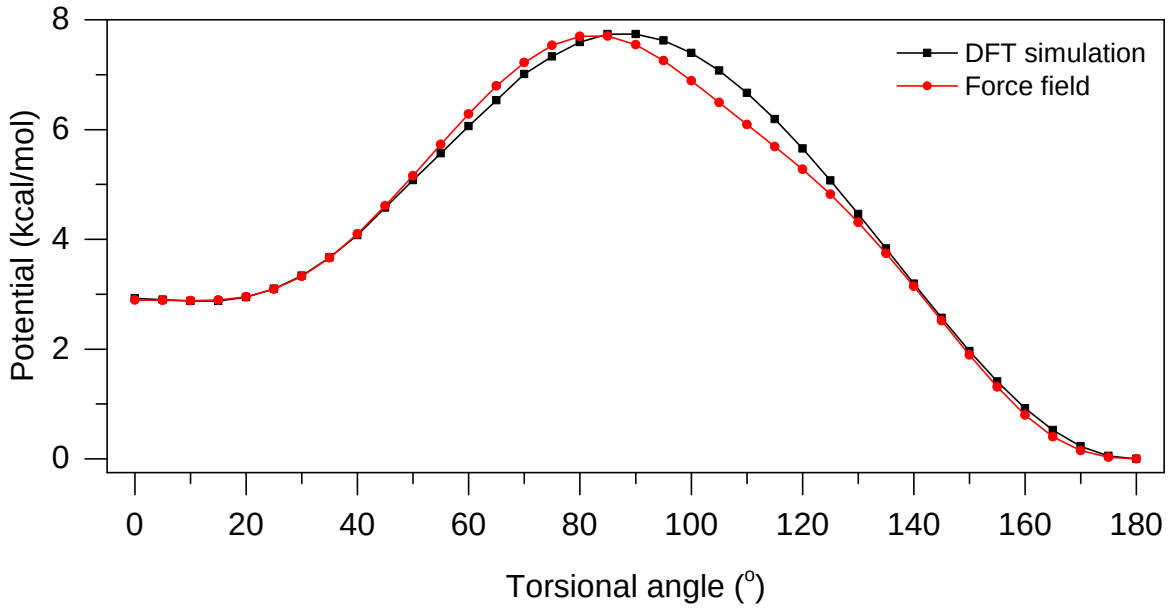


Figure 2.2: Comparison of DPP-T torsional potential calculated at B3LYP/cc-pvtz level of theory and DREIDING force field parametrization. Force field is very effective reproduction of minima, potential steepness around minima and height of potential barrier.

containing 32 monomers.

All molecular dynamics simulations were performed using Forcite module implemented in Materials Studio 6.0. Each of the input geometries was optimised to a local energetic minimum using conjugate gradient method [73] with variable cell parameters and *fine* convergence criteria corresponding to $1.0 \cdot 10^{-4}$ kcal/mol tolerance in energy change. The optimised geometries were subject to 200 ps dynamics with 1 fs time-step at T=300 K in NPT ensemble controlled by Nose thermostat and Berendsen barostat. The system was quenched every 2 ps, ie a snapshot of conformation was taken and optimised to a 0 K minimum every 1000 time-steps. The lowest energy quench output was selected as a new input and the procedure was repeated until there was no improvement in energy and finally verified at T=500 and 1000 K. Quite often it was obvious that the geometry did not converge to an ordered crystalline structure. In such a case I identified specific transitions, such as rotation of a side-chain with respect to the backbone, that lowered the overall energy and incorporated them in a re-designed input structure before repeating the procedure. An example of such a feature minimising energy that is common for most of conjugated polymers is long, fully extended side-chain with hydrogen atoms bonded out of plane of the backbone. Finally, the most stable structures were subject to a longer 500 ps quench at increasing

temperatures (300 K, 500 K, 1000 K) and powder diffraction patterns were calculated to check $\pi$- stacking and interlamellar distances against experimental data.

The most stable structures have been used to generate disordered, non-interdigitated phase. The procedure begins with construction of large supercells, eg 3 layers of 8 $\pi$-stacked decamer in case of IDT-BT. The interlamellar distances were increased to 50 Å such that the systems become non-interdigitated and a 50 ps, high temperature (NPT ensemble, T= 500 K) molecular dynamics simulation was performed to introduce disorder in side-chans at a fixed lattice parameters. This was followed by relaxation of lattice parameters and 400 ps simulation at room temperature to equilibrate the system. Similarly, it is possible to obtain low density, amorphous structure[3] by increasing both interlamellar and $\pi$- stacking distances simultaneously and following the same procedure of relaxation and thermal equilibration.

## 2.3 DFT Software

Calculations presented in this thesis were performed three different softwares: CRYSTAL09, CASETEP and Gaussian09. CRYSTAL09 and CASTEP were used to calculate properties of small molecules in periodic crystalline lattice. Use of periodic boundary conditions enables simulation of low frequency vibrational modes that are crucial for understanding mechanism of charge transport. In case of polymers, the mechanism of charge transport and degree of crystallinity are different: in these semi-crystalline materials we are interested in different region of spectrum corresponding to higher frequency intramolecular modes. For that reason all calculations of polymeric spectra were performed using isolated molecule formalism implemented in Gaussian09.

Gaussian is often regarded as a workhorse of computational chemistry and found numerous applications within the domain of organic semiconductors. Gaussian's single-molecule representation offers tremendous cost advantage against periodic boundary condition implemented in CASTEP and CRYSTAL- as an example, calculation of intramolecular Raman spectra of trimers and tetramers can be accomplished using modern desktop computer, whereas prediction of intermolecular vibrational modes using periodic boundary conditions requires access to national supercomputing facility.

One of the most basic calculations that may be performed using Gaussian is optimization of geometry to the lowest energy configuration. A notable example of such

[3]In disordered structures the molecular packing is a result of initial atomic velocities that are assigned randomly, and hence trajectories are not reproducible. However, statistical properties such as powder diffraction patterns or total energies per mole are reproducible.

calculation was published by Nielsen et al. [74]. Nielsen predicted gas phase conformations of dithenyl-DPP and diphenyl-DPP to illustrate the differences in backbone twist and hypothesize about possible effect of steric hindrance between oxygen atoms of the lactams and phenyl hydrogen atoms on backbone planarity and hence electronic performance. By performing a series of total energy calculations (also known as single point energy calculation) as a function of spatial parameter, it is possible to determine interaction potentials. In this regard, an interesting study of the effect of strain on mobility in C8-BTBT has been published by Kubo et al. [75]. Kubo performed calculations of energy as a function of rotation and translation of a single molecule in the crystal lattice for strained and unstrained systems. By comparing both energy curves Kubo concludes that stress steepens potential curve restricting amplitude of molecular vibrations and hence suppressing dynamic disorder. This hypothesis was verified experimentally- data published by Kubo shows that C8-BTBT 3% strain increases mobility by up to 70%. The same computational routine is used to determine shape of interatomic potential curve. The potential curve is then used to parametrise force field needed for molecular dynamics simulations, as demonstrated in later chapters of this thesis.

Another common application of Gaussian is prediction of molecular orbital distribution and energy levels [76, 77]. In particular, Kronemeijer [78] has shown that molecular orbital distributions in PSeDPPBT demonstrate that both HOMO and LUMO are extensively delocalised over the polymer backbone which is in contrast to many donor-acceptor polymers, where LUMO is localised upon the electron accepting core of the polymer backbone. Gaussian is capable of providing an accurate description of photophysics of donor-acceptor semiconducting polymers [76] that enable interpretation of electronic transitions. Examples include calculation of oscillator strength and resultant UV-Vis absorption spectra for IDT-fDTBT [27] and NDI-T2 [76]. Finally, Gaussian is often used to calculate vibrational modes and resultant mid-IR and Raman spectra, however it is important to realise about inherent weakness of single molecule representation- the lack of treatment of intermolecular interactions. In case of conjugated polymers this has little effect on the accuracy of calculated spectra because dominant contribution comes from high frequency intramolecular bond stretches, however studies of THz domain of the spectrum require periodic boundary conditions. Examples of published vibrational mode assignment and spectra calculated using Gaussian include P3HT [77] and NDI-T2 [79]. Another interesting application of DFT Raman spectra is interpretation of the effect of high pressures on molecular packing- by simulating spectra as a function of varying spatial coordinate it is possible

to reproduce intensity shifts observed in experimental spectra. Notable examples of such studies are investigation of F8-BT backbone planarity published by Schmidtke et al. [33, 34] and study of changes in biphenyl conformations by Zhuravlev [80]. The same methodology involving computation of Raman spectra as a function of spatial coordinate is in a fact a cornerstone of my thesis.

Studies of organic semiconductors that include calculations performed using CASTEP or CRYSTAL codes are rather scarce for couple of reasons. Firstly, these two softwares are only applicable to crystalline systems with known structure and unit cell parameters, which limit the range of materials to small molecules. Secondly, methods of dispersion correction are still under development and hence most of the computational studies of molecular crystals focus on well-understood model systems such as urea or benzoic acid.

A notable exemption is theoretical study of electronic properties of oligoacenes (naphthalene, anthracene, tetracene and pentacene) under pressures up to 25 GPa published by Schatschneider [81]. Schatschneider performed calculations of structure and band gap as a function of pressure using PBE functional with Tkatchenko-Scheffler (TS) dispersion correction. His simulations not only demonstrated excellent agreement between calculated and experimental structures, but also correctly reproduced pressure induced phase transition in tetracene. Although the study did not include any new insights into physics of these materials, calculations performed by Schatschneider provide proof of concept and prove about versatility of TS dispersion correction.

When it comes to calculation of vibrational modes and spectra, significant contribution to numerical techniques and evaluation comes from research groups developing terahertz spectroscopy. In particular, benzoic acid was chosen by several authors [82–84] as a model system to compare theoretical predictions from CASTEP code with experimental terahertz spectra. Burnett et al. [85] published a broad comparison of experimental PETN spectra with DFT calculations performed using CASTEP and molecular mechanics simulations performed using COMPASS. In general, CASTEP simulations have correctly reproduced approximate positions and strengths of vibrational modes, but they often overestimate frequencies. Similarly, research by Civalleri et al. [38], King et al. [86, 87] and Hakey with coworkers [88, 89] was focused on the use of CRYSTAL. The simulations successfully predicted frequencies and intensities of vibrational modes of several systems including urea, ketamine hydrochloride and methamphetamine hydrochloride. As was the case with prior publications based on CASTEP calculations, these studies are centred on methodology and choice of the best functional rather than novel insights into physics. In summary, it is evident that at

least in principle both CASTEP and CRYSTAL are capable to deliver correct mode frequencies and spectral intensities, however an in-depth evaluation has only been performed for relatively small systems and calculation of low-frequency vibrational intensities of organic semiconductors remains a potential challenge.

### 2.3.1 CRYSTAL09

Initially, all calculations involving small molecules were performed using CRYSTAL09 DFT software [90, 91] run on HECToR and ARCHER supercomputing facilities and ANNAPOLIS cluster at the department of chemistry. CRYSTAL performs ab initio calculations on periodic systems within the linear combination of atomic orbitals (LCAO) approximation. The crystalline orbitals $\psi(r,k)$ are expressed as a linear combination of Bloch functions $\phi(r,k)$:

$$\psi(r,k) = \sum_{\mu} a_{\mu}(k)\phi_{\mu}(r,k) \tag{2.20}$$

and the Bloch functions $\phi_{\mu}(r,k)$ are defined in terms of local atomic orbitals $\varphi_{\mu}(r)$:

$$\phi_{\mu}(r,k) = \sum_{g} \varphi_{\mu}(r-A-g)e^{ikg} \tag{2.21}$$

where $A$ is the coordinate of the atom and $g$ is the direct lattice vector. The atomic orbitals $\varphi(r-A-g)$ are expressed as a linear combination of a certain number of Gaussian type functions

$$\varphi_{\mu}(r-A-g) = \sum_{i} d_i G(\alpha, r-A-g) \tag{2.22}$$

They are characterized by the same centre $A$, with fixed coefficients $d_i$ and exponents $\alpha$ defined in the input. Typical computational procedure is to first run geometry optimization until fluctuations of energy and atomic positions are below pre-defined thresholds, and then use resultant geometry as an input for vibrational modes calculation. CRYSTAL09 is a command based program and all simulation parameters are specified by keywords in relevant sections of the input file. The input file consists of six major blocks:

Block#1 *Title*

Block#2 *Geometry input.* This section contains the information about the type of geometry used (CRYSTAL, SLAB, HELIX or MOLECULE keywords).

If periodic crystal geometry is used, one has to specify convention for the space group identification, type of cell for rhombohedral groups (hexagonal or rhombohedral), space group, lattice parameters $(a, b, c, \alpha, \beta, \gamma)$ and a list of atoms in the asymmetric unit together with their fractional coordinates. Typically, the information about the geometry is imported from Cambridge Structural Database and then refined using DFT methods. It is possible to use EXTERNAL keyword to import the geometry from and external CRYSTAL09 file, e.g. if one wants to restart geometry optimisation using partially optimised structure from the previous run.

Block#3 *Type of simulation.* Geometry optimization requires OPTGEOM keyword followed by type of optimization (e.g. FULLOPTG will result in simultaneous optimization of unit cell parameters and atomic coordinates, whereas CELLONLY will keep fractional atomic coordinates fixed and optimise lattice constants) and a list of parameters controlling the self-consistent-field procedure. In my case it was especially important to specify TOLDEG (root mean squared energy gradient), TOLDEX (root mean squared on estimated displacements) and TOLDEE (threshold of energy change between optimization steps). Vibrational modes calculation can be initiated by FREQCALC keyword, again followed by list of relevant parameters.

Block#4 *Basis set.* For each type of atom one must specify the atomic number and the number of shells of the atomic basis set. For each one must specify type of basis set used (0,1 or 2) and type of shell (s, sp, p etc. denoted by numbers), number of Gaussian functions, shell electronic charge and scale factor. Furthermore, for every Gaussian function one has to specify the exponent $\alpha$ and coefficient $d$. This procedure may seem complicated, but there are numerous programs using Gaussian-type basis set and this part of input file may easily be imported directly from EMSL Basis Set Database [92]. However, it must be emphasized that the shell structure defined in the input file does not represent the physical shell structure, for example some artificial empty shells may be added to account for the polarization.

Block#5 *Hamiltonian.* One can choose between pure Hartree-Fock or DFT based methods. If DFT is chosen, the exchange-correlation functional must be specified- in my case all calculations were performed using B3LYP hybrid functional. XLGRID and XXLGRID keywords increase the density

of points, at which DFT integrals are evaluated. The more dense the mesh the better the accuracy, however the computational cost scales non-linearly with the size of the grid and it is important to find a reasonable compromise.

Block#6 *Other keywords.* GRIMME keyword calculates a London-type pairwise empirical correction to the energy as proposed by Grimme [93], in order to include long-range dispersion contributions to the computed ab initio total energy and gradients. When using GRIMME command one has to specify a number of parameters both globally (scaling factor, steepness, cutoff distance and number of atomic species) and for every type of the atom in the system (atomic number, dispersion coefficient and van der Waals radius). A more detailed discussion of how Grimme approximation affects the accuracy of the simulation can be found in the original paper [93]. TOLINTEG followed by five numbers specifies so called truncation criteria for Coulomb and HF exchange integrals. These criteria are important when vibrational modes are calculated, but for practical reasons they will not be discussed here in detail. As discussed above, it is possible to mix Fock and Kohn-Sham matrices. This can be done by using FMIXING keyword followed by a ratio of mixing. LEVSHIFT specifies eigenvalue level shifting. The technique involves addition of a negative energy shift to the diagonal Fock/KS matrix elements of the occupied orbitals and thus reducing their coupling to the unoccupied set. Finally, SHRINK keyword controls shrinking factor which is used to generate a grid of **k** points in reciprocal space according to Pack-Monkhorst method. The effect of varying SHRINK values will be discussed in the "Results" section. A more in-depth discussion of relevant keywords can be found in CRYSTAL09 manual [90].

CRYSTAL produces numerous output files. Most of them are used to store information about previous iteration and can be used to restart the simulation if the run has been abruptly terminated, however their meaning and structure will not be discussed. In general, CRYSTAL may be executed in three modes: serial, parallel (PCrystal, up to 64 cpu's) and so-called massively parallel mode(MPPCrystal). For most of the time massively parallel mode was used on Hector, but sometimes it was necessary to execute the simulation in serial mode using local Annapolis cluster.

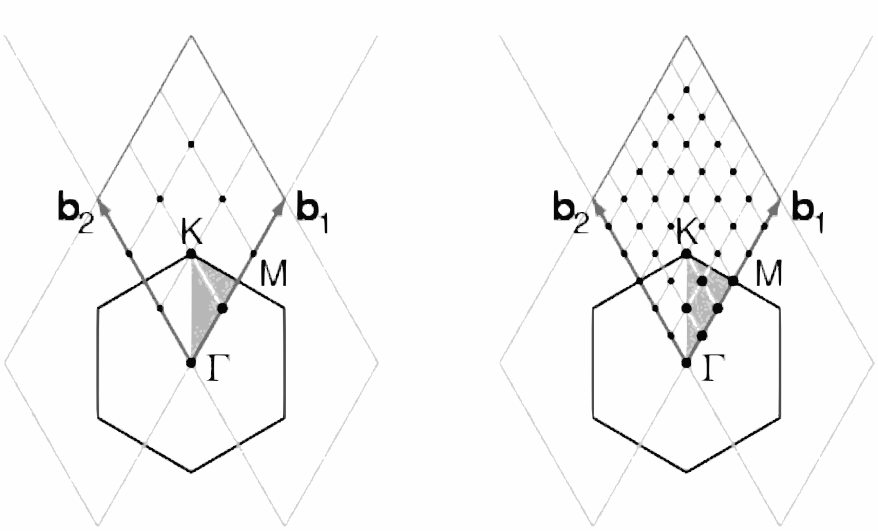


Figure 2.3: The figure presents the reciprocal lattice cell of 2D graphite (rhombus) and the coordinates of the k-points according to a Pack-Monkhorst sampling, with shrinking factor 3 and 6. Higher shinking factor result in finer grid f k-points. Adopted from [90].

### 2.3.2 CASTEP

Unlike CRYSTAL, CASTEP uses plane wave basis set to perform calculations on periodic systems. The main advantage of using periodic basis set relates to Bloch's theorem, which states that in a periodic system each electronic wave function can be written as a product of a cell-periodic part and a wavelike part:

$$\psi(r,k) = e^{ikr}\phi(r) \tag{2.23}$$

The cell periodic part $\phi(r)$ can be then expanded using a basis set consisting of a discrete set of plane waves whose wave vectors are reciprocal lattice vectors $G$ of the crystal:

$$\phi(r) = \sum_{k} C_{k,G} e^{iG\,r} \tag{2.24}$$

hence each electronic function can be written as a sum of plane waves $e^{i(k+G)r}$ , where $C_{k,G}$ are complex Fourier coefficients, and the sum is over all wave vectors with the right periodicity. Each of the Fourier basis set functions $e^{iGr}$ represents a plane wave traveling in space in direction perpendicular to the vector $G$. In principle, there are an infinite number of plane waves required for such an expansion, however the coefficients

$C_{k,G}$ become smaller as the $\mid G \mid^2$ becomes larger. Therefore, the plane wave basis set can be defined to include only plane waves that have kinetic energies smaller than some particular cutoff energy given by:

$$E_{\text{cutoff}} = \frac{\hbar^2}{2m} \mid G \mid^2 \tag{2.25}$$

The truncation of the basis at a finite value will result in an error in the computed total energy and its derivatives. The magnitude of the error will depend on the $E_{\text{cutoff}}$, hence it is possible to systematically reduce the error by increasing the value of the cutoff energy. The typical procedure to determine the correct $E_{\text{cutoff}}$ is to run a series of ground state energy calculations for a set of different cutoff values until the convergence is reached. A more detailed discussion of parameter choice is given in chapter 4.

The very large $G$ components describe the region of space where the wave function is varying very quickly [94] and it would be impractical to represent such functions using plane waves since the size of the basis set would be prohibitive. This is especially the case for core electrons bound by strong Coulomb potential due to nucleus. The wave functions near the nuclei are, in a fact, less important since they don't affect the chemical, mechanical or electronic properties very much compared to valence electrons. All-electron DFT methods treat core and valence electrons on an equal footing and require vast amount of computational time making them unsuitable to study complex, organic systems. The alternative way to model electron-ion interactions is to replace the core electrons and strong ionic potential with a weaker pseudopotential that acts on a set of a pseudo wave functions rather than true valence wave functions. There are numerous ways to construct pseudopotentials, however I only used particular class of functions known as norm-conserving pseudopotentials. A more detailed discussion of pseudopotential method has been published by Payne et al [94] and Hamann et al. [95]. All pseudopotentials used were downloaded from CASTEP repository.

Geometry of the system and relevant simulation parameters are specified in two input files: "input.cell" and "input.param". The .cell file is made of following blocks:

Block#1 *Title*

Block#2 *Unit cell.* The geometry may be specified either as a set of Cartesian vectors (LATTICE_CART keyword) or in terms of lattice vectors magnitudes and the angles between them (LATTICE_ABC keyword). The same geometry inputs as for simulations done using CRYSTAL09 were used.

Block#3 *Pseudopotentials.* This section contains information about pseudopotential files. All pseudopotentials were downloaded from Castep's CCPForge

depository.

Block#4 *Atomic coordinates.* In this section all atomic positions within unit cell are specified. Positions can be specified by absolute vectors (POSITIONS_ABS) or fractional coordinates (POSITIONS_FRAC).

Block#5 *Cell symmetry.* In this block one can specify the symmetry of the system. By using SYMMETRY_GENERATE keyword it is possible to find and force the cell into the highest symmetry group that applies to the structure. Keywords FIX_ALL_CELL and FIX_ALL_IONS are used to impose constraints on the system e.g. during geometry optimisation. I run simulations for two cases: a fully relaxed structure (both parameters *false*) and a fixed unit cell with unconstrained ionic coordinates (FIX_ALL_CELL *true*). This is equivalent to FULLOPT and CELLONLY parameters previously used with CRYSTAL09. Some simulations also required SNAP_TO_SYMMETRY keyword. If the experimental crystallographic data is for some reason diffuse, CASTEP would struggle finding the highest symmetry of the system. It is, however, possible to intentionally adjust fractional coordinates so that the symmetry condition is fulfilled. A more detail discussion about importance of this keyword is included in Small Molecules chapter.

Block#6 *Brillouin zone sampling k-point.* The density of k-point sampling has a profound impact on accuracy of electronic ground state optimisation. Set of k-points at which the Brillouin zone is to be sampled can be specified either by listing k-points or defining Monkhorst-Pack [90] grid in terms of a minimum k-point spacing. Since the number of k-points used affects computational efficiency, it was necessary to probe the convergence of ground state energy a function of k-point density. I decided to control k-points by KPOINTS_MP_SPACING keyword, so that it was possible to evaluate the convergence against a single input parameter.

The input.param file contains all the details about type of simulation and computational methods used. Following keywords were used to control simulations:

cut_off_energy A parameter used to control $E_{\text{cutoff}}$ of the basis set. The detailed discussion of how to choose a proper value of this parameter is included in Small Molecules chapter.

finite_basis_corr — The basis set typically includes all plane waves with energies below the specified $E_{\text{cutoff}}$. This corresponds to all points in the reciprocal lattice that lie within a sphere, whose radius is related to reciprocal lattice vectors $G$ of the crystal. Any variation of lattice vector will result in change of reciprocal lattice vectors and effectively modify predefined $E_{\text{cutoff}}$. As a consequence the basis set may become incomplete leading to errors in ground state energy and stress tensor, known as *Pulay Stress.* It is possible to systematically correct the basis set on the fly using so called *finite basis set correction* method. The use of basis set correction involves series of additional ground state energy calculations during the run and given the size of the system it was decided not to use basis correction due to computational constraints.

xc_functional — This parameter specifies exchange-correlation functional used. There are numerous functionals implemented in CASTEP, however all simulations were performed using PBE functional.

sedc_apply — This keyword specifies the semi-empirical dispersion correction scheme that was used to account for the van der Waals interactions. There are several schemes implemented, however I only used Tkatchenko-Scheffler [57] since it works best with PBE functional.

fix_occupancy — This keyword is used to fix the occupancy of bands. Mandatory for phonon DFT calculations.

elec_energy_tol — The convergence tolerance for finding the ground state energy as an energy per atom during self-consistent field loop. The default value is $10^{-5}\ eV$, however phonon calculations normally require much better convergence and for many calculations $10^{-11}\ eV$ was used.

elec_convergence_win — This parameter specifies number of consecutive iterations with convergence criteria met to finish the optimisation.

task — There are several types of calculations implemented in CASTEP. *SinglePoint* was used to evaluate the ground state energy dur-

| | |
|---|---|
| | ing convergence tests. *GeometryOptimisation* was used to optimise the geometry before starting final vibrational frequencies calculations using *Phonon* mode. |
| geom_method | Algorithm used for geometry optimisation. Typically, BFGS method was used. I have also tested damped molecular dynamics as a way of resolving problems with convergence. |
| geom_energy_tol | The tolerance for finding convergence of the appropriate free energy per atom during a geometry optimisation. This value is not the same as *elec_energy_tol*- for every geometry there is recursive electronic optimisation to a ground state before spatial optimisation is started. Phonon calculations require geometry converged to a higher tolerance than default value hence $0.5 \cdot 10^{-6}\ eV/atom$ threshold was used. |
| geom_force_tol | The convergence tolerance for the maximum force on the ions when finding the ground state ionic positions. |
| geom_disp_tol | The convergence tolerance for the maximum ionic displacement in a step when finding the ground state ionic positions. |
| phonon_method | Algorithm used for phonon calculation. The first order differential Raman cross-section depends on derivative of polarizability tensor with respect to normal mode coordinates. The polarizability tensor, on the other hand, is derived by calculating second order derivatives of energy with respect to atomic positions by construction of force-constant matrix [96]. The spatial derivatives of polarization can be calculated either by using linear response or finite displacement method, however for Raman intensities calculations only finite displacement is implemented. A more detailed discussion of phonon calculation methods is included in CASTEP manual. |

As a final remark, I would like to briefly comment on calculation of Raman spectra. Firstly, let us introduce concept of electric polarizability tensor $\alpha$. Static electric polarizability is a measure of the ease with which the charge density of a system will get distorted by an external field:

$$\mathbf{p} = \alpha \mathbf{E} \tag{2.26}$$

where **p** is the induced dipole moment of an atom and **E** is the electric field that induces the dipole moment. Atomic and molecular polarizabilities are important in many areas- a large fraction of the electrostatic intermolecular energy is related to this this quantity, in particular for systems without a permanent dipole moment [49]. Mathematically, polarizability tensor is defined as a derivative of energy **E** with respect to field **F**:

$$\alpha_{ij} = -\left(\frac{\partial^2 E}{\partial F_i \partial F_j}\right) \tag{2.27}$$

Following Porezag and Penderson [96], the first order differential Raman cross section for the Stokes component of the i-th vibrational mode of frequency $\nu_i$ is given by:

$$\frac{d\sigma_i}{d\Omega} = \frac{(2\pi\nu_s)^4}{c^4}\left|\mathbf{e}_S \frac{\partial \alpha_{jk}}{\partial Q_i}\mathbf{e}_L\right|^2 \frac{h(n_i+1)}{8\pi^2\nu_i} \tag{2.28}$$

where $\nu_S$ is the frequency of scattered light, $\mathbf{e}_S$ and $\mathbf{e}_L$ are the unit vectors of the electric field direction for the scattered and the incident light, $\alpha_{jk}$ is the polarizability tensor, $Q_i$ is the normal mode coordinate and $n_i$is the Bose-Einstein statistical factor for i-th mode. As one can see, the intensities of Raman scattering depend on the square of differential of polarizability with respect to the normal coordinates. From equation 2.27 it follows that the polarizability itself is already the second derivative of the energy with respect to the electric field and hence Raman intensities are a third order property. In consequence, simulation of Raman intensities require extremely well converged calculations to obtain accurate spectra and intrinsic numerical precision of an algorithm used to evaluate derivatives can be an issue. In CASTEP dipole moment, polarizability and their derivatives with respect to atomic coordinates are determined numerically by differentiating energies and forces with respect to electric field vector according to scheme published by Porezag and Pederson [96]. The alternative is to compute the derivatives analytically, which is more stable numerically but elaborate in terms of programming since it involves solving the so-called coupled-perturbed Kohn-Sham equations [49]. The analytical method is implemented in Gausian09, where Raman intensities are calculated according to methodology published by Frisch et al [97].

### 2.3.3 Gaussian

The quantum chemical formalism implemented in Gaussian09 is the same as in CRYSTAL09. Gaussian makes use of atom-centred basis set with linear combination of

molecular orbitals and most of its capabilities are generally similar to CRYSTAL09, however it is much better suited for calculations performed on isolated molecules in vacuum state and hence was used to simulate properties of single polymer strands. All calculations were made using B3LYP hybrid functional in conjunction with 6-31G(d,p) basis set generated internally by the software. The input geometries ware constructed and edited manually using GaussView- a dedicated GUI package. GaussView has also been used to automatically generate input files specifying type of task, interatomic connectivity and all relevant keywords. Since there were no periodic boundary conditions, I did not perform convergence tests as was the case with crystalline small molecules.

For every polymer, I always started by constructing a simple dimer and running geometry optimisation using *opt* keyword, keeping zero charge and singlet spin. The next step was to investigate the torsional potential and charge distribution in order to parametrise the force field parameters required for molecular dynamics simulations. This was realized by running a series of single point energy calculations with *SP* keyword. The optimised structure had the lowest total energy by definition. By changing a torsional angle and repeating single point energy calculation, typically at 5° intervals, it was possible to scan the height of potential barrier $\Delta E(\theta)$ with respect to the lowest energy configuration: $\Delta E(\theta) = E(\theta) - E_{\text{minimum}}$. Once the shape of torsional potential is known, one could fit classical force field to recover the angular dependence and run molecular dynamics simulations.

By using periodic boundary conditions it is possible to calculate set of vibrational modes including low frequency intermolecular modes. However, for an isolated molecule in vacuum phase one can access only higher frequency intramolecular modes- the size of the molecule limits the wavelength and hence frequency of vibrations. In theory high frequency modes, such as carbon bond stretching, do not require use of long strands, however the wave function is often extended over several monomers and use of system that is too short results in artifacts- it is therefore important to perform phonon calculation on biggest possible system. In practice the size of the system is limited by computational resources as the cost of simulation scales as a power law with number of atoms. In most cases the simulations were limited to tetramers except for NDIT2, where trimer was the upper limit due to to size of the monomer. In all cases the side chains were replaced by a single $CH_3$ group- the side chains have limited contribution to vibrational modes of the backbone, yet they have significantly increase computational complexity[4].

[4]Substitution of a single $CH_3$ group instead of complete side chains is a standard procedure present

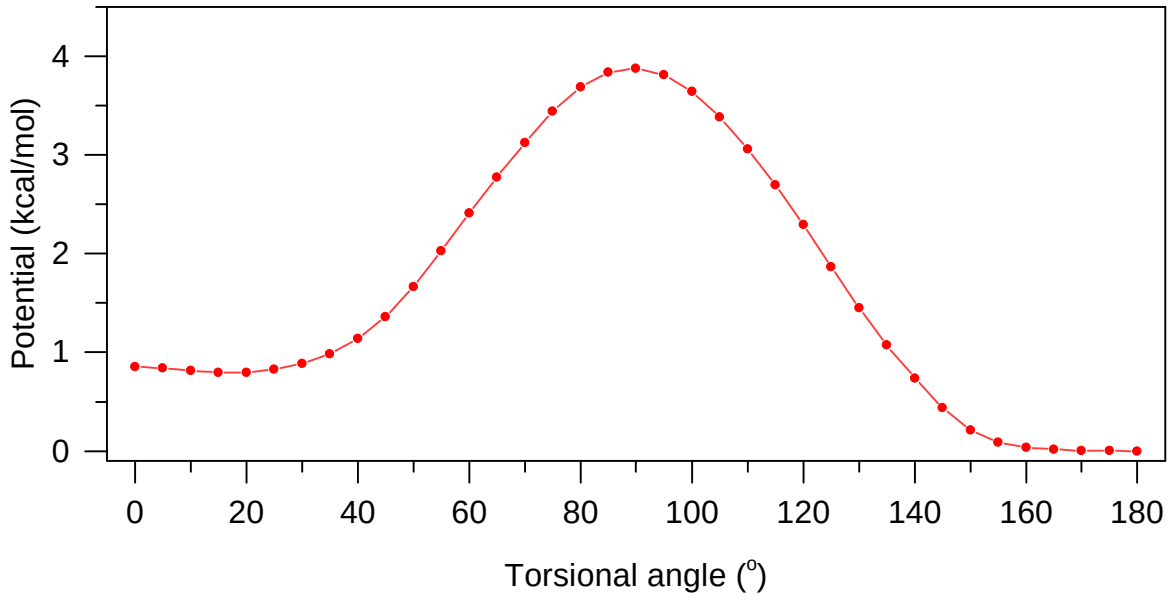


Figure 2.4: An example of IDT-IDT torsional potential calculation. Every point on the graph represents a single point energy calculation for a fixed geometry. The absolute value of lowest energy has been subtracted.

After optimisation of a single monomer, a dimer was constructed by adding two monomers and the new structure was optimised. The procedure was repeated until final size of the strand was obtained, with last optimisation threshold set to *tight*. Using GaussView the convergence criteria can be set to *standard, tight* and *very tight* rather than a specific numerical value as was the case for CRYSTAL09 and CASTEP. For some systems, the choice of convergence setting had a significant effect on vibrational modes- it was therefore necessary to evaluate this effect by making comparison with experimental data. A more detailed discussion is given in Results section.

Having optimised the geometry, I performed phonon calculation using *freq=Raman* keyword. For every system it was necessary to compare spectra generated using standard, tight and very tight convergence setting. After choosing appropriate thresholds I modified the torsional angle and repeated Raman calculation. This can be done either by manually changing the bond torsion keeping the rest of structure fixed or by imposing constraint on the bond and relaxing the structure using redundant coordinates. Since I was comparing vacuum phase strand with no alkyl chains to a packed thin film, the choice of a method was based on comparison with experimental Raman spectra. Gaussian's output file contains information about frequencies of the modes and corresponding activities. The activities were used as an input to calcu-

in several publications [39, 40, 98, 99]

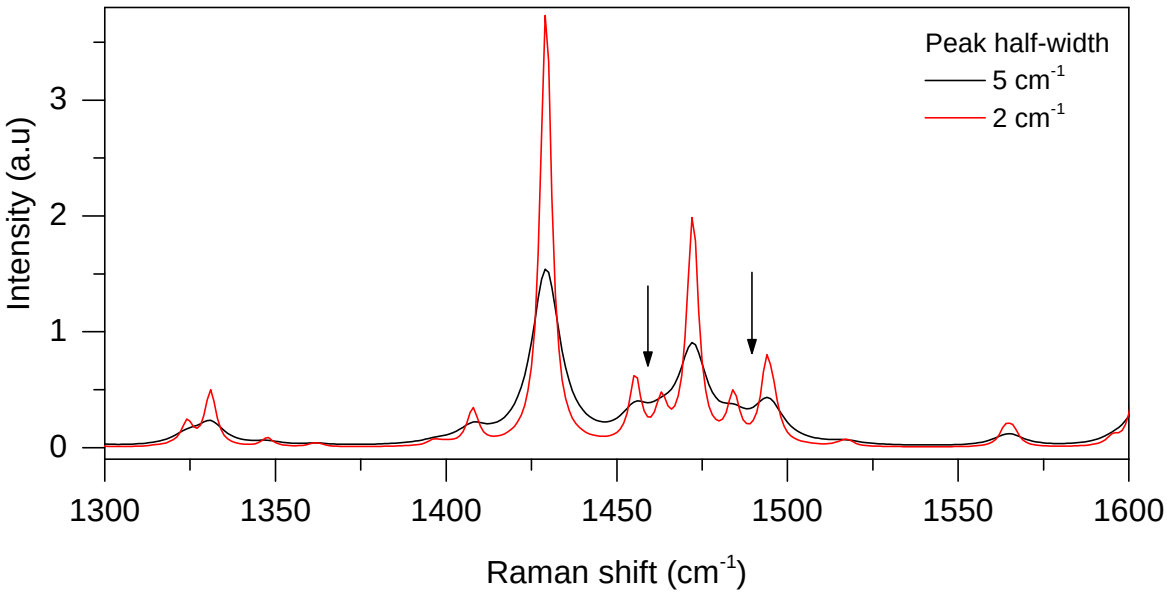


Figure 2.5: Comparison of NDIT2 Raman intensities generated with 2 and 5 $cm^{-1}$ Gaussian peak half-widths. Both data sets were generated using the same input Raman activities. Regions with closely spaced modes (marked with arrows) are prone to artifacts- the ratio of the peak intensities depends on half-width chosen to generate the spectrum.

late intensities of complete spectra using GaussView built-in module, however it allows generation of spectra Gaussian peaks only- it was therefore necessary to choose correct peak half-width so that the shape of the spectrum resembled experimental spectrum that was not purely Gaussian[5]. In some cases choice of half-width was crucial- if there are multiple closely spaced modes, the height of resultant peak will depend on degree of overlap between separate modes, as demonstrated in Figure 2.5. Moreover, since peak intensities depend on choice of DFT functional it is not possible to make a direct comparison between experimental and DFT peaks to extract the exact torsional angle. Instead, one has to calculate ratio of relevant DTF peaks and compare the angular dependence with ratio derived from experiment, i.e. it is possible to qualitatively determine if the backbone is planarizing or not rather than perform quantitative analysis of backbone torsion.

[5]The experimental data were fitted using Gaussian, Lorentzian and Voigt models. It was found that Lorentzian model resulted in best fit.

# Chapter 3

# Experimental Methods

This section gives an overview of experimental techniques that were used to study intramolecular vibrational modes of organic semiconductors. I present design and operational properties of diamond anvil cell that was custom made to fit my experimental setup and briefly discuss measurements of Raman spectra that were performed using standard, off-the-shelf commercial equipment.

## 3.1 High Pressure Measurements

High-pressure physics is a particularly strong example of a cross-disciplinary area of science that relies upon complementarity of various experimental techniques to characterize novel materials and their phase transitions. The ability to achieve the most extreme conditions at elevated pressures or temperatures and reach the boundaries of material strength are usually not goals on their own- the evolution of complex sample environments and new spectroscopic techniques require a constant development of high pressure instrumentation. Quite often, as was the case with experiments performed by me, pressures obtained during the experiment are far from current records of extreme conditions. However, other factors such as geometry of the spectrometer, range of x-ray incidence angles needed to solve a structure or absorbance of diamond anvils often play crucial role and require custom designs of high pressure instrumentation. The range of experimental techniques and materials studied under high pressures is impressively broad: initial measurements of compressibility and electrical resistance were followed by experiments involving x-ray and neutron diffractometry of chemical elements and gases at both low and high temperatures. Over time more sophisticated techniques such as Brillouin scattering, high magnetic fields and inelastic x-ray scattering were added to the spectrum of experiments and studies were extended to complex

semiconducting systems, rare earth elements, molecular crystals, protein crystallization [100] or even *in situ* studies of living cells metabolism [101].

High pressure techniques were pioneered by Bridgman- the era roughly from 1910 to 1950 was dominated by the so-called Bridgman anvil and piston-cylinder devices, both of which were invented by Bridgman for simple resistance measurements at pressures up to 100 kbar (10 GPa). The most important innovation of post-Bridgman era was invention of diamond anvils that replaced previously used anvils made of tungsten carbide. First diamond anvil cell (DAC) was developed by Weir and co-workers at National Bureau of Standards in 1959 [102] and quickly followed by other designs leading a new era of science at extreme conditions. Current frontiers of high pressure physics are driven by nanocrystalline diamonds enabling pressures above 600 GPa [103] and CVD grown designer diamonds incorporating magnetic coil and electrical probes for in-situ measurements. A more in-depth discussion of DAC types and related experimental techniques can be found in reviews by Jayaraman [104] and Holtzapfel [105].

Currently used pressure cells can be divided into two types according to their principle of operation: diamond anvil and piston cylinder cells. Piston cylinder cells are designed to use a piston to pressurise samples through pressure transmitting medium. The cylindrical body of the cell provides sample space but also guides and supports the piston, which is driven by external press. Compared to anvil cells, piston cylinder cells offer much bigger volume of sample space of order of 100 $mm^3$, however most designs do not incorporate any optical access and are mostly suited for transport measurement as well as neutron scattering. On the practical side, the maximum obtainable pressure is limited to 3-4 GPa [106] and the main technical challenge is to prevent leaks of the pressure medium, which often makes them rather troublesome. The leak tight design is especially important, since unlike in diamond anvil cells the pressure cannot be measured spectroscopically- the typical method involves a manganin coil incorporated in sample chamber with electrical connection to the outside equipment. So far piston cylinder cells were not commonly used to study organic semiconductors, however I am aware of at least one research group that made successful attempt to measure FET characteristics under high pressures [107]. Takeya and co-workers developed an instrument that allows measurement of mobility and Hall coefficient as a function of pressure [75]. Studies of pentacene indicate that pressures up to 1 GPa suppress thermal fluctuations leading to increased intermolecular coupling, charge mobility and transport coherence. Even though these results were published in a renowned journal, they gained rather limited recognition if judged by a number of citations. However,

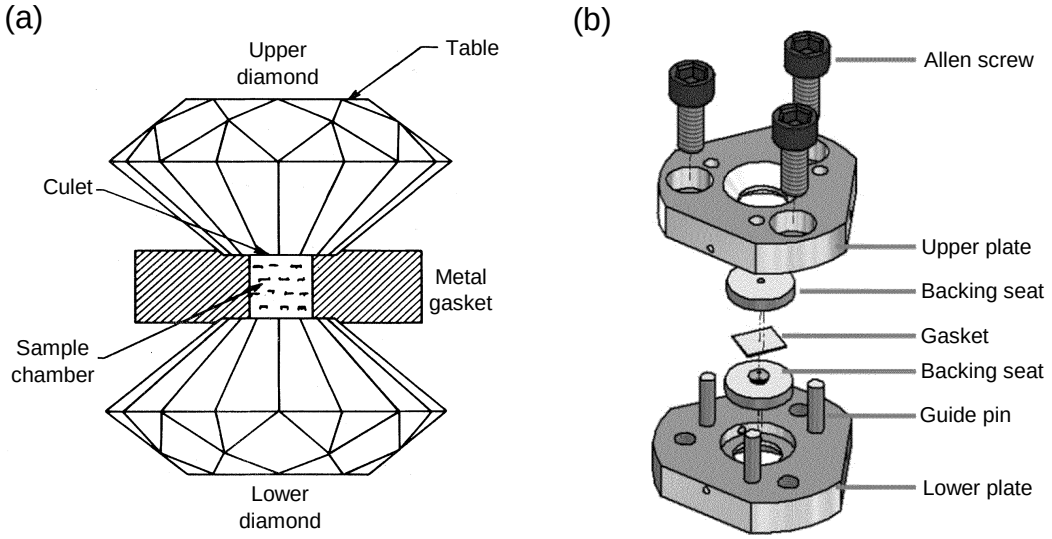


Figure 3.1: Schematic (**a**) of a basic part of diamond anvil cell configuration, with a metal gasket for sample confinement in a pressure medium and backing diamonds that are used to pressurise the medium. Panel (**b**) illustrates an exploded view of Merrill-Bassett cell design that was used during the project. Figures adapted from [108] and [104].

in my opinion the technique is promising tool to study structure-property relations in conjugated polymers and could be used to complement my studies of backbone conformation described in latter sections.

Unlike piston cylinder cells, diamond anvils enable optical access and are well suited for spectroscopy and x-ray diffraction studies. Unparalleled strength of diamond provides access to pressure range of orders of magnitude larger compared to piston cylinder instruments at an expense of sample space volume, which is typically around 0.1 $mm^3$. This is especially troublesome when assembling the cell in experiments where the orientation of a sample is important such as transport measurements in high magnetic fields or single crystal diffraction. Regardless of technical details, the principle of DAC operation is straightforward: the sample is contained between two diamonds with flat, polished culets and a metal gasket which has a cylindrical hole drilled through in order to create a sample chamber, as shown in Figure 3.1**a**. Gasket seals the setup and sample chamber filled with pressure transmitting medium is pressurised by applying opposed forces to upper and lower tables of diamonds. All experiments reported in this thesis were performed using custom-made DAC based on the original design of Merrill-Bassett cell [108, 109]. Although Merill-Bassett design was first published in 1974 [109], it is in constant development and in some of its as-

pects remain superior to modern designs. Initially, Merril-Bassett cell was designed to be mounted on an x-ray goniometer head and the key advantages of this type of DAC are very compact size, simplicity of design and wide-angle optical access. An exploded view of Merill-Bassett cell is shown in Figure 3.1**b**. The cell has a minimum number of moving parts and guide pins that simplify cell loading and assembly. The pressure is adjusted by three Allen screws that tighten the body. It is a very simple, yet sometimes problematic mechanism- the main disadvantage is lack of precise control over pressure increments. In my case, the first data point could be anywhere between 0.17 and 0.7 GPa and there is no reliable way to make it reproducible. Secondly, pressure increments are not constant throughout the experiment- as a rule of thumb one may expect the increment to be equal 10 to 15% of current value of pressure, but not less than 0.3 GPa. This property of screw-driven cell was not relevant to my experiments, however could be troublesome when precise control of phase transition is needed.

### 3.1.1 Cell design and operation

The key issue of high pressure Raman spectroscopy is signal to noise ratio. Typically, measured intensity of Raman signal is lower by an order of magnitude when compared to ambient conditions due to absorbance of diamond, reflectance at interfaces and scattering within pressure medium. These effects are even more pronounced in case of organic thin films due to limited scattering volume, low absorbance and dominant photoluminescence background- even if data is collected close to detector's saturation limit, subtraction of photoluminescence baseline results in a significant level of noise. Another aspect to consider were mechanical properties of organic films suspended in liquid pressure medium- because they tend to form large, entangled clusters it is difficult to load them into narrow sample chamber in a manner that guarantees lack of air bubbles.

The best way to address issue of low signal to noise ratio is to use lens with higher magnification. This approach inevitably leads to question of lens's working distance, which is of order of few mm for lenses with 50× magnification, whereas typical thickness of diamond and backing plate is in excess of 15 mm. Since I intended to use Leica PL Fluotar L 50x/0.55NA microscope lens with working distance of 8 mm, it was necessary to modify the original Merrill-Bassett design by reducing thickness of plates and backing seats as indicated on Figure 3.2. Currently available Merrill-Bassett cells are designed to withstand pressures of up 35 GPa providing very generous safety margin- even though I reduced structural strength, it is estimated that my cell

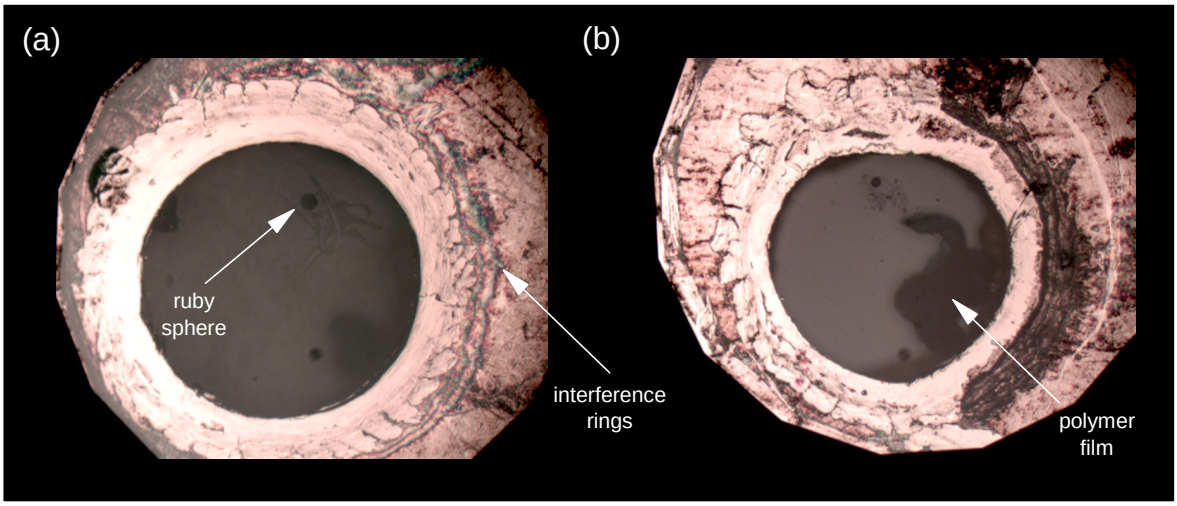


Figure 3.2: Photograph of DAC sample chamber as viewed under the microscope. Panel (**a**) depicts 400 μm wide opening in the gasket after the cell has been sealed at approximately 0.2 GPa. Newton's interference rings indicate that diamonds are in contact with the gasket and chamber is filled with pressure medium. The ruby sphere and vacuum grease are clearly visible inside the opening. At high pressures (**b**) volume of sample chamber is reduced and shape of opening in the gasket becomes irregular.

should be operational up to 8-10 GPa[1] and did not exhibit any major deformations when tested at 5 GPa. In case of conjugated polymers, 5 GPa is a practical limit due to broadening of peaks and decrease of signal strength. The volume of sample chamber was expanded by using 800 μm wide diamond culets and 400 μm hole in the gasket. Large diameter of gasket opening enabled convenient sample loading, making the cell well suited for studies of thin films.

All polymer films were prepared using the same processing conditions as were reported by authors of prior studies of charge transport. Films were spun on PSS coated substrates so that wet transfer method could be used. $25 \times 25$ mm gaskets made of CuBe alloy were indented to 150 μm thickness and drilled centrally to create sample chamber[2]. Before gaskets were aligned on top of a diamond, a ruby sphere used for pressure calibration was attached to a centre of a diamond culet using vacuum

[1]When it comes to estimation of accessible range of pressures, the key parameter that is taken into consideration is the diameter of diamond culet and table. There are no quantitative models that could accurately predict strength of a natural diamonds with given geometry- instead, type of diamond cut and culet diameter are chosen according to an empirical rule of thumb. Diamonds used during my experiments were designed, procured and machined by Alamx-easilab.

[2]CuBe alloy is commonly used for making gaskets, since it combines high yield strength with excellent machinability. Gaskets were cut from 0.4 mm thick metal sheet using standard bench shear and drilled using Proxxon bench drill. Higher pressures and temperatures typically require gaskets made of stainless steel that are drilled using spark erosion method.

grease. After alignment of the gasket, sample chamber was filled with excess amount of pressure medium[3] and polymer film was loaded using fine needle. There are several standardized and tested pressure media. Most of them are water-based, however I decided to use fluorinert CF70 to ensure that probability of sample oxidation is minimised. Due to low boiling point, fluorinert is problematic as a pressure medium because it evaporates quickly meaning that the time interval between filling sample chamber with medium and pressurizing loaded cell is relatively short. One way to extend loading time frame is to precool medium and body of the cell to 4° C so that evaporation rate is reduced and there is enough time to precisely align the sample on the diamond and ensure there are no air bubbles inside the chamber. After loading, cell is sealed using Allen screws and inspected under the microscope. A photograph of properly loaded and sealed cell is shown in Figure 3.2 **a**. One can clearly identify a ruby sphere inside the sample chamber and interference pattern around the gasket opening. Interference pattern is an indication that gasket and diamond are in a close contact at a minimum value of pressure that guarantees air tightness. Since the pressure medium is transparent, interference is the only way to determine presence of medium at low pressures. Absence of interference pattern suggests that the cell was not properly secured and the medium has already evaporated or that the cell has been pressurised to more than 0.7-1.0 GPa. During operation, three Allen screws are gradually tightened in order to increase the the pressure inside the cell. Pressurization does not occur instantaneously- although every turn of the screw results in a sharp increase in pressure, there is a secondary drift that can last for a couple more minutes. The effect of pressure on gasket geometry is shown in Figure 3.2 **b**- the radius of gasket opening is reduced and curvature becomes irregular. A non-circular opening is an effect of uneven force distribution across diamond culets and indicates that further increase of pressure may result in damage of the cell. Deformation of the gasket occurs in the plastic region of stress-strain curve and therefore the experiment is generally irreversible. The only way to reduce the pressure is by leaking the medium out of the gasket hole. This is an uncontrolled, rapid process that may result in anhydrostatic conditions and was never used- all of the data were collected in ascending order of pressure.

The pressure inside sample chamber was calibrated using ruby fluorescence method.

[3]The purpose of pressure transmitting medium is to create uniform hydrostatic conditions inside the sample chamber. In other words, the never directly compressed by the dimonds- instead, it is free to float in a liquid medium that fills the sample chamber bounded by gasket and diamonds. Materials typically used as pressure medium include ethanol-water mix, liquified gasses such as nitrogen or helium and different types of fluorinert oil.

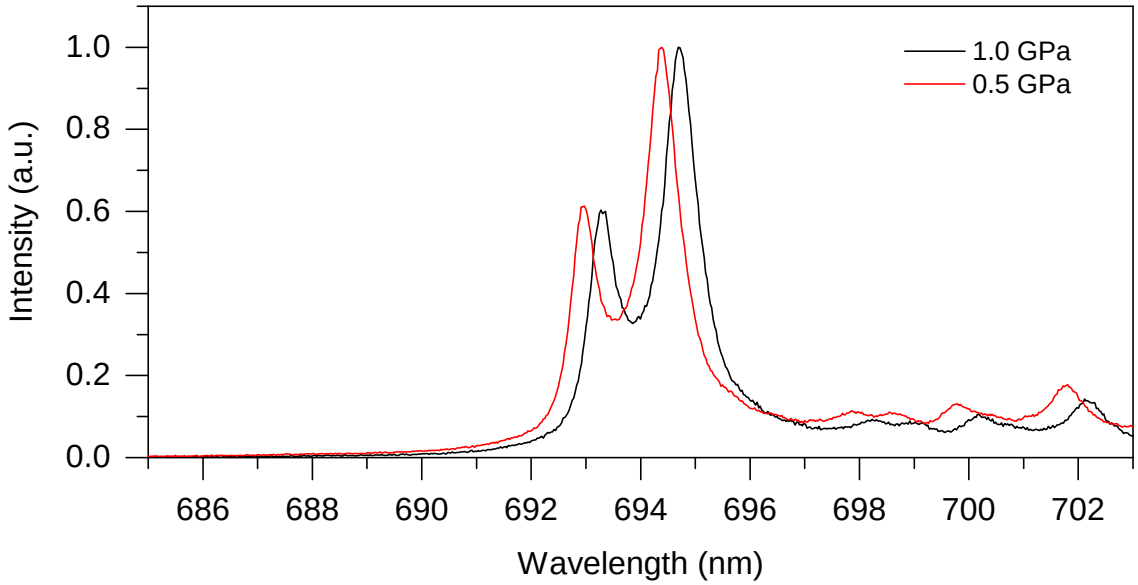


Figure 3.3: PL spectra of ruby sphere under hydrostatic conditions at 0.5 and 1.0 GPa. Shift in main peak position is used to determine the value of pressure inside sample chamber according to model developed by Mao et al [110]. Broadening of peaks would indicate anhydrostatic pressure distribution.

The fluorescence method, originally developed by Mao et al [110], is based on shift in position of ruby lines as a function of external hydrostatic pressure. Collimated 633 nm line of HeNe was used to excite ruby sphere positioned inside sample chamber and the fluorescence doublet lines (R1 and R2 at 692.7 nm and 694.2 nm respectively) were detected using CCD camera. The shift in peak position with respect to atmospheric pressure is used to determine value of pressure inside the chamber according to equation proposed by Mao:

$$P' = \frac{A}{B}\left[(\lambda'/\lambda_0)^B - 1\right] \tag{3.1}$$

where A and B are semi-empirical parameters fitted from reference data, $\lambda_0$ is a reference line at ambient pressure and $\lambda'$ is measured ruby line. I used A=1920 GPa and B=9.61 according to empirical fit published by Dewaele et al [111].

## 3.2 Raman spectroscopy

First discovered by Chandrasekhar Raman in 1928, Raman scattering is widely used to probe the intra- and inter-molecular vibrational modes of materials. While both Raman and IR spectroscopy probe vibrational states, the selection rules for the active

modes differ between the two. In Raman spectroscopy, the active modes are those for which the polarizability of the molecule is altered by interaction with the incident light, while in the case of IR spectroscopy, a vibrational mode is active if the dipole moment of the molecule is altered by the excitation.

In experimental setup the sample is irradiated by laser beam with frequency $\upsilon_0$, some of which is scattered within the material. The scattering process consist of Rayleigh scattering, which is of the same frequency as incident beam, and Raman scattering at observed frequency $\upsilon_0 \pm \upsilon_m$, where $\upsilon_m$ is frequency corresponding to the energy of one of the vibrational states of the material, as illustrated in Figure 3.4. The majority of the Raman scattering is of lower energy than the incident light $\upsilon_0 - \upsilon_m$ and is known as the Stokes Raman scattering. The Raman scattering having greater energy than the incident beam $\upsilon_0 + \upsilon_m$ is known as the anti-Stokes Raman scattering. In this thesis, only Stokes Raman scattering will be discussed. One further classification of Raman scattering refers to resonance. In non-resonant Raman scattering incident light frequency $\upsilon_0$ is below bandgap energy of the sample, which was the case with materials studied by us. In resonant Raman the energy of incident light is similar or greater than that of an electronic transition of the studied material. As a consequence a resonance occurs enhancing intensity of vibrational modes that are coupled to electronic transitions. Raman spectroscopy has previously been used to study organic conjugated materials. The extensive list of molecules includes polydiacetylene, para-substituted oligo-phenyls [112] and many further studies of small molecules [113], numerous conjugated polymers such as P3HT [114] or NDI-T2 [79] and carbon-based structures such as graphite [115], carbon nanotubes and graphene.

Raman spectroscopy provides a unique fingerprint of material vibrational modes, and hence geometry, enabling not only identification of unknown materials but also differentiation between polymorphs of the same chemical. In principle any change of geometry that alters either frequency or amplitude of vibrations within a molecule can be detected using Raman spectroscopy, as I demonstrate studying vibrational modes of polymer backbone in later chapters of the thesis. Almost any DAC is suitable for Raman spectroscopy, provided the conical opening behind the diamond is adequate. In a fact, Raman is one of the most frequently reported methods in high pressure optical spectroscopy. The technique is inherently simple to use because the same apparatus is used for pressure calibration using ruby fluorescence. Raman spectroscopy offers structural information about the organic materials under pressure even when x-ray diffraction measurements are not feasible. There is, however, a major difficulty in analysis of Raman spectra- unlike x-ray diffraction pattern, Raman spectra cannot be

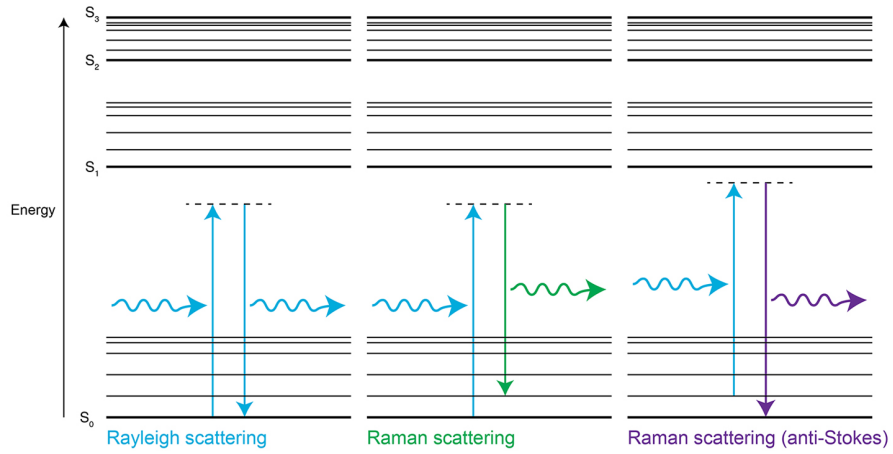


Figure 3.4: Rayleigh and Raman scattering energy diagram. $S_0$, $S_1$ and $S_2$ bold lines indicate electronic energy levels, whereas finer lines denote higher energy (electronic plus vibrational) levels and dashed line denotes virtual energy levels. Figure courtesy Renishaw.

systematically "solved" to obtain the exact conformation and the structural information is mostly qualitative. Interpretation of Raman spectra requires prior knowledge and assignment of vibrational modes. Information about modes is typically derived from DFT simulations, however intensity of calculated spectra depend on choice of algorithms and calculations can be difficult to perform in case of "soft", van der Waals bonded molecules such as organic semiconductors. For that reason I do not interpret Raman spectra quantitatively; instead, I search for steady trends in theoretical results and interpret them qualitatively.

Information on the interatomic binding forces, charge transfer effects and structural instabilities can be extracted from the pressure-induced shifts in in the phonon energies [104]. In most cases, Raman mode frequencies shift to higher energies with increasing pressure. The phonon dispersion under pressure is described in terms of the mode Grüneisen parameters $\gamma_i$ defined by

$$\gamma_i = -\frac{\partial ln\upsilon_i}{\partial lnV} = \frac{1}{\beta\upsilon_i}\left[\frac{\partial\upsilon_i}{\partial P}\right] \tag{3.2}$$

where $\upsilon_i$ is the phonon frequency, $\beta$ is the isothermal compressibility, $V$ is the volume of the crystal and $P$ is the pressure. $\gamma_i$ is usually positive, since vibrational frequencies almost always increase with compression. The value of Grüneisen parameter varies several orders of magnitude [115], generally following a scaling rule $\gamma_i \approx \upsilon_i^{-2}$ such that low energy, intermolecular modes have large $\gamma_i$, and high energy, intramolecular modes

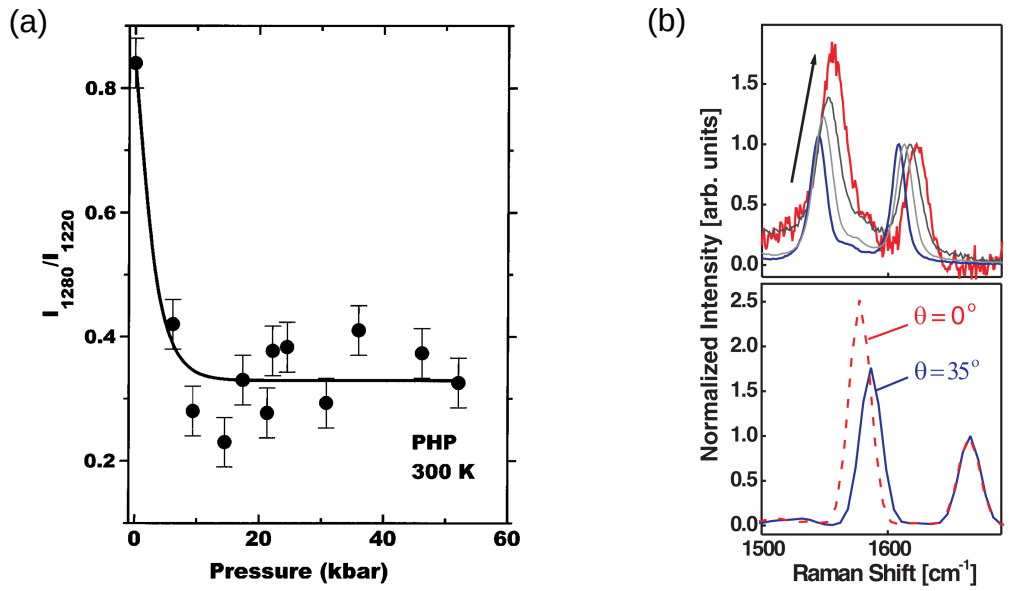


Figure 3.5: Examples of published data demonstrating effects of high pressures on molecular planarity. Ratio of Raman peak intensities is used as an indicator. Panel (**a**) was adapted from study of parahexaphenyl published by Guha et al [112]. Panel (**b**) depicts experimental (top) and theoretical (bottom) studies of F8BT published by Schmidtke et al [34]. Arrow indicates increasing pressure from ambient (navy) to 1.8 GPa (red). Theoretical spectra were calculated as a function of torsional angle between F8 and BT units.

have small $\gamma_i$. High Grüneisen parameters of intermolecular modes correlate with large changes in intermolecular distance, and similarly the small Grüneisen parameters of intramolecular modes confirm that high pressure has a modest effect upon covalent bonds in conjugated materials. In a typical molecular crystal, one finds that Raman peaks of the intramolecuar modes are distinctly segregated from the low frequency Raman peaks of the intermolecular modes. Because of the high compressibility external modes, which are well separated at low pressures, get closer to internal modes as the pressure is increased. In the high pressure spectra many more lines are seen [104] as a result of Davydov splitting. Davydov splitting, which is not resolved in ambient pressure and room-temperature spectra, arise in internal-mode frequencies as a result of increased intermolecular interactions- the splitting occurs if more than one equivalent molecular entity is present in the unit cell.

Not only shift in mode frequency, but also change in relative intensity of specific Raman modes can provide information about evolution of molecular conformation as a result of applied hydrostatic pressure. A notable example is study of parahexaphenyl (PHP) published by Guha et al [112], which demonstrates that the intensity ratio

$I_{1280}/I_{1220}$ corresponding to C-C stretch mode and C-H in-plane bending mode can be used as a measure of torsional angle between phenyl rings. In a comparison of X-ray and Raman data it was shown that $I_{1280}/I_{1220}$ decreases with decreasing torsional angle between phenyl rings. As the ratio decreases saturating at 1.5 GPa, it was suggested that hexaphenyl planarises under pressure to achieve a geometry of smaller volume [112]. By means of DFT calculations it was demonstrated that 1220 $cm^{-1}$ mode is coupled to the delocalized electronic states and therefore enhanced with increasing conjugation [80]. In comparison, 1280 $cm^{-1}$ mode is relatively insensitive to increased $\pi$-conjugation and hence the intensity ratio $I_{1280}/I_{1220}$ can be used as an indicator of greater planarity and more extended conjugation at high pressure. Similar studies were published for PPV, where ratios of intensity $I_{1167}/I_{1622}$ and $I_{1543}/I_{1622}$ can be related to conjugation length and chain planarity [116]. Both of these ratios increase under hydrostatic pressure indicating a more planar PVV structure. Finally, Schmidtke and co-workers [33, 34] performed measurements of photoluminescence and Raman spectra of F8BT conjugated polymer at pressures up to 8 GPa. F8BT has two main modes associated with conjugated backbone- the ring stretching modes of the polyfluorene (F8) and benzothiadiazole (BT) at 1608 $cm^{-1}$ and 1545 $cm^{-1}$ respectively. It was shown that the ratio of intensities $I_{1545}/I_{1608}$ exhibit clear pressure dependence. Experimental studies were complemented by DFT simulation of mode intensities together with HOMO and LUMO topologies as a function of torsional angle between F8 and BT units. Simulation of intensities demonstrates that the increase of $I_{1545}/I_{1608}$ ratio can be attributed to planarization of polymer backbone. The same methodology of high-pressure Raman spectroscopy combined with DFT simulation of torsion-dependent mode intensities is presented in latter chapters of this thesis.

Another method that can be used to probe molecular structure and conformation using Raman spectroscopy is heteroatom substitution. Substitution of one atom with another from the same group of periodic table is attractive as a method to locally modify effective force constants and hence vibrational properties. A simple demonstration of such strategy is isotopic substitution, such as deuterination of polythiophene published by Shao and co-workers [117]. As may be expected, substitution of heavier atom causes a shift of mode frequencies towards lower wavenumbers. Similar effect is observed in polythiophenes (P3HT) if sulphur atoms in thiophene is replaced with selenium (P3HS) [118], however according to Tsoi and co-workers [118] shift of main Raman peaks towards lower wavenumbers in P3HS is not simply a result of substitution of an atom with grater mass, but also grater coplanarity of the conjugated backbone. A pronounced change in molecular conformation upon fluorination

of polyoctylthiphene (P3OT) backbone has been reported by Fei and co-workers [77]. In fluorinated polyoctylthiophene (F-P3OT) two main Raman peaks associated with collective stretches of C-C and C=C bonds are both shifted to higher wavenumbers indicating shorter bond lengths. In this example shift in mode frequencies coincides with sharpening of C=C mode- reduction of the FWHM by a factor of two indicated significant reduction in the width of the distribution of molecular conformations. According to Fei both effects can be interpreted as a result of backbone planarization and increase of structural order. Other notable examples of studies relating changes in Raman spectra to morphology include comparison of regioregular and regiorandom derivatives of P3HT [119] and investigation of pentacene films grown using various deposition conditions [120].

All experimental Raman spectra presented in this thesis were collected with Horiba T64000 triple grating spectrometer using 532, 632 or 750 nm laser line and 1200 lines/mm diffraction grating. Total spectral range that could be accessed was about 50-3000 $cm^{-1}$ with an average spectral resolution of about 2 $cm^{-1}$ and before each experiment the system was calibrated using silicone line as s reference. During each experiment laser wavelength was selected to minimise PL background of the sample. Pressure cell was positioned on the Raman sample stage so that diamonds and gasket opening were on the optical axis of incident laser beam. Incident beam was expanded, re-collimated and passed through a microscope objective onto sample chamber. Scattered signal was collected in backscattering configuration through the same objective. In order to maximise signal to noise ratio Leica PL Fluotar L 50x/0.55NA objective with high numerical aperture was used. The same setup was used to calibrate pressure inside the cell using ruby fluorescence method. Ruby PL spectra were fitted with Lorentzian model using build-in Horiba software. The Raleigh scattering was removed using holographic notch filter. Raman scattering and white light (photoluminescence) were detected using charge-coupled device (CCD) cooled to -73 °C. Energy of the Raman scattering is recorded as a 'Raman shift' in wavenumbers ($cm^{-1}$) relative to the excitation line. Stokes Raman scattering is denoted with positive energy, and anti-Stokes scattering is denoted with negative energy.

## 3.3 Materials

In this thesis I investigate seven different compounds: two small molecules and five conjugated polymers. Before proceeding to research outcomes I would like to briefly introduce and summarize compounds that are subject of my thesis:

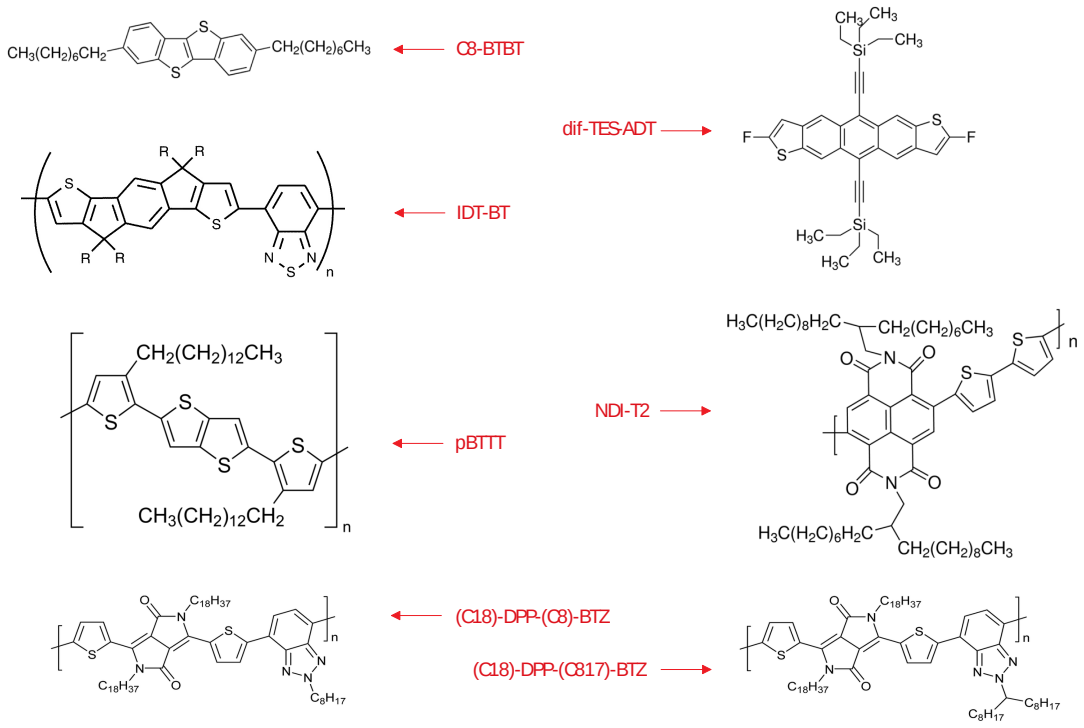


Figure 3.6: Chemical structures of materials investigated in the thesis.

- The first small molecular system is 2,7-Dioctyl[1]benzothieno[3,2-b][1]benzothiophene often referred to as C8-BTBT. C8-BTBT is a p-type, wide band gap (~3.8 eV) semiconductor renowned for exceptionally high carrier mobility. Average mobilities around 16 $cm^2V^{-1}s^{-1}$ were reported [121, 122] with highest vales up to 43 $cm^2V^{-1}s^{-1}$ in strained films grown using off-centre spin coating method [15]. C8-BTBT forms films with high degree of in-plane crystallinity [122] and edge-on, herringbone packing motif [123].

- diF-TES-ADT (2,8-Difluoro-5,11-bis(triethylsilylethynyl)anthradithiophene) is another small molecular system. Just as C8-BTBT, diF-TES-ADT is a p-type semiconductor, however is has narrower band gap of 2.2 eV [124] and exhibits lower mobilities of about 1.5 $cm^2V^{-1}s^{-1}$ for films prepared using spincasting method [125]. The structure of thin films demonstrates crystalline, but less uniform morphology than C8-BTBT: there are two possible, often coexisting molecular orientations, namely edge on and face on [126], however edge on fraction has a dominant contribution to charge transport. The main motivation to include diF-TES-ADT in my studies was lower, compared to C8BTBT, number of electrons per unit cell. It is therefore more practical to test computational methodologies with diF-TES-ADT

before setting up a more expensive simulation of C8-BTBT.

- pBTTT (poly(2,5-bis(3-alkylthiophene-2-yl)thieno[3,2-b]thiophene) is a p-type semiconducting conjugated polymer. pBTTT has a bandgap of 2 eV and demonstrates carrier mobility of up 0.1 $cm^2V^{-1}s^{-1}$ [127]. pBTTT belongs to family of early semiconducting polymers that were designed to achieve long-range order, since it has long been believed that outstanding device performance originates from highly ordered structures. pBTTT is therefore one of the most crystalline systems among conjugated semiconducting polymers- it has two-dimensional in-plane packing motif composed of lamellae of edge-on, π-stacked conjugated backbones [127]. This packing motif enables two charge-transport pathways: along the conjugated backbones and in the direction of $\pi$-stacking, both aligned parallel to the transistor channel. In terms of charge mobility pBTTT is an obsolete system, however it is very well understood and hence acts as a model system to evaluate high-pressure technique of Raman spectroscopy.

- IDT-BT (indacenodithiophene-benzothiadiazole) represents a novel class of high mobility donor-acceptor semiconducting polymers. IDT-BT is a p-type semiconductor with narrow bandgap of 1.8 eV [128] and high saturation mobility of 2.5 $cm^2V^{-1}s^{-1}$ [26]. It is the least crystalline system studied in my thesis; in a fact some authors described morphology of IDT-BT as a near amorphous [26]. Contrary to pBTTT, charge transport in IDT-BT is not dependent on extended crystalline order- rigid polymer backbone is presumably the main transport pathway and only occasional $\pi$-stacking is required to relay the charge carriers [6]. The coexistence of high structural disorder, low energetic disorder and high carrier mobility seems rather counter intuitive making IDT-BT one of the most interesting systems among those studied in my thesis.

- Derivatives of diketopyrrolopyrrole (DPP) are among some of the highest mobility ambipolar systems known today. In my thesis I investigate two recently published [18] derivatives of diketopyrrolopyrrole-benzotriazole (DPP-BTZ): one with linear side chains at DPP unit and branched at BTZ unit (denoted as (l-C18)-DPP-(b-C17)-BTZ) and other with linear side chains at both DPP and BTZ units (denoted as (l-C18)-DPP-(l-C8)-BTZ)). The first of the polymers has a band gap of 1.25 eV, hole mobility of 2.4 $cm^2V^{-1}s^{-1}$ and electron mobility of 1.5 $cm^2V^{-1}s^{-1}$, while second has a band gap of 1.32 eV and demonstrates lower charge carrier mobilities (0.48 $cm^2V^{-1}s^{-1}$ for holes and 0.31 $cm^2V^{-1}s^{-1}$ for electrons) [18]. Both systems

show a semi-crystalline structure, although GIWAXS patters suggest that (l-C18)-DPP-(l-C8)-BTZ) is somehow more ordered.

- The latter system investigated is NDI-T2, a copolymer of naphthalene diimide (NDI) and bithiophene (T2) also known under commercial name as Polyera N2200. NDI-T2 is a n-type semiconductor that has been intensively studied for use as an electron acceptor in organic solar cells [129]; it has a narrow bad gap of 1.93 eV and carrier mobilities up to 0.85 $cm^2V^{-1}s^{-1}$ in top-gate transistors [84]. NDI-T2 possesses a complex microstructure: spin-coated films show prevalent amorphous structure with preferential face-on orientation relative to the substrate [130]. Such kind of packing motif is apparently in contrast with high electron moblility, since usually edge-on packing is considered preferential, facilitating the hopping between adjacent conjugated segments along transistor channel [79]. Even more surprising, NDI-T2 demonstrates drastic transformation of crystallographic structure from mostly face-on to edge-on upon annealing near melting temperature [131], however the process does not improve charge carrier mobility [79]. Finally, it is known that depending on deposition conditions, NDI-T2 exhibit either microsegregation of donor and acceptor parts or overlap between adjacent polymer chains. The ability to control relative packing of adjacent chains by deposition routine is of particular interest for my research, since it enables me to investigate the effect of side chain packing on properties and nanostructure of the polymer backbone.

The chemical structures of the systems discussed above are summarised in figure 3.6. As one can see, the choice of systems spans large domain: from crystalline small molecules through conjugated polymers with varying degree of crystallinity and different transport characteristics.

# Chapter 4

# Small Molecules

In dispersion bonded crystalline semiconductors coupling of charge carriers to low frequency lattice fluctuations, such as translational phonon modes, is believed to be of key importance for observed decrease in carrier mobility with increasing temperature [132]. In such systems high mobility arises intrinsically from high transfer integrals that allow charge carriers to form delocalized states. One of factors governing charge localization is dynamic disorder, which arises from thermal fluctuations of transfer integrals [21]. Some authors suggest that in the highest mobility systems that are known at present, film deposition and device optimisation have been developed to an extent that static charge carrier traps are no longer major cause of charge localization and dynamic disorder becomes dominant factor limiting charge transport [133, 134]. One possibility to reduce effects of dynamic disorder is to weaken electron-phonon coupling and hence lower the sensitivity of transfer integrals to intermolecular vibrational modes [135]. A detailed understanding of strength of thermal lattice fluctuations as a function of molecular packing is needed to guide rational design of novel systems with high charge mobilities. However, these interactions are not well understood at molecular level and we lack widely available probes of structural dynamics.

Unfortunately, low energy vibrations are challenging to probe experimentally-methods based on X-ray scattering, such as thermal diffuse scattering (TDS), are not particularly well suited for studies of organic materials because of weak interaction and hence poor spatial resolution [136]. Raman and infrared spectra, although accessible in the low frequency region corresponding to translational modes, do not provide a direct insight into atomic displacements and difficult to interpret. To my knowledge one of the most successful experimental techniques that is used to probe lattice dynamics in small molecules is diffuse transmission electron microscopy (TEM) that was reported by Eggeman [136]. TEM benefits from fact that electrons interact

more strongly with matter compared to X-rays allowing greater resolution even for light atoms. It is, however, problematic to establish a link between molecular structure and TEM data- diffraction patterns cannot be "solved" in reverse and one have to calculate theoretical pattern based on hypothetical atomic trajectories simulated using molecular dynamics. Since molecular dynamics are not an ab initio method, the quality of simulation depends on researcher's intuition to make a correct guess of input geometry and accuracy of force field parametrization. Paradoxically, force field parametrization is based on DFT simulation of up to few molecules in a vacuum phase (i.e with non-periodic boundary conditions)- such method by definition does not account very well for long range dispersion forces present in periodic systems. In consequence, there is an urgent need to develop purely ab initio method that accounts for periodicity and dispersion correction in a more rigorous manner. Such simulations would explicitly return atomic displacements and hence guide design of compounds with weak thermal lattice fluctuations.

In this chapter I present computational studies of vibrational modes of C8-BTBT and diF-TES-ADT. Following sections include detailed discussion of method development and their subsequent evaluation using DFT formalism. Initially, I decided to use CRYSTAL09 code due to implementation of Gaussian basis set and semi-empirical Grimme dispersion correction. Although CRYSTAL09 and Grimme method of dispersion correction were thoroughly tested in case of simple organic compounds, I encountered unforeseen technical difficulties due to incorrect implementation of numerical methods in the software- oddly enough, the error was manifesting its presence only in specific, large and weakly bonded materials and hence remained undetected until I asked software developers to carefully analyse my simulations. As a consequence, I was forced to seek for alternatives to CRYSTAL09 code and in the later sections I demonstrate geometry optimization and calculation of vibrational modes using CASTEP, which is based on plane wave basis set. In my opinion, computational cost and performance of existing computers restrict large-scale screening of vibrational modes in small molecular systems with periodic boundary conditions. Nevertheless, I report detailed assessment of both DFT codes and discuss their applicability to studies of crystalline organic semiconductors.

# 4.1 Computational results using CRYSTAL09

## 4.1.1 C8-BTBT

C8-BTBT was my first system of interest. As mentioned in previous section, accuracy and effectiveness of the simulation depend on several input parameters. It was therefore decided to roughly follow the method and parameters used by Civalleri [38] to compute vibrational modes of molecular crystals. I adopted the same hybrid functional (B3LYP), type of basis set (6-31G(d,p)[92]) and level of accuracy in evaluating the Coulomb and exchange series (TOLINTEG values) and size of the grid (XLGRID), however for final geometry optimisation it was decided to use tighter convergence criteria for energy, gradient and displacement in order to improve accuracy of phonon calculation. Geometry of the asymmetric unit was imported from Cambridge Structural Database[137] and all hydrogen bonds were initially normalized to a standard setting.

Before starting geometry optimisation it was necessary to evaluate the effect of different SHRINK values on the final energy of the system. The evaluation was done by running a series of simulations with default convergence criteria and comparing the final energies and cell parameters. In order to obtain the total energy of the system, a single-point energy calculation was run using FINALRUN keyword. The comparison of energies of the system for different SHRINK values is given in Figure 4.2. As one can see, for SHRINK values higher than (4;4) the energy remained roughly constant. Similarly, lattice parameters and unit cell volume were decreasing as a function of SHRINK, but remained constant for (5;5) and (6;6). In a fact, (5;5) has the lowest energy, however at (6;6) the computational efficiency was higher by about 25% and since the energy difference was negligible it was decided to use the value which offered better performance.

The next step was to perform final geometry optimisation using tight convergence criteria (TOLDEE =$10^{-10}$ Hartree; TOLDEG = $3 \cdot 10^{-5}$ a.u and TOLDEX = $12 \cdot 10^{-5}$ a.u.), which were necessary to start vibrational modes calculation in the later part of the project. I set up a simulation making use of 608 CPUs and with wall time of 24h, however for an unknown reason the run has been terminated after 6,5 h. Direct inspection of the output file revealed that the program has correctly recognized and read the input geometry, and after performing 63 complete optimisation cycles suddenly crashed returning following error message:

```
At line 168 of file libgrimme.f90 (unit = 78, file = '& ')
Fortran runtime error: Permission denied trying to open file '/tmp/gfortrantmp4GgUva'
```

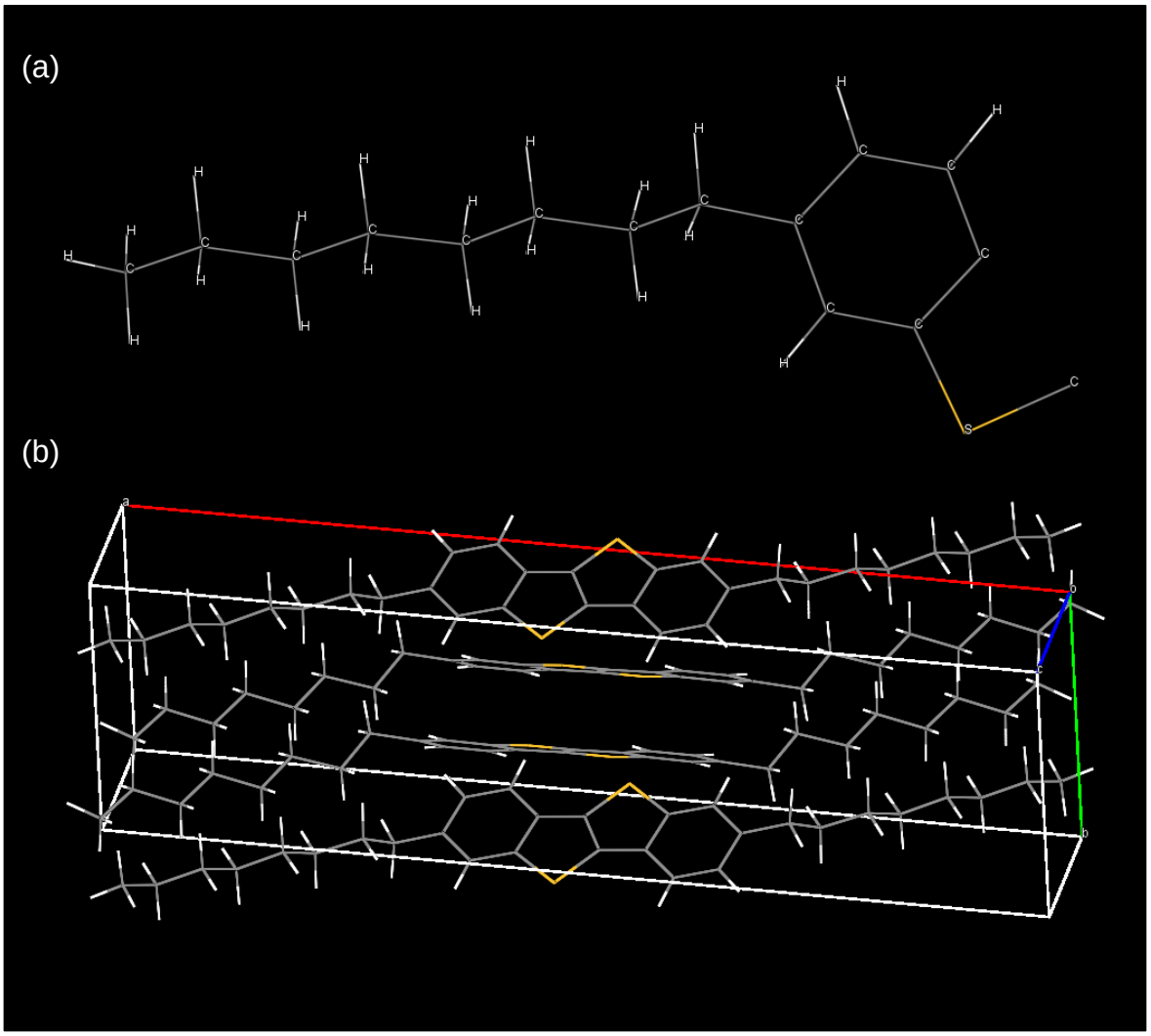


Figure 4.1: Structure of C8-BTBT asymmetric unit (**a**) and packing of C8-BTBT molecules within a unit cell (**b**). Crystal structure was imported from Cambridge Structural Database[137]

This has been initially diagnosed as a result of HECToR instability. The typical procedure was to insert RESTART keyword in OPTGEOM section of the input file and the program should restart automatically from the last complete optimisation step (optinfo.dat) file. Restart was terminated after 13 minutes and subsequent inspection of the output file revealed that program correctly imported geometry form the previous optimisation step, but assigned "Not a Number" values of $\alpha, \beta$ and $\gamma$ lattice constants in the next step and finally crashed:

```
********************************************************************************
LATTICE PARAMETERS (ANGSTROMS AND DEGREES) - BOHR = 0.5291772083 ANGSTROM
```

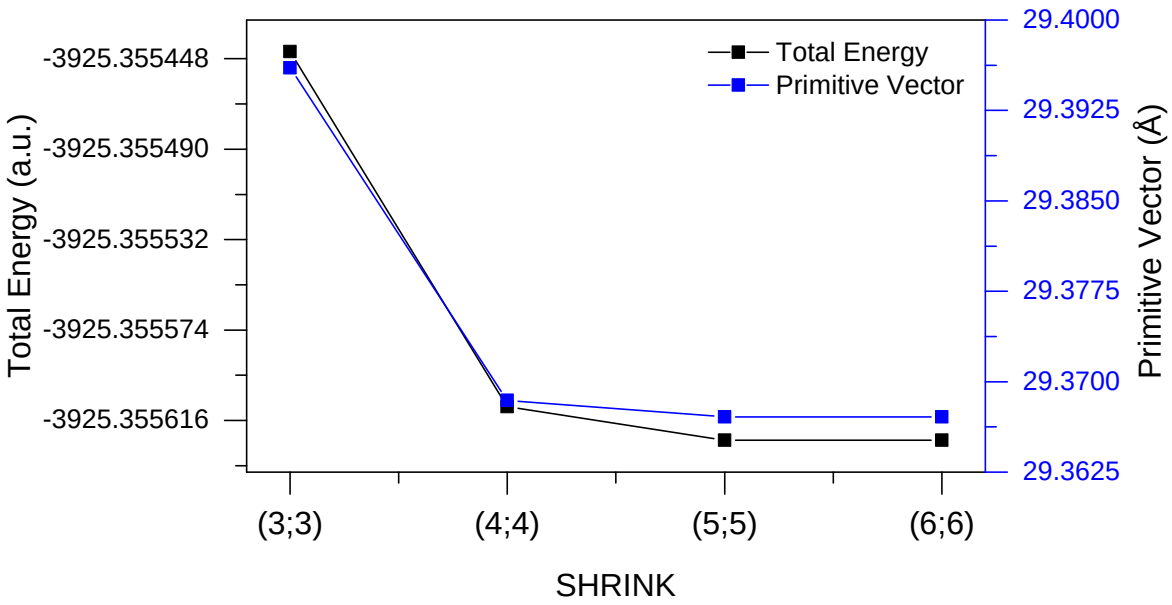


Figure 4.2: Total Energy of the system (in autonomous units) and primitive vector $\hat{a}$ as a function of SHRINK parameter.

```
PRIMITIVE CELL - CENTRING CODE 1/0 VOLUME=      0.000000 - DENSITY      Inf g/cm^3
A                 B                 C                 ALPHA      BETA       GAMMA
0.00000000        0.00000000        0.00000000          NaN        NaN        NaN
WARNING **** MINV3 **** THE DETERMINANT OF THE DIRECT LATTICE VECTORS IS VERY SMALL
********************************************************************************
```

For practical reasons I am going to omit sequence of steps undertaken to diagnose the issue. This error was finally recognized by software developers as a bug in the code. The source of the error was rather difficult to track for two reasons: firstly, it was evident only when C8-BTBT crystal structure was used as an input, but not in case of diF-TES-ADT. Secondly, simulations crashed only when restarted from checkpoint files using HECToR supercomputer, but where fine if the same sequence of steps was executed using local computing cluster. This behaviour was rather counter intuitive, but the code compiled on HECToR was modified to make parallelization more efficient and unfortunately other users have never experienced similar problems.

It was decided to continue simulations using serial[1] version of the software installed on Annapolis computing cluster. The simulation has been restarted using output data form optimisation step number 140. The geometry import, SCF iteration and force

[1]There are two parallel implementations of Crystal code aimed for simulations on large computing clusters. PCrystal supports 10s of cores whereas MPPCrystal can distribute the task between 100s of cores In comparison, serial implementation runs on a single CPU supporting only few cores at a time.

calculation took about a week and afterwards the optimisation process was progressing at a steady pace of one step per day. The efficiency has been dramatically reduced compared to MPPCrystal completing 145 steps per day, however the serial mode calculation proved to be very stable. After completing 40 geometry optimisation steps the displacement convergence conditions have been satisfied:

```
********************************************************************************
PREDICTED ENERGY CHANGE     -0.149E-06
MAX GRADIENT      0.000849  THRESHOLD          0.000045 CONVERGED NO
RMS GRADIENT      0.000115  THRESHOLD          0.000030 CONVERGED NO
MAX DISPLAC.      0.000085  THRESHOLD          0.000180 CONVERGED YES
RMS DISPLAC.      0.000012  THRESHOLD          0.000120 CONVERGED YES
TTTTTTTTTTTTTTTTTTTTTTTTTTTTTTTT OPTI      TELAPSE  1920302.25 TCPU  1163610.51
********************************************************************************
```

Although max and rms gradient were much above the predefined threshold, they remained unchanged for at least five consecutive optimisation steps. In theory, the iterative method should always result in a fully converged structure provided that the number of steps is large enough, but in practice it may be assumed that the gradient has already approached asymptotic value. The resultant geometry was ready to be used as an input for simulation of vibration modes, however it was absolutely impractical- phonon calculations are longer and more demanding than geometry optimisation and in my judgment such simulation would exceed the time frame of the project. Finally, I decided to cease simulations of C8-BTBT and wait till the bug is fixed in next stable release of the code, which unfortunately did not happen within a time frame of my computational grant.

### 4.1.2 diF-TES-ADT

Because of the problems that were encountered during C8-BTBT structure optimisation it was decided to look for a molecule with smaller number of atoms, which could be much easier to simulate using DFT. diF-TES-ADT seemed to be a perfect candidate, since it has 76 atoms in the unit cell compared to 144 in C8-BTBT. Again, the same functional and basis set were used. The relevant input was imported form EMSL basis set exchange [92] and parameters used to evaluate Grimme dispersion correction were copied from Grimmie's original paper [93]. The input geometry was imported from Cambridge Structural Database and all hydrogen bonds were normalized to a standard setting. As for C8-BTBT, it was decided to evaluate the effect of SHRINK value on the total energy of the system. During the first simulation the SCF convergence was not achieved within the limit of 500 steps and the run has been terminated. The total energy and the change of energy were fluctuating from cycle to cycle:

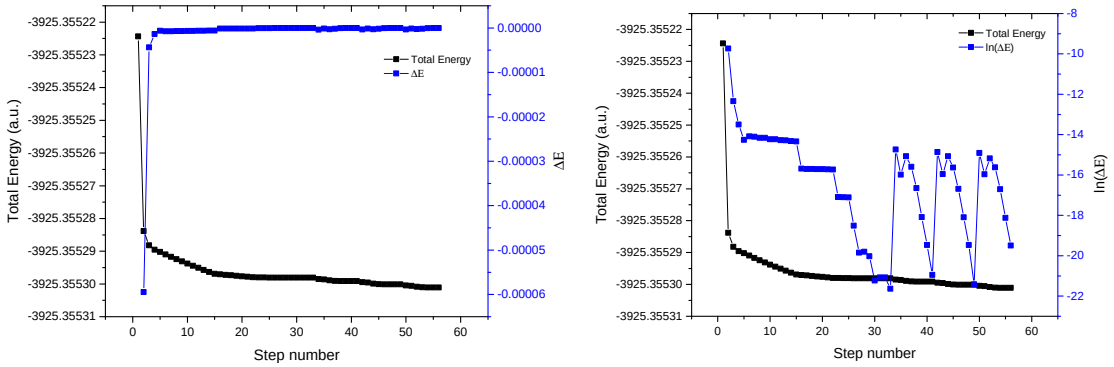


Figure 4.3: Total energy of the system during final geometry optimization. The change of energy between subsequent steps is plotted on the left panel. The right panel shows natural logarithm of $\Delta E$. The periodic features suggest that the optimization algorithm overestimates the rms forces.

```
CYC 361 ETOT(AU)   4.588630519540E+01 DETOT -4.30E+02 tst   7.05E+01 PX   9.46E+02
CYC 362 ETOT(AU)   4.436839988869E+02 DETOT  3.98E+02 tst   1.76E+01 PX   9.46E+02
CYC 363 ETOT(AU)   7.290339219827E+01 DETOT -3.71E+02 tst   2.74E+01 PX   9.46E+02
CYC 364 ETOT(AU)   4.761063538740E+02 DETOT  4.03E+02 tst   6.12E+01 PX   9.46E+02
```

and finally became divergent. An effect like that typically follows from fact that the x-ray diffraction data contains imprecise information about the length of hydrogen bonds. Since the input geometry that was used had normalized bond lengths, I came up with a somehow counter-intuitive idea to repeat the simulation using original structure with uncorrected bond lengths. This guess proved to be successful and a series of simulations with different SHRINK values were started. Comparison of the energies of the system for different values of the SHRINK are given on Figure 4.5. The lowest energy of the system was obtained with SHRINK (6;6). Figure 4.5 indicates that SHRINK (5;5) resulted in abnormal energy of the system and lattice constants whereas SHRINK (7;7) returned values that were fully consistent with (6;6), but it was more expensive computationally. However, $\hat{a}$ lattice parameter shrank by 10% compared to the original x-ray diffraction data and therefore it was decided to run two separate simulations: full geometry optimization and optimisation of atomic coordinates within a fixed unit cell ("atomic" on the Figure 4.5). Both geometry optimizations converged successfully after 61 and 70 steps, respectively.

Calculation of vibrational modes was performed using FREQCALC command. The EXTERANAL command was used to import optimised geometries from output files produced during previous runs. Simulation performed on fully optimised structure

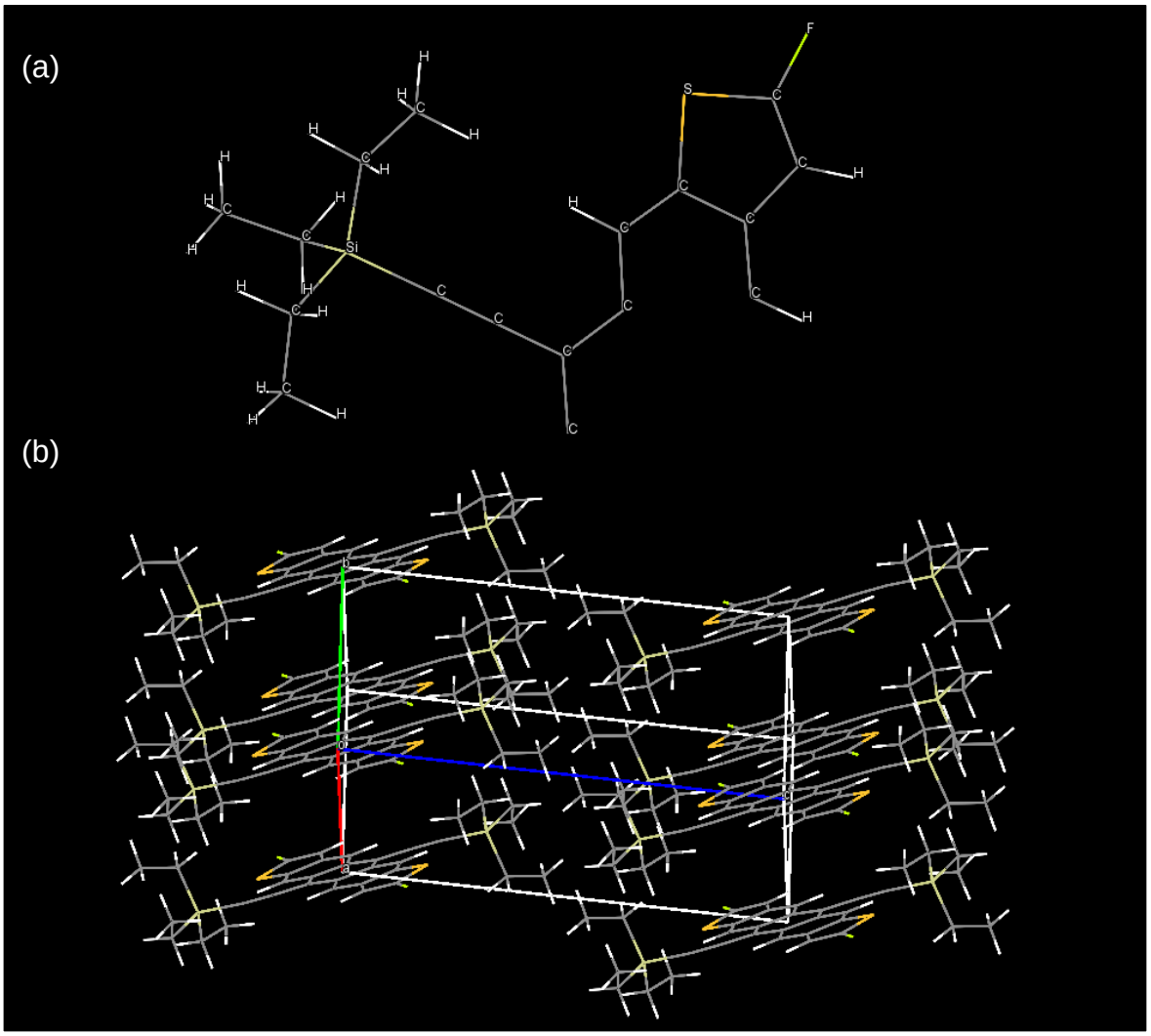


Figure 4.4: Structure of diF-TES-ADT asymmetric unit (**a**) and packing (**b**) of diF-TES-ADT molecules within a unit cell. Crystal structure was imported from Cambridge Structural Database [137]

returned 228 vibrational modes with frequencies between $-6.90$ cm$^{-1}$ and 3282.45 cm$^{-1}$ including both Raman and infrared active modes. It is especially interesting to look at the first four modes ("A" stands for active mode, "I" for inactive):

| | MODES | EIGV (HARTREE**2) | FREQUENCIES (CM**-1) | (THZ) | IRREP | IR | INTENS (KM/MOL) | RAMAN |
|---|---|---|---|---|---|---|---|---|
| 1– | 1 | −0.9895E−09 | −6.9039 | −0.2070 | (AU ) | A | ( 0.00) | I |
| 2– | 2 | −0.6427E−09 | −5.5640 | −0.1668 | (AU ) | A | ( 0.00) | I |
| 3– | 3 | −0.3856E−09 | −4.3099 | −0.1292 | (AU ) | A | ( 0.00) | I |
| 4– | 4 | 0.1578E−07 | 27.5710 | 0.8266 | (AG ) | I | ( 0.00) | A |

The first three modes are acoustic translations of the whole unit cell and in prin-

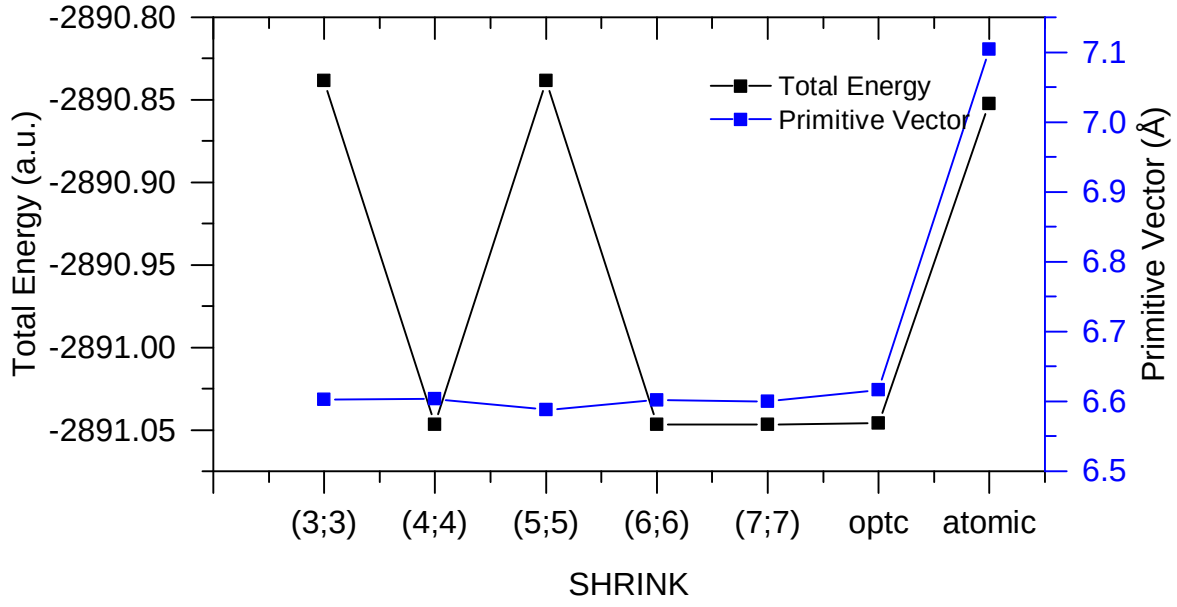


Figure 4.5: The energy of the system (expressed in autonomous units) and primitive vector $\hat{a}$ as a function of SHRINK parameter. "optc" refers to final geometry optimisation with shrink (6;6) and tight convergence threshold. "atomic" refers to optimisation of atomic coordinates within fixed unit cell with shrink (6;6) and tight convergence threshold.

ciple should have zero frequency. The negative (or in a fact complex) frequencies of the first three modes indicate some inaccuracy of the simulation, but since negative frequencies are close to zero one may conclude that the overall quality of the data is quite good. The same simulation was performed using input geometry with optimised atomic coordinates but fixed unit cell coordinates:

| MODES | | EIGV | FREQUENCIES | | IRREP | IR | INTENS | RAMAN |
|---|---|---|---|---|---|---|---|---|
| | | (HARTREE**2) | (CM**-1) | (THZ) | | | (KM/MOL) | |
| 1- | 1 | -0.6901E-08 | -18.2326 | -0.5466 | (AG ) | I | ( 0.00) | A |
| 2- | 2 | -0.1182E-08 | -7.5467 | -0.2262 | (AU ) | A | ( 0.00) | I |
| 3- | 3 | -0.6523E-09 | -5.6052 | -0.1680 | (AU ) | A | ( 0.00) | I |
| 4- | 4 | -0.3601E-09 | -4.1651 | -0.1249 | (AU ) | A | ( 0.00) | I |
| 5- | 5 | 0.3021E-08 | 12.0636 | 0.3617 | (AU ) | A | ( 0.00) | I |
| 6- | 6 | 0.9947E-08 | 21.8889 | 0.6562 | (AG ) | I | ( 0.00) | A |

As one can see, the first four modes have unphysical frequencies. The high negative and Raman active frequency of the first acoustic mode indicates that the data is less accurate compared to a fully optimised unit cell. The comparison between experimental Raman spectra collected at room temperature and theoretical frequencies of vibrational modes is shown on Figure 4.6(**a**) and (**b**). Direct assignment of theoretical modes to experimental spectra is virtually impossible without knowledge of specific

mode intensities due to close spacing between the modes.

The accuracy of the vibrational modes calculations depends on two major factors: convergence of geometry optimisation and precision of numerical methods used to calculate derivatives. Since the geometry was well converged I decided to increase number of points at which numerical derivatives are calculated. The NUMDERIV keyword is used to specify the algorithm used to numerically evaluate the gradient, however it affects the time needed to complete the simulation. It was decided to change the algorithm from different quotient formula to a central-difference method [91] effectively doubling the number of points at which the gradients are calculated. The run has not finished within 24h and was restarted using RESTART keyword. Unfortunately, the restart was unsuccessful and following error was returned:

```
PE RANK 841 exit signal Segmentation fault
```

The simulation was restarted again using PCrystal and again returned an error message:

```
ERROR **** SYMMETRIZE_DIR **** IPPA ALLOCATION
```

The origin of this error was attributed to a bug in part of the code responsible for setting up the grids used to evaluate the density functional terms. Given the fact that the C8-BTBT system is much more computationally expensive than dif-TES-ADT and the bug was not going to be fixed before release of the next version of CRYSTAL software, it was concluded that the project cannot be continued.

### 4.1.3 Summary

Formalism of Gaussian orbitals provides a promising framework for multi-parallel simulations of large organic systems. Since CRYSTAL09 was a well-established simulation tool used for smaller systems it was reasonable to assume that MPP-CRYSTAL, which is parallelised implementation of the code, would enable first of its kind opportunity to study organic semiconducting crystals using DFT methods. The decision to endeavour and use recent version of the code compiled on a custom supercomputer was based on an assumption that since MPP-CRYSTAL is stable when simulating smaller systems, it can easily be scaled up if one has an access to a computer that is powerful enough. This proved to be wrong and it was realized that above certain number of atoms per unit cell software becomes numerically unstable. The serial mode, however, was not efficient enough to study large organic system within a reasonable time framework. Moreover, the version of the code that was used did not include functionality to predict intensities of Raman active modes and hence limited my ability to match experimental

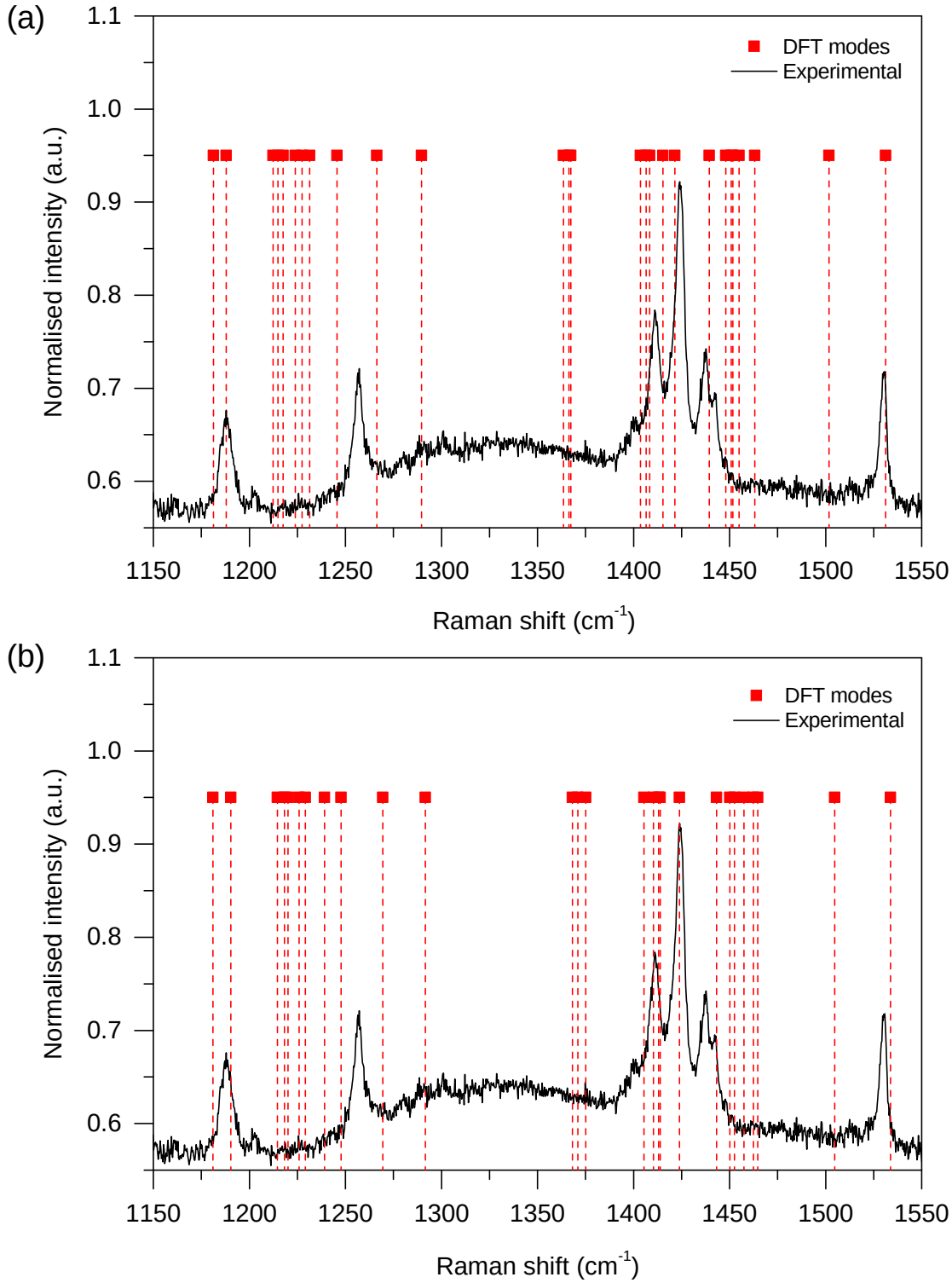


Figure 4.6: Comparison of experimental dif-TES-ADT Raman spectra (**black**) with theoretical (**red**) vibrational frequencies calculated for atomic positions optimised within a fixed unit cell (**a**) and fully optimised geometry (**b**). The frequencies of vibrational modes were rescaled using empirical B3LYP scaling factor [138].

spectra with calculated vibrational frequencies. As the release of a new version of the code was delayed it was decided to use CASTEP as a promising alternative, since CASTEP has been proven to be very stable when running on HECToR. However, one should be able to successfully reproduce the above results including intensities of Raman spectra using CRYSTAL14, which was not available at the time when these simulations were performed.

## 4.2 Computational results using CASTEP

### 4.2.1 C8-BTBT

As with CRYSTAL09, preliminary simulations were needed to make a correct choice of set of parameters. For plane wave basis set the only parameter to be optimised is the electronic kinetic energy cut-off $E_{\text{cutoff}}$. Indeed, the quality of plane wave basis set is specified by this single parameter. The higher the $E_{\text{cutoff}}$ the better the basis set, however at some point the computational cost of increasing $E_{\text{cutoff}}$ becomes prohibitive and therefore it is important to find optimal value of cut-off parameter. Another parameter that has to be optimised is spacing of k-points in the Brillouin zone to be sampled. The first step was to optimise the structure using $E_{\text{cutoff}}$=350 eV and 0.06 $\mathring{A}^{-1}$ k-spacing so that the optimisation was quick yet accurate enough. In order to probe the effect of different values of $E_{\text{cutoff}}$, I performed several single point energy calculations using previously optimised structure. The values examined were in the 350 to 1600 eV range with 50 eV step. Total energies of the system as a function of cut-off energy are shown in Figure 4.8. Given the fact that the change in total energy decreased exponentially with basis set cutoff, it was concluded that $E_{\text{cutoff}}$=1100 eV guarantees reasonable compromise between accuracy and computational efficiency. With established basis set it was necessary to examine the influence of k-point spacing on the energy convergence. Again, using the same input geometry, I calculated single point energy for different values of k-point spacing as shown in Figure 4.7. I decided to run subsequent simulations with 0.04 $\mathring{A}^{-1}$ spacing since it was close enough in terms of total energy to smaller values of spacing, yet the simulation wall time was three times shorter than at 0.03 $\mathring{A}^{-1}$.

The next step was to optimise the geometry with fixed cell parameters to tighter convergence criteria before starting phonon calculations. Initially, geometry optimisation was unsuccessful with forces oscillating around a constant value and not converging within 500 steps, as shown in Figure 4.9, and returning warning message about the symmetry of the system:

```
BFGS: finished iteration   500 with enthalpy= -5.84201333E+003 eV

+-------------+-----------------+-----------------+-------------+-----+ <-- BFGS
| Parameter   |      value      |    tolerance    |    units    | OK? | <-- BFGS
+-------------+-----------------+-----------------+-------------+-----+ <-- BFGS
|   dE/ion    |  2.455526E-011  |  5.000000E-007  |          eV |  Yes | <-- BFGS
|   |F|max    |  2.071310E-004  |  5.000000E-005  |       eV/A |  No  | <-- BFGS
|   |dR|max   |  1.955848E-006  |  1.000000E-004  |           A |  Yes | <-- BFGS
+-------------+-----------------+-----------------+-------------+-----+ <-- BFGS
```

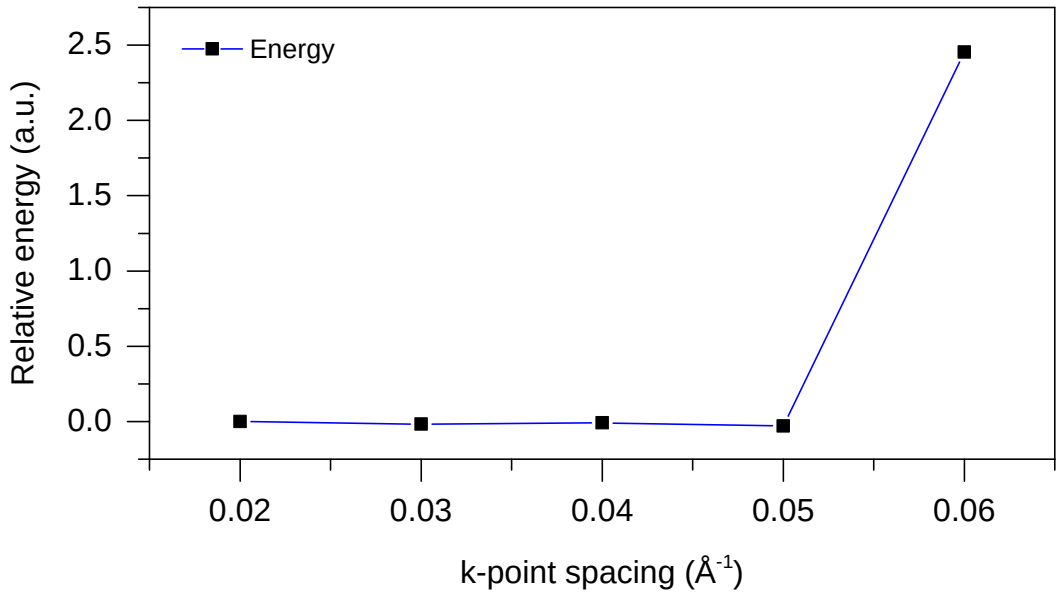


Figure 4.7: Total energy of the system vs k-point sampling at $E_{\text{cutoff}}$=1100 eV. The total energy at $k = 0.02$ Å was subtracted as a reference data.

```
BFGS : WARNING - Geometry optimization failed to converge after        500 steps

!-------------------------------------------------------------------------------!
!                                                                               !
!                      * * *     W A R N I N G     * * *                      !
!                                                                               !
!   Atomic positions are slightly inconsistent with symmetry operations,        !
!   (although the discrepancy is lower than value of SYMMETRY_TOL).             !
!    In severe cases this could lead to seriously inaccurate results.           !
!                                                                               !
!   It is recommended that symmetries are satisfied to a tolerance of 1e-8au    !
!   or better. Consider one or more of the following:                           !
!     - Adjust input so that atomic positions and symmetry are consistent.      !
!     - Use SNAP_TO_SYMMETRY keyword in the cell file to adjust co-ordinates.   !
!     - Reduce the value of SYMMETRY_TOL in the cell file.                      !
!     - Remove incorrect symmetry operations from .cell file.                   !
!                                                                               !
!-------------------------------------------------------------------------------!
```

It was necessary to include dispersion correction as it was done using Grimme method with CRYSTAL09. I used Tkatchenko-Scheffler [57] method since it was known to work well with PBE functional that I was using. *snap_to_symmetry* keyword was used to force the system into proper symmetry group and *elec_energy_tol* value was set to $10^{-11}$ eV to increase the convergence tolerance for finding ground state, however the subsequent geometry optimisation did not converge to a predefined tolerances:

```
BFGS: Warning - looks like this system is as converged as possible.
```

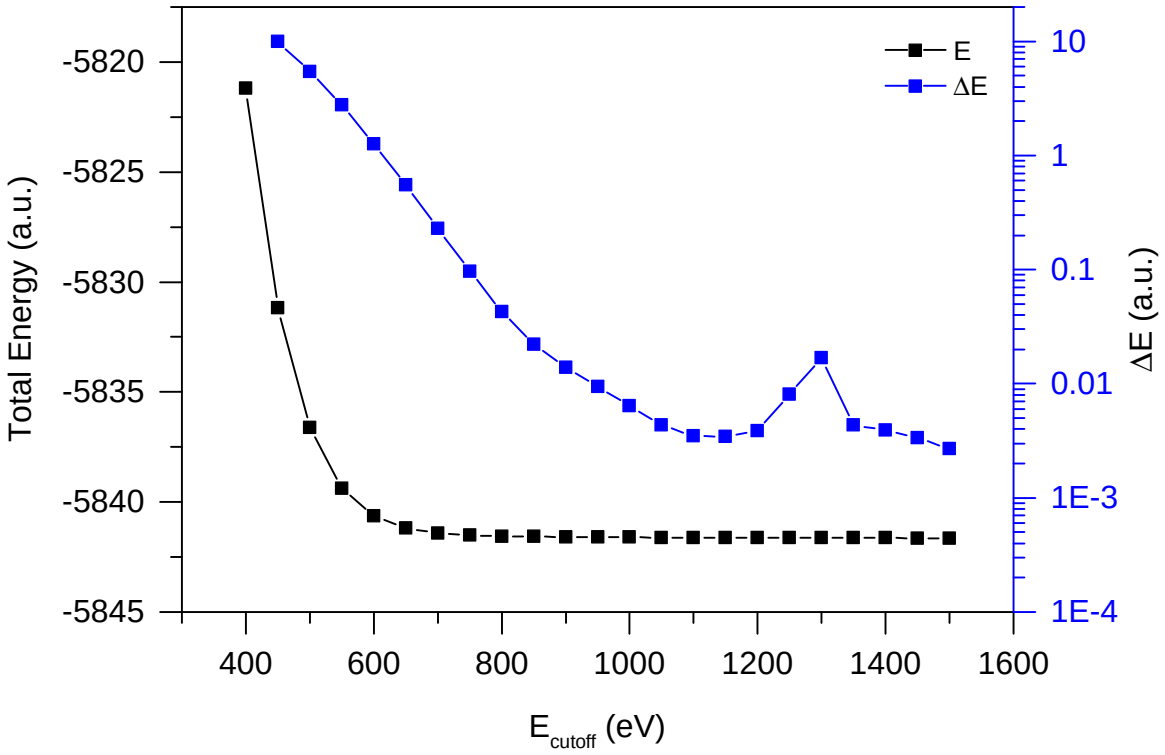


Figure 4.8: Total energy of the system (**black**) and change in energy (**blue**) between subsequent steps vs basis cutoff energy.

```
        Maybe your geometry convergence tolerances are too tight?

BFGS: finished iteration   103 with enthalpy= -1.16915042E+004 eV

+-------------+-------------------+-------------------+-------------+-----+ <-- BFGS
| Parameter   |       value       |     tolerance     |    units    | OK? | <-- BFGS
+-------------+-------------------+-------------------+-------------+-----+ <-- BFGS
|  dE/ion     |   1.712477E-007   |   5.000000E-007   |          eV | Yes | <-- BFGS
|  |F|max     |   3.743847E-003   |   5.000000E-005   |       eV/A  | No  | <-- BFGS
|  |dR|max    |   8.927557E-005   |   1.000000E-004   |           A | Yes | <-- BFGS
+-------------+-------------------+-------------------+-------------+-----+ <-- BFGS
BFGS : Geometry optimization completed successfully.
```

Nevertheless I decided to use resultant geometry as an input for a phonon calculation. The calculation was successful, however it returned six negative frequencies which is somehow worrying given the fact, that the first three acoustic modes should have zero frequency[2]:

```
+-------------------------------------------------------------------------+
+  E N D   O F   R A M A N   I N T E N S I T Y   C A L C U L A T I O N  +
```

[2]Columns denote (from left to right): mode number, mode frequency, type of irreducible representation, IR intensity, IR activity (Y denote active, N denote inactive), Raman intensity, Raman activity (Y denote active, N denote inactive).

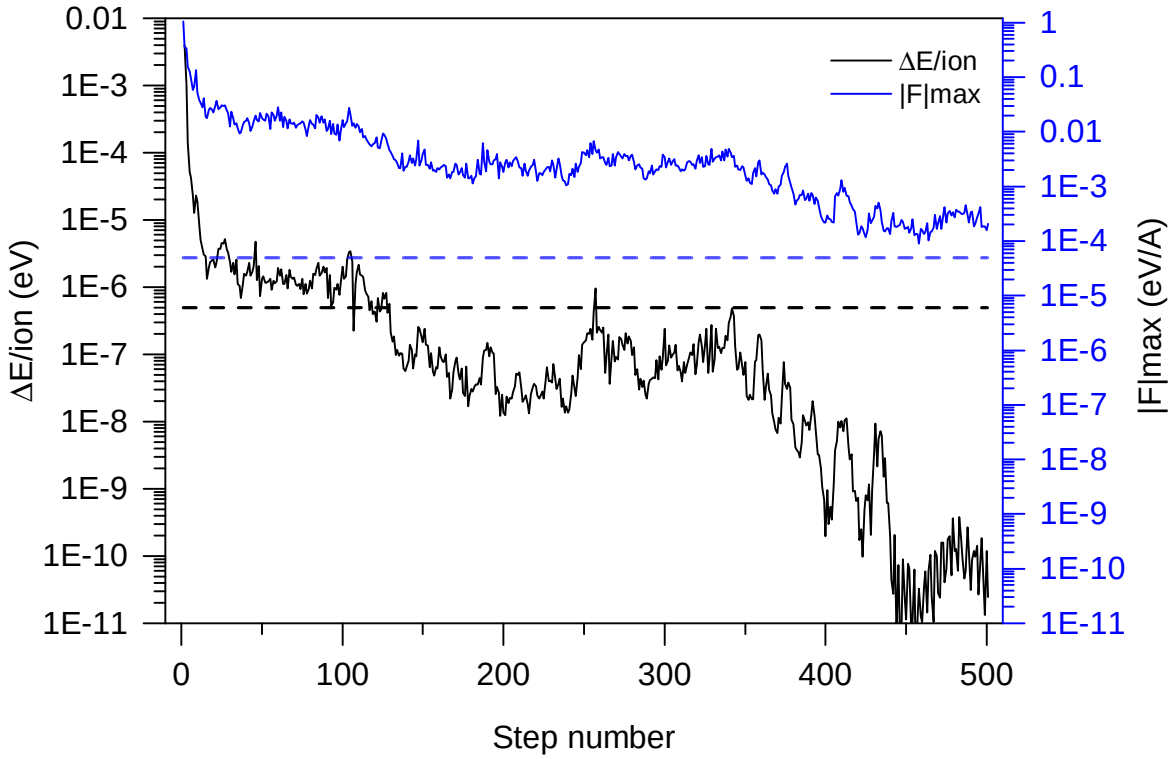


Figure 4.9: Change in energy per ion (**black**) and maximum force (**blue**) during fixed cell geometry optimisation of C8-BTBT. No dispersion correction has been applied. Convergence tolerances are defined by dashed lines.

```
+                                                                                +
+================================================================================+
+ ------------------------------------------------------------------------------ +
+  q-pt=     1 (   0.000000   0.000000   0.000000)      1.0000000000              +
+ ------------------------------------------------------------------------------ +
+  Acoustic sum rule correction <  18.192771 cm-1 applied                        +
+     N      Frequency irrep.     ir intensity active  raman intensity active   +
+              (cm-1)          ((D/A)**2/amu)              (A**4)               +
+                                                                                +
+     1      -52.569758    a          0.0000000  N           0.0000000  Y      +
+     2      -46.061472    b          0.0000000  Y           0.0000000  N      +
+     3      -40.342036    c          0.0000000  N           0.0000000  Y      +
+     4      -18.919642    d          0.0000108  Y           0.0000000  N      +
+     5       -0.056872    d          0.0001334  N           0.0000000  N      +
+     6       -0.045723    d          0.0000865  N           0.0000000  N      +
+     7       15.953447    c          0.0000000  N           1.9224665  Y      +
+     8       17.732895    b          0.0019925  N           0.0000000  N      +
+     9       25.257258    b          0.0001399  Y           0.0000000  N      +
+    10       27.981615    d          0.0018054  Y           0.0000000  N      +
+    11       30.536380    a          0.0000000  N           4.3869181  Y      +
+    12       32.861081    b          0.0000807  Y           0.0000000  N      +
+    13       43.146708    b          0.0000722  Y           0.0000000  N      +
```

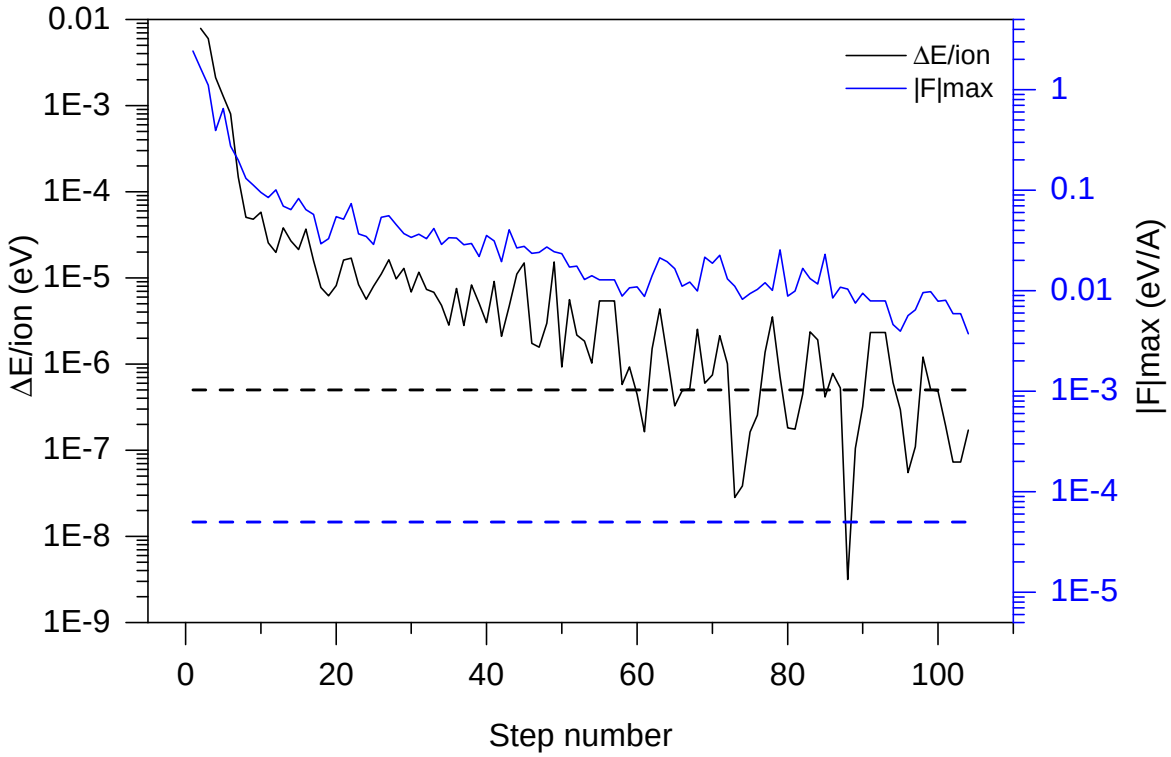


Figure 4.10: Change in energy per ion (**black**) and maximum force (**blue**) during fixed cell geometry optimisation with TS dispersion correction scheme. Convergence tolerances are defined by dashed lines.

Using calculated mode frequencies and activities I generated Lorentzian peaks multiplying each activity by temperature dependent Boltzmann factor using dos.pl script provided with CASTEP. Comparison of resultant spectra and experimental data collected at room temperature is shown in Figure 4.11(**a**) and (**b**). Although the error in acoustic modes is up to 50 $cm^{-1}$, the comparison with experimental data demonstrates that the actual uncertainty is less than 10 $cm^{-1}$ and calculated intensities are correct enough to assign them to experimental peaks. In order to improve geometry optimisation and, as a result, spectra calculation I have tried to apply damped molecular dynamics method instead of BGFS algorithm. In principle BGFS method is the most effective one since it predicts where the minimum is and bypasses some of the intermediate optimisation steps. The drawback of this method is manifested when, in a complex energy landscape, prediction algorithm overshoots the local minimum. Damped molecular dynamics uses the critical damping regime and, although more computationally expensive, should converge to a minimum given enough steps. The maximum force during the optimisation is plotted in Figure 4.12. The lowest value

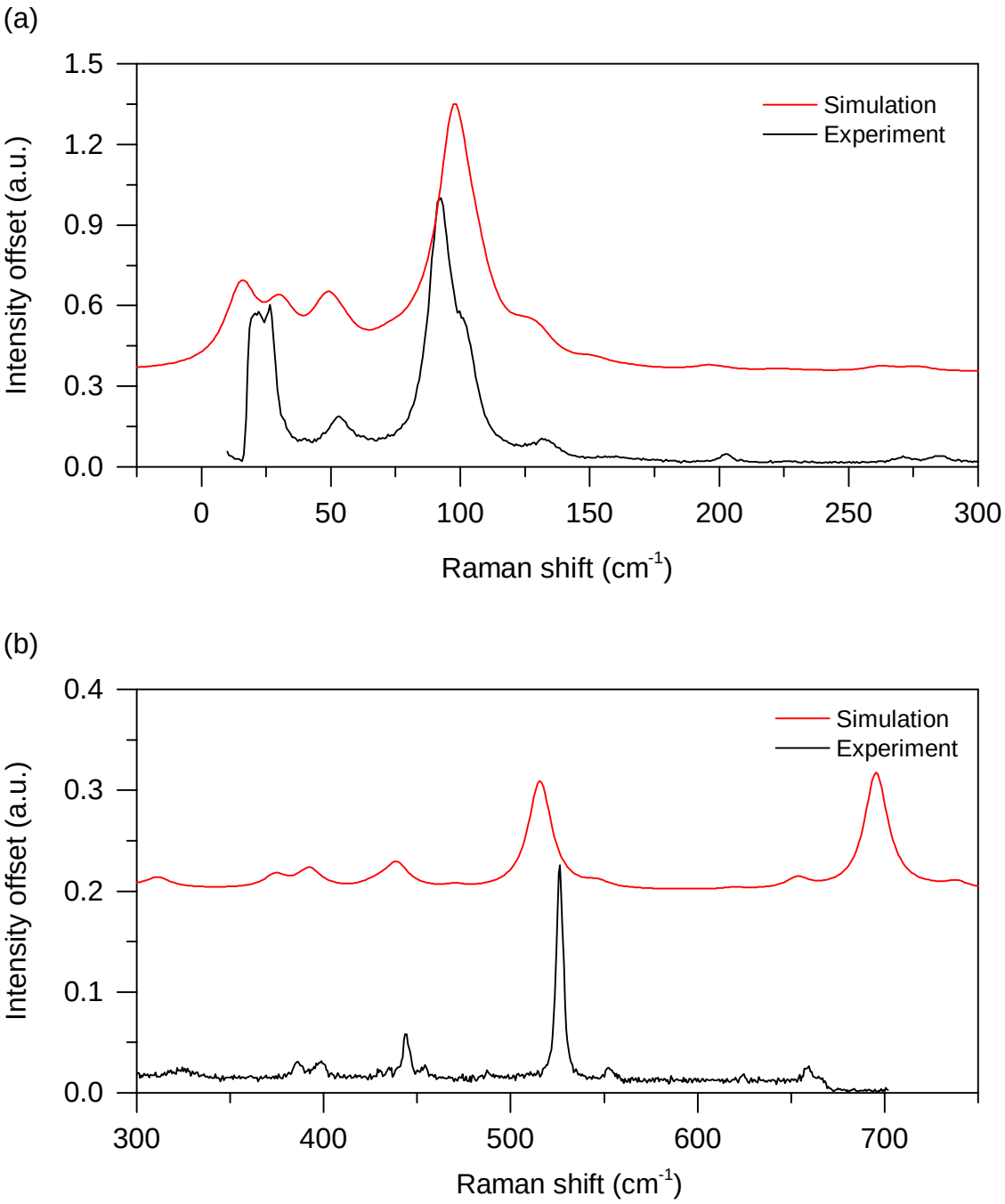


Figure 4.11: Comparison of theoretical (**red**) and experimental (**black**) Raman spectra of C8-BTBT corresponding to intermolecular (**a**) and intramolecular (**b**) vibrational modes at room temperature. Periodic plane wave formalism implemented in CASTEP is very effective in reproducing experimental spectra both in terms of vibrational frequencies and mode intensities. Mode frequencies were not rescaled by empirical scaling factor.

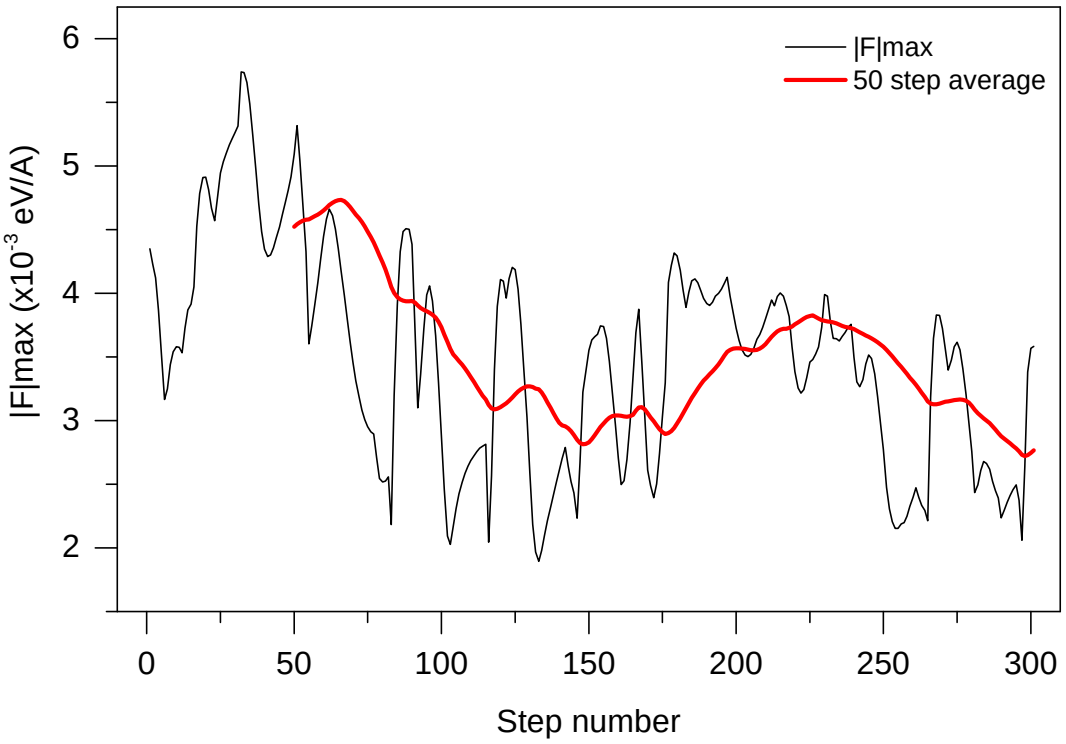


Figure 4.12: Maximum force (**black**) and 50 step average (**red**) during damped molecular dynamics geometry optimisation.

achieved is smaller than when using gradient method but still two orders of magnitude bigger than the recommended tolerance. If one assumes that the $F_{\max}$ follows geometric series, i.e. it halves on average every 300 steps, the total number of steps required to converge the optimisation would be around 21000. This would be equivalent to running the simulation on ARCHER for 60 hours using 288 cpus. Given the fact that the $F_{\max}$ might not follow geometric decay I found that computational cost of such optimisation is prohibitive. I have also tried to optimise both ionic positions and unit cell parameters simultaneously, which effectively corresponds to a system at 0 K. The convergence of $F_{\max}$ and energy is shown on Figure 4.13. The convergence tolerances were satisfied after 181 optimisation steps, however I did not proceed with phonon calculation due to computational budget constraints.

### 4.2.2 diF-TES-ADT

As for C8-BTBT I started by running rough geometry optimisation followed by series of single point energy calculations to determine the optimal basis set energy cut-off. The convergence of energy is shown in Figure 4.14. I decided to use 1100 eV in all

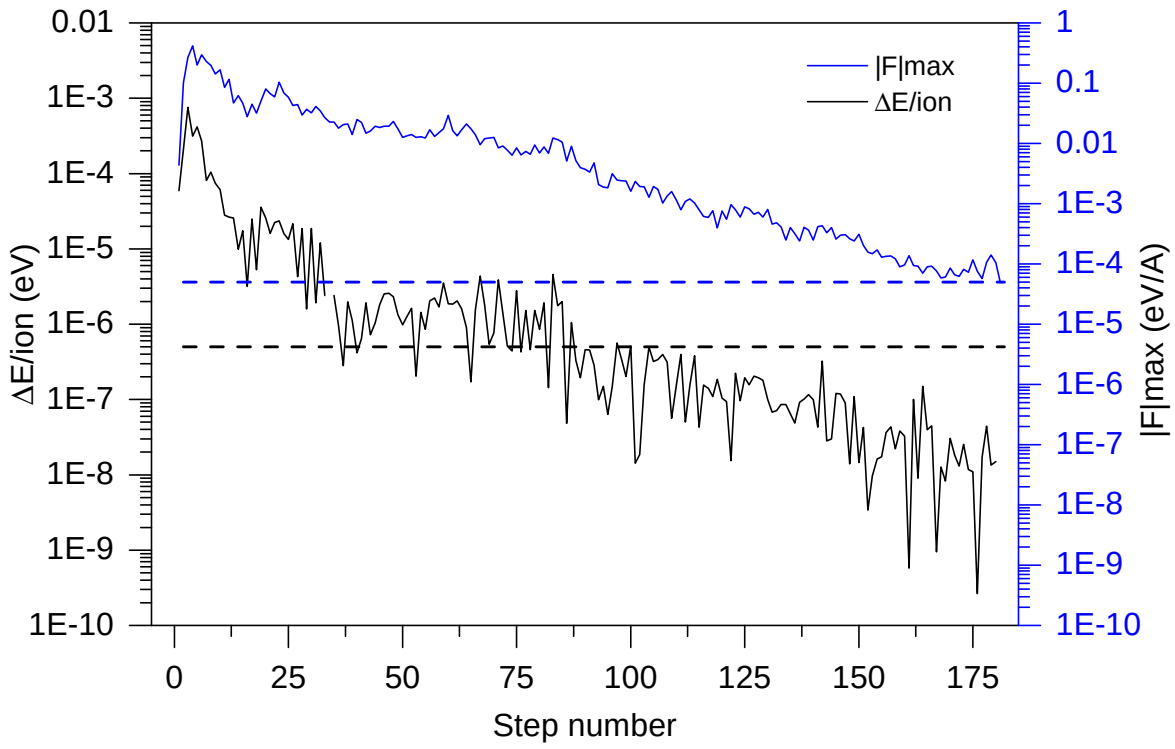


Figure 4.13: Change in energy per ion (**black**) and maximum force (**blue**) during variable cell C8-BTBT geometry optimisation. Convergence tolerances are defined by dashed lines.

subsequent simulations. Results of k-point convergence tests are shown in Figure 4.15. I decided to use 0.03 $Å^{-1}$ as an optimal k-spacing value. After convergence tests I started final geometry optimisation. Again, I optimised positions of atoms within fixed unit cell using the same convergence parameters as previously for C8-BTBT. Convergence of $F_{\max}$ and $\Delta E/ion$ is shown in Figure 4.16. Geometry optimisation converged successfully after 260 steps, however I did not continue phonon calculation due to constraints of computational budget.

### 4.2.3 Summary

Direct comparison of spectra calculated using CRYSTAL09 and CASTEP was not possible because of bug in the code. As expected the plain wave formalism was less computationally efficient, in terms of CPU hours, than Gaussian wave functions. Tkatchenko-Scheffler dispersion correction clearly did not work well when used to optimise "soft" crystals such as C8-BTBT, where significant contribution to the total energy comes from dispersion interactions. This effect was manifested in convergence

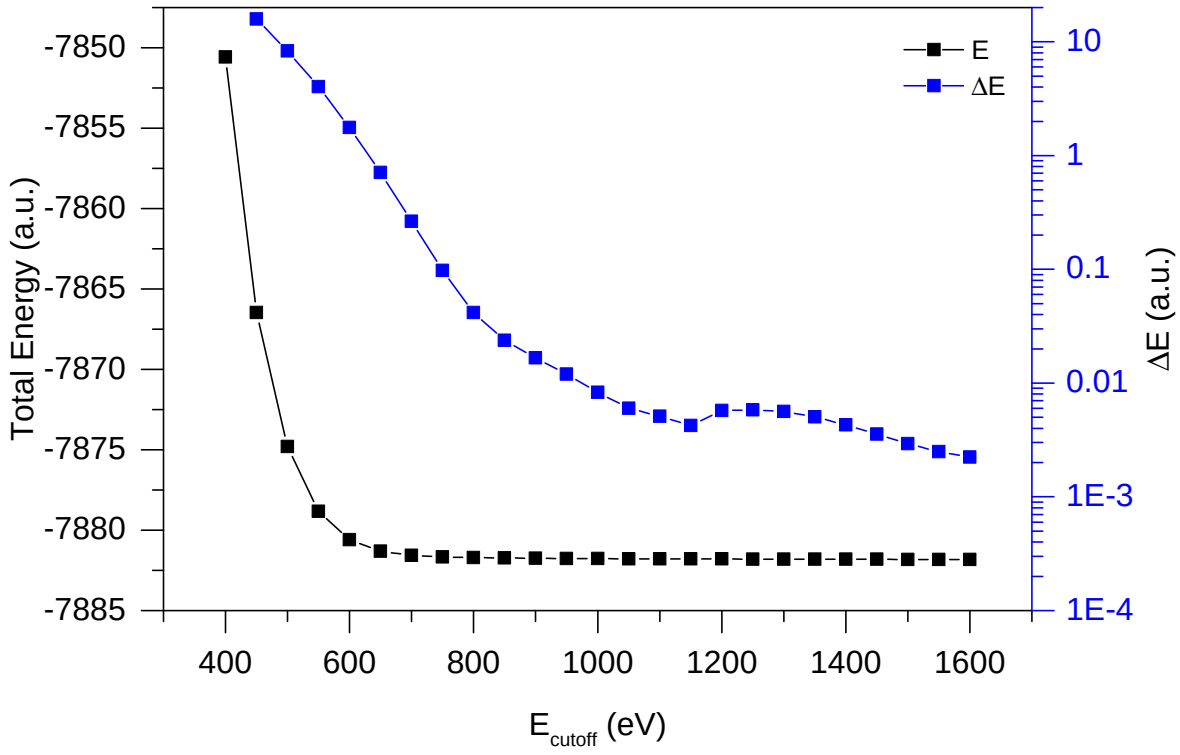


Figure 4.14: Total energy of the system (**black**) and change of energy (**blue**) between subsequent steps vs basis cut-off energy.

of $F_{\max}$ during geometry optimisation of C8-BTBT and diF-TES-ADT with fixed unit cell- although the same methodology and computational methods were used, behaviour of these systems was different. BGFS optimisation algorithm proved to be fast, yet susceptible to a non-parabolic energy landscape around the minimum, which is typical for hydrogen bonded systems, whereas damped molecular dynamics was not robust enough to work with systems as big as C8-BTBT. Fixed cell C8-BTBT structure optimisation did not converge to a predefined thresholds and subsequent phonon calculation resulted in six complex frequencies up to -52.6 $cm^{-1}$ suggesting significant error in calculation of frequencies, however final Raman intensities were in surprisingly good agreement with experimental data, both in terms of relative intensities of the peaks and their positions. With typical error in the frequencies being around 10 $cm^{-1}$ it was possible to match experimental and theoretical modes. Given the fact that both fixed cell diF-TES-ADT and fully relaxed C8-BTBT structure optimizations converged, it is reasonable to assume that the methodology presented in previous paragraphs is a valid method to study temperature dependence of Raman modes using aharmonic approximation. Computational cost of such study was prohibitive at the

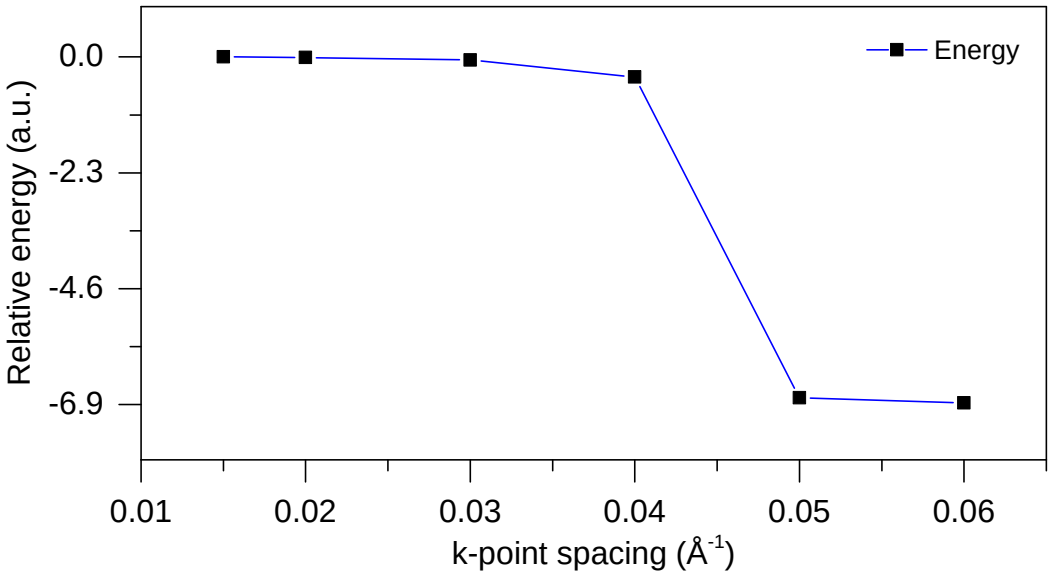


Figure 4.15: Total energy of the system vs k-point sampling at $E_{\text{cutoff}}$= 1100 eV. The total energy at $k = 0.06$ Åwas subtracted as a reference data.

time when these simulations were performed, however with an advent of more robust computers it will become possible to investigate intermolecular vibrational modes of small molecular systems using density functional theory.

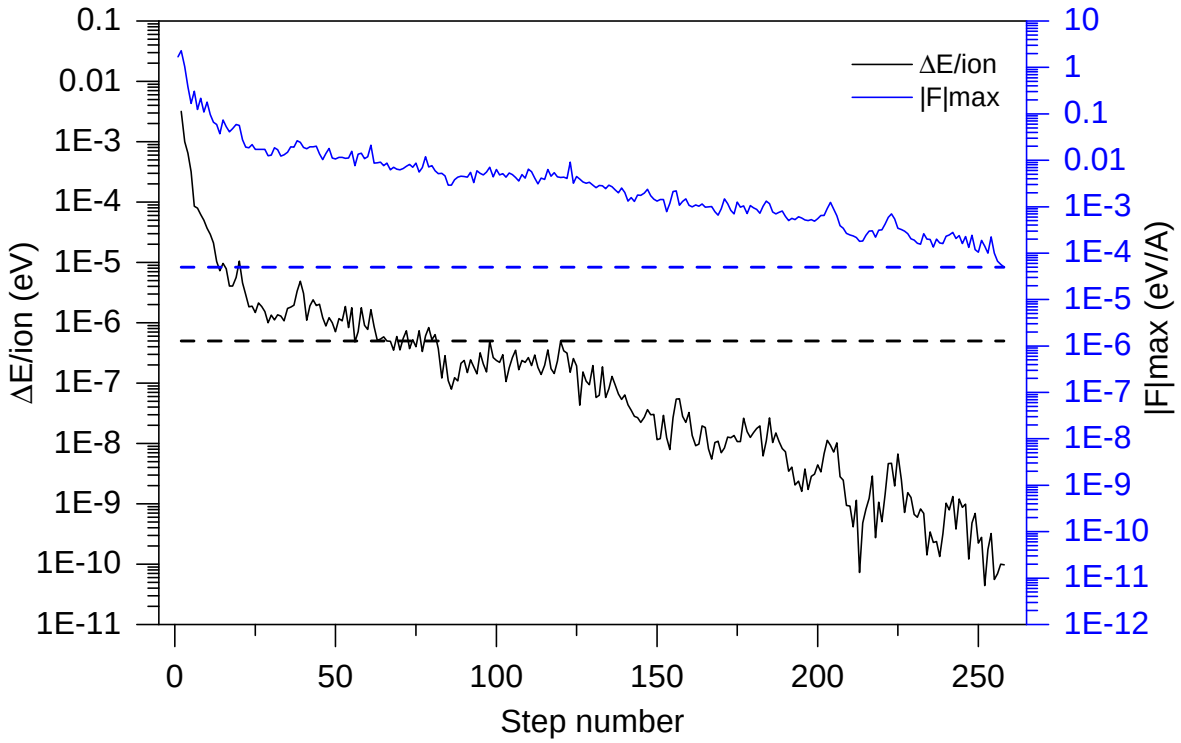


Figure 4.16: Convergence of maximum force (**blue**) and change in energy per ion (**black**) during fixed cell diF-TES-ADT geometry optimisation. Convergence tolerances are defined by dashed lines.

# Chapter 5

# pBTTT

pBTTT is a crystalline system with a well-established molecular order and lamellar stacking. Both microstructural and electronic properties of this system have been published before [68, 127, 139], including studies of the effect of lattice disorder and intermolecular aggregation on charge transport [139]. Because of in-depth understanding of pBTTT physics, it often acts as a reference and comparison in studies of donor-acceptor polymers such as IDT-BT or NDIT2 [26] and therefore it was decided to evaluate high pressure Raman techniques using this system.

In its crystalline phase, pBTTT monomers adapt an essentially coplanar conformation along the backbone allowing neighbouring polymer backbones to assemble in a closely packed, tilted face to face arrangement resulting in an extended, ordered $\pi$-stacked lamella with tilted, interdigitated side chains [127]. As demonstrated by use of molecular dynamics simulations the close packed structure is believed to foster planarity of the backbone with deviations restrained by nonbonded interactions with neighbouring chains resulting in a long range order [68]. This idealized structure is, however, unlikely to be the dominant type in an experimental spun thin film. It is therefore important to model structural disorder that is present in semi-crystalline domains. To do so, we began by calculating the torsional potentials along the backbone using DFT methods as was described in Methods section. pBTTT backbone has, in a fact, two degrees of torsional freedom: there is thiophene-thiophene (T-T) bond between adjacent monomers and two thiophene-thienothiophene (TT-T) bonds within each monomer that could contribute to backbone disorder. For T-T bond, there are two possible energetic minima- an anti-parallel with sulfur atoms pointing in opposite directions at 0° and parallel at 180° as shown in Figure 5.1. Given the height of potential barrier at 90° one may conclude that both minima are stable, however only anti-parallel configuration results in a straight backbone necessary for lamellar

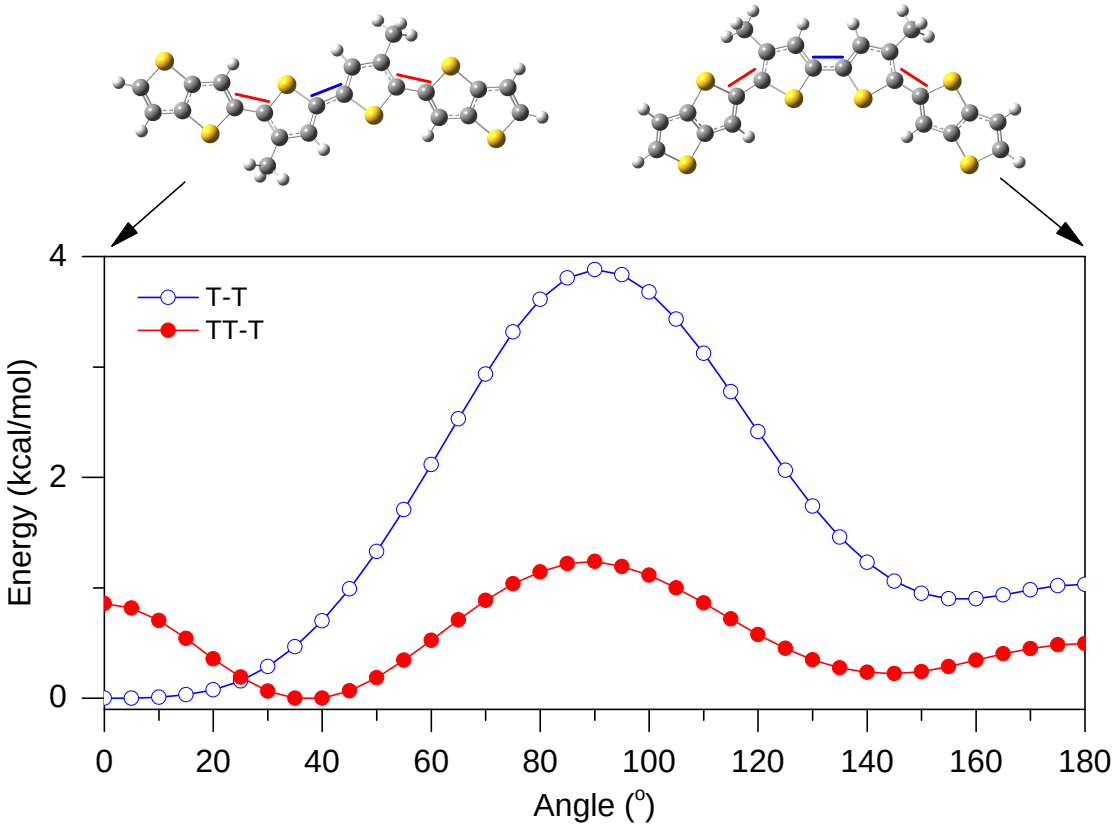


Figure 5.1: DFT calculations of pBTTT torsional potentials. There are two possible orientations of T-T bond: anti-parallel at 0° and parallel at 180° (**top row**). Anti-parallel configuration is necessary for the chain to be linear.

stacking reported by McCulloch et al. [127]. It follows that the dominant configuration of T-T bond should be planar even in the absence of inter-chain interactions. TT-T bond has two well defied minima at around $25° - 35°$ off the planar plane with steep potential barriers, which is a clear indication that in the semi-crystalline phase the TT-T torsion might be the dominant force driving the disorder of the backbone.

## 5.1 Raman spectra

In order to verify the above hypothesis we decided to measure Raman spectra of a thin film as a function of external hydrostatic pressure. Before loading the pressure cell, polymer film has been spun and processed in exactly the same manner as for FET devices to ensure that the morphology and microstructure match samples used for studies of electronic properties. The high pressure technique has previously been reported as an effective way to planarize F8BT backbone [33, 34] hence one might

expect a similar result in case of pBTTT. The experimental spectra are shown on Figure 5.2. There are four main peaks in the $1393 - 1492$ cm$^{-1}$ range corresponding to intramolecular vibrational modes associated with conjugated backbone and intense, narrow peak at 1330 cm$^{-1}$ corresponding to diamond Raman line. Based on calculation of vibrational modes performed using Gaussian09, one can identify 1393 cm$^{-1}$ as a C=C bond stretching mode localised on thiophene rings as shown on Figure 5.5. Similarly, peaks at 1419 cm$^{-1}$ and 1492 cm$^{-1}$ correspond to intraring stretching modes localised on thienothiophene ring while 1462 cm$^{-1}$ peak represents collective bond stretching modes that are distributed along the backbone. As the pressure increases all Raman peaks shift to a higher frequencies and broaden, which is a typical effect due to compression of lattice vectors, with signal becoming noisy because of intense PL background. One can see, however, that the intensity of 1419 cm$^{-1}$ peak is decreasing with respect to 1393 cm$^{-1}$ and 1492 cm$^{-1}$ peaks. To quantify this effect we decided to fit Lorentzian peaks to the experimental data and derive pressure-dependent ratios of peak intensities, as shown in Figure 5.2. There is a clear pressure dependence of 1393 cm$^{-1}$ to 1419 cm$^{-1}$ intensity ratio with an increase by 64% between 0.2 and 3.0 GPa. Similar effect has been observed with 1393 cm$^{-1}$ to 1462 cm$^{-1}$ intensity ratio, however the error in peak fitting does not necessarily represent the true error- 1462 cm$^{-1}$ peak is broader and less pronounced than other peaks which makes fitting procedure susceptible not only to signal to noise ratio, but also to choice of subtracted PL baseline which was not included in the error analysis. Similarly, 1393 cm$^{-1}$ to 1492 cm$^{-1}$ intensity ratio suggest much weaker pressure dependence, but since both peaks are well defined against the background quantitative analysis is less prone to be an artifact due to background subtraction. In conclusion, Raman data shown in Figure 5.2 clearly demonstrate that intramolecular vibrational modes of pBTTT are pressure dependent, suggesting change in backbone conformation.

A more in-depth analysis of fitted peaks is shown in Figure 5.3. Frequencies and Full-Width Half-Maximums were normalised to data collected at 0.2 GPa, so that y-axis represents a ratio of peaks fitted at a given pressure to peaks fitted at 0.2 GPa. For clarity I decided to colour-code vibrational modes localised on thiophene ring (**blue**) and thienothiophene (**red**). Inspection of shifts in mode frequencies (**top**) reveals increase of force constants and reduction of bond lengths, however interpretation of this effect is somehow troublesome- shifts to higher frequency are typical effects observed in high pressure experimental Raman spectra and it is difficult to isolate shifts of frequency originating from changes in backbone conformation versus bulk compression. For example, 1393 cm$^{-1}$ peak shifts to 1406 cm$^{-1}$ at 3 GPa and such change in

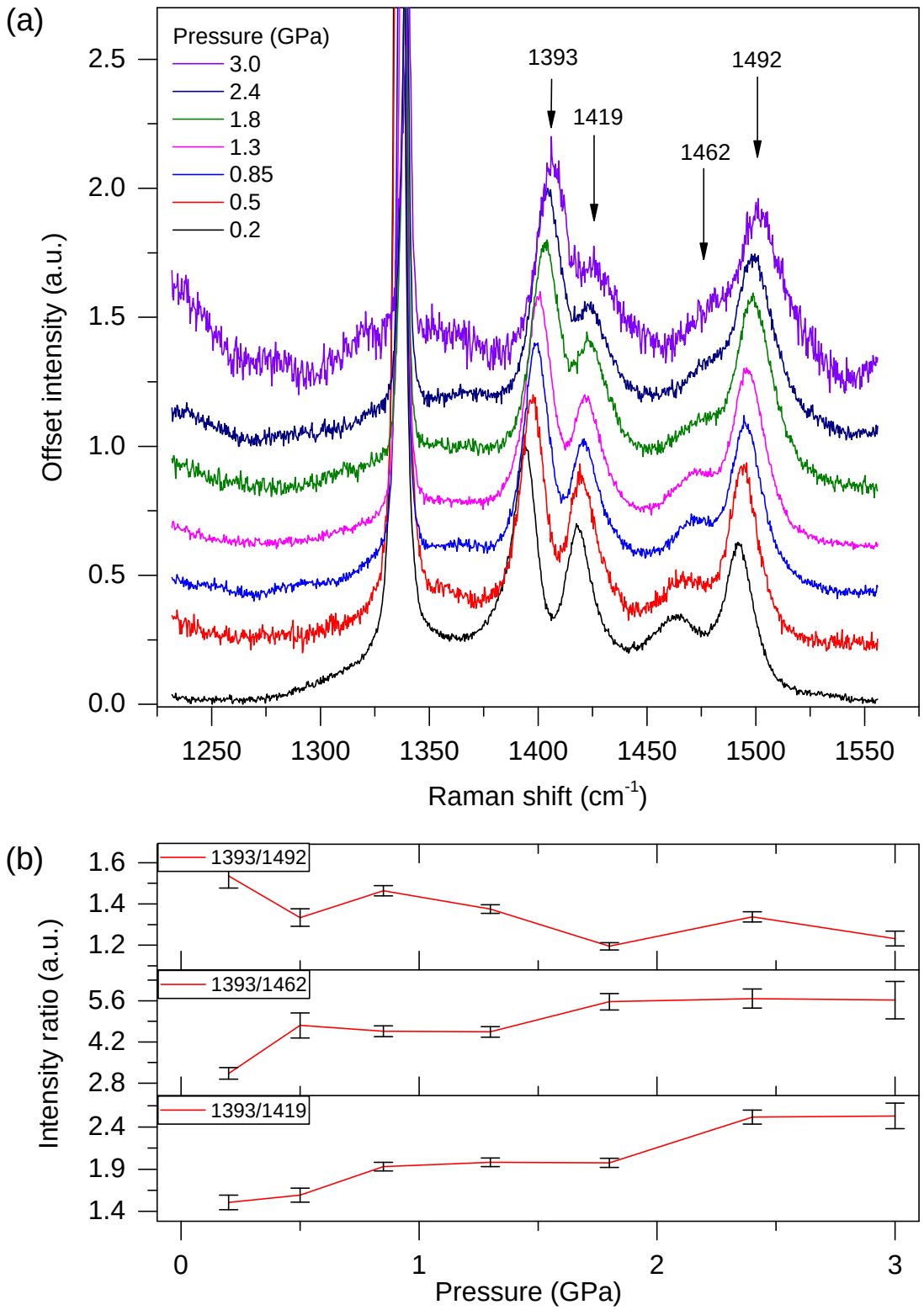


Figure 5.2: Experimental pBTTT Raman spectra (**a**) and selected peaks intensity ratios (**b**) as a function of hydrostatic pressure. Spectra were acquired using $\lambda = 784$ nm; background noise was fitted using straight line.

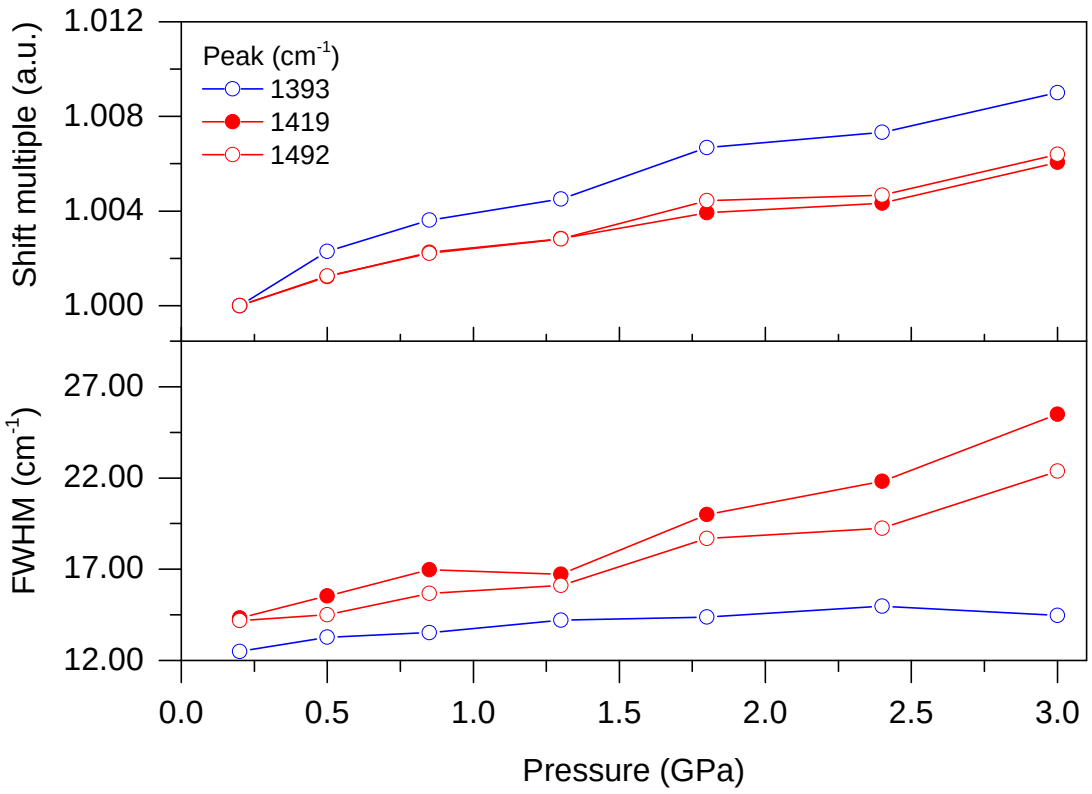


Figure 5.3: Changes in fitted mode frequencies (**top**) and peak FWHM (**bottom**) as a function of pressure for modes localised on thiophene ring (**blue**) and thienothiophene (**red**). All values were normalised to data collected at 0.2 GPa.

mode frequency is not spectacular- as a comparison I would like to make a reference to studies of effect of backbone fluorination of P3OT published by Fei and co-workers [77]. According to Fei, fluorination results in planarization of the backbone and shift of Raman peak corresponding to C=C vibrational mode by 47 $cm^{-1}$ towards higher frequency. In this context, shift of thiophene stretching mode by 13 $cm^{-1}$ on the scale of 2.8 GPa change in pressure is not particularly informative when it comes to understanding of backbone conformation. However, there are interesting trends in pressure dependent widths of the peaks. As in case of mode frequencies, peak broadening is a typical feature of high pressure Raman spectra, but there is a pronounced difference between modes localised on thiotphene and thienothiophene. As one can see, FWHM of 1393 $cm^{-1}$ peak remains almost constant above 1.3 GPa, whereas 1419 $cm^{-1}$ and 1492 $cm^{-1}$ peaks exhibit significant and steady broadening. During the experiment FWMH of 1392 $cm^{-1}$ peak increased from 12.5 $cm^{-1}$ to 14.5 $cm^{-1}$ whereas FWMH of 1419 $cm^{-1}$ and 1492 $cm^{-1}$ peaks increased from 13.1 $cm^{-1}$ to 25.5 $cm^{-1}$ and from 14.2 $cm^{-1}$ to 22.4 $cm^{-1}$ respectively. In comparison, Fei reports that FWMH of C=C

mode decreased from 26.0 $cm^{-1}$ to 13.1 $cm^{-1}$ as a result of P3OH backbone fluorination. Data demonstrated that thiophene units contain much narrower distribution of conformations compared to thienothiophene suggesting that T-T bonds might be near planar and rigid whereas TT-T bonds are susceptible to disorder.

To interpret pressure dependence I performed DFT simulations of Raman spectra for different torsional angles. As mentioned before, pBTTT backbone has two degrees of torsional freedom that have to be analyzed. Rather than starting with a vacuum state optimized geometry we used a fragment of previous molecular dynamics simulation of semi-crystalline phase by selecting a random tetramer out of a bigger system. The selected tetramer had a random distribution of torsional angles with average $\theta_{\mathrm{T-T}} = 5.85°$ and $\theta_{\mathrm{TT-T}} = 22.9°$. Calculated intensities corresponding to original input (**MD**) are shown on Figure 5.4(a). Simulation of molecular dynamics Raman spectra were complemented by a series of simulations with modified $\theta_{\mathrm{TT-T}}$ angles while keeping $\theta_{\mathrm{T-T}}$ bonds fixed at the same values as in MD output. One can see that the original MD spectra are best reproduced by setting $\theta_{\mathrm{T-TT}} = 30°$ which is somehow surprising given the fact, that the average MD torsional angle was 22.9° and the system with $\theta_{\mathrm{TT-T}}$ fixed at 20° resembles neither experimental nor MD spectra. Likewise analysis was performed for T-T bond as shown in Figure 5.4(b). At $\theta_{\mathrm{TT-T}} = 30°$ calculated Raman spectra exhibit a remarkable sensitivity to T-T bond planarity- there is an order of magnitude, almost discrete change in 1460 $cm^{-1}$ (1419 $cm^{-1}$ in experimental) peak intensity when the torsional angle is reduced from 1° to 0.5°, however the peak shows no dependence in the $1 - 5°$ range. We have tried to repeat the same procedure for $\theta_{\mathrm{TT-T}}$ values different than 30°, but the effect of planarization was less pronounced suggesting that one cannot consider $\theta_{\mathrm{T-T}}$ and $\theta_{\mathrm{TT-T}}$ as independent degrees of freedom.

In order to explain pressure dependence of vibrational modes and experimental Raman spectra we decided to treat torsional degrees of freedom as being coupled. To some extend the experimental spectra resemble a crossover of 5.4(a) and (b) with 1419 $cm^{-1}$ peak decreasing and 1492 $cm^{-1}$ increasing at the same time. We decided to look at the effect of simultaneous variation of $\theta_{\mathrm{TT-T}}$ and $\theta_{\mathrm{T-T}}$, again starting with an initial structure equivalent to molecular dynamics simulation of a semi-crystalline phase. As shown in Figure 5.5(b) we calculated Raman spectra for a number of intermediate states between original MD geometry and structure with $\theta_{\mathrm{T-T}} = 0°$ and $\theta_{\mathrm{TT-T}} = 30°$. 1455 $cm^{-1}$ peak (1419 $cm^{-1}$ in experimental) is steadily decreasing with respect to 1425 $cm^{-1}$ (1393 $cm^{-1}$ in experimental) whereas 1540 $cm^{-1}$ (1492 $cm^{-1}$ in experimental) is increasing with respect to 1425 $cm^{-1}$, which is in qualitative agree-

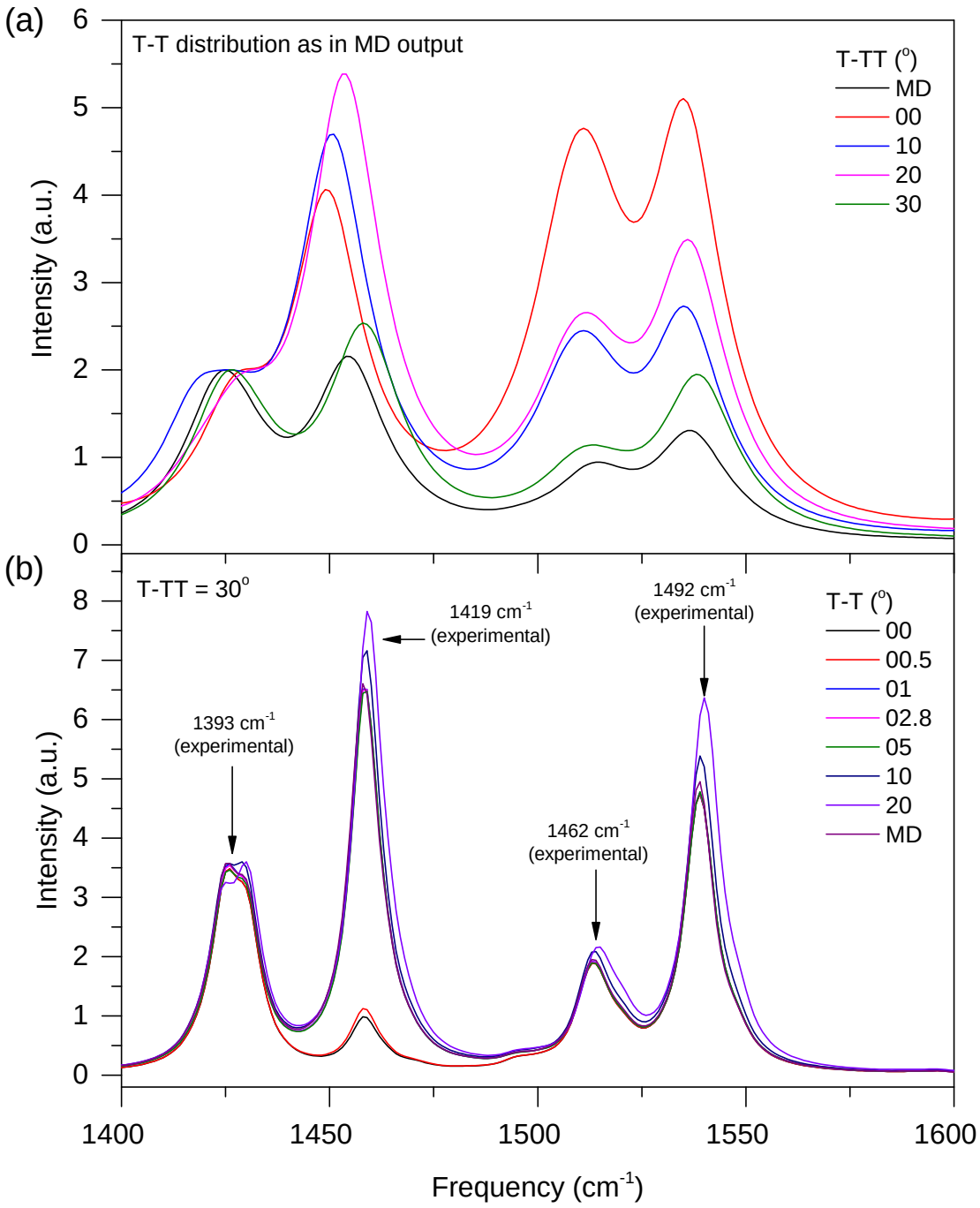


Figure 5.4: (**a**) DFT calculated Raman intensities of a selected fragment of molecular dynamics output (**MD**) and as a function of TT-T bond torsion while keeping T-T bond fixed at the same values as in MD. (**b**) DFT calculated Raman intensities as a function of T-T bond torsion at TT-T= 30°. Modes marked with arrows were assigned to experimental peaks. 1492 $cm^{-1}$ mode exhibit almost discrete change in mode intensity during T-T bond planarization. Frequency scale represents raw DFT values that were not rescaled by an empirical B3LYP factor.

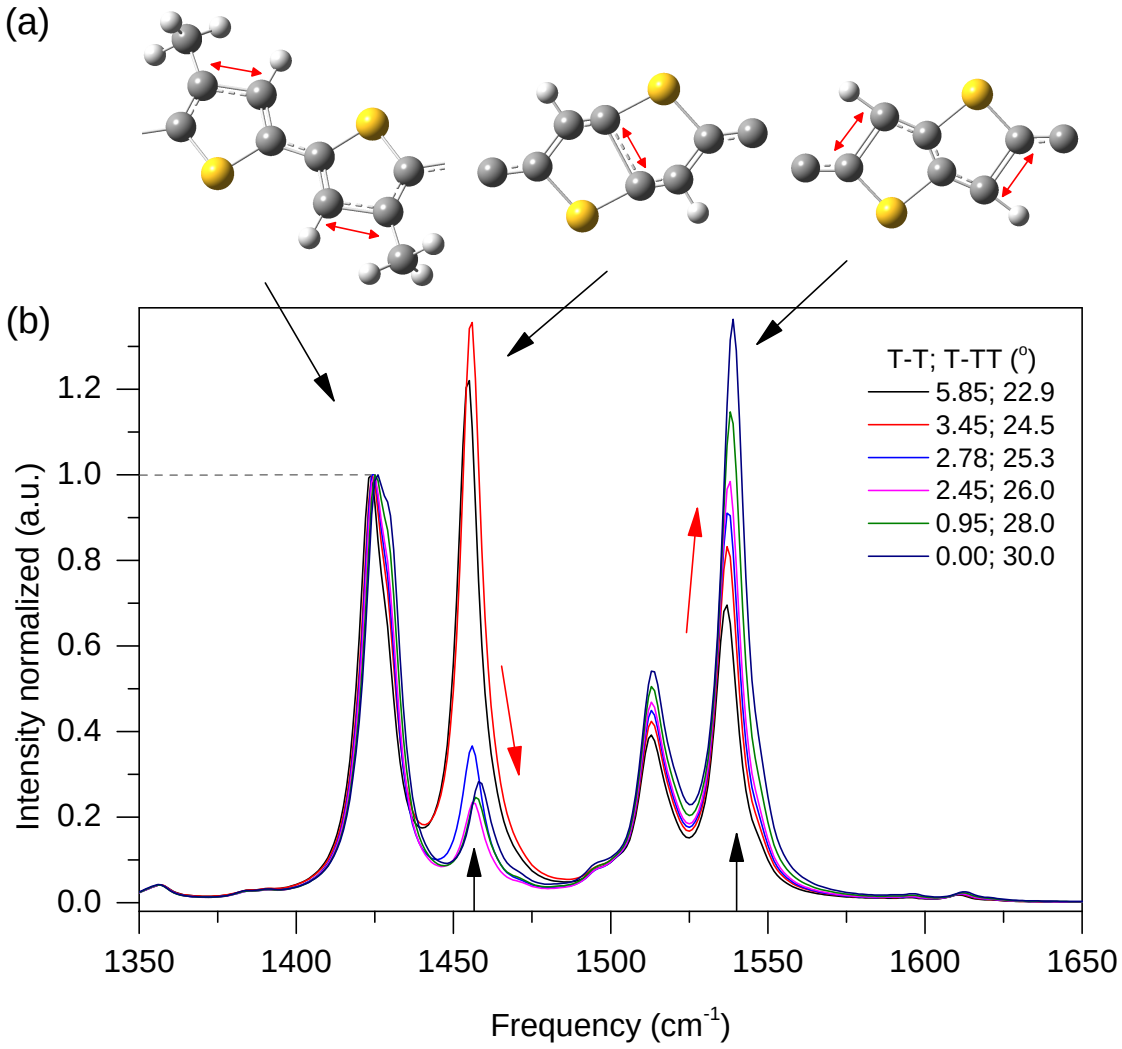


Figure 5.5: (**a**) visualization of vibrational modes. (**b**) DFT reconstruction of pressure dependent Raman spectra with intensities normalized to 1425 $cm^{-1}$ peak. We were simultaneously planarizing $\theta_{T-T}$ and deplanarizing $\theta_{TT-T}$ torsional angles.

ment with experimental intensity ratios shown in Figure 5.2. We used GaussView to visualize vibrational modes assigned to experimental Raman peaks as shown on Figure 5.5(a). 1425 $cm^{-1}$ peak corresponds to thiophene ring stretching modes, whereas 1455 $cm^{-1}$ and 1540 $cm^{-1}$ peaks represent different thienothiopene ring stretching modes.

## 5.2 Summary

Experimental Raman data together with DFT simulations clearly suggest that the polymer backbone exhibits two simultaneous processes as a result of external pressure-

$\theta_{\mathrm{T-T}}$ bond planarization and $\theta_{\mathrm{TT-T}}$ bond deplanarization. The data also suggest that in the spun thin film the backbone is not planar with a considerable degree of disorder, which is consistent with theoretical TT-T torsional potential. Previous studies of conjugated polymers under high pressures [33, 34] demonstrated planarization of the backbone, which is not the case with pBTTT. A possible explanation could be based on simple consideration of the density of the system- external pressure forces the system into most densely packed structure which may be planar, but does not have to be. In highly crystalline polymers conformation of the backbone is an interplay between intrinsic torsional potentials and steric interaction of side chains. In low density limit, such as solution, side chains have enough empty space to adopt lowest energy configuration and one may expect that the backbone conformation is defined by torsional potentials of the backbone. Contrary, in closely packed phase steric interactions become dominant driving force at the expense of torsional potentials- we suppose this is the case with pBTTT under high pressures.

# Chapter 6

# IDT-BT

Over last decade, performance of the devices has greatly improved as a wide variety of molecular structures have been studied. The molecular design has evolved from amorphous polymers used in xerography, where low-mobility transport dominated by disorder is modelled as a hopping states localized on short conjugation segments, to a more ordered semi-crystalline polymers such as P3HT and pBTTT. Until recently, the most common approach to achieve high charge mobility was to design a system that adapts edge-on, lamellar self-organization with a liquid-crystalline-like molecular packing as it has long been believed that the outstanding device performance originates form highly ordered structures with optimally oriented domains. pBTTT, with its extended conjugated backbones and lamellae of alkyl side chains became a benchmark system, but has hardly led to further advancement since even in these highly crystalline systems the effects of disorder has not been overcome. The transport properties are still affected by pervasive conformational and energetic disorder resulting in charge localization, that limits mobilities in field-effect transistors to 0.1-1 $cm^2V^{-1}s^{-1}$. Recent reports of surprisingly high mobilities exceeding 1 $cm^2V^{-1}s^{-1}$ in several donor-acceptor copolymers have caused much excitement. These polymers consist of a sequence of alternating electron-rich donor and electron-deficient acceptor blocks and often have complex, non -linear backbones. In contrast, their microstructure is typically much less crystalline than pBTTT and the backbones appear to have a less pronounced, or even absent, long range order[6]. An example of such system that exhibits weak and broad X-ray diffraction peaks indicating significant degree of conformational disorder, as shown in Figure 6.1, is IDT-BT previously described by McCulloch and coworkers[6, 7]. The reported OFET mobilities are up to 3.6 $cm^2V^{-1}s^{-1}$[6] suggesting that IDT-BT has a distinct structure-properties relationship. VASE and NEXAFS measurements published by Zhang[6] indicate that IDT-BT exhibit no preferred in-

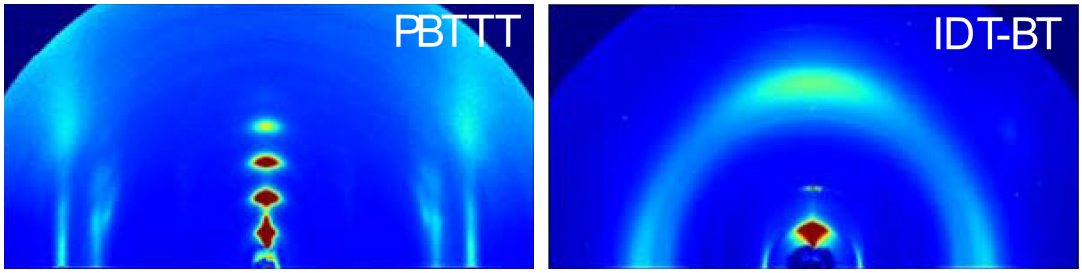


Figure 6.1: Grazing-Incidence Wide-Angle X-ray Scattering (GIWAXs) measurements of PBTTT and IDT-BT. Data adapted from[139].

plane backbone orientation and there is no reason to believe that there is a distinct interface orientation. Without knowledge about the microstructure it is therefore difficult to draw any conclusions regarding mechanism of charge transport. A hypothesis reported by Zhang[6] points to a quasi-1D transport along the backbone with intermittent $\pi$ linkages to adjacent chains suggesting that the backbone conformation, rather than interactions of alkyl chains, plays crucial role. The lack of established methodology that could be used to prove or disprove that hypothesis was the major driving force for experimental and computational results presented in the rest of this chapter.

A study of energetic disorder and transport properties of both IDT-BT and pBTTT has been published by Venkateshvaran and coworkers[26]. IDT-BT has not only one of the highest mobilities, but also the most-ideal electrical characteristics. Figure 6.2 **a** shows output characteristics of a top-gate IDT-BT FET with film annealed at 100°C. The device exhibits near-ideal performance with low threshold voltage, contact resistance and a high saturation mobility of 1.5-2.5 $cm^2V^{-1}s^{-1}$ extracted from near quadratic current dependence on gate voltage. The direct extraction of the gate voltage dependent mobility suggest metal-oxide-semiconductor FET-like model with a thermally activated, but a gate-voltage-independent mobility. As shown on Figure 6.2 **b** the mobility in pBTTT strongly increases with gate voltage at lower temperatures, whereas in IDT-BT it was nearly independent of gate voltage above $|V_{gate}| > 20$ V across the entire range of temperatures suggesting, that the energetic disorder in IDT-BT is significantly lower than in the pBTTT. The degree of energetic disorder can also be quantified using Seebeck coefficient $\alpha$ determined experimentally by measuring the electromotive force that develops across a material in response to an applied temperature differential. The comparison of measured Seebeck coefficients indicate significant less trapping in IDT-BT than in pBTTT or PSeDPPBT with majority of IDT-BT charge carriers residing in mobile states (please refer to [26] for a more detailed expla-

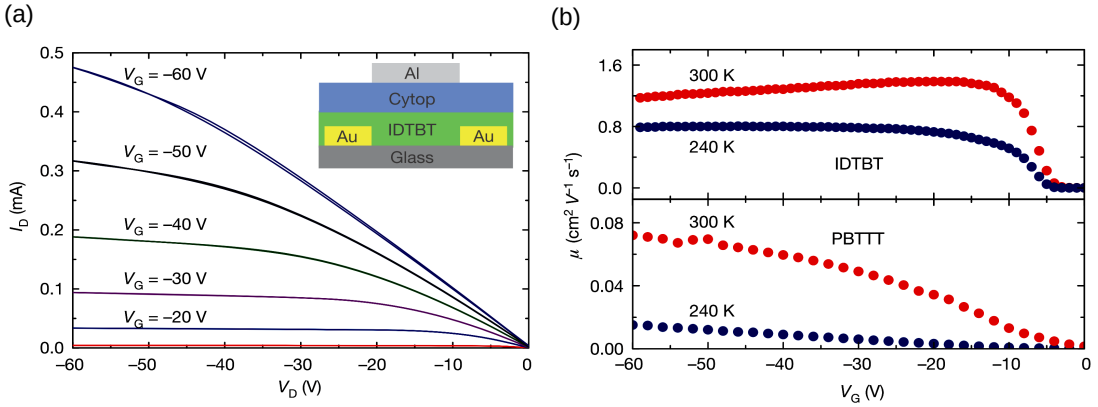


Figure 6.2: Transistor characteristics of IDT-BT based FET compared with pBTTT. (**a**) Room-temperature output characteristics and device architecture of a typical IDT-BT organic FET with channel length L=20 μm and channel width W = 1 mm. (**b**) Gate-voltage dependence of saturation mobility μ at 300 and 240 K for patterned IDT-BT (**top**) and PBTTT (**bottom**) devices. Data courtesy of Mark Nikolka.

nation of the methodology). The study of Seebeck coefficient has been complimented by optical absorption measurements by photothermal deflection spectroscopy. This technique provides a bulk-sensitive way of probing energetic disorder by estimating the Urbach energy extracted from the optical absorption coefficient in the vicinity of the band gap. IDT-BT was found[26] to exhibit the Urbach energy of 24 meV, which was the lowest value reported in a conjugated polymer (by comparison, pBTTT has Urbach energy of 47 meV).

The results discussed in previous paragraph clearly demonstrate that donor-acceptor copolymers without extended structural order can exhibit higher charge mobility and lower degree of energetic disorder than crystalline conjugated polymers. It is therefore important to understand what is the microstructural origin of this effect. IDT-BT cannot simply be modelled as a classical rigid-rod system- its degree of solubility in a range of solvents suggest degree of chain flexibility that is not common for such polymers. The important question to address is whether exceptional properties of IDT-BT originate in certain features of molecular design that may not yet be implemented in other polymers with comparable mobilities but with less ideal transport characteristics. To do so, I decided to study the properties and disorder of polymer backbone, as was previously done for pBTTT, and search for thermodynamically stable bulk microstructures using large-scale molecular dynamics simulations.

## 6.1 High Pressure Raman

Because of scarcity of microstructural data I begun by calculating vacuum-phase torsional potentials and minimum-energy conformation, as was previously done for pBTTT. Compared to pBTTT, IDT-BT is a much less complicated system since the backbone has only one degree of torsional freedom that has to be considered. The DFT torsional potential between IDT and BT units is shown on Figure 6.3 **b**. Regardless of the relative orientation of BT and IDT units the preferred configuration is always planar with a steep potential barrier at 90°, suggesting well defined energetic minima. This result was verified with a geometry optimisation performed on a larger molecule as shown on Figure 6.3 **b**. It is important to consider all possible conformers and their total energies. Unlike BT, the IDT unit is not straight- for a long linear molecule we require a similar number of units pointing "up" and "down", ideally in an alternating order as shown in Figure 6.3. BT unit, regardless of orientation, always preserve linearity of the molecule which means that for a polymer chain consisting of N monomers there are $2^N$ possible configurations of BT units, all with comparable energy. This result by itself is interesting in the context of structural disorder- for a given chain length there are several possible linear geometries with negligible difference in total energy, meaning that IDT-BT is a system capable of accommodating increase of entropy without major change in microstructure.

I decided to examine the dependence of theoretical spectra on torsional angle as shown in Figure 8.5. The spectra exhibit clear correlation between intensity of peaks and torsion, hence one would expect that, if there is a torsional disorder present in as-deposited film, backbone would be planarized by applying a hydrostatic pressure of a few GPa as was previously reported for F8BT[34]. The experimental spectra as a function of external pressure are shown in Figure 6.5. Because of intense PL background and low signal-to-noise ratio there were only two peaks that could be effectively fitted using Lorentzian model, namely 1533 $cm^{-1}$ and 1606 $cm^{-1}$. Within a margin of experimental error the calculated ratio of intensities shows no dependence upon change of pressure suggesting that the IDT-BT backbone in as-deposited films is indeed already planar or remarkably resilient to effect of hydrostatic pressure. The two experimental peaks were identified as aromatic ring stretching modes as illustrated in Figure 6.6: 1533 $cm^{-1}$ peak corresponds to collective C=C and C-C bonds stretching mode localized on benzothiadiazole (BT) ring whereas 1606 $cm^{-1}$ peak corresponds to collective C=C and C-C bonds stretching mode localized on indacenodithiophene (IDT) six-membered ring. As one can see, DFT calculation predicts that the frequency of 1606 $cm^{-1}$ peak is not expected o shift upon planarization. This effect presumably

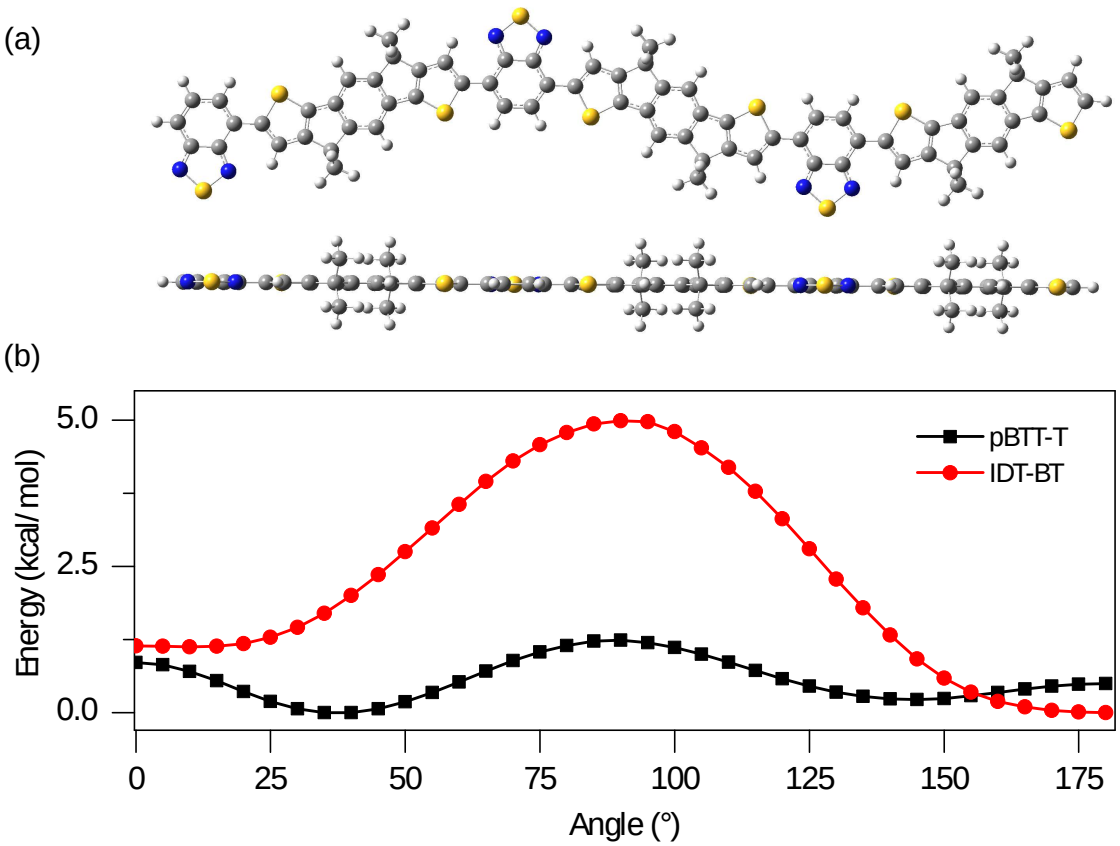


Figure 6.3: DFT optimised (**a**) vacuum-phase of IDT-BT exhibiting perfectly planar backbone and comparison (**b**) of IDT-BT and pBTTT torsional potentials at B3LYP/cc-pvdz level of theory.

follows from fact that six-membered ring is separated from bond between IDT and BT units by two five-membered rings on both sides and hence one may expect force constants to be independent of torsional angle. The theoretical ratio of intensities exhibit clear variation for $\theta_{IDT-BT} > 10°$ , however one cannot deduce the exact value of torsional angle by making a direct comparison of peak intensities between experiment and theory- the DFT calculation can only be used to identify qualitative trends in data rather than quantitative analysis. The consistent interpretation of both theoretical and experimental Raman spectra demonstrates that even in the disordered, as-deposited films the backbone torsion is impressively independent of structural disorder.

Analysis of fitted peak frequencies and full-width half-maximums is shown in Figure 6.7. Upon increase in pressure up to 2.5 GPa, peaks shifted respectively from 1533 $cm^{-1}$ to 1542 $cm^{-1}$ and from 1606 $cm^{-1}$ to 1615 $cm^{-1}$ indicating increase of effective force constants. Both peaks exhibit very consistent shift in peak frequencies by similar

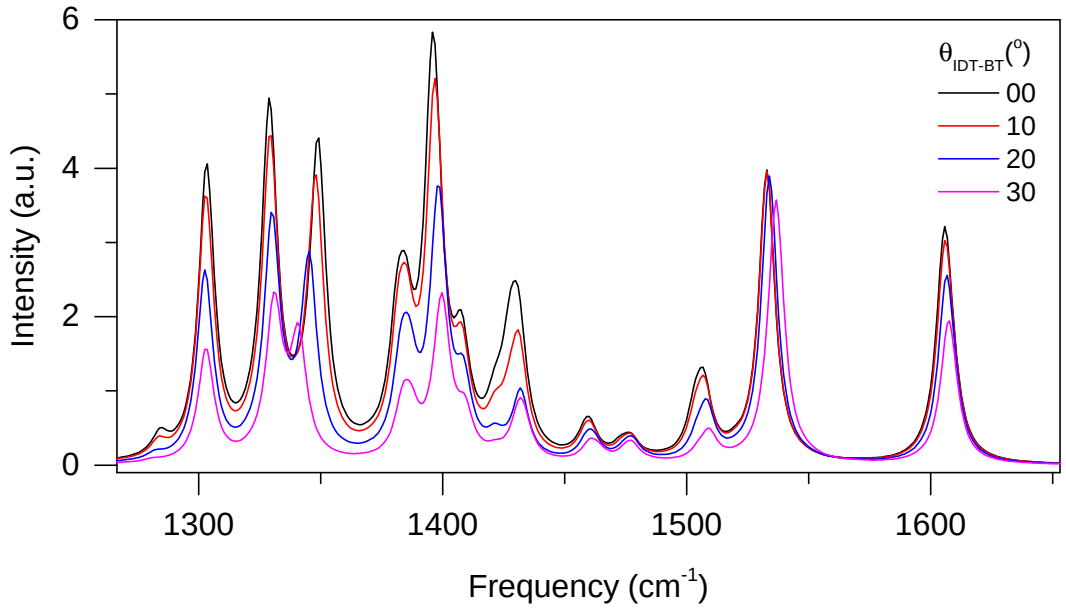


Figure 6.4: DFT Raman spectra as function of IDT-BT torsional angle.

pressure-dependent scaling factor suggesting that the observed effect originates from bulk compression rather than change of backbone conformation. In addition to this, both modes demonstrated narrow distribution of molecular distributions at ambient pressure with FWHM of 1533 $cm^{-1}$ and 1606 $cm^{-1}$ modes equal 14.5 $cm^{-1}$ and 13.7 $cm^{-1}$, respectively. At 2 GPa FWHM of 1533 $cm^{-1}$ peak increases to 20.4 $cm^{-1}$ whereas FWHM of 1606 $cm^{-1}$ increases to 18.7 $cm^{-1}$. Broadening of peaks indicates wider distribution of backbone conformations, however such change in Raman spectra is commonly observed at high pressures and FWMH scaling factor is consistent with F8Bt data published by Schmidtke and co-workers[34]. It is worth noting that even at 2 GPa distribution of molecular conformations, as indicated by values of mode FWHM, is not particularly wide- for example, Fei et al.[77] reports that FWHM of the 1445 $cm^{-1}$ C=C mode peak in P3OT is equal to 26.0 $cm^{-1}$ at an ambient pressure.

## 6.2 Molecular Dynamics

Unlike DFT based optimisation methods, molecular dynamics simulations depend critically on quality of input structures and force field parametrization. Whereas most of DFT algorithms scan energy landscape in a systematic method and should, at least in principle, converge to a minimum in a vacuum phase, the molecular dynamics simulation of a bulk material has several constraints and will typically quench to nearest local

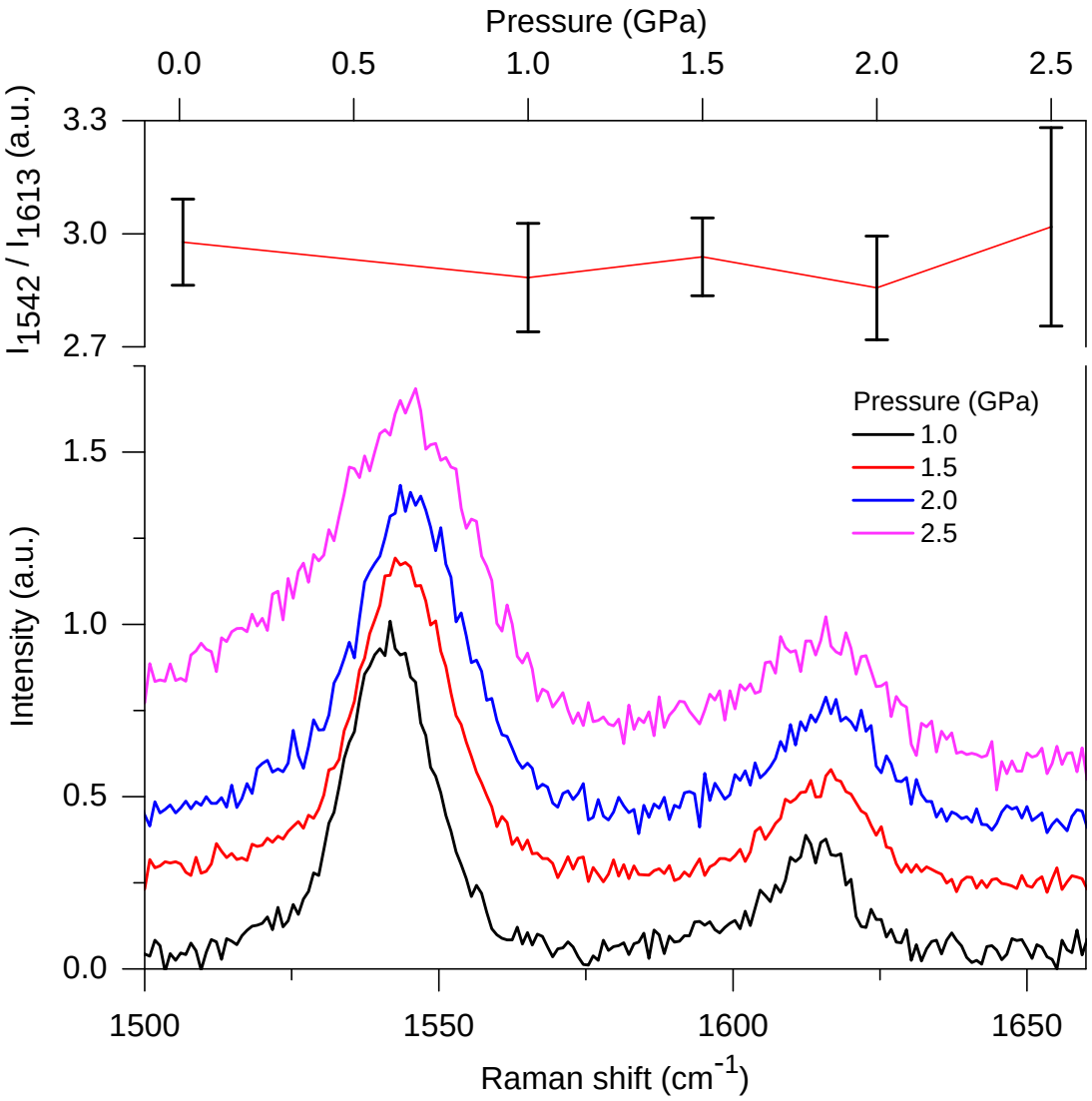


Figure 6.5: IDT-BT experimental Raman spectra as a function of external pressure. Due to photoluminescence background there were only two peaks that could be fitted. The ratio of their intensities shows lack or weak pressure dependence. Spectra were acquired using $\lambda = 532$ nm laser line. Background noise was fitted using straight line.

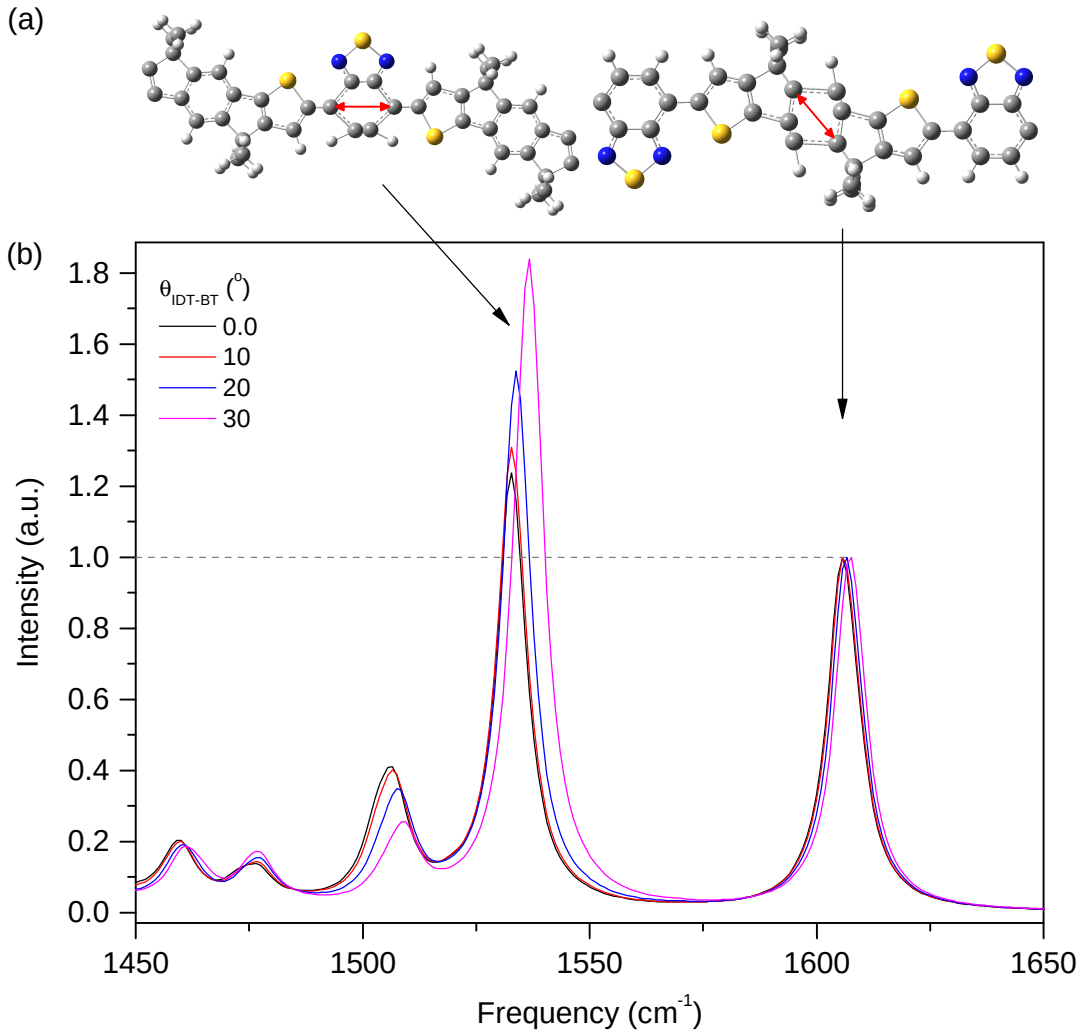


Figure 6.6: (**a**) visualization of BT and IDT ring stretching modes. (**b**) mode intensities as a function of torsional angle. Intensities were normalized to IDT stretching mode.

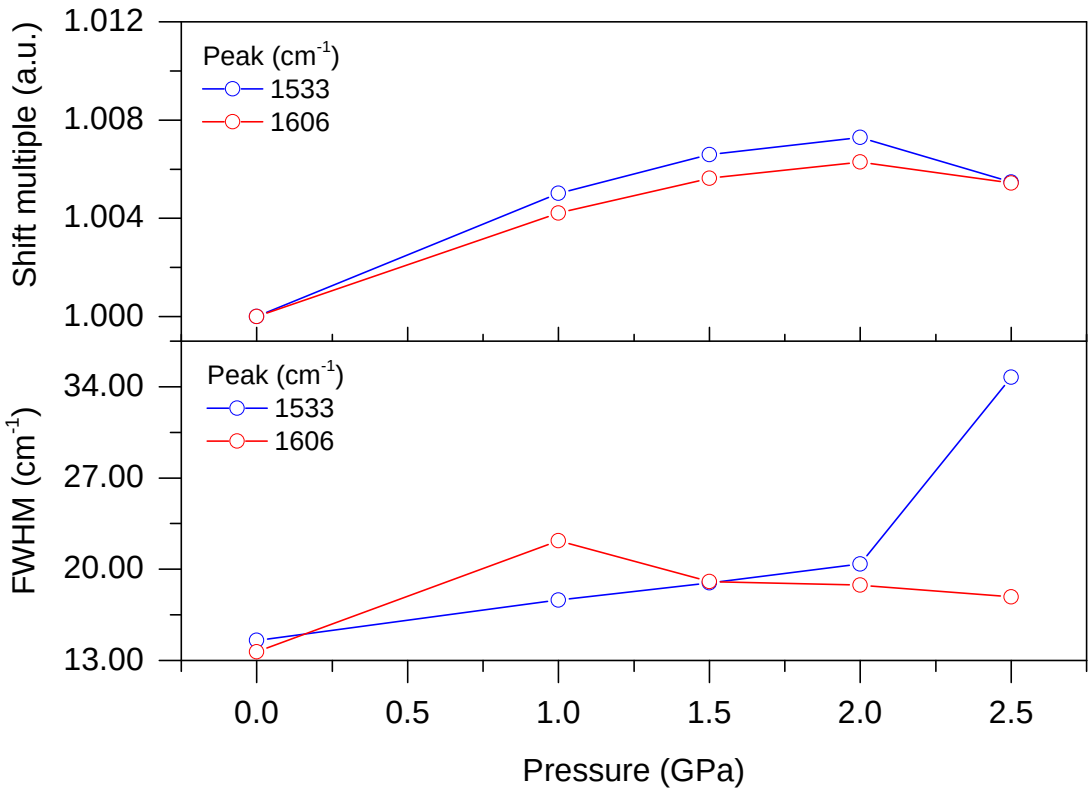


Figure 6.7: Scaling of 1533 $cm^{-1}$ and 1606 $cm^{-1}$ peak frequencies (**top**) and FWHM (**bottom**) as a function of applied pressure. Major change of 1533 $cm^{-1}$ width at 2.5 GPa is an outlier following from peak asymmetry.

minimum. There is a constant interplay of two contradicting factors- in order to overcome a local potential barrier one has to increase thermal energy and hence disorder of the system, which inevitably reduces probability of quenching to a more ordered, lower energy configuration. This is a classic example of *infinite monkey theorem* used by Arthur Eddington to illustrate the foundations of statistical mechanics- a far from equilibrium input may converge to a lowest energy structure given long enough time to evolve and high enough frequency of quenching, but it is rather naive to explore such a possibility in practice given the mutually exclusive probability of *not* finding the minimum. Instead, I want to maximise the chance of finding stable phase by making an educated guess about possible structure and setting lower thermal energy. As described later in this section, I came up with several possible input structures, each resulting in a distinct output structure. This makes molecular dynamics method extremely robust yet dependent on statistical probability of quenching at the "right" time and intuition, or rather prior experience, of a researcher.

A typical way of setting up an input unit cell is to use vacuum phase DFT-optimised

polymer strain and reconstruct experimental length-scales determined by x-ray diffraction and NMR spectroscopy. At the time when input structures were constructed the NMR data were not available and the diffraction pattern published by Zhang et al[6] offered a rather limited insight into unit cell. The (200) and (010) reflections corresponding to d-spacing values of 2.6 and 0.38 nm were identified as lamellar stacking of the backbones along the alkyl side chains and π-stacking, respectively. Both reflections were described as broad and wide arcs, suggesting that the corresponding crystallites were small and had large orientation distribution. Zhang estimated correlation lengths based on Scherrer's equation[6] to be ≈2 lamellae and 8-9 π-stacks for (200) and (010). Collectively, the diffraction data suggest long correlation length for π-stacking with extended and disordered side chains which does not indicate any particular order within the unit cell.

Given the scarcity of meaningful experimental data I had to explore all possible configurations that were reasonable given my previous experience. Because of computational limitations I used two stacked dimers per unit cell. I started by designing a bare backbone dimer without any alkyl chains using DFT-optimised molecule. For a single dimer one can use either parallel (↑↑) or anti-parallel (↓↑) configuration of monomers giving 4 possible orientations of IDT. Two dimers can be stacked again either in parallel (Figure 6.8 **a**) or anti-parallel (Figure 6.8 **b**) configuration to form a unit cell resulting in 16 possible inputs. Furthermore, it is unknown if the polymer chains are stacked directly on top of each other as in Figure 6.8 **b** or shifted with respect to each other along the lamellar direction as in Figure 6.8 **a**. Typically, one would scan shift along the lamellar direction in four steps equal 0.25 length of a dimer increasing total number of possible IDT unit conformations to 64, not to mention BT units. In practice optimization of such a large set of possible geometries is never executed, as number of inputs can easily be reduced by considering symmetry of the system and the rule of thumb is that more symmetric unit cells yield lower total energy. However, the most complex part of finding a right input are certainly alkyl chains. As suggested by Zhang[6] I assumed that the alkyl chains are extended and interdigitated. I started with fully extended chains attached to the backbone at a right angle (Figure 6.8 **a**) followed by various configurations incorporating tilted chains, for example in *Z* or herringbone pattern as shown in Figure 6.8 **b** and **c**. Herringbone arrangements are particularly expensive computationally since the top row is not a repetition of bottom one meaning that a supercell method has to be used. Another aspect to consider is the way side chains are bonded to a common backbone carbon atom- they can either be bonded in -trans or -cis configurations as shown in Figure

6.8**a** and **d** respectively. Initially, I was only considering -trans arrangement since it results in a more uniform distribution of matter within a unit cell, however I observed that a spontaneous evolution into -cis configuration often reduces energy of the system and hence I decided to consider both cases. The overall number of possible inputs was prohibitive to study- it was decided to reduce the sample space based on symmetry arguments, very ununiform distribution of matter such as overlapping side chains, or significant increase of energy of the system during brief preliminary simulation. Finally, I selected 12 input structures that were, in my opinion, most promising ones and I proceeded with standard dynamics and geometry optimisation as was described in Methods section.

Most of the input structures did not converge to a low-energy, highly-ordered crystalline phases and for a practical reasons I am only going to discuss selected outputs. The four output structures with the lowest energy possess a remarkable number of common features- the alkyl chains are fully extended at a right angle to the backbone and interdigitated no matter if in a -cis or -trans configuration. Regardless of the relative orientation of IDT units the backbones are straight, almost planar and stacked directly on top of each other without any shift along lamellar direction. I have fully tested the hypothesis of shifted backbones, however such input structures always resulted in higher overall energy and waved backbones as if the system was pretending to recoil to a direct stack. The unit cells have approximately the same primitive vectors and angles. Figure 6.9 **f** shows view of structure **a** along the lamellar direction. The characteristic tilt of conjugation plane and interdigitation of alkyl chains was observed in all low energy structures and most of disordered output. As discussed previously, there is no proof that such a unique set of packing leitmotifs does indeed represent a global minimum of the energy landscape. It is however reasonable to assume most of the structural features shown in Figure 6.9 would be present in a crystalline phase of an experimental thin film. Structure **a** is particularly interesting one- it is not only the lowest in energy among all examined inputs but also the one that was the least likely to facilitate backbone linearity. As discussed in High Pressure Raman section, the DFT simulations of a vacuum phase predict non-linearity of IDT units arranged in parallel (↑↑). my initial guess was that a perfectly linear molecule requires IDT units to be arranged in alternating “up” and “down” configurations, while having all IDT’s in the same configuration would result in the most arched molecule. As shown on Figure 6.9 the non-linearity of IDT has been accommodated via rotation of BT unit. Surprisingly this leads to a lower energy than in structure **b** were IDT units are arranged in alternating order such that the strain should be perfectly linear.

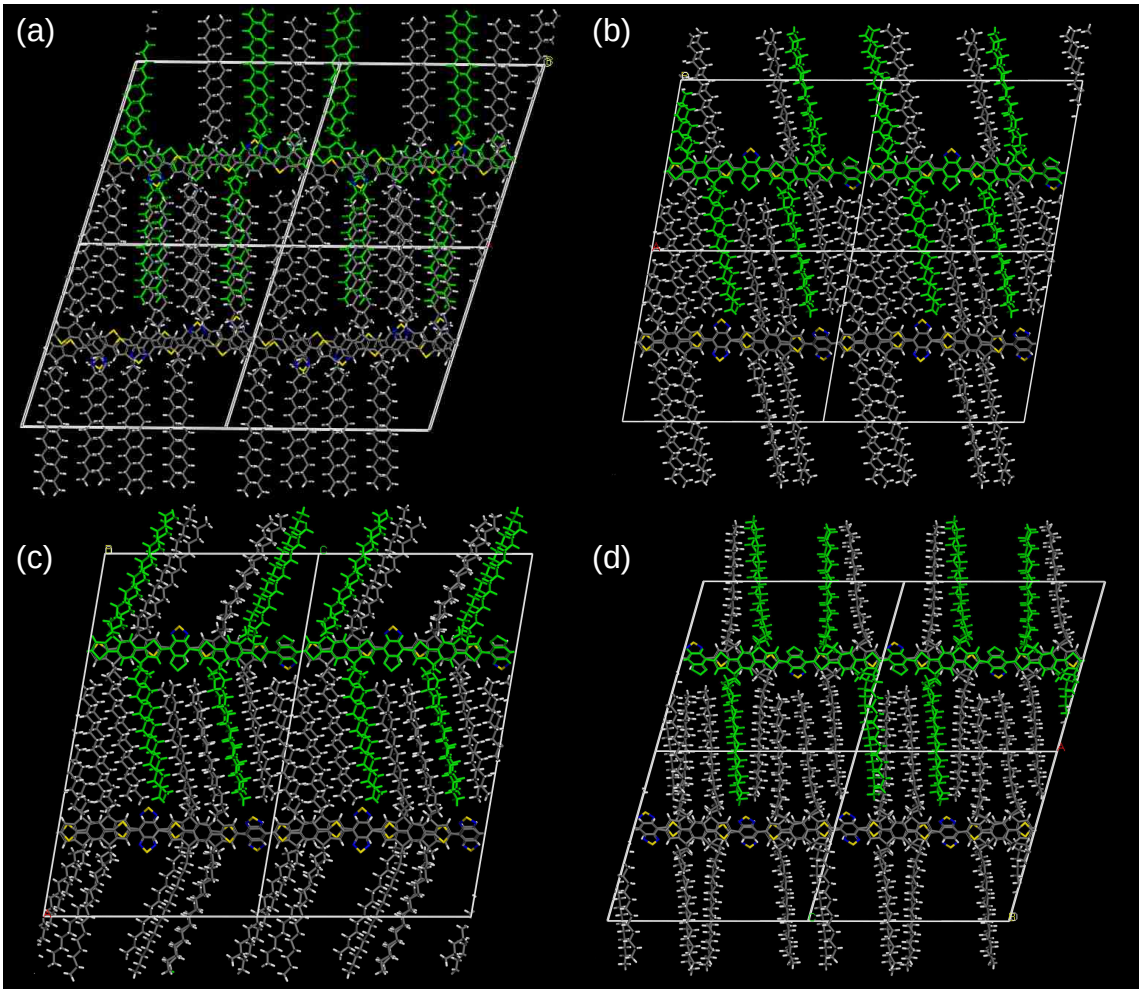


Figure 6.8: Selected examples of input structures used for molecular dynamics geometry optimisation. (**a**) polymer chains shifted along lamellar direction with perpendicular sidechains in -trans configuration. (**b**) polymer chains stacked directly with tilted sidechains. (**c**) example of herringbone interdigitation. (**d**) sidechains in -cis configuration.

Moreover, the negligible energy difference between structures **a** to **c** suggest, that the orientation of BT unit does not significantly influence the system, both when it comes to orientation with respect to neighbouring IDT unit and stacked BT unit. As a consequence, one may suggest hypothesis about rather unique property of IDT-BT- within set of all possible configurations of IDT and BT units the chance that a system picked at random will result in an ordered structure is higher, when compared to previously known polymers. Together with experimentally proven lack of pressure dependence of backbone vibrational modes, this attribute of IDT-BT provides a valid framework to explain the ability to adapt structural disorder without compromising transport properties.

All of the crystalline structures that were found had conjugation distances inconsistent with experimental data. Figure 6.9 **f** shows simulated diffraction pattern of the most thermodynamically stable structure **a**. The peak corresponding to characteristic distance of 4.05 Å has been identified as π-stacking, while other structures had conjugation length in the range $4.0 - 4.2$ Å meaning, that the ordered structures would be unlikely to be present in experimental film. It was therefore decided to force the system into a more disordered phase by temporary increasing interlamellar distance and temperature followed by annealing at lower temperature as was described in Methods section. The resultant structures retained backbone conjugation, although the alkyl chains became disordered and were no longer interdigitated. Contrary to common experience, the more disordered structure had torsion free backbone and conjugation distance in agreement with experimental X-ray data even though the overall density has been reduced. The effect of increase of structural disorder has been illustrated by similar simulations performed on a much larger scale by my collaborators from Mons University [26]. Figure 6.10 shows non-interdigitated structures of pBTTT and IDT-BT, respectively. In relation to their crystalline phases the backbone conformations in these disordered structures differ significantly between the polymers- IDT-BT adopts a wavy, yet remarkably planar, largely torsion- free backbone; the deviation from planarity remains exceptionally small (torsion angle of $5.2 \pm 4.0°$). In contrast, pBTTT chains, while maintaining a linear conformation, explore a broader range of torsion angles ($27.2 \pm 14.6°$ between thiophene and thienothiophene).

The simulations of disordered structures were complemented by a longer runs evolving into fully amorphous and non-conjugated systems. As described in Methods section, both interlamellar and interchain distances were artificially increased and the system was allowed to freely evolve at an elevated temperature. Such a molecular dynamics simulation is meaningful and provides data for statistical analysis only if

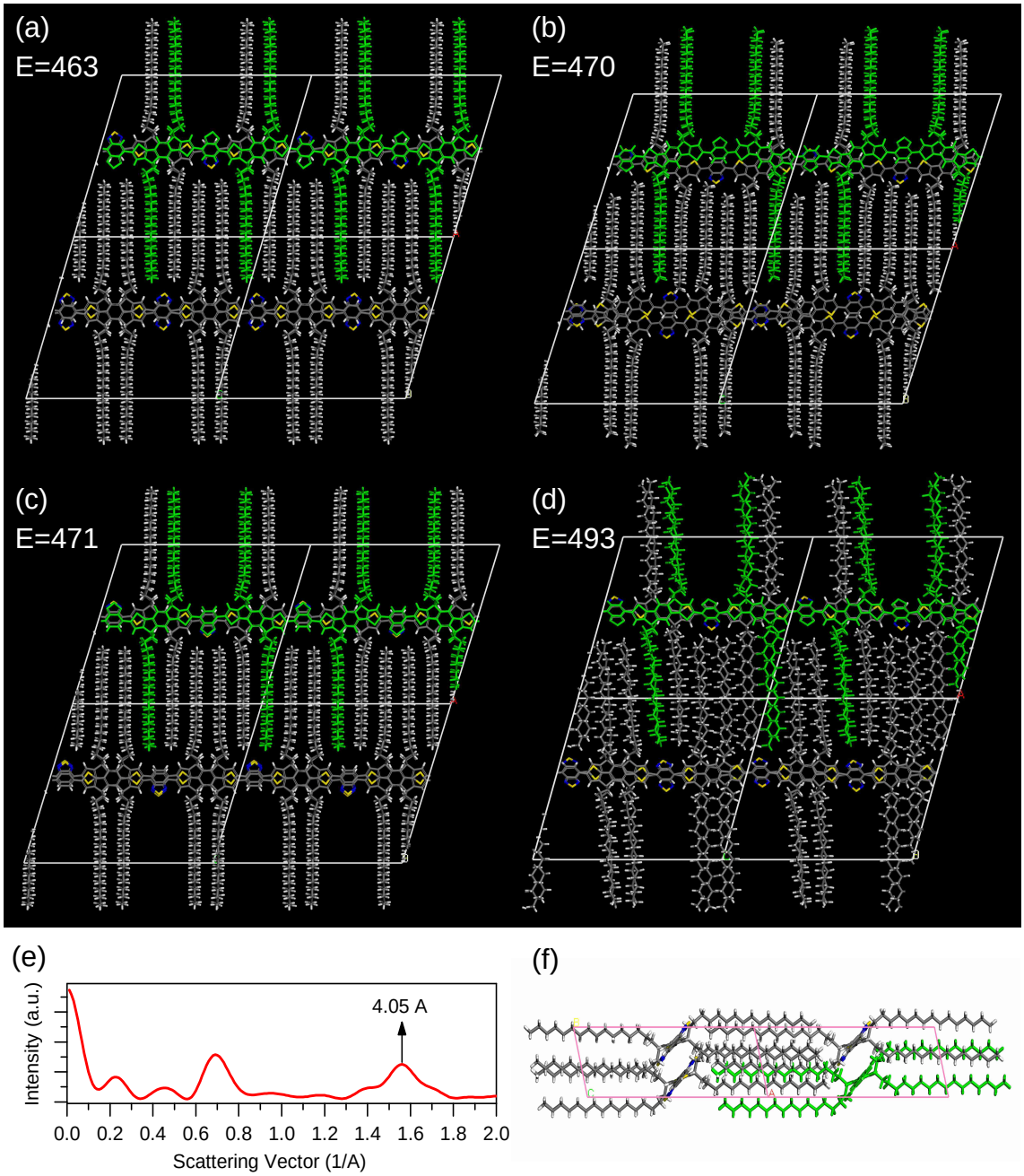


Figure 6.9: (**a-d**): four output structures and their corresponding total energies expressed in kcal/mol. (**e**) simulated powder x-ray diffraction pattern of the lowest energy structure. The peak at 4.05 Å has been identified as π-stacking. (**f**) view along the lamellar direction of the lowest energy structure. The BT unit is out of IDT plane by approx 7°.

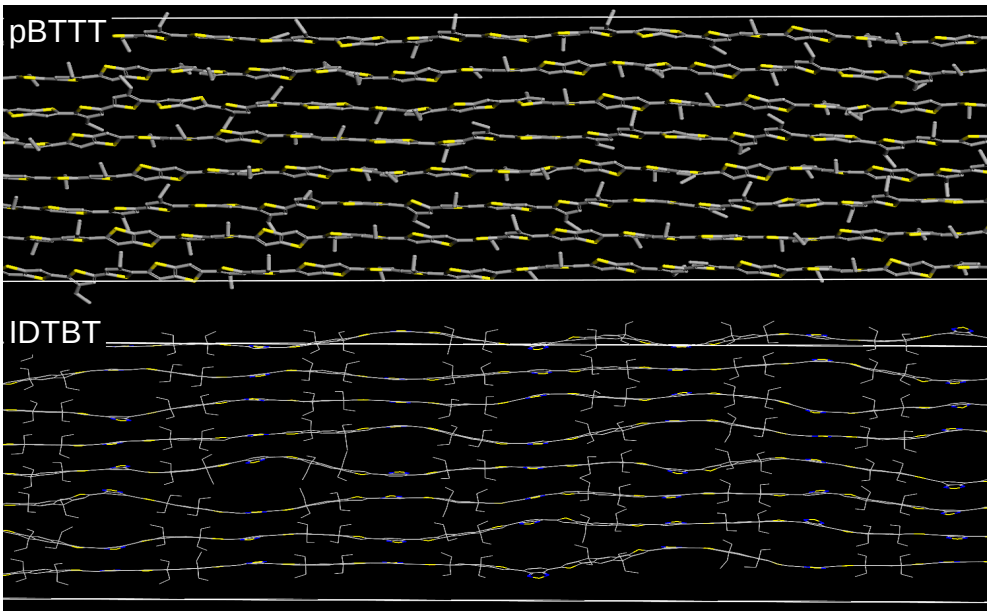


Figure 6.10: Disordered phases of pBTTT and IDT-BT. The side-chains have been removed for clarity. pBTTT accommodates disorder via backbone torsion while IDT-BT preserves planarity. Data courtesy of Vincent Leamur.

the boundary conditions are not periodic on a short scale meaning that one has to use largest possible supercell. However, the computational cost scales as a power law with the number atoms within a unit cell and hence requires extensive use of computing cluster. Simulations of amorphous phases of pBTTT, IDT-BT and NDIT2 were performed by out collaborators at Mons University. The resultant structures and snapshots of selected polymer chains are shown in Figure 6.11. As previously, IDT-BT backbones were nearly torsion-free with disorder accommodated by bending. This effect has not been observed in case of pBTTT and NDIT2: one can clearly see that in both cases there is a significant degree of torsion along the backbone. The degree of torsion can be quantified by making a statistical analysis of the deviation form planarity. Surprisingly, in an amorphous phase IDT-BT has an average torsional angle of $6.4 \pm 5.0°$ which is smaller than in previously simulated crystalline phase. The IDT-BT backbone resilience to torsional disorder seems to be a unique feature among all systems that were studied so far- by comparison TT-T in pBTTT and NDI-T bonds explore a much wider span of torsional angles ($53.8 \pm 19.4°$ and $44.7 \pm 21.4°$ respectively) in the amorphous phase.

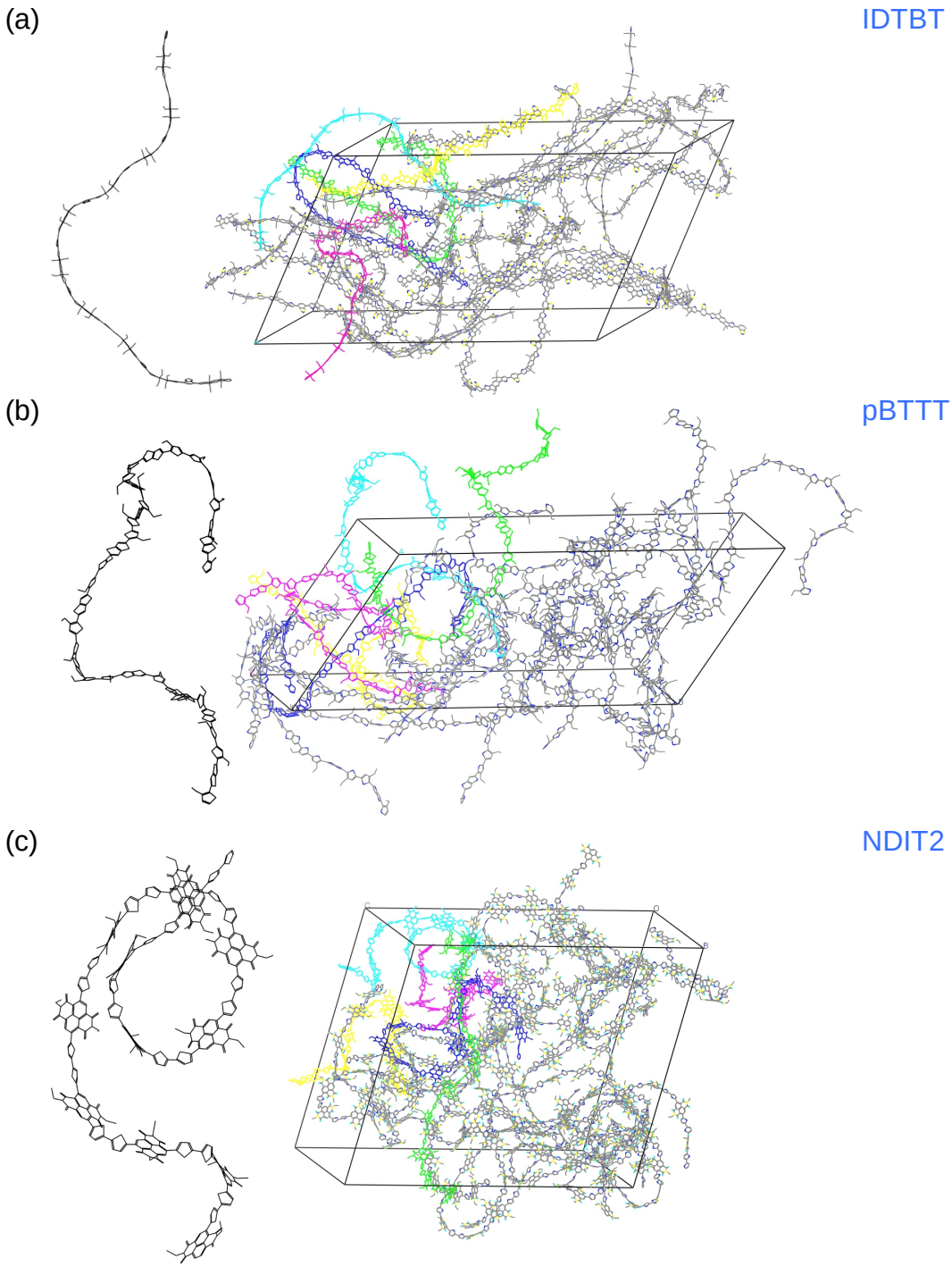


Figure 6.11: Comparison of amorphous structures of IDT-BT, pBTTT and NDIT2 respectively. For each polymer I present a single unit cell with side-chains stripped for clarity and a randomly selected backbone to illustrate the varying degree of torsional disorder. Data courtesy Vincent Leamur.

## 6.3 Summary

In summary, the direct experimental evidence for a pressure-resilient Raman spectra together with DFT simulations provide a valid framework to explain the lack of torsional disorder in IDT-BT. The symmetry and height of the torsional potential between IDT and BT units and the linearity of BT unit suggest a structure that can easily accommodate an increase in entropy (as defined via number of microstates of the system) without significant change of the overall energy. This hypothesis was verified by use of molecular dynamics simulations: I managed to obtain a set of structures with unique relative orientations of building blocks, yet yielding similar energies and conjugation distances. Finally, by exploring both non-interdigitated and fully amorphous structures I proved that in case of IDT-BT the degree of torsional variation of the backbone does not increase significantly with the overall disorder of the system regardless of the thermal energy. Moreover, the dominant mechanism to accommodate the disorder along the polymer strand is by bending, rather than twisting, of the backbone. This property makes IDT-BT a rather uncommon system when compared to other reference polymers such as pBTTT and NDIT2, which exhibit a correlation between the order of side-chains and torsion of the backbone. I suppose this is a consequence of very specific molecular design of IDT-BT: as one can see in Figure 6.3 the torsional potential facilitates planarity and is steeper when compared to pBTTT, thereby effectively making backbone more resilient to steric interactions between the side-chains.

# Chapter 7

# DPP-BTZ

After successful validation of high pressure Raman technique using pBTTT and more venture research on IDT-BT I looked for a system that is high in carrier mobility, yet understood well enough to make a valid conclusion about structure-property relationship and possibly suggest new patterns of molecular design. I decided to study diketopyrrolopyrrole (DPP) based polymers, since family of DPP derivatives includes some of the highest mobility ambipolar systems known today with reported FET mobilities of up to 12 $cm^2V^{-1}s^{-1}$ for holes and up to 6.3 $cm^2V^{-1}s^{-1}$ for electrons [140, 141]. Although accuracy of these numerical values is subject of an ongoing debate regarding the methodology of mobility extraction, it is generally accepted that DPP-based polymers are among the best performers. When it comes to molecular structure, DPP unit is usually flanked by aromatic side units such as thiophene or selenophene, with some authors suggesting [74] that units including five-membered rings tend to exhibit less backbone torsion compared to six- membered rings and hence improved OFET performance. Above hypothesis has been based on a vacuum-phase simulation of equilibrium torsional angle in phenyl-DPP and theinyl-DPP. The causation between type of the ring unit and improved backbone co-planarity has not been proven experimentally since so far the choice of experimental techniques used to probe backbone planarity was scarce, however correlation between type of aromatic ring and OFET performance has been published by Nielsen and coworkers [74] as a part of an extensive review of DPP polymers. DFT simulations on isolated molecules make a valid foundation to form a hypothesis why some derivatives perform better than others, but in a bulk phase torsion of the backbone is often far from a vacuum phase equilibrium state- there is a clear gap in experimental evidence that might be used to explain the observed correlation in terms of molecular design and mechanism of disorder accommodation. Second factor that governs the OFET performance is

choice of side-chains: it is widely accepted that the side-chain substitution exerts an important influence on the backbone conformation of conjugated polymers and may even determine the ability to form an ordered structure [39]. Choice of the right type (e.g. branched or linear) and length of side-chains is an important part of the molecular design that has a major effect on electrical performance. Despite increasing number of publications on this topic, no universal set of rules for the design of side-chains exists up to date. In a number of conjugated polymers it has been found that introduction of branched, instead of linear, side-chains improves solubility but is often detrimental for transport properties. However, Zhang et al.[142] found that in several DPP-based polymers branched side-chains can also improve carrier mobility by supposedly facilitating favourable backbone alignment and planarity. His argument regarding the backbone torsion is based on a redshift of UV-VIS absorption peak in a crystalline phase with respect to a solution. The technique is referenced to a work published by McCullough in 1993 [143] where similar shift of absorption peak was reported for poly(3-alkylthiophenes) (PAT). It is important to realize that this technique is a measure of relative change of electronic conjugation length and not the actual microstructure. The argument relating backbone planarity to conjugation length can be traced back to a study of thermochromic transition in P3HT published by Winokur and co-workers in 1989 [114]. At that time capabilities to calculate spectra using first principles or crystalline structures using molecular dynamics were rather limited and the argument was based on an implicit evidence. I suppose that in the early studies of structure-property relationships of semiconducting polymers it was assumed that planarity and ordered lamellar stacking were coexisting phenomena, hence the reference to conjugation length. As was demonstrated by use of molecular dynamics [26, 39], there exist systems which have co-planar units belonging to neighbouring strands, but are not planar along a single strain, or even systems that demonstrate lamellar stacking despite significant torsional disorder, such as non-interdigitated phase of pBTTT. The influence of side unit and type of alkyl chains on backbone planarity clearly lacks explicit experimental evidence, hence I saw a potential to apply high pressure Raman spectroscopy to address some of the questions regarding structure-property relationship in DPP-based polymers.

My choice of system were two recently synthesized derivatives of DPP-BTZ: first with linear side-chains at DPP unit and branched side-chains at BTZ unit [(l-C18)-DPP-(b-C17)-BTZ] and second with linear side-chains at both DPP and BTZ units [(l-C18)-DPP-(l-C8)-BTZ] as shown in Figure 7.1. Both systems were synthesized using the same route and extensively characterized by my group both in terms of

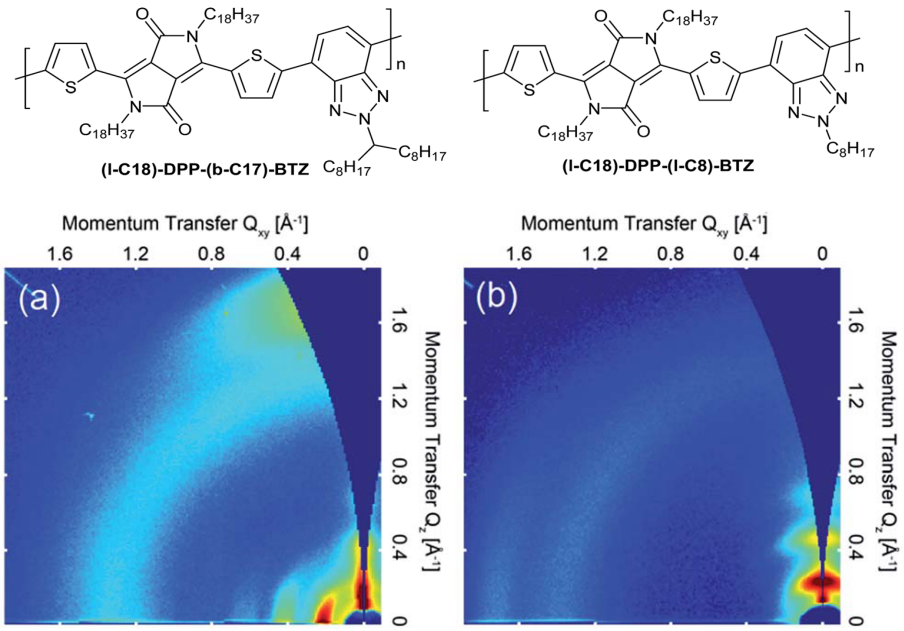


Figure 7.1: Chemical structures and corresponding 2D GIWAXS patterns of (a) (l-C18)-DPP-(b-C17)-BTZ and (b) (l-C18)-DPP-(l-C8)-BTZ films annealed at 110° C. Figures adapted from Gruber et al. [18]

structural and electronic properties, as reported by Gruber et al [18]. The BTZ unit was supposed to facilitate planarity of the backbone, whereas different kinds of side-chains were chosen to study the effect of chain density on the film microstructure.

The 2D GIWAXS patterns of polymer film annealed at temperatures required to achieve maximum charge transport are presented in Figure 7.1. Both films show a semi-crystalline structure, however (l-C18)-DPP-(l-C8)-BTZ appears to be more ordered since up to three diffraction peaks can be distinguished along $Q_z$ direction. Position of (100) peak corresponds to a lamellar stacking distance of 25.7 and 28.6 Å in (l-C18)-DPP-(l-C8)-BTZ and (l-C18)-DPP-(b-C17)-BTZ respectively. In case of (l-C18)-DPP-(b-C17)-BTZ, the weak ring at 1.3 $Å^{-1}$ is most likely caused by packing of disordered side-chains. Both systems demonstrate a relatively short distance of $\pi - \pi$ stacking in the range of approximately 3.6 Å. Surprisingly, the positioning of a branched side-chain at the BTZ unit leads to fairly ordered thin film structure, which is untypical given the commonly suggested rules of molecular design. It is interesting to note that, according to Gruber et al [18], a high degree of thin-film order is already present at low annealing temperatures of 110 °C and can be further improved using higher annealing temperatures up to 300 °C.

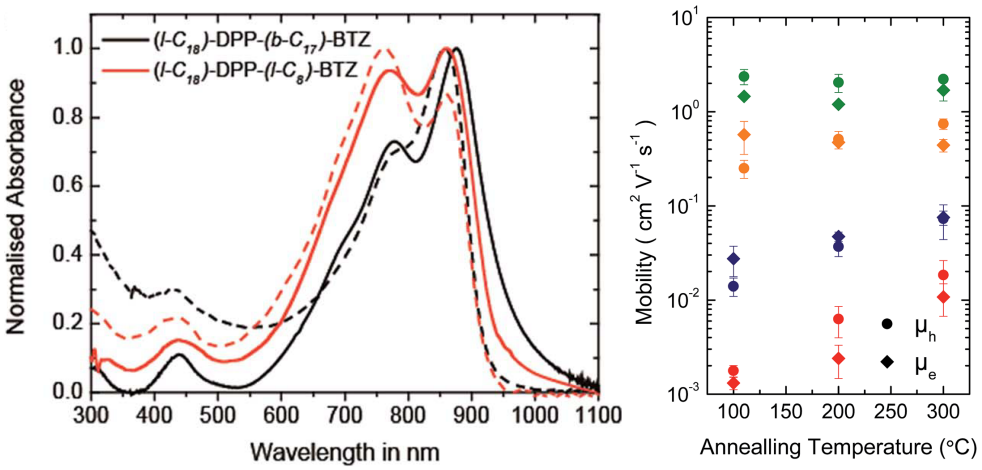


Figure 7.2: Comparison of UV-VIS spectra (left) measured in chlorobenzene solution (**dashed lines**) and thin films (**solid lines**). Dependence (right) of electron (diamonds) and hole (circles) mobilities on annealing temperature in (l-C18)-DPP-(b-C17)-BTZ (**green**) and (l-C18)-DPP-(l-C8)-BTZ (**orange**). Blue and red data points indicate two other derivatives that were not investigated by me, namely (l-C16)-DPP-(l-C8)-BTZ and (l-C20)-DPP-(l-C8)-BTZ . Figures adapted from Gruber et al. [18].

UV-VIS spectra indicate that (l-C18)-DPP-(l-C8)-BTZ has a larger band gap of 1.32 eV compared to 1.25 eV for the (l-C18)-DPP-(b-C17)-BTZ. The formation of film out of solution has an interesting result on the spectra, as shown in Figure 7.2. The film formation has no effect on the position of absorption peaks of (l-C18)-DPP-(l-C8)-BTZ, however in case of (l-C18)-DPP-(b-C17)-BTZ there is a clear red shift of the main peak from 858 to 875 nm suggesting longer conjugation length. In terms of charge transport properties (l-C18)-DPP-(b-C17)-BTZ has an average electron mobility around 1.5 $cm^2V^{-1}s^{-1}$ with maximum value ranging up to 2.4 $cm^2V^{-1}s^{-1}$, whereas in case of (l-C18)-DPP-(l-C8)-BTZ mobilities are around 0.48 $cm^2V^{-1}s^{-1}$. Even though mobilities exceeding 3 $cm^2V^{-1}s^{-1}$ have been published for devices using bottom gate structures [144], mobilities achieved with (l-C18)-DPP-(b-C17)-BTZ are among the highest values reported for DPP-based polymers in top-gated structures. As obvious from the transport data, introduction of a branched side-chain at the BTZ unit significantly improves transport properties when compared to linear side-chain. According to Gruber [18] a possible explanation for this might be planarization of the polymer backbone, however there is no explicit experimental evidence supporting that statement. Although this might be true, I propose that in case of these two derivatives the main driving force responsible for microstructural order is steric interaction of side-chains rather than backbone torsional potential- i.e. it might be the case

that the planarity of the backbone is the effect, rather than the cause of a particular microstructure.

## 7.1 Torsional potentials

As with IDT-BT I decided to begin with calculation of vacuum-phase torsional potentials. DPP-BTZ backbone has, at least in principle, two degrees of torsional freedom since there is a single thiophene (T) unit separating diketopyrrolopyrrole (DPP) and benzothiazole (BTZ). The comparison of DFT-calculated torsional potentials is shown in Figure 7.3 **b**. First obvious feature of torsional potentials is the symmetry around 90°, well defined potential barrier and minima corresponding to planar configurations already suggesting a possibility of highly ordered polymer backbone. The BTZ-T bond is particularly interesting since it very closely follows torsional potential of IDT-BT. The slope around minima configuration is steeper and the energy difference between 0° and 180° configurations is smaller compared to IDT-BT. It is interesting to recall the argument from previous chapter regarding the possible number of IDT-BT microstates possessing similar total energies regardless of BT configuration. Since BTZ is a linear unit just like BT, the hypothesis relating the entropy and energy is even more valid if one considers only bare backbone- regardless of the energetic minimum occupied by BTZ during film formation, aggregation leads to a linear, planar molecule with negligible energy difference when compared to other conformers. Such a consideration neglects effects of side-chains at BTZ unit- in practice the energy difference between the $\theta_{\mathrm{BTZ-T}} = 0°$ and 180° states would be dominated by steric effects. It would certainly be interesting to investigate DPP-BTZ with the shortest possible alkyl group at the BTZ. However, one can imagine that the "energetic switching cost" is lower for short, branched side-chains easily filling empty space, which could possibly explain why (l-C18)-DPP-(b-C17)-BTZ has a superior performance when compared to (l-C18)-DPP-(l-C8)-BTZ. The interpretation of DPP-T potential is more complex, since neither DPP nor thiophene are linear. The requirement for T-DPP-T unit to preserve linearity is anti-parallel (↓↑) arrangement of thiophenes. My simulations demonstrate that the preferred orientation is when sulphur atom points away from oxygen at DPP which correspond to a minimum at $\theta_{\mathrm{DPP-T}} = 180°$ as shown in Figure 7.3b. Steepness of the potential around that global minimum guarantees resilience to a torsional disorder- it is more likely that any disorder present will be accommodated by BTZ-T bond meaning that the T-DPP-T unit can be modelled as a fixed, rigid block. The hypothesis based on DFT calculated potentials is, in a fact, supported by

experimental evidence recently reported by Chaudhari and coworkers [98]. Chaudhari performed NMR measurements of DPP-DTT in solid state and solution. In DPP-DTT, the DPP unit is flanked by thiophenes on both sides just as in DPP-BTZ. NMR data clearly indicate highly planar backbone structure with thienopnehe hydrogen weakly coupled to DPP oxygen atoms, as shown in Figure 7.3. The other, less likely possibility is the local minimum and plateau at $\theta_{\mathrm{BTZ-T}} = 0^{\circ}$ where flat energy landscape could lead to some degree of torsional disorder in vacuum phase, however interaction with adjacent stacked backbone would probably planarize it anyway. To sum up, theoretical torsional potentials suggest a highly planar and ordered backbone with fixed geometry of T-DPP-T block and BTZ-T bond being the only degree of freedom.

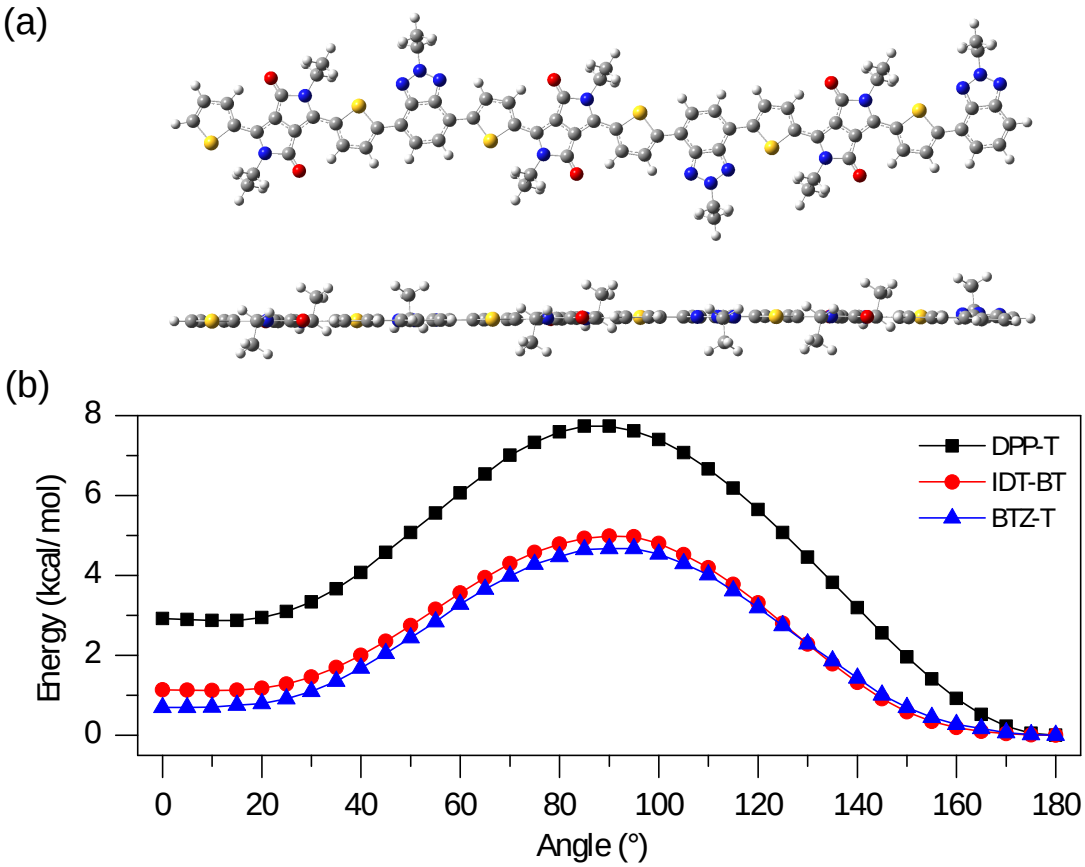


Figure 7.3: A minimum energy configuration (**a**) and a comparison (**b**) of torsional potentials in IDT-BT and DPP-BTZ calculated at B3LYP/cc-pvdz level of theory. The torsional potential between BTZ and thiophene almost matches IDT-BT, although it is steeper around 0° minimum and should result in at least the same degree of planarity. The minimum of DPP-T potential at 180° (corresponding to sulfur pointing towards nitrogen as in **a**) is very well defined and in theory should lock-in this degree of freedom.

## 7.2 High pressure Raman

Both derivatives of DPP-BTZ were studied using previously described method incorporating diamond anvil cell. The experimental Raman spectra collected as a function of hydrostatic pressure are shown in Figures 7.4 and 7.5. In both cases the spectra are very similar qualitatively with four distinct peaks, marked by arrows, that could be effectively fitted using Lorentzian model. As discussed in later paragraphs, vibrational modes were identified using DFT simulation. 1365 $cm^{-1}$ mode corresponds to C=C bond stretching localized on benzothiazole (BT) unit, whereas 1420 $cm^{-1}$ mode has been assigned to C-C bond stretching along the alkyl chain. Similarly, I identify

1430 $cm^{-1}$ mode as collective C-N and C=C bonds stretching localized on thiophene and diketopyrrolopyrrole (DPP). Finally, 1520 $cm^{-1}$ mode originates from C=C bond stretching localised on DPP unit. All four modes are visualized in Figure 7.11 **a**.

Any pressure dependence of intensity ratio that could be deduced from the data is not as obvious as in case of pBTTT or F8BT. Instead, I observe a rather typical peak broadening and frequency shift as was the case with IDT-BT. To quantify effects of pressure I calculated ratios of peak intensities as a function of external pressure. As previously, error bars at each data point denote the discrepancy between fitted and model Lorentzian peaks and does not include error due to PL background subtraction done by hand, which means that the actual uncertainty might be higher. I conclude that there is no obvious pressure dependence of intensity ratios. In both systems $I_{1365}/I_{1410}$ and $I_{1365}/I_{1520}$ ratios have comparable values and exhibit no obvious pressure dependence given the error due to background subtraction. In my opinion the only indication of possible pressure dependence is demonstrated by $I_{1365}/I_{1430}$ in (l-C18)-DPP-(l-C8)-BTZ although the magnitude of trend is definitively much smaller when compared to pBTTT or F8BT.

Analysis of frequency shifts and peak broadening as a function of pressure is shown in Figures 7.6 and 7.7. In both derivatives all four peaks exhibit very coherent shift towards higher frequencies indicating stiffening of effective force constants. Direct comparison of mode frequencies between two derivatives is not possible since pressure points do not overlap, however modes in derivative with both linear and branched side chains have somehow lower frequencies than in derivative with all-linear side chains. For example, in (l-C18)-DPP-(b-C17)-BTZ spectra 1410 $cm^{-1}$ peak shifts to 1419 $cm^{-1}$ at 3.06 GPa, whereas in (l-C18)-DPP-(l-C8)-BTZ spectra the same peak shifts to 1431 $cm^{-1}$ at 2.05 GPa. Shifts of mode frequencies suggest that effective force constants present in (l-C18)-DPP-(l-C8)-BTZ backbone are more susceptible to change in pressure when compared to (l-C18)-DPP-(b-C17)-BTZ, possibly due to lower interchain separation at ambient pressure and higher compressibility. On average mode frequencies do not shift by more than 7 $cm^{-1}$ per 1 GPa and it is rather difficult to draw any conclusions about backbone conformations based on mode frequencies.

Inspection of peak FWHM as a function of pressure provides insight into distribution of molecular conformations. In particular, FWHM of 1365 $cm^{-1}$ peak associated with BT ring stretching mode seems to be resilient to change of pressure in case of (l-C18)-DPP-(l-C8)-BTZ. (l-C18)-DPP-(b-C17)-BTZ spectra demonstrate that FWHM of the same peak is pressure dependent, however it does not exceed 23.7 $cm^{-1}$ even at 3.8 GPa. It is therefore reasonable to formulate a hypothesis about resilience of

T-BTZ bond to torsional disorder in both derivatives. Contrary, 1520 $cm^{-1}$ peak corresponding to DPP ring stretching mode demonstrate clear broadening above 2.0 GPa with maximum FWMH of 38.3 $cm^{-1}$ in case of (l-C18)-DPP-(b-C17)-BTZ. Given the FWHM and pressure dependence of 1520 $cm^{-1}$ mode it is reasonable to conclude that DPP exhibits wide distribution of molecular conformations and that backbone of (l-C18)-DPP-(b-C17)-BTZ derivative is presumably less ordered than backbone of (l-C18)-DPP-(l-C8)-BTZ.

To draw a meaningful conclusion about the data I had to optimize the geometry, calculate theoretical spectra and identify vibrational modes. Unlike previous systems, DPP-BTZ proved to be a rather difficult and complex system as I was facing ongoing problems with energy convergence. In principle the torsional potential predicts ideally planar structure in the lowest energy configuration, however in practice I have noticed that isolated polymer chain in vacuum phase exhibits small ($\pm 3°$) variation in torsional angle along the backbone. Typically, a problem like that can be addressed by increased convergence threshold, however in this case "tight" threshold did not fully planarize the backbone and "very tight" did not converge at all. I experienced similar convergence issue with C8-BTBT and it seems to be typical in materials with weak bonding dominated by dispersion forces, where energy landscape is not convex enough around the minimum to converge geometry using standard methods. Alternatively, one can enforce planarity of the system by specifying a $C_s$ point group with mirror plane corresponding to the polymer backbone. As shown in Figure 7.1, side-chains are pointing out of backbone plane and one would have to rotate them by 90° away from the lowest energy state to fulfil the $C_s$ symmetry. I decided to simply test different combinations of point groups and convergence thresholds as shown in Figure 7.9. The difference between "default" and "tight" convergence is negligible for most of the modes, however forcing the system into $C_s$ point group not only results in new peaks, but also changes intensities of some peaks to levels incompatible with experimental spectra. As a result I decided that an unconstrained system would be a better starting point to examine torsional dependence of spectra. Another important aspect to consider when there are no periodic boundary conditions is the size of the system. Ideally, one would prefer to run spectra simulations on a system a big as possible, but in practice the limit is typically a tetramer given the computational cost. A single monomer of DPP-BTZ contains several more atoms than, for example, IDT-BT and it turned out to be impossible to calculate spectra for a tetramer. One potential way to overcome hardware limitation is to reduce the overall number of electrons in the simulation by removing some of the side-chain carbons. As previously, I performed

a series of test simulations to evaluate correlation between mode intensities and side-chain length, as shown in Figure 7.10. The height of 1400 $cm^{-1}$ and 1450 $cm^{-1}$ peaks together with shape of 1550 $cm^{-1}$ peak clearly demonstrate that shorter side-chains should not be used.

Having verified methodology I proceeded with usual simulation of Raman spectra as a function of torsional angle. As mentioned before, it was assumed that the only degree of freedom to consider is T-BTZ bond. The resultant normalized spectra and visualization of vibrational modes are shown in Figures 7.11 **b** and 7.11 **a** respectively. I marked bonds exhibiting highest amplitude with red arrows, however such a representation is rather simplified- in a fact all of the vibrational modes are compound and extended along the backbone, involving simultaneous vibrations of DPP, BTZ and T rings. This is very different to what was observed previously in pBTTT and IDT-BT, where peaks representing stretching modes of a single unit could be isolated. The only exception is 1410 $cm^{-1}$ peak, which I identified as a in-phase vibration of hydrogen atoms belonging to a side-chain. DFT predicts that the best indicator of torsional variation is intensity of 1340 $cm^{-1}$ peak, however I am rather unlucky since in experimental spectra the peak overlaps with a much stronger 1332 $cm^{-1}$ diamond line. Within the range of pressures that were used it is possible to replace diamonds with sapphire anvils, but they were not available at the time. The theoretical ratio of 1365 $cm^{-1}$ to 1520 $cm^{-1}$ is in almost perfect agreement with experiment whereas 1410 $cm^{-1}$ and 1430 $cm^{-1}$ peak intensities seem underestimated. The variation of 1365 $cm^{-1}$ peak intensity clearly indicates that if ambient pressure angle was above 10°, the planarization should result in a decrease of any ratio involving that peak. This effect is even more pronounced in case of 1575 $cm^{-1}$- although it was impossible to fit that peak due to low signal to noise ratio, a visual inspection of experimental spectra demonstrate that the only change was usual peak broadening and the low intensity suggest an already planar or near-planar backbone conformation. The origin of apparent increase of $I_{1365}/I_{1430}$ in (l-C18)-DPP-(l-C8)-BTZ remains unknown- if it was due to change in torsion, a similar cross-correlation in $I_{1365}/I_{1410}$ and $I_{1365}/I_{1520}$ should be observed, which was not the case. The lack of cross-correlation points us to a conclusion that the apparent pressure dependence of $I_{1365}/I_{1430}$ is in a fact a matter of experimental uncertainty rather than actual signature of changing microstructure. If the average torsion at an ambient pressure was less than 10°, it would nevertheless be very difficult to detect experimentally given the fitting uncertainty arising from PL background. The only peak, or rather group of peaks, that exhibit a steady and uniform variation of intensities with torsional angle is at 1460 $cm^{-1}$, however in the

observed spectra they were indistinguishable from the noise.

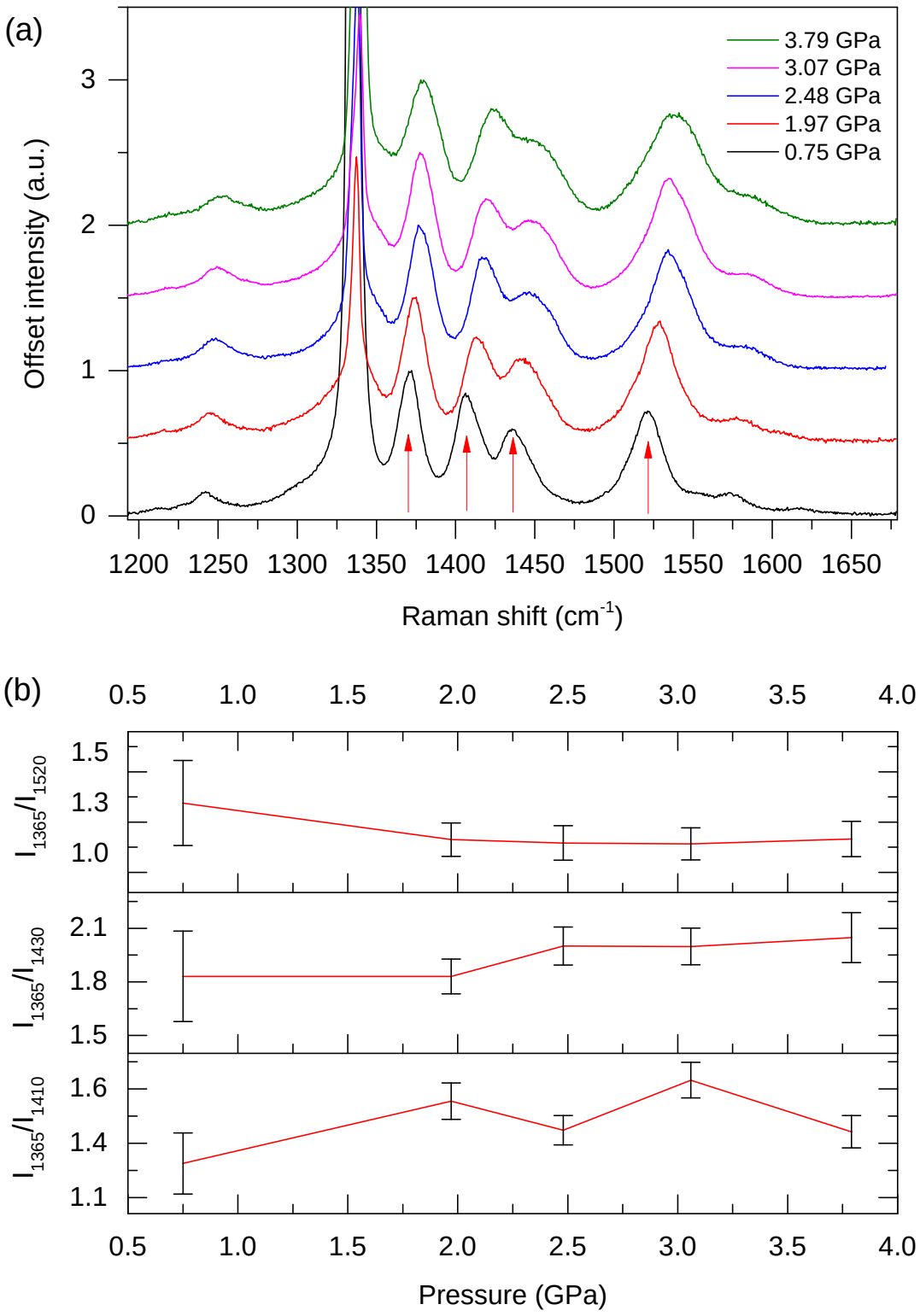


Figure 7.4: Experimental Raman spectra (**a**) and selected ratios of intensities (**b**) as a function of pressure for (l-C18)-DPP-(b-C17)-BTZ. Arrows denote peaks that were fitted. Spectra were acquired using $\lambda = 632$ nm laser line.

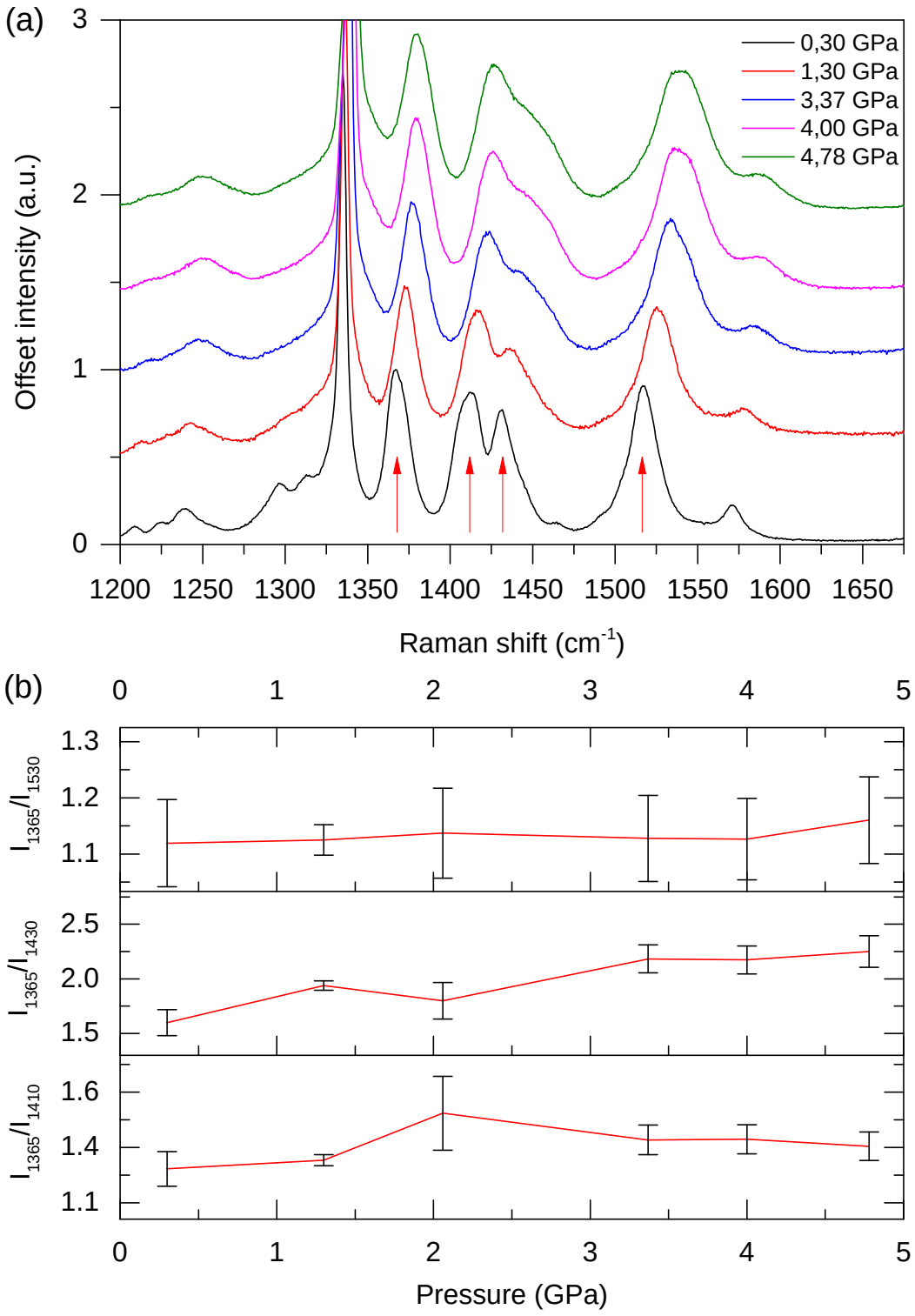


Figure 7.5: Experimental Raman spectra (**a**) and selected ratios of intensities (**b**) as a function of pressure for (l-C18)-DPP-(l-C8)-BTZ. Arrows denote peaks that were fitted. Spectra were acquired using $\lambda = 632$ nm laser line.

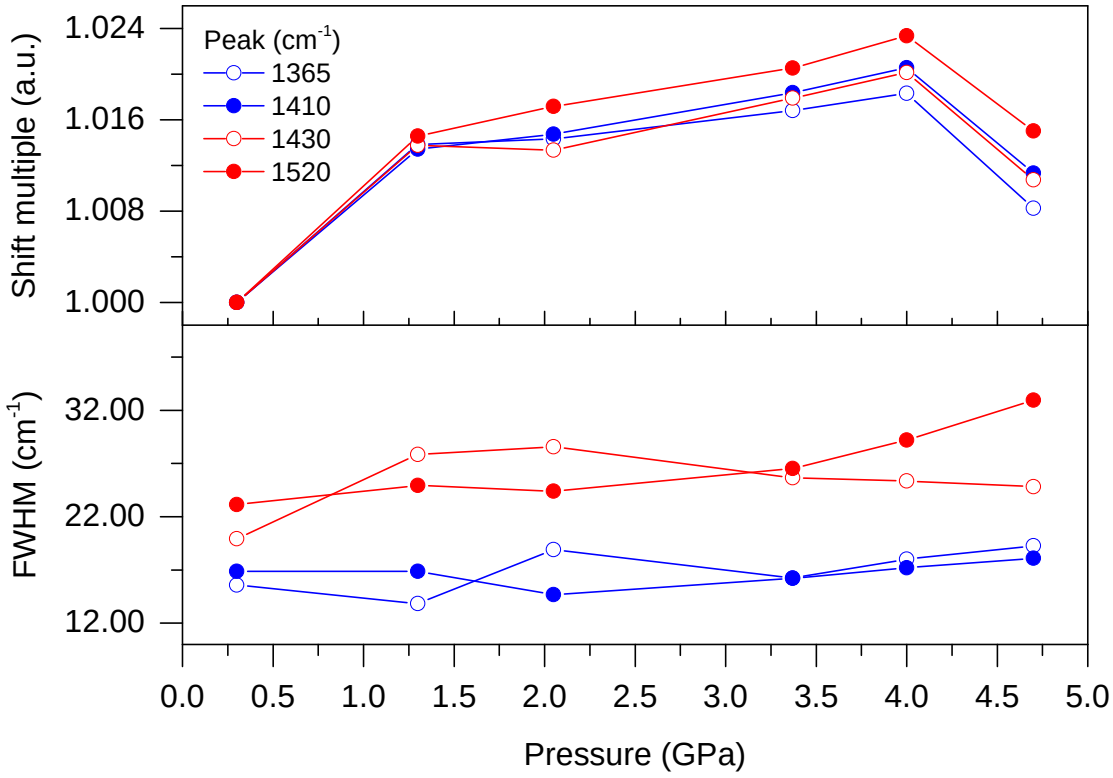


Figure 7.6: (l-C18)-DPP-(l-C8)-BTZ frequency scaling factor and mode FWHMs as a function of pressure.

To summarize, torsional potentials of DPP-BTZ mimic IDT-BT and predict a planar backbone in a vacuum phase. Linearity of BTZ unit together with negligible difference in energy of both planar minima suggest that there are several possible microstates of the polymer backbone yielding the same total energy and molecular packing, if one neglects the effect of side-chains. This hypothesis leads to the same mechanism of disorder accommodation as was previously suggested for IDT-BT. Moreover, experimental Raman spectra exhibit lack of consistent pressure dependence. Experimental and theoretical evidence points to a planar or nearly planar backbone configuration, but even if it is not the case I am convinced that the backbone is resilient to any major change in torsional angle. All of the above suggest that systems based on DPP-BTZ backbone should, at least as a theoretical limit, demonstrate a similar ability to overcome structural disorder as IDT-BT.

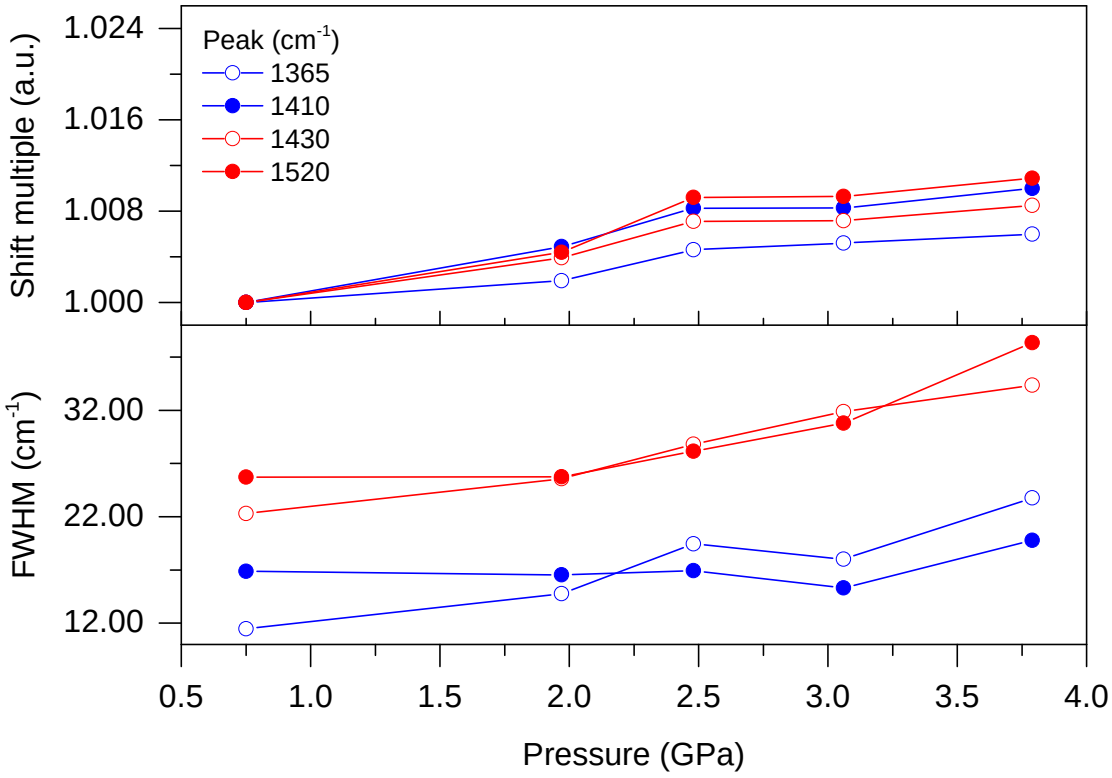


Figure 7.7: (l-C18)-DPP-(b-C17)-BTZ frequency scaling factor and mode FWHMs as a function of pressure.

## 7.3 Molecular Dynamics

So far I have have only studied properties of a backbone neglecting effects arising due to interactions between side-chains. As mentioned previously, side-chains are the driving force defining microstructure in the crystalline phase and hence electrical performance. The only way to probe difference between linear and branched alkyl chains is to perform large scale molecular dynamics simulation to determine the minimum energy structure and track evolution of a system as the degree of structural disorder is gradually increased, as was previously described for IDT-BT. In principle, one would expect that in a crystalline phase the disorder would be dominated by steric interactions between side-chains rather than torsional potentials of the backbone, whereas disordered, low density phase should approach the limit of vacuum phase dominated by backbone torsion.

As I previously discussed in IDT-BT chapter, there are several ways to construct a unit cell just by considering different relative orientations of building blocks. For simplicity I am only going to discuss highly symmetric or periodic structures, since

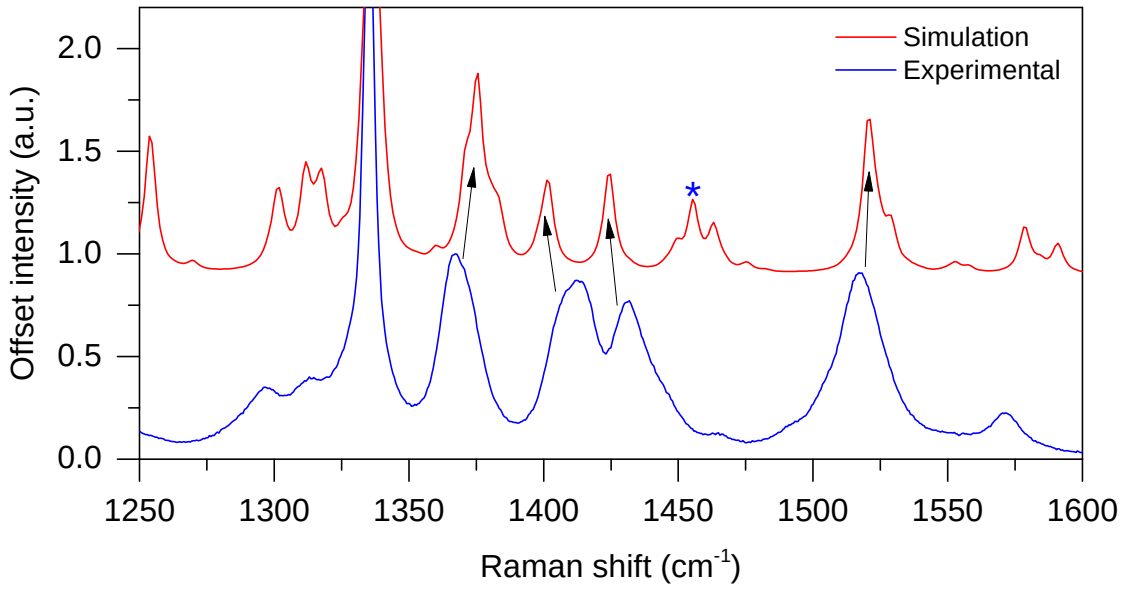


Figure 7.8: Comparison of experimental (l-C18)-DPP-(l-C8)-BTZ spectra at 0.3 GPa and vacuum phase DFT spectra plotted with 2.5 cm Gaussian peak half-width. (∗) denotes stretching mode of single thiophene at the loose end of polymer chain that should not be present in periodic structure. DFT spectra were rescaled by empirical B3LYP factor.

empirically they are more likely to converge into thermodynamic minimum. Let's denote DPP unit rotated clockwise with respect to vertical axis as (↑), as well as BTZ unit with side-chain pointing up. For example, structure shown in Figure 7.3 has a parallel (↑↑↑) configuration of DPPs and anti-parallel (↑↓↑) arrangement of BTZ units. The all-parallel configuration of DPPs results in a linear chain regardless of BTZ orientation, since BTZ is always linear on its own. Similarly, if two neighbouring DPP units are anti-parallel (↑↓), the resultant DPP-BTZ-DPP block would be locally curved and hence subsequent pair of DPP has to be an "inverse" in order to preserve long range linearity, eg $(\downarrow\uparrow;\uparrow\downarrow;\cdots)$. Now let's consider density of side-chains for different kinds of DPP-BTZ-DPP: in a $(\uparrow_{\mathrm{DPP}}\uparrow_{\mathrm{BTZ}}\downarrow_{\mathrm{DPP}})$ configuration all side-chains point in the same direction resulting in alternating regions of high density and empty voids meaning that any equilibration of the distribution of matter would inevitably result in disordered alkyl chains. Similarly, a $(\uparrow_{\mathrm{DPP}}\downarrow_{\mathrm{BTZ}}\downarrow_{\mathrm{DPP}})$ arrangement leads to a more dispersed distribution of side-chains and $(\uparrow_{\mathrm{DPP}}\downarrow_{\mathrm{BTZ}}\uparrow_{\mathrm{DPP}})$ shown in Figure 7.3 is presumably the most uniform one. It is important to realize that even if a single polymer strand has asymmetrical side-chains it is still possible to construct a unit cell with a fairly uniform spatial density, eg by stacking strands in anti-parrallel or shifting

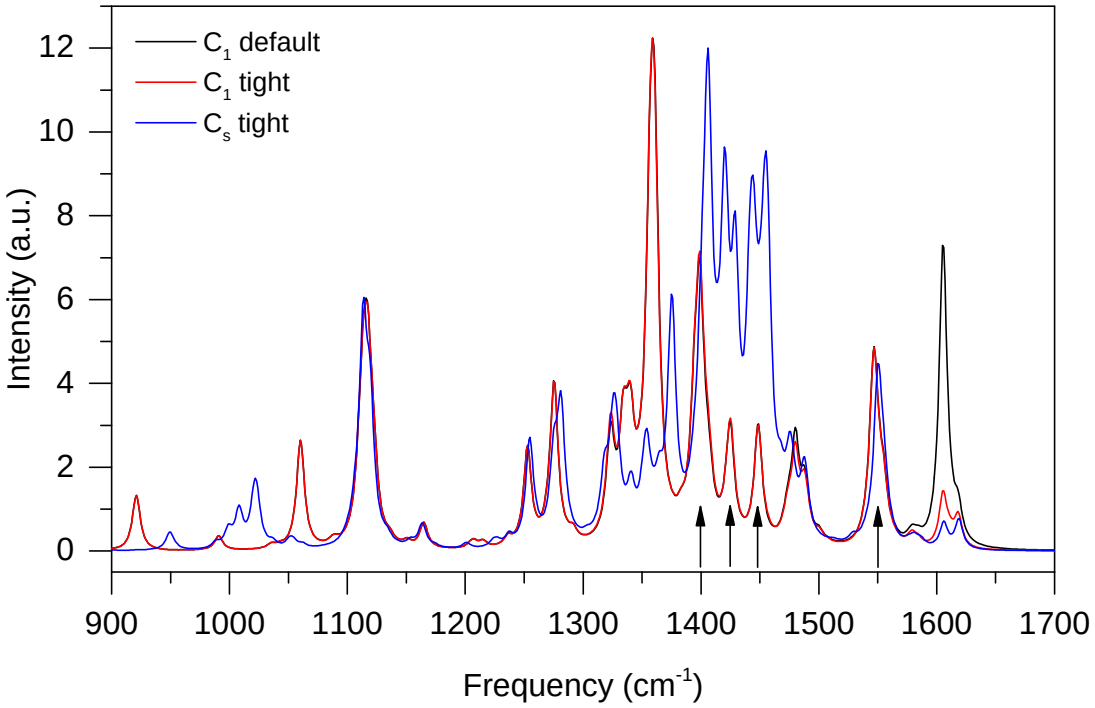


Figure 7.9: Test of simulated Raman spectra as a function of space group ($C_s$ vs $C_1$) and electronic convergence criteria (default vs tight) as implemented in Gaussian. Arrows denote peaks that were assigned to experimental.

strands along lamellar direction, as in rhombohedral cell, so that they mutually fill the empty voids. It is nearly impossible to examine all of the possible inputs and for practical reasons I am going to omit most of the geometries tested and only discuss structures that led to lowest energy configurations in my search for stable crystalline structure.

My first choice was the least complex system with parallel configuration of DPPs and single polymer strand per unit cell, as shown in Figure 7.12 **a**. I began with a near planar structure and fully extended side-chains, which was my best guess of an isolated molecule in a vacuum phase. Although I have never optimized such a big system using DFT, my previous experience suggests that repulsion between hydrogen atoms typically leads to a straight, extended alkyl chains. I followed a standard procedure of geometry optimization, dynamical evolution at finite temperature and quenching as was previously done for IDT-BT. A unit cell with a single polymer strand is a rather simplistic approach, since it only limits possible outcomes to a very periodic ones and obviously can not evolve into system containing matching, asymmetric blocks a in supercells. Nevertheless it is effective computationally and gives a hint about possible

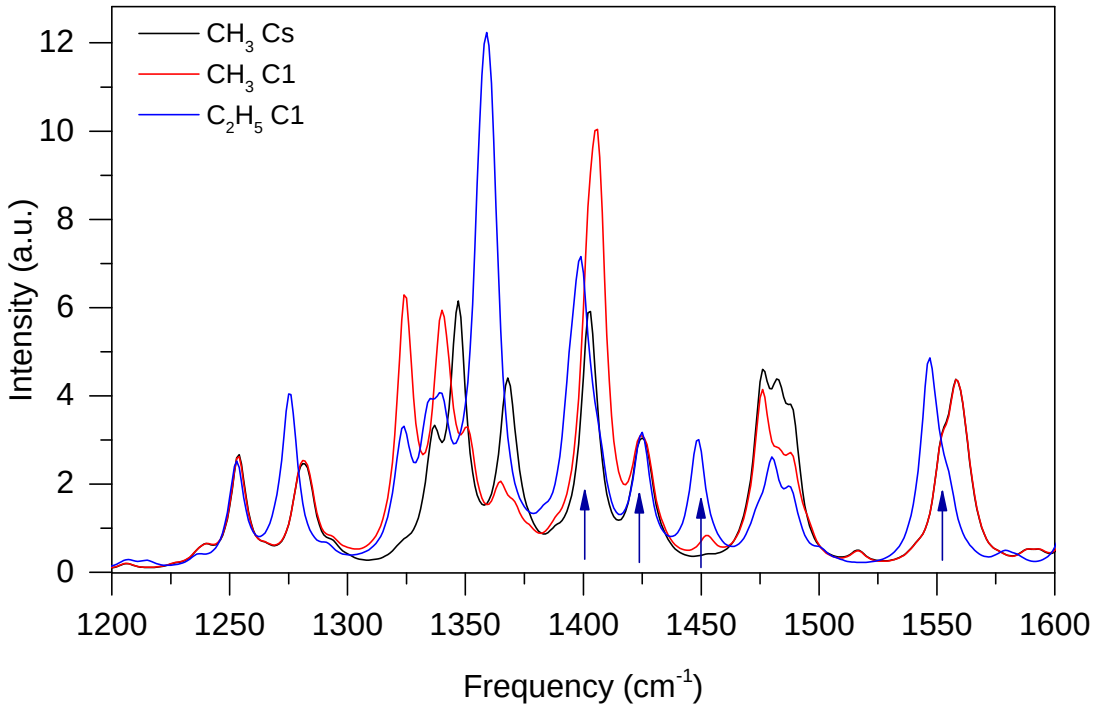


Figure 7.10: Test of simulated Raman spectra as a function of alkyl chain length and space group. Arrows denote peaks that were assigned to experimental

orientation of side-chins or relative shift of lamellae along the backbone direction. A lowest energy output incorporating a single strain per unit cell is shown in Figure 7.12 **b**. One can see extended and interdigitated side-chains adopting Z-like configuration. The view along the polymer backbone suggest that branched BTZ chains fill the empty voids between linear DPP chains and the unit cell evolved from orthorhombinc to triclinic lattice. Even though the structure is fairly ordered there were two factors suggesting that it is far from actual minimum- the very clear deplanarization of the backbone seems to be incompatible with previous results and ultimately results in $\pi$-$\pi$ stacking distance of more than 4 Å, which I find unphysical.

I decided to proceed using supercells containing two polymer strands per unit cell as shown in Figure 7.13. My initial guess was the simplest structure with one-to-one conjugation, parallel DPP units and fully extended alkyl chains. The output geometry shown in Figure 7.13 **b** demonstrates a significant improvement with respect to the previous attempt- the backbone is more planar and calculated $\pi$-stacking distance is in agreement with experiment. However, disorder of side-chains pointed us to a conclusion that although this structure is a possible one, it is certainly not the lowest energy one- following the example of IDT-BT and other previously published systems

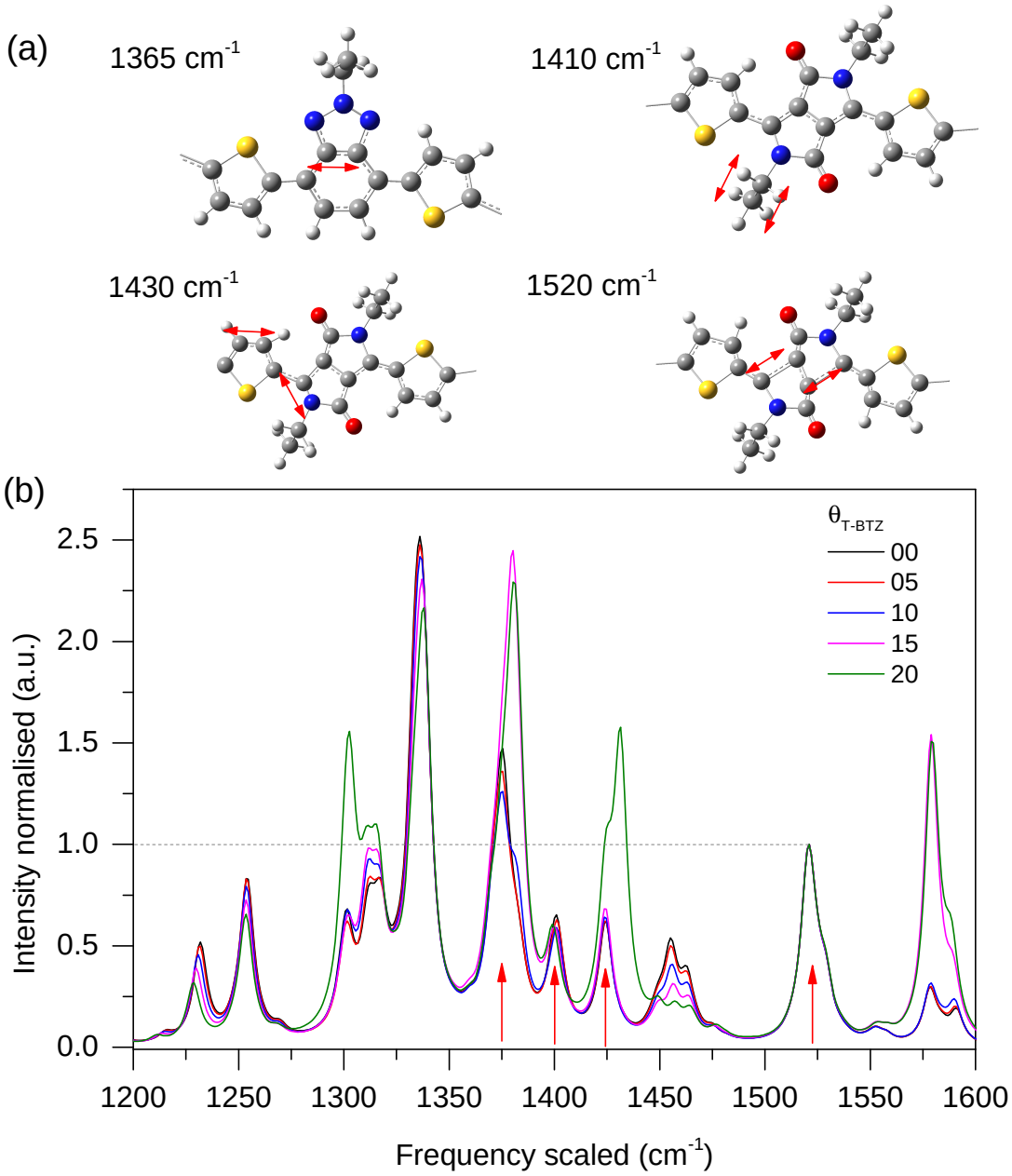


Figure 7.11: Visualization of selected vibrational modes (**a**) and corresponding DFT Raman spectra (**b**) calculated as a function of T-BTZ torsion. In panel (**a**) arrows denote largest amplitude vibrations (smaller amplitude displacements corresponding to the same frequency are not shown). In panel (**b**) arrows denote peaks that were assigned to experimental frequencies of 1365 $cm^{-1}$, 1410 $cm^{-1}$, 1430 $cm^{-1}$ and 1520 $cm^{-1}$. Frequency axis has been scaled by B3LYP empirical coefficient [96].

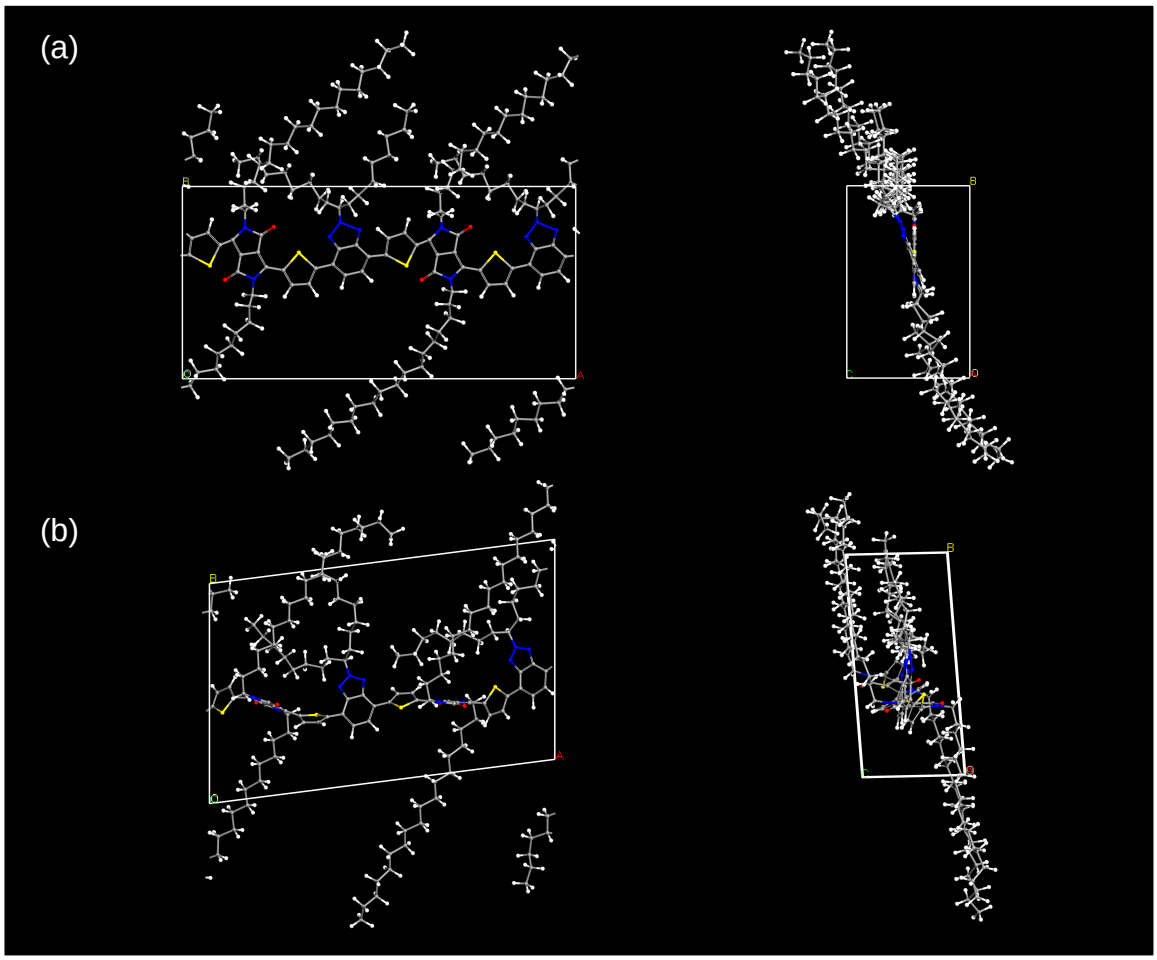


Figure 7.12: Molecular dynamics input (**a**) and output (**b**) structures of (l-C18)-DPP-(b-C17)-BTZ containing a single strand per unit cell. DPP units are in parallel configuration.

I expected a more regular pattern. A breakthrough step was the idea to squeeze and rotate the branched chains out of plane. This step was rather counter-intuitive, since DFT simulations predict fully extended alkyl chains in the plane of polymer backbone. There is no point in discussing all possible geometries that were tested and I am going to introduce only four input structures that lead to the lowest energy outputs, as shown in Figure 7.14. In a fact all of them were designed with a prior experience derived from previous unsuccessful attempts, hence it is no surprise that they share several similarities. In brief, I tested different orientations of DPP units along common polymer strand (parallel vs. anti-parallel) and different relative orientations of conjugated polymer backbones within a unit cell. For example structure (**a**), with parallel DPPs and direct stacking, is most reminiscent to the initial guess shown in

Figure 7.12 whereas structures (**b**)- (**d**) represent different ways of setting DPPs and whole backbones in an anti-parallel configuration. One can notice that side-chains are always interdigitated and arranged in a way to fill the empty voids- this is not the only strategy that was adapted, but structures that were non-intedigitated or had irregular distribution of matter did not converge to low energy configurations. The corresponding outputs are shown in Figure 7.15. The two lowest energy structures are the ones where polymer strands are stacked directly, i.e. in my notation they are in parallel configuration, regardless of their relative orientation within a single polymer strand. It is somehow surprising that linear chains are not necessarily an extension of DPP axis as predicted by DFT simulations- this effect is clearly manifested in structure (**c**) where both straight-on and angled alkyl chains are embedded within a regular structural motif. Based on these four structures one can conclude that DPP-BTZ has a rather unique property- within a narrow range of total energies one can design an ordered structure having a virtually random orientation of DPP units as long as the linear alkyl chains are extended and interdigitated in the plane of polymer backbone, and branched chains are out of polymer plane. As previously, I am keen to suggest that at least in theory there are several structurally distinct yet energetically compatible microstates, as was the case with IDT-BT. I calculated theoretical powder diffraction pattern of the lowest energy output as shown in panel (**e**). There is a distinct peak at 4.05 Å which resembles similarly looking peak of IDT-BT pattern, however there is one more peak at 3.55 Å that could represent $\pi - \pi$ stacking as well. Although both peaks are diffuse one cannot define a definite value of staking distance, a 4.05 to 3.55 Å interval appears to be physically possible. Panel (**f**) shows cross-view of the lowest energy structure. The polymer backbone appears to be less planar when compared to crystalline structure of IDT-BT. Outputs suggest that the average torsional angle $\theta_{\mathrm{DPP-T}}$ is equal 10.1° if linear alkyl chains are in the axis of DPP (structure (a)) and 20.3° if chains are angled. The corresponding values of $\theta_{\mathrm{BTZ-T}}$ are 6.2° and 12.0° suggesting that the major contribution to torsional disorder is DPP-T bond, possibly due to a more complicated packing of alkyl chins that are not a right angle to the backbone as in BTZ. Assuming that all four structures are likely to coexist in a crystalline phase one would expect $\theta_{\mathrm{DPP-T}}$ to be approximately in the range of 10 to 15°, which seems to consistent with pressure dependent Raman spectra.

The same procedure using inputs incorporating the same orientations of building blocks was reproduced for (l-C18)-DPP-(l-C8)-BTZ. It is somehow unsurprising that the most successful combinations result in the lowest energy structures for both derivatives. As previously I am going to omit most of the possible combinations tested

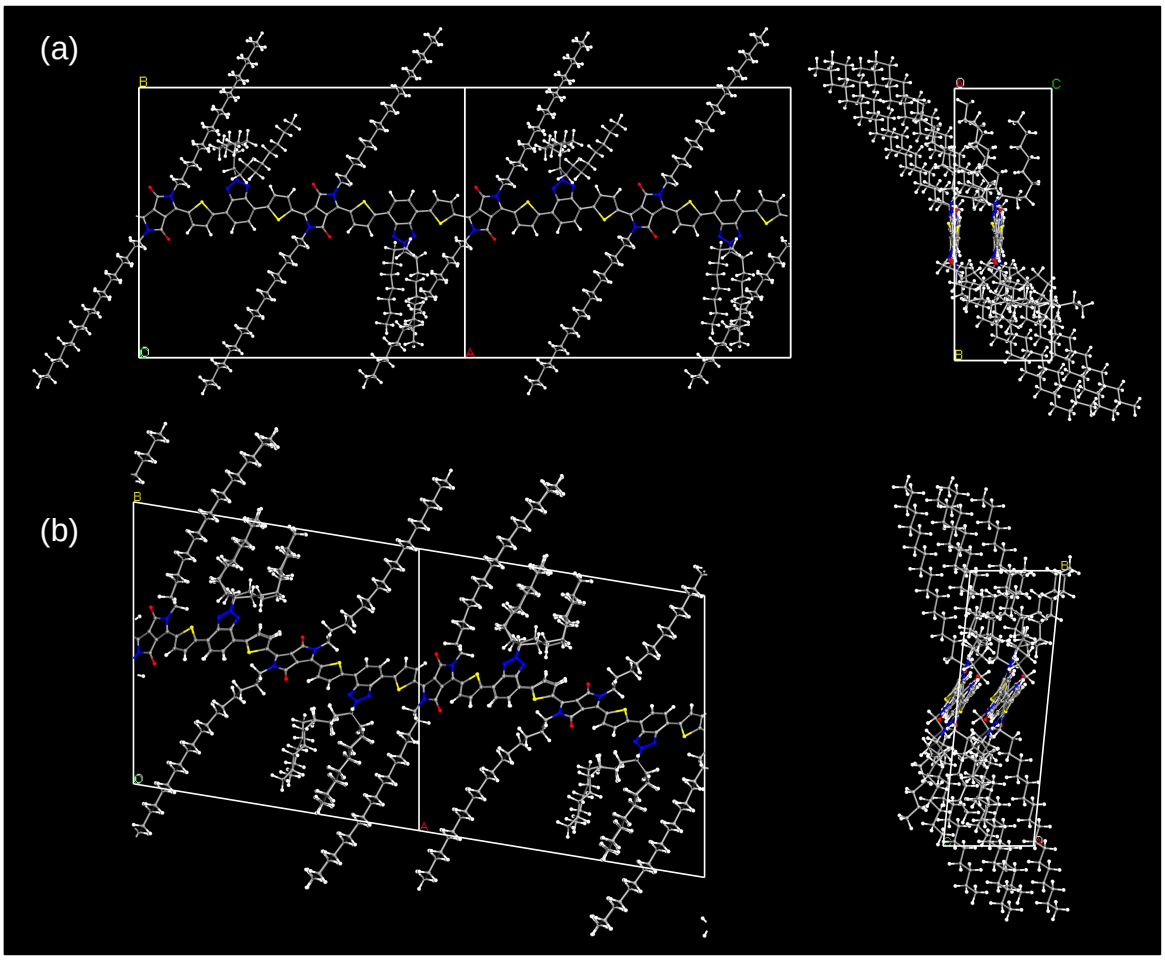


Figure 7.13: Molecular dynamics input (**a**) and output (**b**) structures of (l-C18)-DPP-(b-C17)-BTZ containing a double strand per unit cell. DPP units are in parallel configuration.

and present visualization of only four best performing inputs is shown in Figure 7.16. The input geometries are basically the same as for (l-C18)-DPP-(b-C17)-BTZ with substituted alkyl chains at the BTZ unit. Following the same procedure of dynamic evolution and quenching as previously, I performed a complete convergence of geometry into lowest energy states. The resultant output structures are shown in Figure 7.17. The overall spread of energies seems to be similar to (l-C18)-DPP-(b-C17)-BTZ.

Interestingly, structures appear to be much less symmetric and visually ordered, yet their total energies are up to 120 kcal/mole lower than in corresponding outputs of (l-C18)-DPP-(b-C17)-BTZ as is the case with structure (**b**). A simple explanation involves number of atoms per mole- since I reduced the size of the system it is reasonable to assume that the energy stored in pairwise interactions would scale proportionally.

Structures (**c**) and (**d**) have less ordered alkyl chains at DPPs- they are either arched or angled. Intuitively, I was expecting increased degree of order due to lower density and more space to fully extend the chains. The result was opposite: the system tried to equilibrate by increasing the density and reducing interlamellar spacing. As a result, alkyl chain scaffold was compressed leading to an increased disorder. Panel (**f**) illustrates structure (**a**) as viewed along the direction of polymer backbone. Comparison with Figure 7.15(**f**) demonstrates that the backbone of (l-C18)-DPP-(l-C8)-BTZ appears to more planar than (l-C18)-DPP-(b-C17)-BTZ. The average $\theta_{\mathrm{DPP-T}}$ is equal 10.2° which is an 0.1° increase with respect to branched derivative but with smaller variance. The question is whether one defines backbone planarity in terms of mean or variance, but I can certainly conclude that both systems are qualitatively more planar than most of the systems I am aware of except of IDT-BT. The powder diffraction pattern (**e**) of the lowest energy output (**a**) has two distinct peaks at 4.27 and 3.57 Å. Unlike previously, they are well defined and given a more planar backbone I am convinced that the 4.27 Å peak does not represent $\pi$-stacking distance meaning that stacking distances of (l-C18)-DPP-(l-C8)-BTZ and (l-C18)-DPP-(b-C17)-BTZ are 3.57 and 3.55 Å respectively. The maximum value of $\pi$-stacking as calculated for structures (**b**)- (**d**) was 3.9 Å for (l-C18)-DPP-(b-C17)-BTZ and 3.63 Å for (l-C18)-DPP-(l-C8)-BTZ. I find these results to be in a very good agreement with experimental 3.6 Å published by Gruber [18]. In summary, I conclude that crystalline structures predicted by molecular dynamics suggest that (l-C18)-DPP-(l-C8)-BTZ is likely to be more planar and closer stacked compared to (l-C18)-DPP-(b-C17)-BTZ.

Following optimization of crystal structure I decided to gradually increase the degree of disorder as was previously done for IDT-BT. Due to lack of computational resources I have only managed to investigate medium size systems- a single polymer strand was 12 monomers long and there were 8 strands per unit cell. The results that were obtained do not allow a meaningful statistical analysis, however they are perfectly valid qualitatively and simulations of large scale supercells are currently being performed by my collaborators at the University of Mons in Belgium. The aim was to investigate causation between disorder of alkyl chains and polymer backbone. Starting from the most stable structures, larger supercells were built with artificially increased interlamellar distance so that side-chains were no longer interdigitated. Structures were subject to a short fixed volume molecular dynamics simulation at high temperature, so that the side-chains became disordered, followed by a variable-cell equilibration of density and finally a longer evolution at room temperature as described in Methods section. The resultant output structures of (l-C18)-DPP-(b-C17) and (l-

C18)-DPP-(l-C8)-BTZ are shown in Figures 7.18 and 7.19 respectively. Qualitatively, both derivatives exhibit several similarities: alkyl chains are disordered both in and out of the polymer backbone plane, but the stacking of backbones is not affected. The average torsional angles appear to be relatively unchanged compared to crystalline phases with $\theta_{\mathrm{DPP-T}} = 10.5°$ and $\theta_{\mathrm{BTZ-T}} = 12.5°$. I find these results surprising- visually, there is a clear difference in planarity between crystalline and disordered phases as shown in panel (**b**). This is due to fact, that the maximum deviation from planarity raised up to 33° for BTZ-T bond, but at the same time the number of planar bonds was increased resulting in the same mean but different variance- again, it is a matter of definition of planarity. The view from the side (**c**) clearly demonstrates a mostly planar backbone with isolated deplanarized blocks. The simulation provides a crucial insight into mechanism of disorder accommodation. As one can see, both derivatives of DPP-BTZ accommodate disorder of akyl chains by making backbones wavy rather than twisted. In comparison to other systems, DPP-BTZ demonstrates a similar mechanism as the one I found to be dominant in IDT-BT even though backbones are less planar. It seems that DPP-BTZ is in a fact a less ideal counterpart of IDT-BT, which is not surprising given the similarities of torsional potentials present in both systems. In my opinion it is impossible to determine the exact degree of torsional disorder and make direct comparison with IDT-BT. The vacuum phase DFT simulation of Raman spectra predicts that change of peak intensities is meaningful for $\theta_{\mathrm{BTZ-T}} \geq 15°$meaning that the effect of planarization would not be observed experimentally if my molecular dynamics simulation of disordered phase is consistent with the actual thin film. Nevertheless, I certainly conclude that systems based on DPP-BTZ backbone are among some of the most planar, or at least torsion-resilient, systems that I am aware of.

Finally, I decided to simulate a low-density amorphous phase. Although GIWAXS patterns suggest that the empirical structures are more crystalline when compared with IDT-BT, I wanted to investigate what happens when the regular stacking order is no longer present. The methodology was similar as with disordered structures, however this time initial interlamellar distance was increased both in the direction of alkyl chains and perpendicular axis of $\pi-$ stacking, followed by the same process of thermal equilibration and long term evolution. The resultant output structures could not be visualized in a meaningful manner due to overall disorder therefore I extracted a single polymer strands without alkyl chains as shown in Figure 7.20. Selected backbones represent a single snapshot taken from a longer simulation and cannot be directly compared on the basis of their disorder however one can clearly see that bending

rather than twisting is the dominant mechanism of disorder. Both strands had similar average values of torsional angles: for (l-C18)-DPP-(l-C8)-BTZ I found $\theta_{\mathrm{DPP-T}} = 21.2\pm6.2^\circ$ and $\theta_{\mathrm{BTZ-T}} = 16.5\pm5.3^\circ$ whereas corresponding values for (l-C18)-DPP-(b-C17)-BTZ were $22.4\pm6.3^\circ$ and $21.6\pm5.7^\circ$ respectively. In my opinion both derivatives are qualitatively the same and type of side chains does not matter in case of amorphous structure. However, in order to verify the above statement quantitatively one would have to perform a simulation of a larger system and average torsional angles over time. Such a simulation is beyond my computational capabilities, but my collaborators from Mons University are already working on an in-depth statistical analysis of larger systems.

## 7.4 Summary

Experimental studies of crystalline structures and electronic properties of both derivatives suggest that polymers based on DPP-BTZ backbone are potential candidate for yet another system where structural order is not necessarily coupled with transport characteristics. DFT simulations of backbone torsional potentials suggest close similarities between IDT-BT and DPP-BTZ predicting a planar structure. The Raman spectra did not demonstrate any major pressure-dependent effects and some minor changes in intensities that were present could not be justified as a result of backbone planarization. Comparison with theoretical Raman spectra suggests that either the deviation from planarity is less than $15^\circ$ or the backbone torsion is completely resilient to external pressure. Furthermore, I performed a series of molecular dynamics simulations to determine crystalline, semi-crystalline and amorphous phases of both derivatives. Although different alkyl chains resulted in different packing and primitive vectors, I did not observe any significant differences between backbone confirmations in both derivatives that were studied. Theoretical diffraction patterns of crystalline phases suggest a stacking distance that is an agreement with experimental GIWAXS data. I have managed to find several crystalline structures yielding similar total energies, yet having very different relative orientations of building blocks. In my opinion this is due to symmetry of torsional potentials, their minima corresponding to planar configurations and linearity of BTZ unit. As a result, there are several structurally distinct microstates corresponding to a narrow range of energies. An introduction of disordered, non-interdigitated side chains in semi-crystalline phase did not result in stacking defects or significant change of backbone conformation. Although the spread of DPP-T and BTZ-T torsional angles increased, mean values remained unchanged

with respect to a crystalline interdigitated phase. To my knowledge the backbone of DPP-BTZ is one of the most disorder-resilient, regardless of alkyl chains used. Molecular dynamics simulation of a low density amorphous phase indicates that backbones accommodate structural disorder mostly by bending rather than twisting, which clearly resembles my previous studies of IDT-BT. I do not know whether pressure independent Raman spectra of IDT-BT and DPP-BTZ is a coincidence or a desirable common feature. It is rather difficult to draw a meaningful conclusion on structure-property relationship in DPP-BTZ, however if I were to make a recommendation regarding future molecular design I would emphasize the fact that in DPP-BTZ and IDT-BT the BT torsional potential not only has minima corresponding to a planar structure, but is symmetric as well. Together with linearity of BT unit it results in structures that can locally "switch" the orientation of a single unit without affecting long-range geometry. This hypothesis could explain what happens during formation of a thin film and why both IDT-BT and DPP-BTZ do not require annealing at high temperatures to achieve desirable transport characteristics. In a way one could argue that in both systems the backbone design is already promoting low energetic disorder and the limiting factor is the choice of side chains. If this hypothesis is true, it would be possible to quickly screen new systems by computing backbone torsional potentials before time consuming synthesis and experimental characterization takes place. The idea of high-throughput in silico screening has already led to a discovery of new, high mobility small molecules [31], but to my knowledge similar methods have never been applied to screen donor-acceptor conjugated polymers.

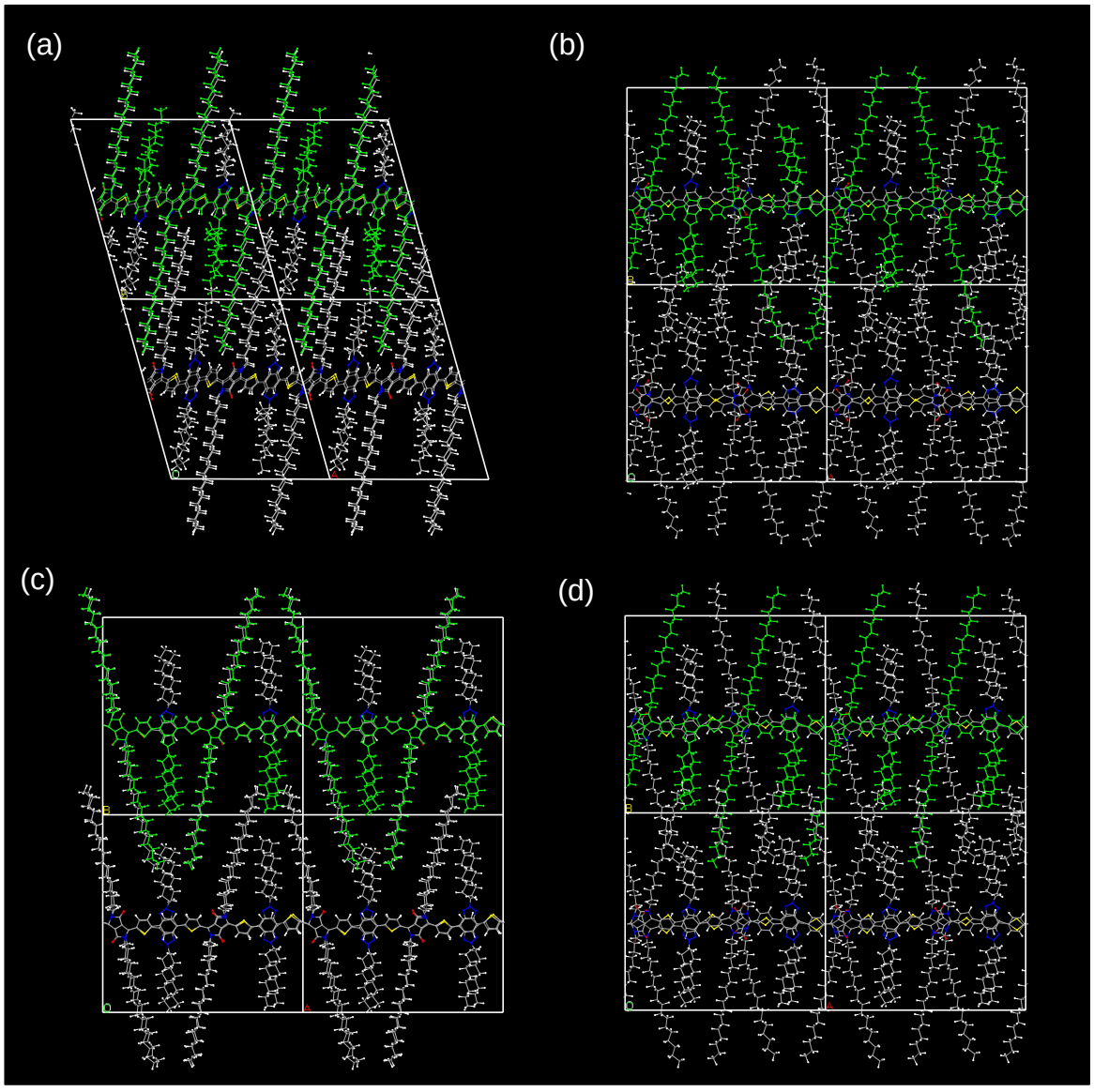


Figure 7.14: (**a**) to (**d**): four input structures of (l-C18)-DPP-(b-C17)-BTZ that converged into lowest energy outputs.

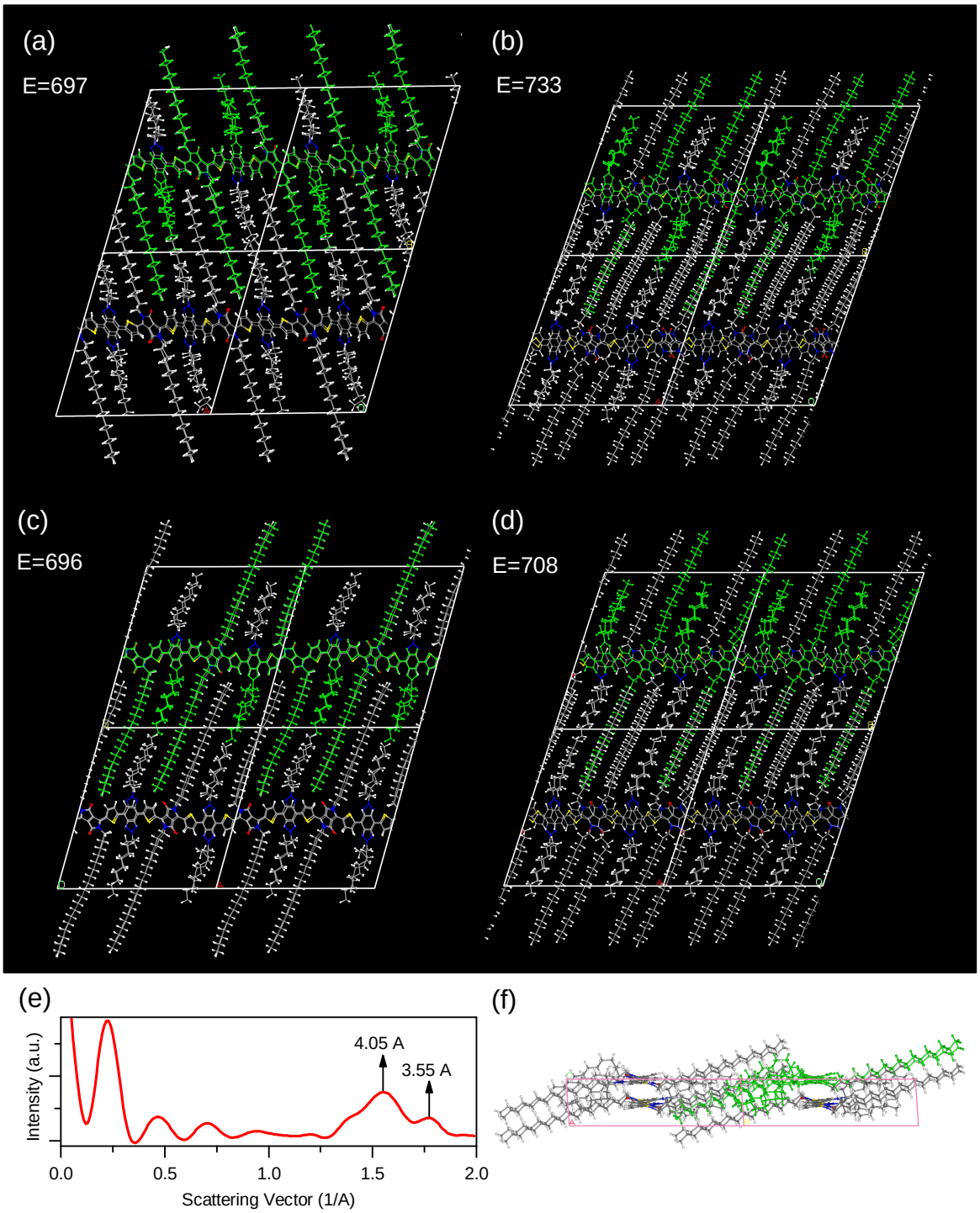


Figure 7.15: (**a**) to (**d**): four (l-C18)-DPP-(b-C17)-BTZ outputs yielding the lowest energy and their respective total energies in kcal/mole. The numbering directly corresponds to Figure 7.14. (**e**): theoretical powder diffraction pattern of the lowest energy structure. (**f**): the lowest energy structure as viewed along the backbone.

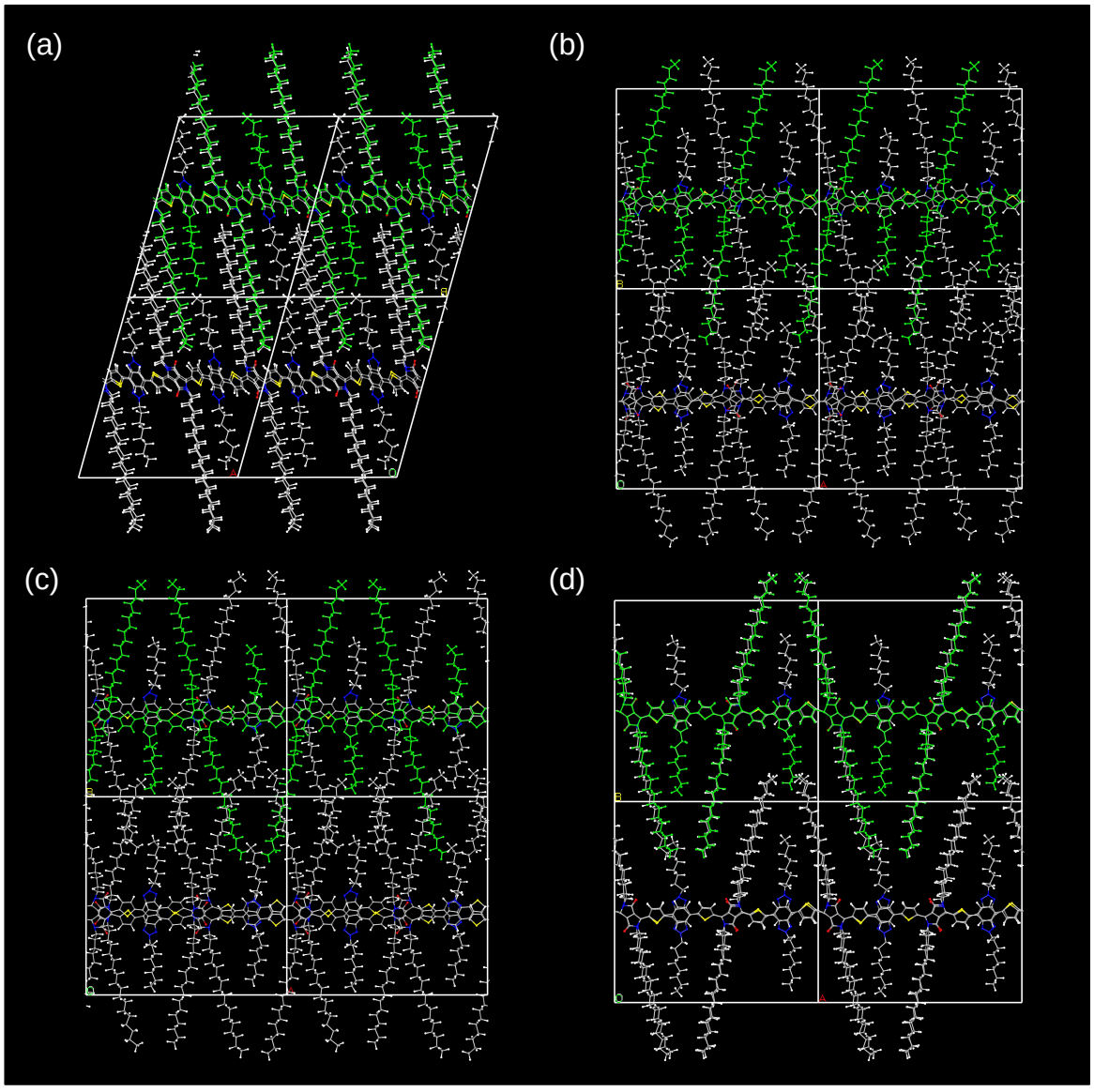


Figure 7.16: (**a**) to (**d**): four input structures of (l-C18)-DPP-(l-C8)-BTZ that converged into lowest energy outputs.

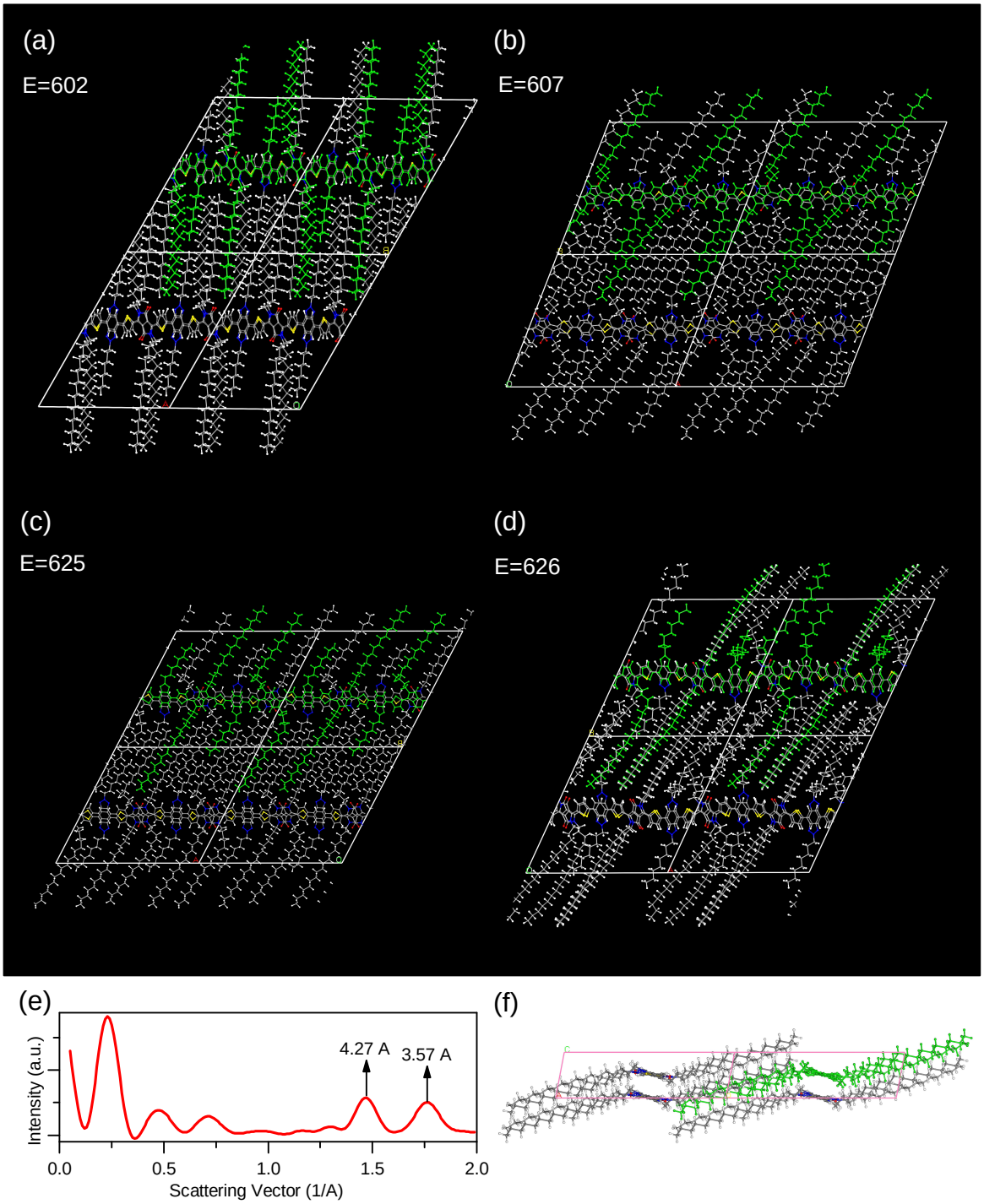


Figure 7.17: (**a**) to (**d**): four (l-C18)-DPP-(l-C8)-BTZ outputs yielding the lowest energy and their respective total energies in kcal/mole. (**e**): theoretical powder diffraction pattern of the lowest energy structure. (**f**): the lowest energy structure as viewed along the backbone.

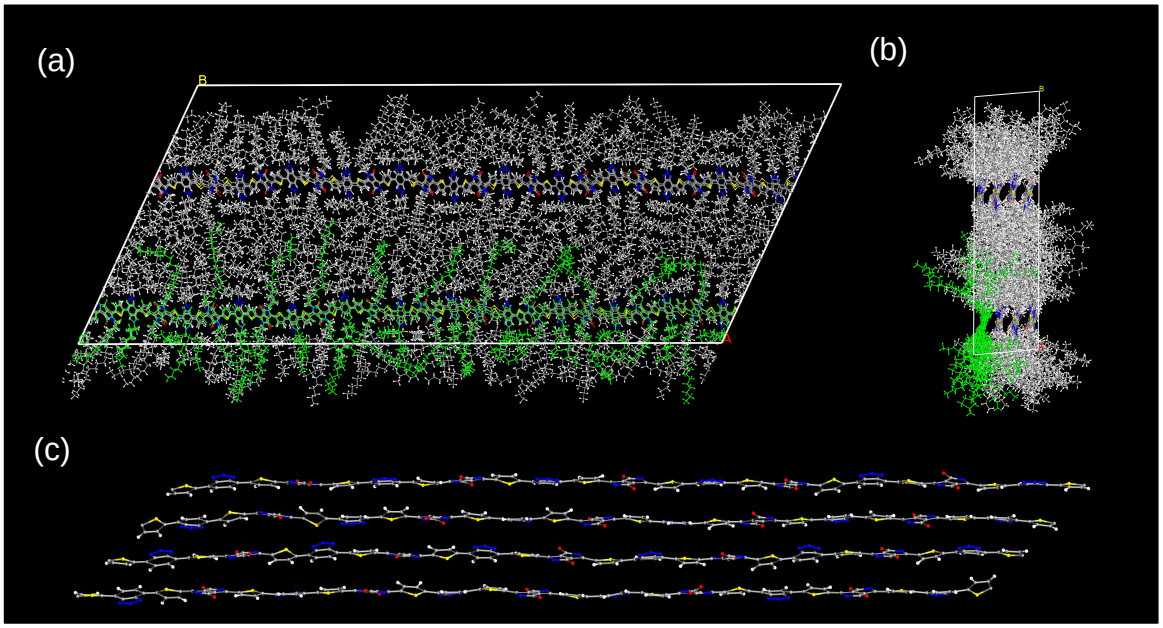


Figure 7.18: Disordered supercell (**a**) of (l-C18)-DPP-(b-C17) including view along the polymer backbone (**b**) and molecular packing of backbones (**c**) in the plane of alkyl chains.

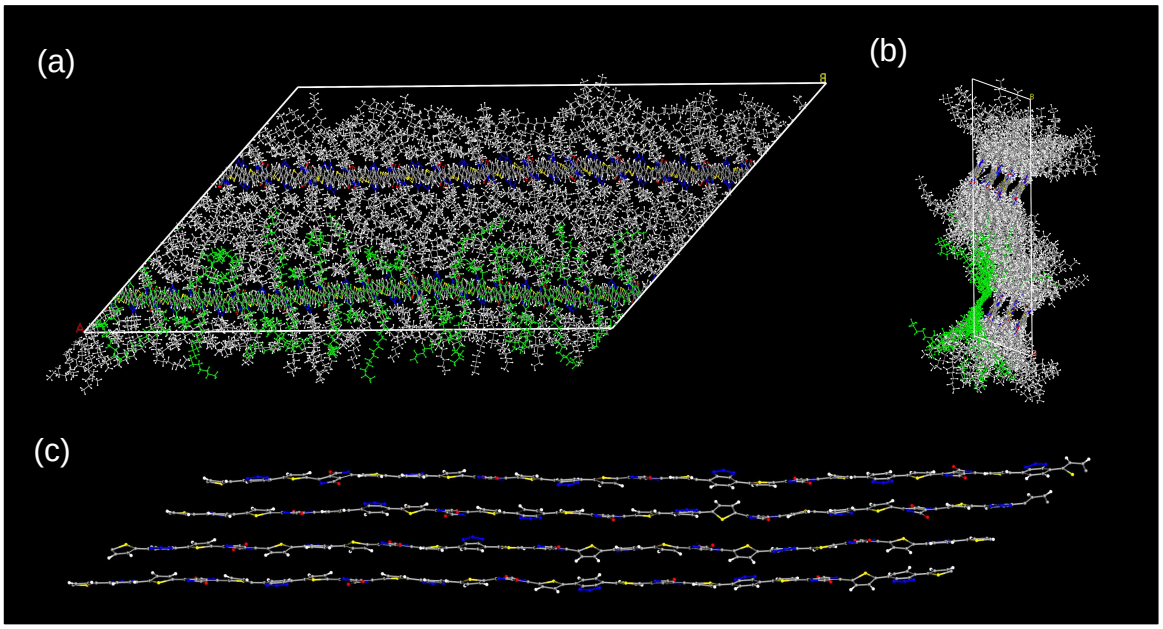


Figure 7.19: Disordered supercell (**a**) of (l-C18)-DPP-(l-C8)-BTZ including view along the polymer backbone (**b**) and molecular packing of backbones (**c**) in the plane of alkyl chains.

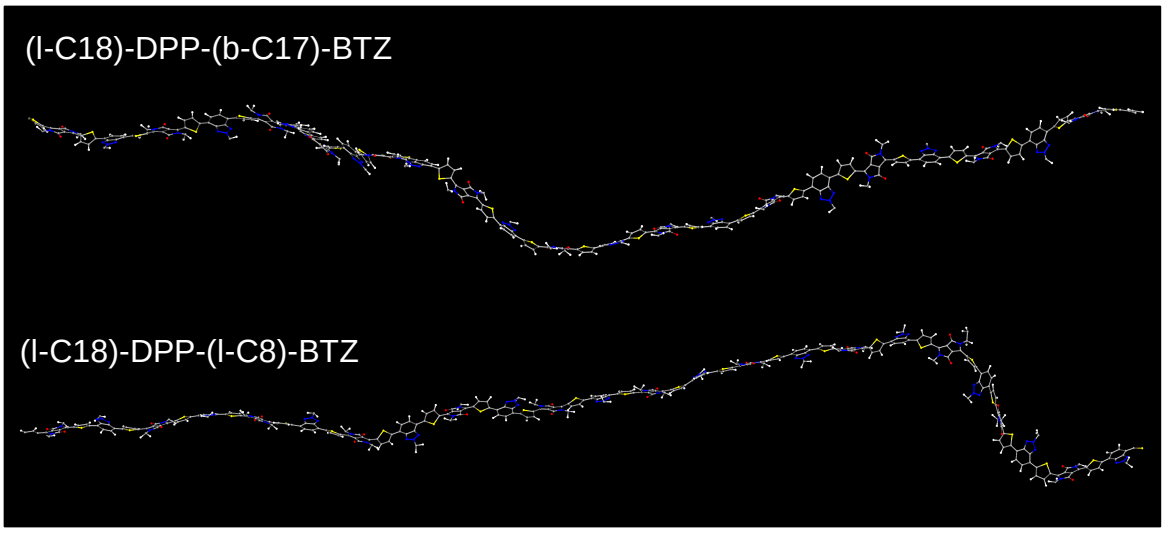


Figure 7.20: Selected polymer strands extracted from amorphous phase simulation. Alkyl chains were removed for clarity. Both systems exhibit bending and twisting of the polymer backbone. Strands were selected at random and do not represent statistical degree of disorder.

# Chapter 8

# NDI-T2

While majority of donor-acceptor polymers are hole-conducting, important progress has been made in the development of high performance, n-type systems in recent years [145]. In 2009 Facchetti and co-workers introduced NDI-T2 (also known under commercial name as Polyera N2200)- a novel n-type donor acceptor system which exhibits excellent electron transport properties with mobilities as high as 0.85 $cm^2V^{-1}s^{-1}$ in a top gate transistor. Caironi and co-workers [41] attributes the observed electron mobility to unusually uniform energetic landscape of sites for charge-carrier transport, which was studied using charge-modulation optical spectroscopy. The evidence supporting a low degree of energetic disorder in NDI-T2 has been further complemented by measurements reported by Kronemeijer et al. [146]. Kronemeijer used photothermal deflection spectroscopy (PDS) to determine the value of Urbach energy, which is correlated with amount of disorder in the material, and found that NDI-T2 has lower degree of disorder when compared to pBTTT and P3HT.

Initially it was assumed that NDI-T2 forms mainly amorphous layers [147], however later studies involving transmission electron microscopy revealed that the structure of the polymer is well ordered on the 10 nm scale [40] exhibiting a fibrular morphology [130] and retains a long range correlation up to one micrometer. Rivnay et al. were the first to show a remarkable degree of in-plane order in as-cast films with an unconventional face-on texture in the bulk. Later it was demonstrated that the morphology of NDI-T2 can be controlled by melt annealing process resulting in a significant change of crystalline order from face-on to edge-on correlated with an increase of overall degree of crystallinity and decrease of disorder [131]. Transport measurements performed on diodes demonstrate a significant drop in the electron-only current upon melt annealing at 300 °C, while little change was observed in case of thin film transistors suggesting that the phase transition is prevalent in the film interior leaving surface

structure mostly unaffected. Using mainly spectroscopic measurements, Steyrleuthner et al. [148] demonstrated that aggregation process, degree of crystallinity and chain orientation can be controlled by deposition conditions- use of chlorobenzene as a solvent, which strongly promotes aggregation in solution, results in mostly face-on orientation of spin coated thin film. Similarly, films spun from thalene:xylene blend exhibit dominant edge-on orientation and in both films the degree of crystallinity could be controlled by annealing temperature. The precise stacking of NDI and T2 units within the crystalline lattice was investigated using transmission electron microscopy (TEM) by Brinkmann et al. [149]. Brinkmann identified two distinct polymorphs: one with segregated stacking of diimide (NDI) and bithiophene (T2) units forming separate columns and another with shift between successive $\pi$-stacked chains leading to $\pi$-overlaps of NDI and T2, as shown in Figure 8.1**a**. Both forms were obtained by different means of epitaxial growth, however it was observed that segregated stack can be transformed into mixed stack by annealing at T $>$ 250 °C. Although mixed stack appears to be more thermodynamically stable, Steyrleuthner reports that both face-on and edge-on films were mainly consisting of chains with segregated packing (form I). Experimental studies of structure were complemented with DFT and molecular dynamics simulations performed by Lemaur and co-workers [40]. Structure minimizing the total energy in a gas phase predicts presence of two NDI-T dihedral minima at 45° and 121°. Surprisingly, aggregation does not lead to a significant planarization of the backbone- corresponding dihedrals in a bulk phase are predicted to be 41° and 135°, respectively. Given the torsion between NDI and T units as well as the perpendicular orientation of the alkyl chains with respect to NDI conjugated cores, as shown in Figure 8.1**b**, Lemaur predicts that donor fragments of adjacent chains must overlap leading to a microsegregation, which is consistent with form I stacking predicted by Brinkmann and experimental results reported by Steyrleuthner. In conclusion, NDI-T2 can exhibit different orientations with respect to substrate, degree of crystallinity and stacking motif depending on processing conditions and thermal treatments. Moreover, the structure that is expected to be thermodynamically favourable is not necessarily dominant in experimental thin films and the backbone conformation is likely to be far from planar configuration.

The reason I decided to investigate NDI-T2 using high pressure Raman technique is twofold. Firstly, NDI-T2 in an intermediate system between pBTTT and IDT-BT in terms of degree of crystallinity and energetic disorder, as was previously demonstrated by Venkateshvaran [26]. I find it somehow natural to complement my previous studies hoping to find some backbone features that exhibit steady trend and could be linked

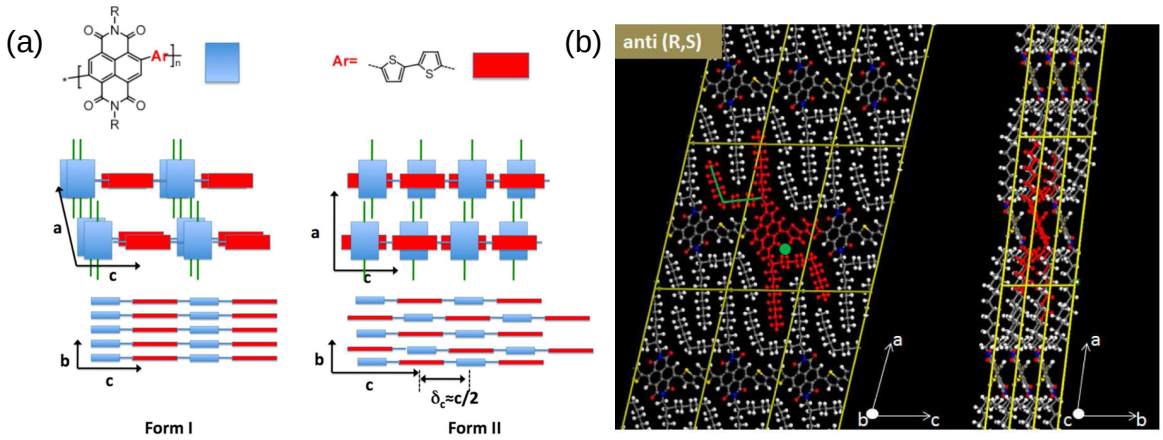


Figure 8.1: Two possible stacking motifs **(a)** identified by Brinkmann. In form I, NDI and T2 units form segregated columns, whereas in form II T2 units are in $\pi$-overlap one with other. Lemaur and co-workers predicted several possible crystalline structures and alkyl chain configurations **(b)** by means of molecular dynamics simulation. One of them, shown in panel is denoted as anti. Figures adapted from [40, 149].

with transport properties. Secondly, NDI-T2 is very well suited to study structure-property relationship, since it has two structurally distinct polymorphs that exhibit different electronic properties. The ability to reduce total number of factors to consider by fixing chemical structure offers an advantage over previous attempts, where general guidelines of molecular design were based on comparison of systems that were both chemically and structurally different. In my opinion the information about possible conformation and physics of NDI-T2 backbone is presumably one of few aspects of this system that have not been extensively investigated, yet several authors emphasize its potentially critical role in charge transport and energetic disorder. It is generally assumed [39–41] that the dihedral between NDI and T units is more out of plane than in pBTTT. Such geometry should clearly define mostly crystalline, ordered structure susceptible to stacking defects and structural disorder as in pBTTT. It is somehow counter intuitive given previous reports about energetic disorder and semi-crystalline structure, hence I decided to investigate vibrational modes hoping to draw meaningful conclusions about NDI-T2 backbone and its role in charge transport.

## 8.1 DFT simulations

I began by optimizing structure and calculating torsional potentials in gas phase, as shown in Figure 8.2. T-T torsional potential exhibits a minimum at 20° in anti-parallel (↓↑) configuration and two shallow minima at 155° and 180° in parallel (↑↑) configu-

ration. The energy landscape around local minima is relatively flat compared to $\sim 3.5$ kcal/mol energy barrier suggesting that there might be variation of T-T dihedral, however switching between parallel and anti-parallel configurations is rather impossible. NDI-T bond has two well defined local minima at 40° and 125° with energetic maxima at 10° and 180° making planar configuration very unlikely. Gas phase simulation of a trimer in lowest possible energy configuration shown in Figure 8.2**a** does not follow torsional potential in exact way: although NDI-T bonds are in agreement with shape of torsional potential, T-T bond became planarized. Planarization of T-T bond is governed by symmetry and steepness of NDI-T potential, since decrease of total energy due to T-T deplanarization to a local minimum would be smaller than corresponding energy gain at one of NDI-T bonds . This effect is clearly visible at the ends of polymer strand where free T units became deplanarized and adapted their global energetic minimum. In other words, it is the NDI-T torsional potential that defines conformation of the polymer backbone. In all subsequent simulations I assume that NDI units are coplanar and fixed within a matrix of alkyl chains as demonstrated by Lemaur [40], hence the only degree of freedom to consider is rotation of fixed, planar [-TT-] unit with respect to NDI. I also assume that T-T bond is at 0° anti-parallel configuration, since 180° parallel configuration does not fulfil linearity condition as shown in Figure 8.2**b**.

Figure 8.3 shows DFT Raman spectra calculated for $\theta_{\mathrm{NDI-T}} = 38°$, corresponding to previously optimised geometry and a more planar structure with $\theta_{\mathrm{NDI-T}} = 35°$. Theoretical spectra do not reproduce experimental intensities very well and exhibit non-linear dependence on torsional angle. Typically, change of dihedral by 3° does not result in such a pronounced change of intensities and for some reason vibrational modes around 1450 $\mathrm{cm}^{-1}$ are especially susceptible to even small variation of the torsional angle. I am convinced that the observed effect is an actual property of NDIT2 rather than artifact or methodological error- a similar effect has been reported [76] for simulated UV-vis spectra where planarization of polymer backbone resulted in redshift of up 80 nm. I also performed additional tests to choose proper input geometries. In principle there are two methods to study relation between torsional angle and Raman spectra- one can either keep the geometry fixed and vary only single bond or relax and re-optimise whole structure for every subsequent change of dihedral. Second method is called redundant coordinates and is implemented in Gaussian. Typically no differences in mode intensities were present regardless of simulation method and non-redundant coordinates were used because of lower computational cost. It is also reasonable to assume that in the bulk phase other bonds are constrained due to presence of side

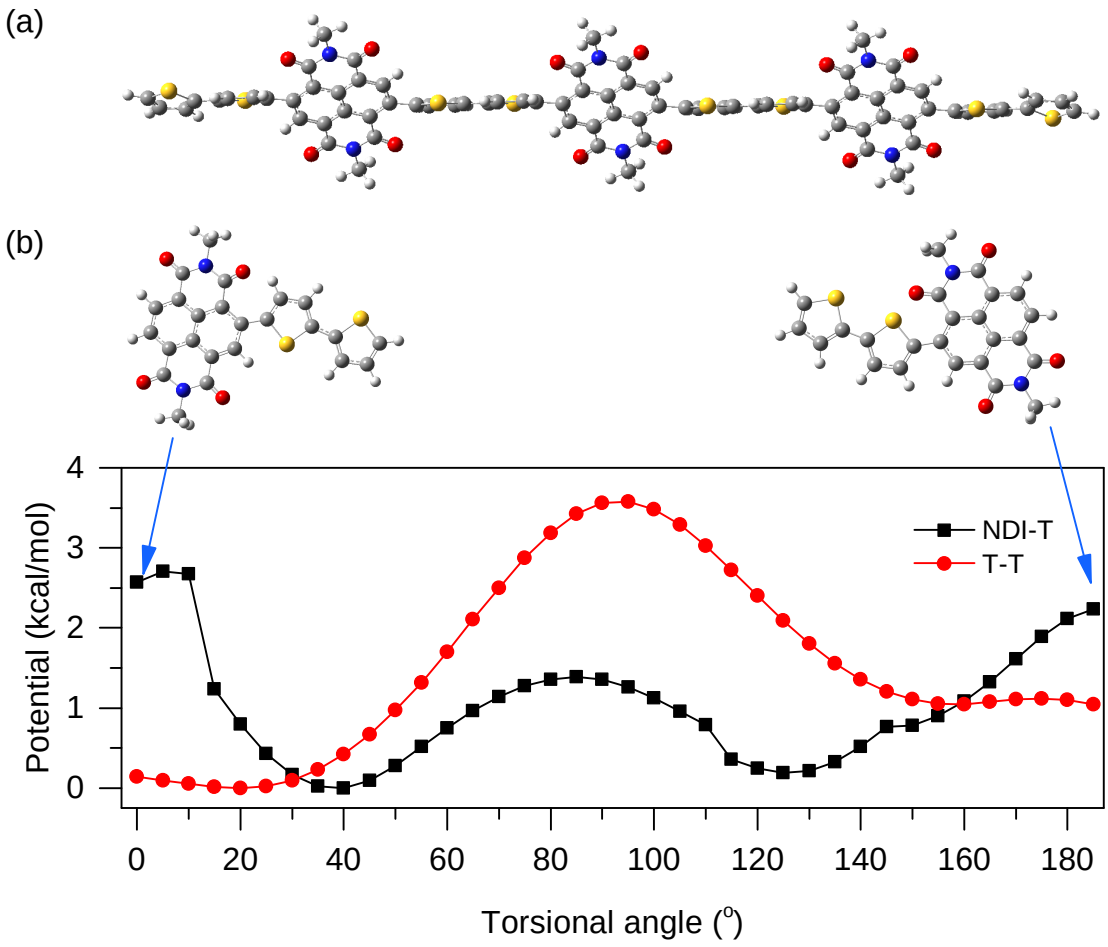


Figure 8.2: (**a**): A vacuum phase optimised geometry. In the lowest energy state $\theta_{NDI-T} = 38°$ and $\theta_{T-T} = 0°$. (**b**): torsional potentials as calculated for a single monomer (**bottom**) and bond orientations (**top**) corresponding to 0° and 180°.

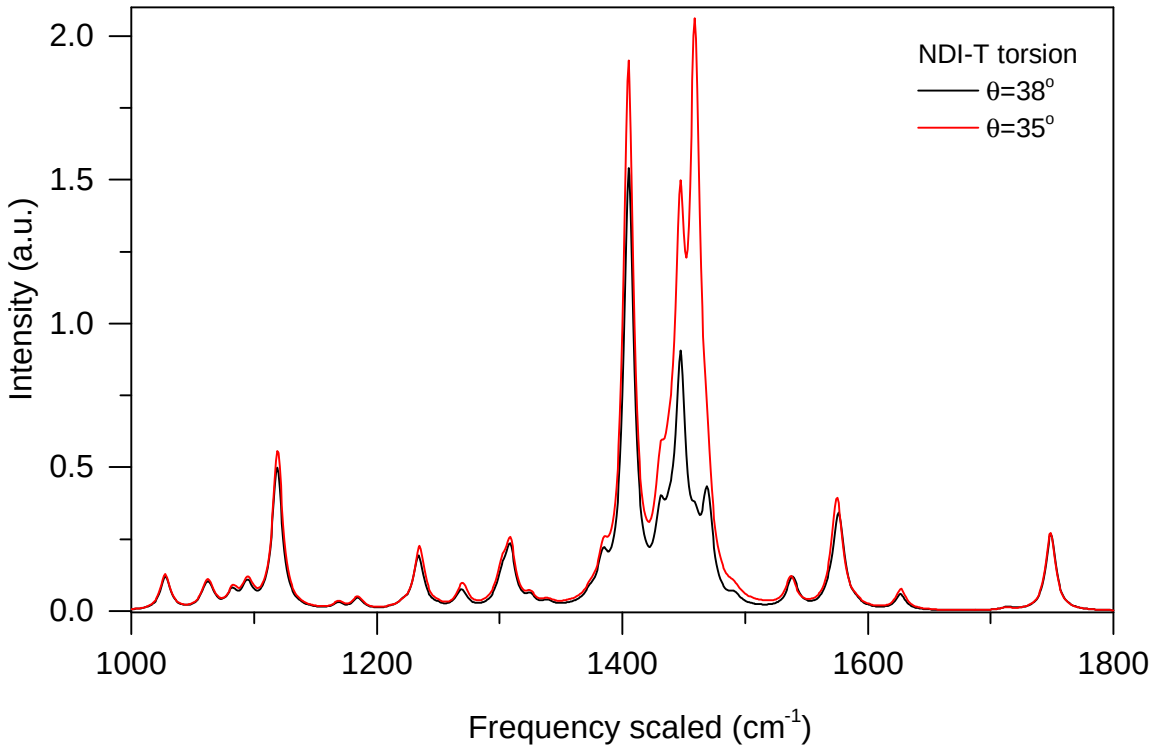


Figure 8.3: The DFT Raman spectra are highly susceptible to deviation from equilibrium at $\theta = 38°$(**black**). Planarization by just 3° (**red**) results in a significant change of intensities for a whole group of modes around 1450 $cm^{-1}$.

chains and hence relaxation of the whole structure in a gas phase would not necessarily represent a correct approach- in fact steric interactions often dominate and determine structural properties of the backbone in a crystalline phase. However, comparison of spectra simulated using redundant and non-redundant coordinates indicate that for some modes around 1450 $cm^{-1}$ there is almost order of magnitude difference in intensities, as shown in Figure 8.4. As previously, this effect is not present in other regions of the spectrum. I do not know what the fundamental cause of observed differences is, therefore I decided to use redundant coordinates as they provide the best reproduction of experimental spectra. Figure 8.5 shows unnormalized spectra calculated for $\theta_{\mathrm{NDI-T}}$ dihedral set to 20°, 10° and 0°. Within range of frequencies typically accessible by Raman spectrometer I identified three vibrational modes at 1430 $cm^{-1}$, 1436 $cm^{-1}$ and 1446 $cm^{-1}$ that exhibit a steady dependence on torsional angle and hence $I_{1430}/I_{1446}$ intensity ratio could act as an indicator of backbone planarization during high pressure experiment. In theory 1405 $cm^{-1}$ peak could be used as well, since it is the most intense peak in a minimum energy configuration and completely disappears up planarization, however the peak is very close to much stronger diamond

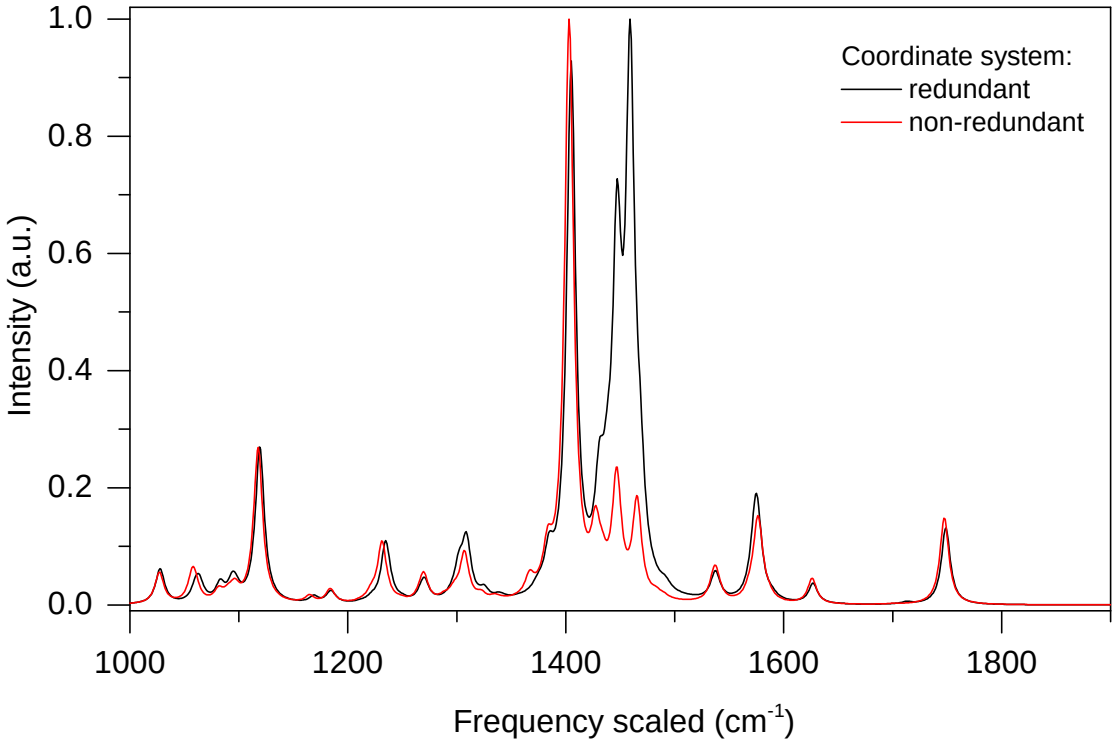


Figure 8.4: The theoretical spectra are sensitive to choice of coordinate system. In redundant coordinates the geometry is reoptimised at a fixed torsional angle. In non-redundant mode one varies the torsional angle keeping other degrees of freedom fixed. Both data sets were generated at $\theta_{\mathrm{NDI-T}} = 35°$ starting from the same, vacuum optimised structure.

line present in high pressure data. Interestingly, comparison of intensities of theoretical and experimental spectra collected under ambient pressure suggest that the system is already far from gas phase equilibrium, however it is unknown what is the error of intensity calculation with 6-31G(d,p) basis set.

## 8.2 High pressure Raman

In order to collect experimental pressure dependent Raman spectra I decided to follow methodology described by Steyrleuthner [148] to prepare thin films with face-on and edge-on orientation. It is expected that films spun from dichlorobenzene are dominantly face-on, whereas use of xylene blend results in mostly edge-on orientation. Figure 8.6 shows Raman spectra of film spun from dichlorobenzene as a function of hydrostatic pressure. The photoluminescence background was subtracted from the original data. I identified thee major peaks in 1400-1500 $\mathrm{cm}^{-1}$ range that exhibit

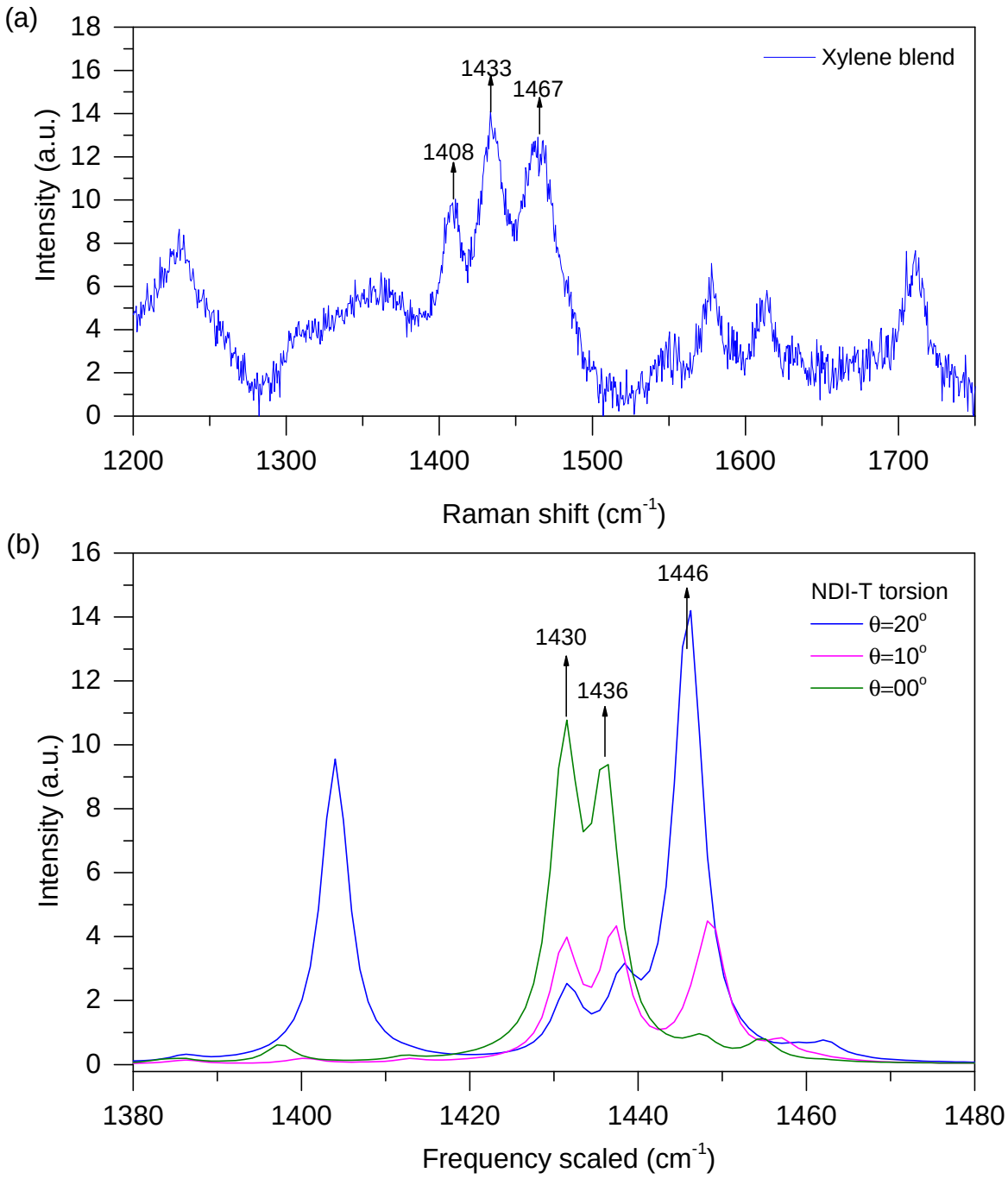


Figure 8.5: Ambient pressure Raman spectra **(a)** of a film spun from xylene blend with subtracted PL background. DFT Raman spectra **(b)** calculated as a function of $\theta_{\mathrm{NDI-T}}$. There are three major, torsion-dependent peaks in the region typically accessible by experimental Raman. Simulation predicts clear angular dependence suggesting that the ratio of 1430 $\mathrm{cm}^{-1}$ and 1446 $\mathrm{cm}^{-1}$ peak intensities could be an indicator of backbone torsion. The frequencies of vibrational modes were rescaled by empirical B3LYP coefficient[48] to match experimental data. Experimental spectra were acquired using 632 nm laser line.

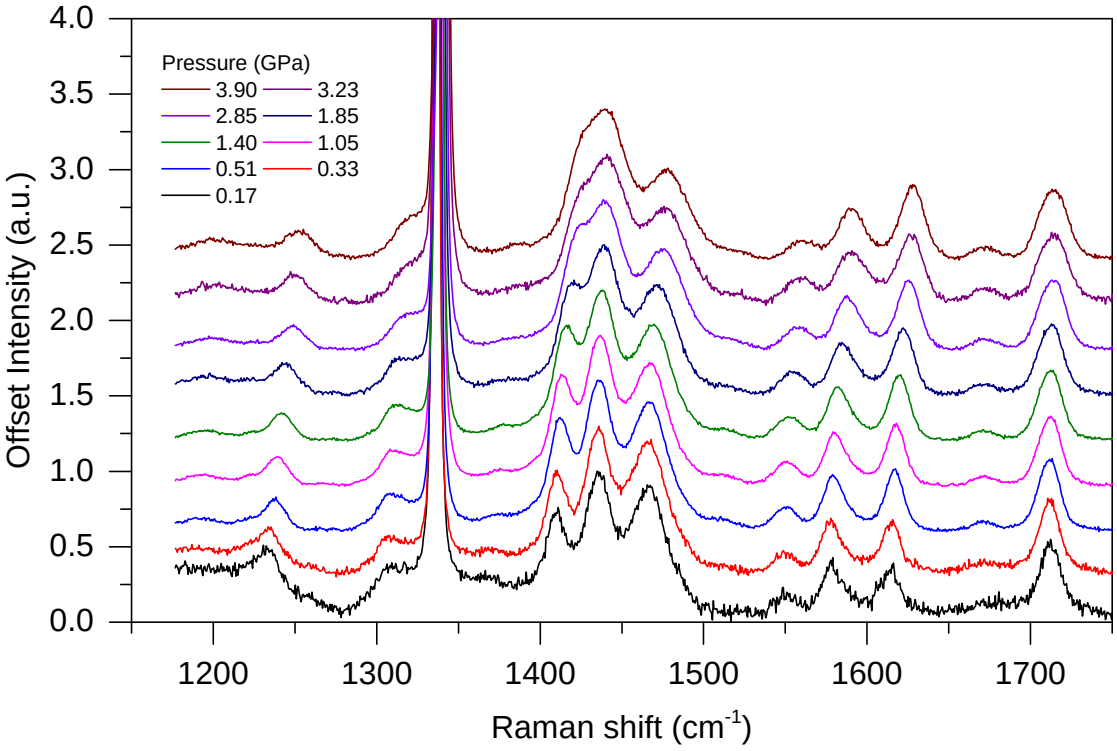


Figure 8.6: Pressure-dependent Raman spectra collected from a sample spun from dichlorobenzene solution. The peak at 1350 $cm^{-1}$ represents diamond line. The signal-to-noise ratio improves as the pressure increases. Spectra were acquired using 632 nm laser line.

pressure dependence other than standard shift in frequency and half-width broadening. In my opinion experimental peak at 1715 $cm^{-1}$ could be assigned to theoretical peak at 1750 $cm^{-1}$ shown in Figure 8.4 and therefore three pressure dependent peaks correspond to theoretical peaks at 1430 $cm^{-1}$, 1436 $cm^{-1}$ and 1446 $cm^{-1}$ as marked on Figure 8.5. Based on DFT simulation I identify 1408 $cm^{-1}$ and 1467 $cm^{-1}$ peaks as collective C=C and C-C bond modes corresponding to successive stretching and compression of six-membered rings of naphthalene-bis(dicarboximide) unit, as shown in Figure 8.12, whereas 1433 $cm^{-1}$ peak results from number of simultaneous, smaller amplitude C=C and C-C bond modes that are distributed over the whole monomer.

The experiment was repeated using sample spun from xylene blend as shown in Figure 8.7. There are no major differences in spectra except of intensity of 1470 $cm^{-1}$ peak, which exhibits even more pronounced pressure dependence compared to sample spun from dichlorobenzene. The design of pressure cell does not allow for a precise control of pressure, however I was lucky to collect two data sets for both films at approximately 3.9 GPa, which enabled a direct comparison of peak intensities.

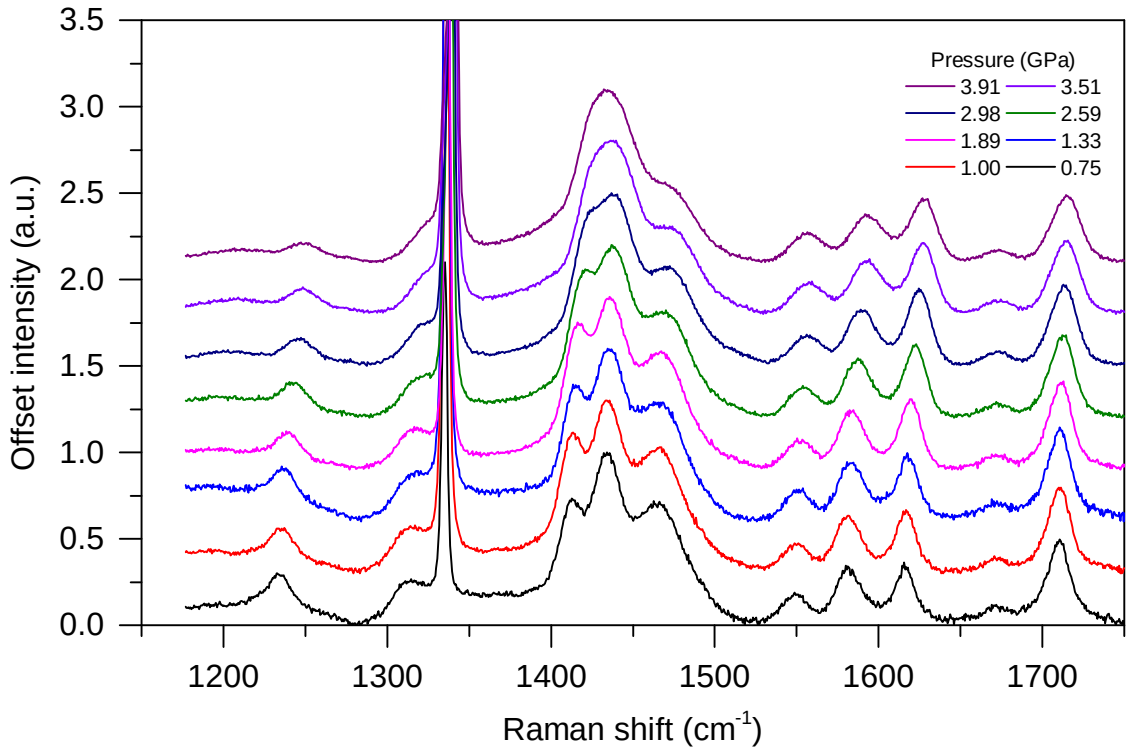


Figure 8.7: Pressure-dependent Raman spectra collected from a sample spun from xylene solution. The peak at 1350 $cm^{-1}$ represents diamond line. The signal-to-noise ratio improves as the pressure increases. Spectra were acquired using 632 nm laser line.

Analysis of mode frequencies and peak widths for films spun from xylene blend and dichlorobenzene is shown in Figures 8.9 and 8.10, respectively. As one can see, in both films all fitted peaks demonstrate shift towards higher frequencies indicating increase of effective force constants. Frequency shifts at 3.9 GPa are consistent in both films and moderate in terms of amplitude. For example, 1408 $cm^{-1}$ peak shifts up to 1425 $cm^{-1}$ in both films. Similarly, 1433 $cm^{-1}$ peak shifts to 1441 $cm^{-1}$ whereas 1467 $cm^{-1}$ to 1478 $cm^{-1}$ if dichlorobenzene is used as a solvent. In case of film spun from xylene the same peaks shift to 1440 $cm^{-1}$ and 1475 $cm^{-1}$, respectively. As one can, both films demonstrate similar frequency shifts and their magnitude is typical for a given range of pressures. However, there is clear difference in spectra collected from both films if one analyses broadening of peaks. Inspection of FWHM values as a function of pressure reveals that in film spun from dichlorobenzene distribution of molecular conformations is almost independent of pressure, whereas in case of film spun from xylene molecular order is pressure-dependent. By comparing the same mode in both films one can see that in xylene peaks are generally wider indicating broader distribution of molecular

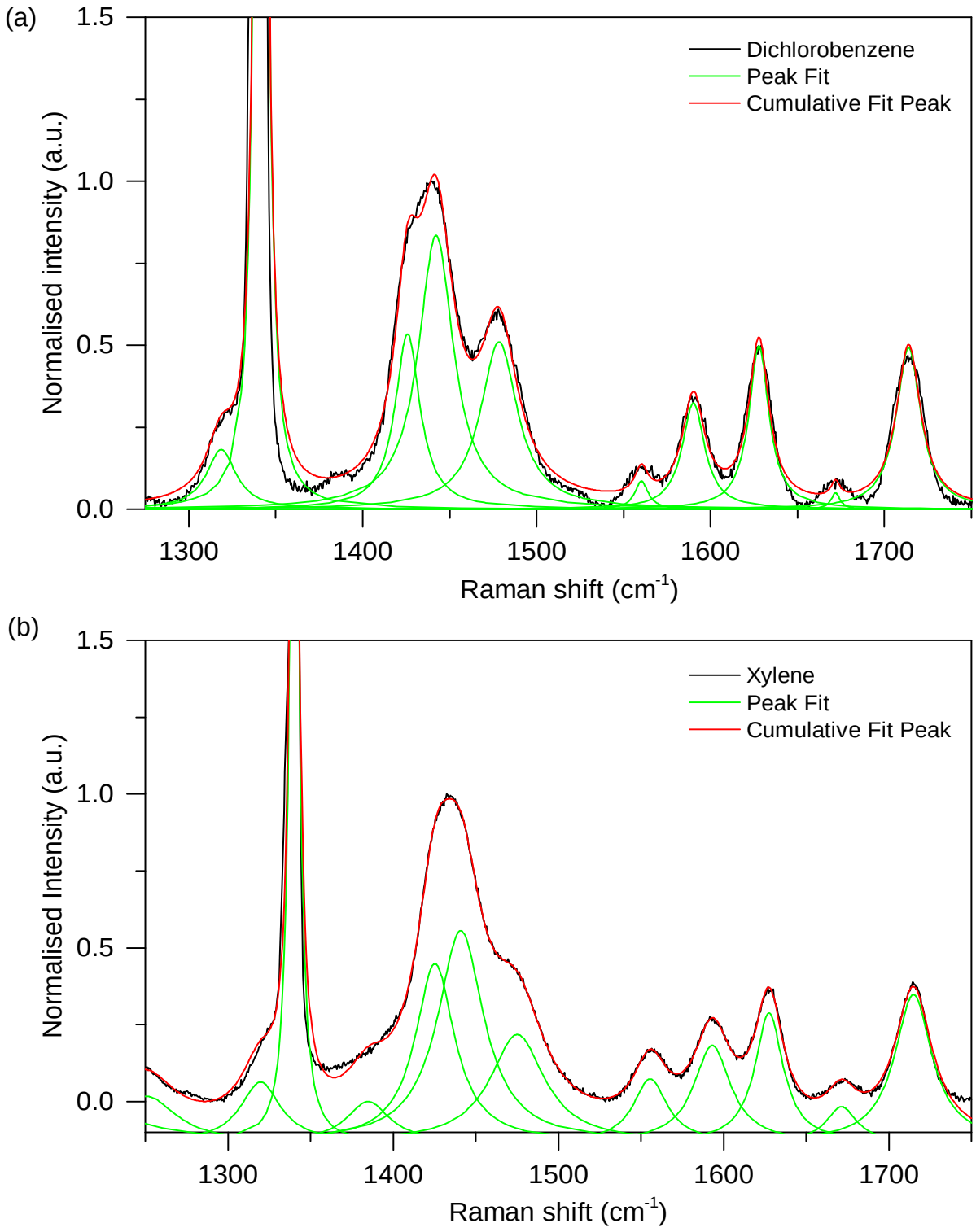


Figure 8.8: Comparison of experimental spectra and Lorentzian fits at 3.9 GPa corresponding to samples spun from dichlorobenzene (**a**) and xylene (**b**) solutions. Green lines represent individual Lorentzian peaks, whereas red line is a cumulative fit. Spectra were acquired using 623 nm laser line.

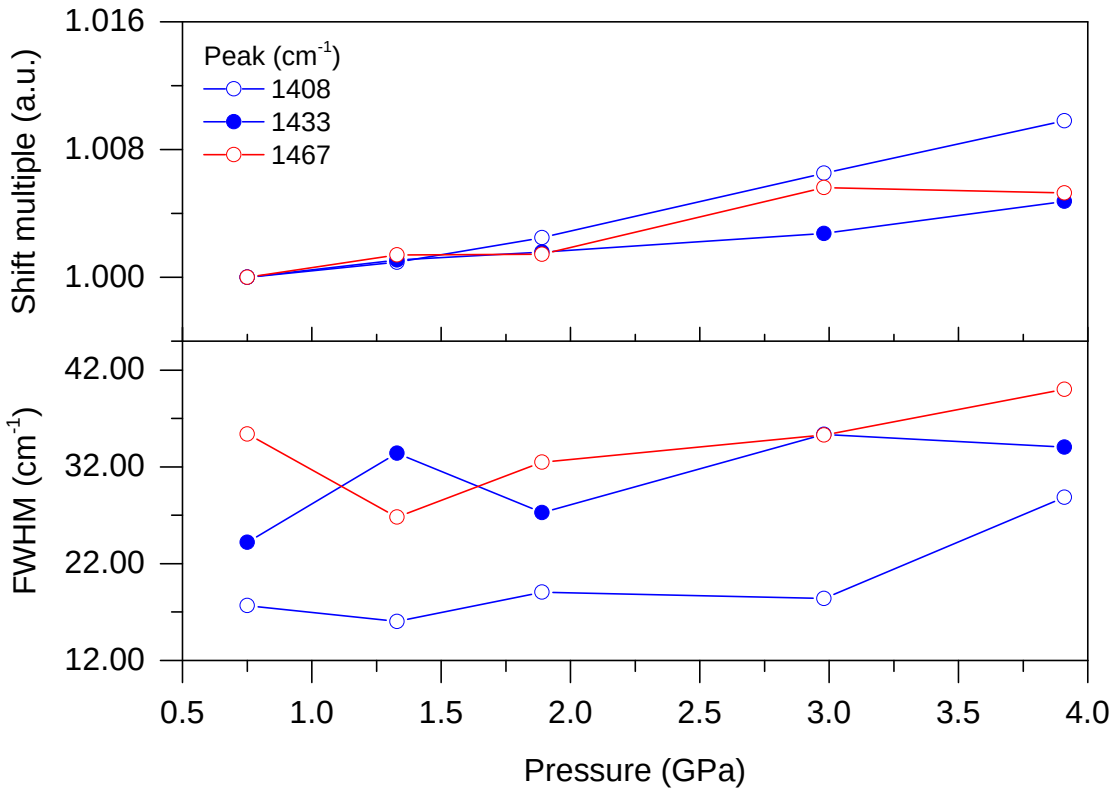


Figure 8.9: Raman spectra collected from thin film prepared using xylene blend exhibit scaling of 1408 $cm^{-1}$, 1433 $cm^{-1}$ and 1606 $cm^{-1}$ peak frequencies (**top**) and their width (**bottom**) as a function of applied pressure.

conformations. In summary, data suggests that in films prepared using xylene the backbone is less ordered and more prone to changes of conformation.

Figure 8.8 shows comparison of experimental spectra and data fitted using Lorentzian model for both films. The modes that I find most meaningful are at 1408 $cm^{-1}$ and 1467 $cm^{-1}$, since the ratios of their intensities are different depending on solvent used. As mentioned in previous section, the ratio of 1408 $cm^{-1}$ and 1467 $cm^{-1}$ intensities can be used as an indicator of backbone planarity suggesting that xylene blend results in a more planar backbone at high pressures when compared to dichlorobenzene. Figure 8.11 shows intensity ratios as a function of applied pressure. Both films exhibit pressure dependence, although it is not as pronounced as in F8BT or pBTTT, and the ratios have similar values up to 1.5 GPa suggesting that the backbone conformation is likely to be the same in as-spun films. However, above 3 GPa the ratio of peak intensities in film spun from xylene blend exhibit bold increase and deviates from sample prepared using dichlorobenzene. The higher $I_{1408}/I_{1467}$ ratio clearly suggests planarization of polymer backbone. To better illustrate this effect I performed

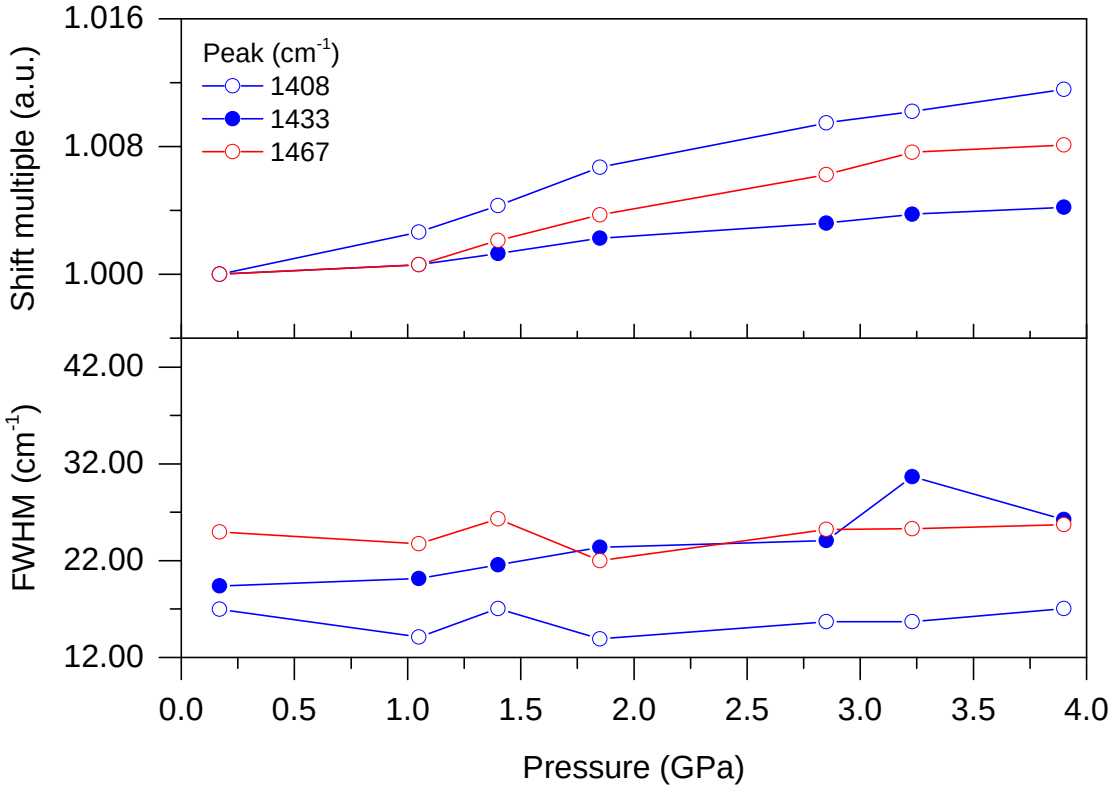


Figure 8.10: Raman spectra collected from thin film prepared using dichlorobenzene exhibit scaling of 1408 $cm^{-1}$, 1433 $cm^{-1}$ and 1606 $cm^{-1}$ peak frequencies (**top**) and their width (**bottom**) as a function of applied pressure.

a higher resolution DFT simulation with dihedral step equal 2.5° as shown in Figure 8.12. The comparison with theoretical spectra suggests that both films were clearly planarized and that backbone of edge-on film is less stiff. This might be somehow surprising given the fact the torsional potential was the same in both cases, however one has to remember that stiffness of a backbone is not limited to intrinsic torsional potentials. In fact, the backbone conformation is defined by competition of forces arising from torsional potentials along the backbone and steric interaction of alkyl chains, which is often dominant factor in well-ordered structures, and face-on film orientation may lead to different side chain packing motif than edge-on orientation. It is also important to remember that one cannot directly compare theoretical and experimental intensity ratios. I am convinced that the trend suggesting backbone planarization is qualitatively correct, however quantitative error of chosen computational method suggests that theoretical spectra at $\theta$ equal 7.5° and 10° do not necessary represent actual conformations at 3.9 GPa.

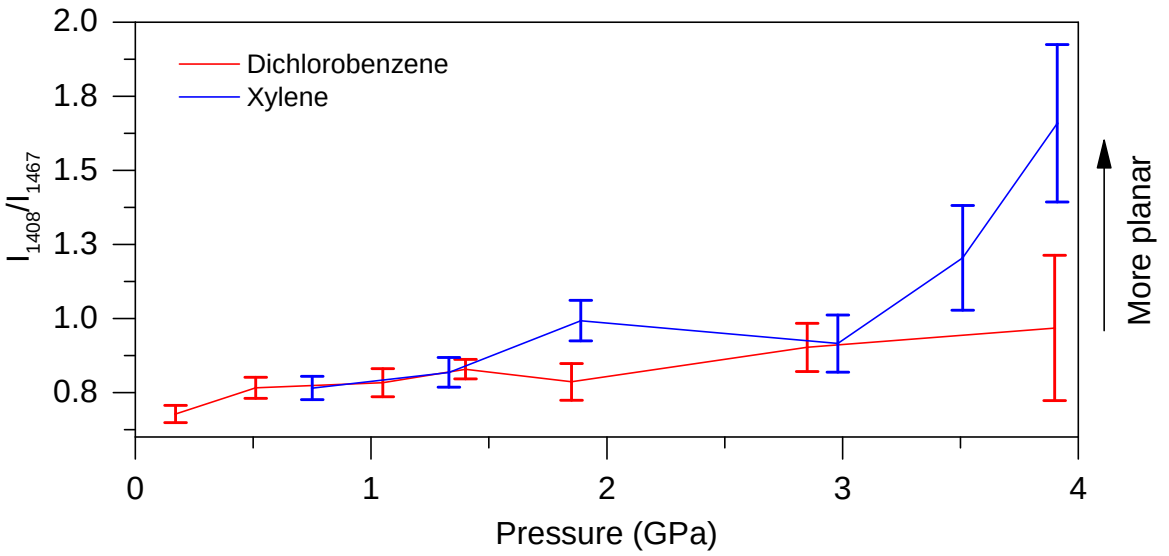


Figure 8.11: Experimental ratio of 1408 $cm^{-1}$ and 1467 $cm^{-1}$ peak intensities as calculated samples prepared using xylene (**blue**) and dichlorobenzene (**red**) solutions. The ratios are pressure dependent with consistent values up to 1.5 GPa and diverge above 3 GPa.

## 8.3 Summary

NDI-T2 is a system particularly well suited for studies of structure-property relationships, since it is possible to control film polymorphism. I demonstrated that the structural and mechanical properties of polymer backbone depend on type of solvent used during film deposition. Both films exhibit planarization and dependence of vibrational modes on external pressure, however backbone of film spun from xylene blend is much more prone to change of torsion. In this particular system there is clear causation between backbone rigidity and transport properties, since films prepared using dichlorobenzene were demonstrated to yield higher charge mobilities compared to xylene regardless of annealing temperature used [148]. My findings are consistent with theoretical study published by Olivier and co-workers [39], where transport properties of NDI-T2 were attributed to backbone stiffness arising from structural microsegregation, size and aspect ratio of donor and acceptor units that lock the non-planar polymer chains in a quasi-frozen conformation.

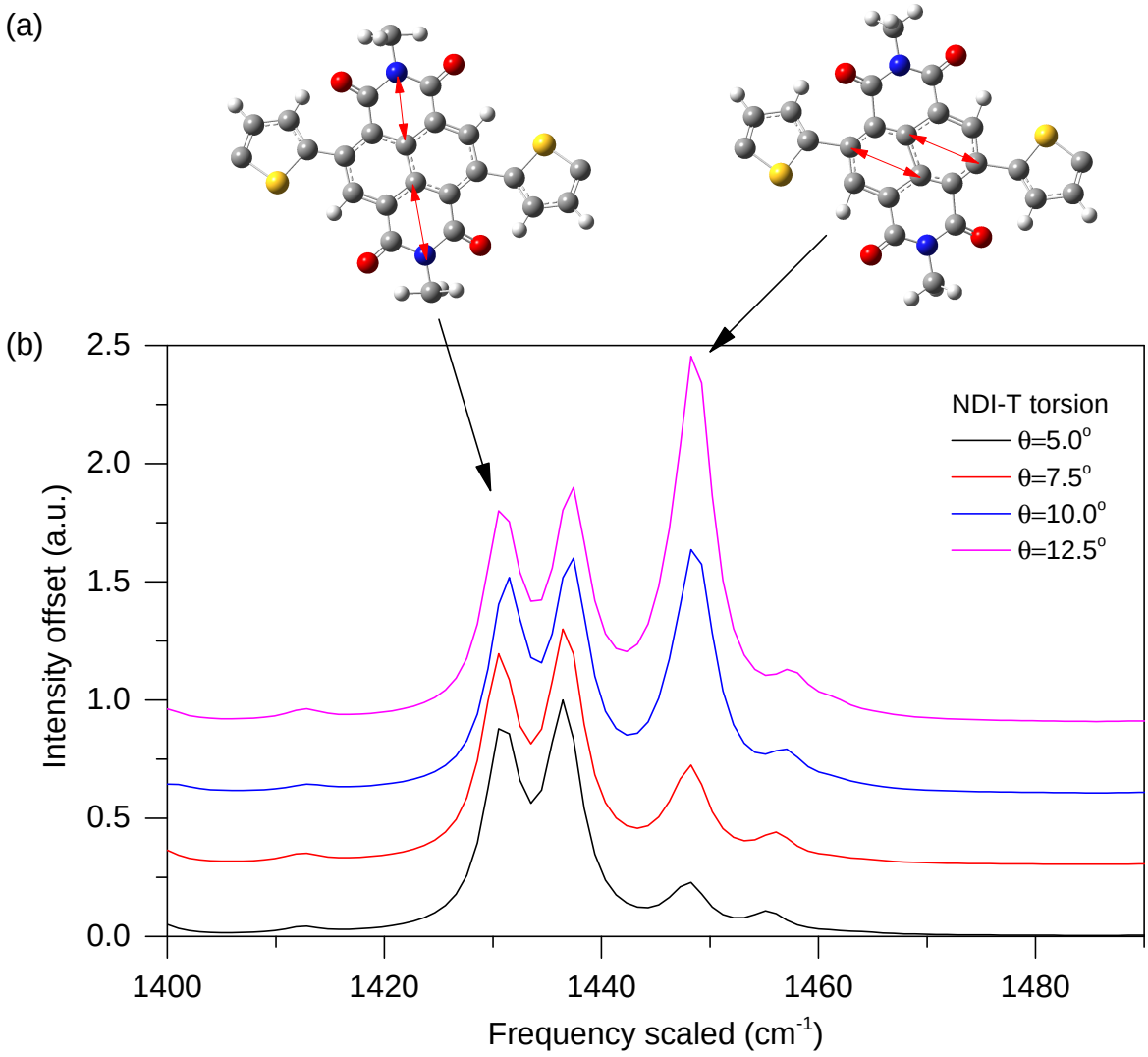


Figure 8.12: Visualization (**a**) of vibrational modes corresponding to oscillation of nitrogen atoms along direction of alkyl chains (1430 $cm^{-1}$) and stretching of naphthalene rings (1446 $cm^{-1}$). A fine-tuned DFT simulation (**b**) of planarization process. The range of angles was chosen to match experimental spectra.

# Chapter 9

# Conclusions and outlook

In this chapter I summarize my studies of lattice dynamics in organic semiconductors and their correlation with charge transport. I investigated two classes of materials- small molecules forming dispersion bonded molecular crystals and conjugated polymers with varying degree of crystallinity and energetic disorder. In case of small molecules I focused on calculating intermolecular vibrations using CASTEP and CRYSTAL09 softwares. These modes, although critical to modulation of transfer integrals and charge transport, are relatively poorly understood- they are difficult to probe experimentally and the only way to calculate their dynamics using ab initio methods is to use computationally expensive periodic boundary conditions. From practical point of view one has to use supercomputing facility to perform DFT simulation on systems as large as small molecules and to my knowledge this has never been published before. In second part of the thesis I investigated backbone conformations of several conjugated polymers by combining high pressure Raman spectroscopy with vacuum phase DFT simulations of intramolecular modes. I was particularly concerned with IDT-BT and DPP-BTZ- two recently synthesized donor-accepor systems that are known to exhibit low degree of energetic disorder. High pressure measurements of their Raman spectra corresponding to backbone vibrational modes suggest planar conformation- an effect that has never been reported for semiconducting polymer. Finally, I report molecular dynamics simulations indicating nearly torsion-free backbone that is resilient to disorder induced by side chains and suggest new rules of rational design.

## 9.1 Small molecules

Recent developments in computational methods of dispersion correction and reports of successful phonon calculations in simple molecular crystals motivated me to perform

simulations of vibrational dynamics in C8-BTBT and dif-TES-ADT. It was somehow disappointing that my ambitions were restrained by bug in CRYSTAL09 code and fact that release of subsequent version of the code was delayed beyond time frame of my computational grant. Nevertheless, I managed to perform successful geometry optimization of C8-BTBT crystal structure and calculate frequencies of modes present in dif-TES-ADT. Predicted mode frequencies suggest that calculation was accurate, when evaluated in terms of industry standards, and previously described methodology can potentially be upscaled to study crystalline small molecules. I decided to repeat mode calculations using plane wave basis set implemented in CASTEP code as an alternative to CRYSTAL09. Plane wave formalism is known to be less well suited for simulations of molecular crystals possessing low degree of symmetry. TS dispersion correction proved to be less efficient than Grimme method and calculation of mode frequencies resulted in several imaginary frequencies. Quality of the simulation was mediocre when judged by the number of imaginary frequencies, however calculated spectra are in surprisingly good agreement with experimental.

In general, calculations proved to be more expensive than initially anticipated and current computing infrastructure is not efficient enough to study systems as large as C8-BTBT on a routine basis- my simulations were performed using latest national supercomputing facility and required substantial research grant. Methodology described in this thesis is not suitable for rational design and screening of novel compounds, but can be selectively applied to provide justification of TEM data. However, general outlook about DTF simulations of intermolecular modes remains optimistic- all of my output files can be used as inputs to restart simulations using updated versions of the software and I believe that improvement of computational efficiency is just a matter of time.

## 9.2 High Pressure Raman

Custom-made diamond anvil cell proved to be versatile tool to study effects of hydrostatic pressure on backbone vibrational modes. In total, I investigated six systems with different degrees of crystallinity, backbone planarity and resilience to side chain disorder. I used pBTTT as a model system to evaluate cell design and DFT techniques. Comparison of theoretical and experimental spectra revealed a complex mechanism of simultaneous T-T bond planarization and T-TT bond deplanarization. Studies of two recently published, high performance systems with low degree energetic disorder (IDT-BT and DPP-BTZ) indicate presence of planar or nearly planar backbones and

suggest correlation between lack of pressure dependence and electronic performance. Moreover, pressure-dependent spectra of two NDI-T2 polymorphs demonstrate that processing conditions influence torsional resilience of the backbone and the difference can be substantial enough to be detected experimentally. In case of NDI-T2, plymorph that exhibits higher charge mobilities has a backbone that is more resilient to external pressure, which clearly supports previous reports and observation that backbone stiffness facilitates charge transport.

I am convinced that there are two main mechanisms that prevent torsional disorder along the backbone: steric interactions between the side chains that extrinsically fix conformation of the backbone, as in NDI-T2, or intrinsic torsional potentials as in IDT-BT and DPP-BTZ. Side chain scaffold and steric interactions are difficult to predict in advance, since they are modelled using molecular dynamics and require prior experimental data. However, DFT vacuum-phase calculation of backbone's torsional potentials is a routine method, do not require any prior knowledge of the system and can be performed before the actual synthesis takes place. In my opinion, screening of torsional potentials should be the first step of rational design. It also implies that rational design is paradoxically more feasible for conjugated polymers even in the absence of crystalline order, which is contrary to current efforts focused on screening of small molecules.

## 9.3 Molecular dynamics

Molecular dynamics simulations of IDT-BT and DPP-BTZ revealed two common features: novel mechanism of backbone disorder and "entropic resilience". In an amorphous phase both systems exhibit limited degree of backbone torsion and structural disorder of the polymer chain is accommodated by bending rather than twisting. Whereas torsion creates disorder on a length scale of single aromatic rings (as in pBTTT), bending is more gentle with typical radius of curvature in the order of few to tens of lengths of a single monomer. This observation led me to formulate hypothesis that although IDT-BT is disordered at a macroscale, at a microscale the disorder is "diffused" to a longer length scale and hence there are no sharp discontinuities that would localize the wavefunction. This is contradictory to pBTTT- in my opinion pBTTT is an example of system that is ordered at a macroscale but disordered at a microscale comparable to delocalization length.

Entropic resilience refers to an observation that in both systems there are several possible ways of arranging monomers and side-chains that nevertheless result in

equivalent crystal packing motifs, which have comparable total energies per mole and linear, torsion-free backbones. In other words, I suggest that in these systems relative orientations of building blocks are not relevant to energetic disorder in the crystalline phase. As an analogy to statistical mechanics, I would argue that there are several structurally distinct microstates that correspond to a single energetic macrostate. It is therefore possible to increase the entropy of the system, which is defined via number of microstates per macrostate, without changing macroscopic backbone conformation and hence transport properties, which means that spatial and energetic disorders are now separate phenomena. In my opinion this unique property follows from fact that in IDT-BT and DPP-BTZ all building blocks are co-linear (as defined in Introduction) and their respective torsional potentials have minima at 0 or 180 degrees.

To explain that in more detail I would consider a simple binomial distribution using previously introduced spin notation. Let us assume that a single building block can be incorporated into the backbone in two possible ways, and one can switch between the states by flipping the block with respect to backbone plane (this notation was defined in Introduction, Figure 1.5). Simplistically, aggregation can be modeled as a permutation of $\uparrow$ and $\downarrow$ states- we select orientations of consecutive building blocks one by one along the backbone and according to their probability. If probability P($\downarrow$) is equal to P($\uparrow$), one recovers a binomial distribution, as shown in Figure 9.1, and the most probable macrostate is one with equal number of $\downarrow$ and $\uparrow$ states. In case of non-colinear monomers, every configuration with equal number of $\downarrow$ and $\uparrow$ states is linear at macroscale[1], but the only configuration that is always locally linear is an alternating sequence of $\downarrow$ and $\uparrow$ states[2] and hence probability of finding defect-free backbone is extremely small. Contrary, co-linear units are indistinguishable and every arrangement of building blocks is both locally and globally linear. The same argument may be applied to explain backbone chirality and torsional disorder- let us assume that torsional potential between two units has minima at $\pm\theta$. In such case there are two states corresponding to ideally helical backbone[3], one state corresponding to non-helical backbone[4] and numerous states in between with varying degree of chirality. The only special case is a system with minima at 0 and 180°- both minima correspond to planar configurations and hence are indistinguishable upon interchange, just as orientation of co-linear building blocks does not affect linearity of the backbone. An obvious recommendation for rational design of novel system would be to select a set

[1] For example ($\uparrow \cdots \uparrow\downarrow \cdots \downarrow$) state made of two locally curved parts is globally linear.
[2] ($\downarrow\uparrow\downarrow \cdots \uparrow\downarrow\uparrow$)
[3] $(\theta, \cdots, \theta)$ and $(-\theta, \cdots, -\theta)$
[4] $(\theta, -\theta, \cdots, \theta, -\theta)$, for example Figure 2 in NDIT-2 section.

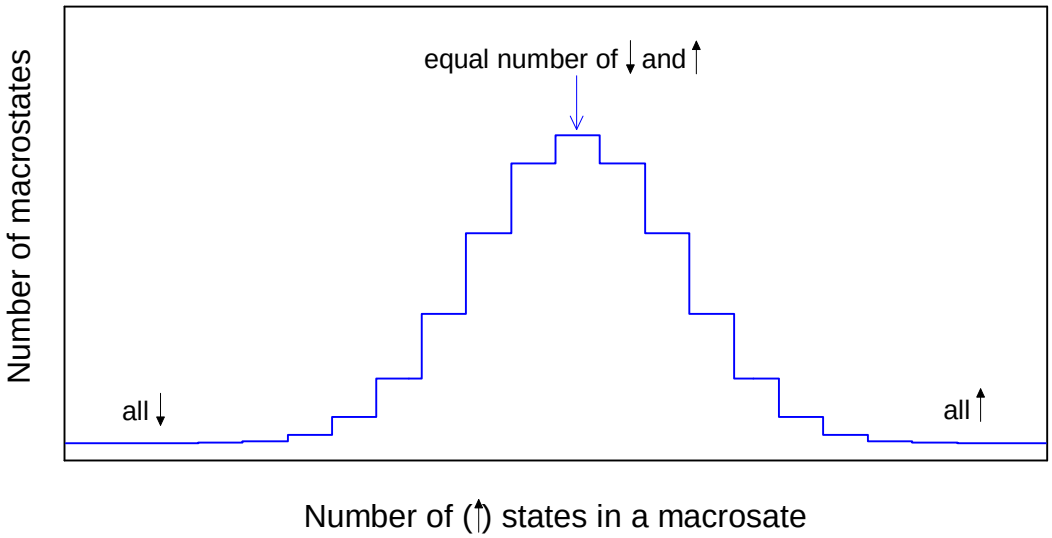


Figure 9.1: Sample binomial distribution of building block orientations for backbone containing 20 units. The most likely macrostate represents a fraction of all possible states.

linear donor and acceptor units and examine to possible combinations of pairwise torsional potentials by means of DFT simulation. By selecting pairs with torsional minima corresponding to planar configurations one could deliberately design a system that limits disorder at length scale comparable to typical charge delocalization at the expense of crystalline order. This tendency to diffuse disorder over longer length scale is apparent in historical evolution from pBTTT to IDT-BT, however it seems to be a result of trial and error rather than deliberate trend.

## 9.4 Outlook

As I briefly described in introduction to Small Molecules chapter, current methodology to simulate TEM spectra is a complex, time consuming process that depends on intuition and proper guess of input structure. DFT simulation of periodic crystal is certainly more rigorous and it would be interesting to continue our simulations using latest versions of software. I am aware of two recent improvements- firstly, new version of CRYSTAL code has been released and now includes new functionality to compute Raman spectra, hence it is possible to make a direct mode assignment based on experimental spectra. Secondly, Stefan Grimme released D3 version of his dispersion correction- older D2 method used by me proved to versatile enough to optimise geometry and calculate vibrational and hence I remain optimistic about applicability

of DFT simulations to characterize lattice dynamics in crystalline small molecules.

Measurements of pressure-dependent Raman spectra and molecular dynamics simulations of disordered phases of IDT-BT and DPP-BTZ led me to hypothesis that low degree of energetic disorder may be correlated with torsional resilience and novel mechanism of degree accommodation. Although there is an apparent correlation between lack of pressure-dependence of Raman spectra and electronic performance, we are missing a direct causation between structural and electronic properties. In my opinion such link could be established by measurements of transport properties as a function of pressure. Rather than finding a common denominator for series of compounds that are structurally and chemically different, I suggest to perform measurements on a singe system subject to varying external conditions as a way to reduce dimensionality of the problem. In Experimental Methods section I briefly discussed piston-cylinder cell developed by Takeya group[75, 107] that may be used to determine charge mobility as a function of external pressure. Since it is already known that backbones of F8BT and NDI-T2 planarize under pressure, in theory it is possible to directly correlate structural parameter with electronic properties and hence validate previously formulated hypothesis. Moreover, measurement of mobility in pressure-resilient system such as IDT-BT would provide a benchmark to evaluate contribution arising from reduced intermolecular distance.

# References


[1] Hideki Shirakawa, Edwin J. Louis, Alan G. MacDiarmid, Chwan K. Chiang, and Alan J. Heeger. Synthesis of electrically conducting organic polymers: halogen derivatives of polyacetylene, (ch). *J. Chem. Soc., Chem. Commun.*, pages 578–580, 1977.

[2] C. W. Tang and S. A. VanSlyke. Organic electroluminescent diodes. *Applied Physics Letters*, 51(12):913–915, 1987.

[3] JH Burroughes, DDC Bradley, AR Brown, RN Marks, K Mackay, RH Friend, PL Burn, and AB Holmes. Light-emitting-diodes based on conjugated polymers. *Nature*, 347(6293):539–541, Oct 11 1990.

[4] Scott Himmelberger and Alberto Salleo. Engineering semiconducting polymers for efficient charge transport. *MRS Communications*, 5(3):383–395, 2015.

[5] Henning Sirringhaus. 25th anniversary article: Organic field-effect transistors: The path beyond amorphous silicon. *Advanced Materials*, 26(9):1319–1335, 2014.

[6] Xinran Zhang, Hugo Bronstein, Auke J. Kronemeijer, Jeremy Smith, Youngju Kim, R. Joseph Kline, Lee J. Richter, Thomas D. Anthopoulos, Henning Sirringhaus, Kigook Song, Martin Heeney, Weimin Zhang, Iain McCulloch, and Dean M. DeLongchamp. Molecular origin of high field-effect mobility in an indacenodithiophene-benzothiadiazole copolymer. *Nature Communications*, 4, Jul 2013.

[7] Weimin Zhang, Jeremy Smith, Scott E. Watkins, Roman Gysel, Michael McGehee, Alberto Salleo, James Kirkpatrick, Shahid Ashraf, Thomas Anthopoulos, Martin Heeney, and Iain McCulloch. Indacenodithiophene semiconducting polymers for high-performance, air-stable transistors. *Journal of the American Chemical Society*, 132(33):11437–11439, Aug 25 2010.

[8] Clayton M. Christensen. *The Innovator's Dilemma: When New Technologies Cause Great Firms to Fail*. Harvard Business School Press, 1997.

[9] Clayton M. Christensen, Michael E. Raynor, and Rory McDonald. What Is Disruptive Innovation? *Harvard Business Review*, December 2015.

[10] A.M. Sze. *Physics of Semiconductor Devices*. John Wiley and Sons, 2007.

[11] Organic Electronics. *www.iapp.de/organische-elektronik.de/en/*.

[12] N. Karl, K. H. Kraft, J. Marktanner, M. Munch, F. Schatz, R. Stehle, and H.-M. Uhde. Fast electronic transport in organic molecular solids? *Journal of Vacuum Science & Technology A: Vacuum, Surfaces, and Films*, 17(4):2318–2328, 1999.

[13] N Karl. Charge carrier transport in organic semiconductors. *Synthetic Metals*, 133:649 – 657, 2003.

[14] J. L. Bredas, J. P. Calbert, D. A. da Silva Filho, and J. Cornil. Organic semiconductors: A theoretical characterization of the basic parameters governing charge transport. *Proceedings of the National Academy of Sciences of the United States of America*, 99(9):5804–5809, 2002.

[15] Yuan Y, Giri G, Ayzner AL, Zoombelt AP, Mannsfeld SC, Chen J, Nordlund D, Toney MF, Huang J, and Bao Z. Ultra-high mobility transparent organic thin film transistors grown by an off-centre spin-coating method. *Nature Communications*, 5(3005), 2014.

[16] J. E. Northrup. Two-dimensional deformation potential model of mobility in small molecule organic semiconductors. *Applied Physics Letters*, 99(6):062111, 2011.

[17] Hajime Kobayashi, Norihito Kobayashi, Shizuka Hosoi, Naoki Koshitani, Daisuke Murakami, Raku Shirasawa, Yoshihiro Kudo, Daisuke Hobara, Yuichi Tokita, and Masao Itabashi. Hopping and band mobilities of pentacene, rubrene, and 2,7-dioctyl[1]benzothieno[3,2-b][1]benzothiophene (C8-BTBT) from first principle calculations. *The Journal of Chemical Physics*, 139(1):014707, 2013.

[18] Mathias Gruber, Seok-Heon Jung, Sam Schott, Deepak Venkateshvaran, Auke Jisk Kronemeijer, Jens Wenzel Andreasen, Christopher R. McNeill, Wallace W. H. Wong, Munazza Shahid, Martin Heeney, Jin-Kyun Lee, and Henning

Sirringhaus. Enabling high-mobility, ambipolar charge-transport in a DPP-benzotriazole copolymer by side-chain engineering. *Chem. Sci.*, 6:6949–6960, 2015.

[19] Tomo Sakanoue and Henning Sirringhaus. Band-like temperature dependence of mobility in a solution-processed organic semiconductor. *Nature Materials*, 9(9):736–740, 2010.

[20] P. G. Le Comber and W. E. Spear. Electronic transport in amorphous silicon films. *Phys. Rev. Lett.*, 25:509–511, Aug 1970.

[21] Veaceslav Coropceanu, Jerome Cornil, Demetrio A. da Silva Filho, Yoann Olivier, Robert Silbey, and Jean-Luc Bredas. Charge transport in organic semiconductors. *Chemical Reviews*, 107(4):926–952, Apr 2007.

[22] Jiro Yamashita and Tatumi Kurosawa. On electronic current in NiO. *Journal of Physics and Chemistry of Solids*, 5(1):34 – 43, 1958.

[23] T Holstein. Studies of polaron motion. *Annals of Physics*, 8(3):325 – 342, 1959.

[24] K. Fesser, A. R. Bishop, and D. K. Campbell. Optical absorption from polarons in a model of polyacetylene. *Phys. Rev. B*, 27:4804–4825, Apr 1983.

[25] C. D. Dimitrakopoulos and D. J. Mascaro. Organic thin-film transistors: A review of recent advances. *IBM Journal of Research and Development*, 45(1):11–27, Jan 2001.

[26] Deepak Venkateshvaran, Mark Nikolka, Aditya Sadhanala, Vincent Lemaur, Mateusz Zelazny, Michal Kepa, Michael Hurhangee, Auke Jisk Kronemeijer, Vincenzo Pecunia, Iyad Nasrallah, Igor Romanov, Katharina Broch, Iain McCulloch, David Emin, Yoann Olivier, Jerome Cornil, David Beljonne, and Henning Sirringhaus. Approaching disorder-free transport in high-mobility conjugated polymers. *Nature*, 515(7527):384–388, Nov 20 2014.

[27] J. W. Rumer, S. Rossbauer, M. Planells, S. E. Watkins, T. D. Anthopoulos, and I. McCulloch. Reduced roughness for improved mobility in benzodipyrrolidone-based, n-type OFETS. *J. Mater. Chem. C*, 2:8822–8828, 2014.

[28] Nicolas Blouin, Alexandre Michaud, David Gendron, Salem Wakim, Emily Blair, Rodica Neagu-Plesu, Michel Belletete, Gilles Durocher, Ye Tao, and Mario

Leclerc. Toward a rational design of poly(2,7-carbazole) derivatives for solar cells. *Journal of the American Chemical Society*, 130(2):732–742, 2008.

[29] Johannes Hachmann, Roberto Olivares-Amaya, Sule Atahan-Evrenk, Carlos Amador-Bedolla, Roel S. Sanchez-Carrera, Aryeh Gold-Parker, Leslie Vogt, Anna M. Brockway, and Alan Aspuru-Guzik. The Harvard Clean Energy Project: Large-scale computational screening and design of organic photovoltaics on the world community grid. *The Journal of Physical Chemistry Letters*, 2(17):2241–2251, 2011.

[30] Johannes Hachmann, Roberto Olivares-Amaya, Adrian Jinich, Anthony L. Appleton, Martin A. Blood-Forsythe, Laszlo R. Seress, Carolina Roman-Salgado, Kai Trepte, Sule Atahan-Evrenk, Suleyman Er, Supriya Shrestha, Rajib Mondal, Anatoliy Sokolov, Zhenan Bao, and Alan Aspuru-Guzik. Lead candidates for high-performance organic photovoltaics from high-throughput quantum chemistry - the Harvard Clean Energy Project. *Energy Environ. Sci.*, 7:698–704, 2014.

[31] Anatoliy N. Sokolov, Sule Atahan-Evrenk, Rajib Mondal, Hylke B. Akkerman, Roel S. Sanchez-Carrera, Sergio Granados-Focil, Joshua Schrier, Stefan C. B. Mannsfeld, Arjan P. Zoombelt, Zhenan Bao, and Alan Aspuru-Guzik. From computational discovery to experimental characterization of a high hole mobility organic crystal. *Nature Communications*, 2, Aug 2011.

[32] Jiri Klimes and Angelos Michaelides. Perspective: Advances and challenges in treating van der Waals dispersion forces in density functional theory. *The Journal of Chemical Physics*, 137(12):120901, 2012.

[33] Johanna P. Schmidtke, Richard H. Friend, and Carlos Silva. Tuning interfacial charge-transfer excitons at polymer-polymer heterojunctions under hydrostatic pressure. *Phys. Rev. Lett.*, 100:157401, Apr 2008.

[34] Johanna P. Schmidtke, Ji-Seon Kim, Johannes Gierschner, Carlos Silva, and Richard H. Friend. Optical spectroscopy of a polyfluorene copolymer at high pressure: Intra- and intermolecular interactions. *Phys. Rev. Lett.*, 99:167401, Oct 2007.

[35] Ruoyu Li, J. Axel Zeitler, Daniele Tomerini, Edward P. J. Parrott, Lynn F. Gladden, and Graeme M. Day. A study into the effect of subtle structural details

and disorder on the terahertz spectrum of crystalline benzoic acid. *Physical Chemistry Chemical Physics*, 12(20):5329–5340, 2010.

[36] Edward P. J. Parrott, J. Axel Zeitler, Tomislav Friscic, Michael Pepper, William Jones, Graeme M. Day, and Lynn F. Gladden. Testing the sensitivity of terahertz spectroscopy to changes in molecular and supramolecular structure: A study of structurally similar cocrystals. *Crystal Growth & Design*, 9(3):1452–1460, Mar 2009.

[37] Roel S. Sanchez-Carrera, Pavel Paramonov, Graeme M. Day, Veaceslav Coropceanu, and Jean-Luc Bredas. Interaction of charge carriers with lattice vibrations in oligoacene crystals from naphthalene to pentacene. *Journal Of The Americal Chemical Society*, 132(41):14437–14446, Oct 20 2010.

[38] Bartolomeo Civalleri, Claudio M. Zicovich-Wilson, Loredana Valenzano, and Piero Ugliengo. B3LYP augmented with an empirical dispersion term (B3LYP-D*) as applied to molecular crystals. *CrystEngComm*, 10(4):405–410, 2008.

[39] Yoann Olivier, Dorota Niedzialek, Vincent Lemaur, Wojciech Pisula, Klaus Mullen, Unsal Koldemir, John R. Reynolds, Roberto Lazzaroni, Jerome Cornil, and David Beljonne. 25th anniversary article: High-mobility hole and electron transport conjugated polymers: How structure defines function. *Advanced Materials*, 26(14):2119–2136, 2014.

[40] Vincent Lemaur, Luca Muccioli, Claudio Zannoni, David Beljonne, Roberto Lazzaroni, Jerome Cornil, and Yoann Olivier. On the supramolecular packing of high electron mobility naphthalene diimide copolymers: The perfect registry of asymmetric branched alkyl side chains. *Macromolecules*, 46(20):8171–8178, 2013.

[41] Mario Caironi, Matt Bird, Daniele Fazzi, Zhihua Chen, Riccardo Di Pietro, Christopher Newman, Antonio Facchetti, and Henning Sirringhaus. Very low degree of energetic disorder as the origin of high mobility in an n-channel polymer semiconductor. *Advanced Functional Materials*, 21(17):3371–3381, 2011.

[42] Richard Liboff. *Introductory Quantum Mechanics*. Addison-Wesley, 1973.

[43] A Szabo. *Modern Quantum Chemistry*. Addison-Wesley, 1996.

[44] P. Hohenberg and W. Kohn. Inhomogeneous electron gas. *Phys. Rev.*, 136:B864–B871, 1964.

[45] W Kohn and LJ Sham. *Phys. Rev.*, 140:A1133–A1138, 1965.

[46] JP Perdew, JA Chevary, SH Vosko, KA Jackson, MR Pederson, DJ Singh, and C Fiolhais. Atoms, molecules, solids, and surfaces - applications of the Generalized Gradient Approximation for exchange and correlation. *Physical Review B*, 46(11):6671–6687, Sep 15 1992.

[47] JP Perdew, S Kurth, A Zupan, and P Blaha. Accurate density functional with correct formal properties: A step beyond the generalized gradient approximation. *Physical Review Letters*, 82(12):2544–2547, Mar 22 1999.

[48] AD Becke. A new mixing of Hartree-Fock and local density-functional theories. *Journal Of Chemical Physics*, 98(2):1372–1377, Jan 15 1993.

[49] William Koch and Max Holthausen. *A Chemist's Guide to Density Functional Theory*. Wiley Verlag, 2007.

[50] John F. Dobson, Angela White, and Angel Rubio. Asymptotics of the dispersion interaction: Analytic benchmarks for van der Waals energy functionals. *Phys. Rev. Lett.*, 96:073201, Feb 2006.

[51] Grimme Stefan, Ehrlich Stephan, and Goerigk Lars. Effect of the damping function in dispersion corrected density functional theory. *Journal of Computational Chemistry*, 32(7):1456–1465.

[52] Hanke Felix. Sensitivity analysis and uncertainty calculation for dispersion corrected density functional theory. *Journal of Computational Chemistry*, 32(7):1424–1430.

[53] Claudio Quarti, Alberto Milani, Bartolomeo Civalleri, Roberto Orlando, and Chiara Castiglioni. Ab initio calculation of the crystalline structure and IR spectrum of polymers: Nylon 6 polymorphs. *The Journal of Physical Chemistry B*, 116(28):8299–8311, 2012.

[54] Daria Galimberti, Claudio Quarti, Alberto Milani, Luigi Brambilla, Bartolomeo Civalleri, and Chiara Castiglioni. IR spectroscopy of crystalline polymers from ab initio calculations: Nylon 6,6. *Vibrational Spectroscopy*, 66:83 – 92, 2013.

[55] Stefan Grimme, Jens Antony, Stephan Ehrlich, and Helge Krieg. A consistent and accurate ab initio parametrization of density functional dispersion correction (DFT-D) for the 94 elements H-Pu. *The Journal of Chemical Physics*, 132(15):154104, 2010.

[56] Qin Wu and Weitao Yang. Empirical correction to density functional theory for van der Waals interactions. *The Journal of Chemical Physics*, 116(2):515–524, 2002.

[57] Alexandre Tkatchenko and Matthias Scheffler. Accurate molecular van der Waals interactions from ground-state electron density and free-atom reference data. *Phys. Rev. Lett.*, 102:073005, Feb 2009.

[58] Tore Brinck, Jane S. Murray, and Peter Politzer. Polarizability and volume. *The Journal of Chemical Physics*, 98(5):4305–4306, 1993.

[59] M. Dion, H. Rydberg, E. Schröder, D. C. Langreth, and B. I. Lundqvist. Van der Waals density functional for general geometries. *Phys. Rev. Lett.*, 92.

[60] Ji ří Klimeš, David R. Bowler, and Angelos Michaelides. Van der Waals density functionals applied to solids. *Phys. Rev. B*, 83.

[61] Javier Carrasco, Biswajit Santra, Ji ří Klimeš, and Angelos Michaelides. To wet or not to wet? Dispersion forces tip the balance for water ice on metals. *Phys. Rev. Lett.*, 106, 2011.

[62] Alston J. Misquitta, James Spencer, Anthony J. Stone, and Ali Alavi. Dispersion interactions between semiconducting wires. *Phys. Rev. B*, 82, 2010.

[63] O. Anatole von Lilienfeld and Alexandre Tkatchenko. Two- and three-body interatomic dispersion energy contributions to binding in molecules and solids. *The Journal of Chemical Physics*, 132(23), 2010.

[64] Filipp Furche and Troy Van Voorhis. Fluctuation-dissipation theorem density-functional theory. *The Journal of Chemical Physics*, 122(16), 2005.

[65] Judith Harl, Laurids Schimka, and Georg Kresse. Assessing the quality of the random phase approximation for lattice constants and atomization energies of solids. *Phys. Rev. B*, 81, 2010.

[66] S. Lebègue, J. Harl, Tim Gould, J. G. Ángyán, G. Kresse, and J. F. Dobson. Cohesive properties and asymptotics of the dispersion interaction in graphite by the random phase approximation. *Phys. Rev. Lett.*, 105, 2010.

[67] Yusuke Tsutsui, Guillaume Schweicher, Basab Chattopadhyay, Tsuneaki Sakurai, Jean-Baptiste Arlin, Christian Ruzie, Almaz Aliev, Artur Ciesielski, Silvia

Colella, Alan R. Kennedy, Vincent Lemaur, Yoann Olivier, Rachid Hadji, Lionel Sanguinet, Frederic Castet, Silvio Osella, Dmytro Dudenko, David Beljonne, Jerome Cornil, Paolo Samori, Shu Seki, and Yves H. Geerts. Unraveling unprecedented charge carrier mobility through structure property relationship of four isomers of didodecyl[1]benzothieno[3,2-b][1]benzothiophene. *Advanced Materials*, 28(33):7106–7114, 2016.

[68] Carl Poelking, Eunkyung Cho, Alexander Malafeev, Viktor Ivanov, Kurt Kremer, Chad Risko, Jean-Luc Bredas, and Denis Andrienko. Characterization of charge-carrier transport in semicrystalline polymers: Electronic couplings, site energies, and charge-carrier dynamics in poly(bithiophene-alt-thienothiophene) [PBTTT]. *The Journal of Physical Chemistry C*, 117(4):1633–1640, 2013.

[69] Niedzialek Dorota, Lemaur Vincent, Dudenko Dmytro, Shu Jie, Hansen Michael Ryan, Andreasen Jens Wenzel, Pisula Wojciech, Mullen Klaus, Cornil Jeromeme, and Beljonne David. Probing the relation between charge transport and supramolecular organization down to Angstrom resolution in a benzothiadiazole-cyclopentadithiophene copolymer. *Advanced Materials*, 25(13):1939–1947.

[70] Sachin R. Chaudhari, John M. Griffin, Katharina Broch, Anne Lesage, Vincent Lemaur, Dmytro Dudenko, Yoann Olivier, Henning Sirringhaus, Lyndon Emsley, and Clare P. Grey. Donor-acceptor stacking arrangements in bulk and thin-film high-mobility conjugated polymers characterized using molecular modelling and MAS and surface-enhanced solid-state NMR spectroscopy. *Chem. Sci.*, 8:3126–3136, 2017.

[71] Stephen L. Mayo, Barry D. Olafson, and William A. Goddard. DREIDING: a generic force field for molecular simulations. *The Journal of Physical Chemistry*, 94(26):8897–8909, 1990.

[72] Andrew R. Leach. *Molecular Modelling: Principles and Applications*. Longman, 1996.

[73] Hestenes R Magnus and Eduard Stiefel. Methods of conjugate gradients for solving linear systems. *Journal of Research of the National Bureau of Standards*, 49(6):409–436, 1952.

[74] Christian B. Nielsen, Mathieu Turbiez, and Iain McCulloch. Recent advances in the development of semiconducting DPP-containing polymers for transistor applications. *Advanced Materials*, 25(13):1859–1880, 2013.

[75] Junto Tsurumi Junshi Soeda Yugo Okada Yu Yamashita Norihisa Akamatsu Atsushi Shishido Chikahiko Mitsui Toshihiro Okamoto Susumu Yanagisawa Hiroyuki Matsui Jun Takeya Takayoshi Kubo, Roger Hausermann. Suppressing molecular vibrations in organic semiconductors by inducing strain. *Nature Communications*, 7(11156), 2016.

[76] Robert Steyrleuthner, Marcel Schubert, Ian Howard, Bastian Klaumanzer, Kristian Schilling, Zhihua Chen, Peter Saalfrank, Frederic Laquai, Antonio Facchetti, and Dieter Neher. Aggregation in a high-mobility n-type low-bandgap copolymer with implications on semicrystalline morphology. *Journal of the American Chemical Society*, 134(44):18303–18317, 2012.

[77] Zhuping Fei, Pierre Boufflet, Sebastian Wood, Jessica Wade, John Moriarty, Eliot Gann, Erin L. Ratcliff, Christopher R. McNeill, Henning Sirringhaus, Ji-Seon Kim, and Martin Heeney. Influence of backbone fluorination in regioregular poly(3-alkyl-4-fluoro)thiophenes. *Journal of the American Chemical Society*, 137(21):6866–6879, 2015.

[78] Auke J. Kronemeijer, Enrico Gili, Munazza Shahid, Jonathan Rivnay, Alberto Salleo, Martin Heeney, and Henning Sirringhaus. A selenophene-based low-bandgap donor-acceptor polymer leading to fast ambipolar logic. *Advanced Materials*, 24(12), 2012.

[79] Ester Giussani, Daniele Fazzi, Luigi Brambilla, Mario Caironi, and Chiara Castiglioni. Molecular level investigation of the film structure of a high electron mobility copolymer via vibrational spectroscopy. *Macromolecules*, 46(7):2658–2670, 2013.

[80] K. K. Zhuravlev and M. D. McCluskey. Infrared spectroscopy of biphenyl under hydrostatic pressure. *The Journal of Chemical Physics*, 117(8):3748–3752, 2002.

[81] Bohdan Schatschneider, Stephen Monaco, Alexandre Tkatchenko, and Jian-Jie Liang. Understanding the structure and electronic properties of molecular crystals under pressure: Application of dispersion corrected DFT to oligoacenes. *The Journal of Physical Chemistry A*, 117(34):8323–8331, 2013.

[82] Peter Uhd Jepsen and Stewart J. Clark. Precise ab-initio prediction of terahertz vibrational modes in crystalline systems. *Chemical Physics Letters*, 442(4):275 – 280, 2007.

[83] Masae Takahashi, Yoshiyuki Kawazoe, Yoichi Ishikawa, and Hiromasa Ito. Interpretation of temperature-dependent low frequency vibrational spectrum of solid-state benzoic acid dimer. *Chemical Physics Letters*, 479(4):211 – 217, 2009.

[84] Hui Yan, Wen-Hui Fan, and Zhuan-Ping Zheng. Investigation on terahertz vibrational modes of crystalline benzoic acid. *Optics Communications*, 285(6):1593 – 1598, 2012.

[85] Burnett Andrew D., Kendrick John, Cunningham John E., Hargreaves Michael D., Munshi Tasmin, Edwards Howell G. M., Linfield Edmund H., and Davies A. Giles. Calculation and measurement of terahertz active normal modes in crystalline PETN. *ChemPhysChem*, 11(2):368–378.

[86] Matthew D. King and Timothy M. Korter. Effect of waters of crystallization on terahertz spectra: Anhydrous oxalic acid and its dihydrate. *The Journal of Physical Chemistry A*, 114(26):7127–7138, 2010.

[87] Matthew D. King, Patrick M. Hakey, and Timothy M. Korter. Discrimination of chiral solids: A terahertz spectroscopic investigation of l- and dl-serine. *The Journal of Physical Chemistry A*, 114(8):2945–2953, 2010.

[88] Patrick M. Hakey, Damian G. Allis, Matthew R. Hudson, Wayne Ouellette, and Timothy M. Korter. Terahertz spectroscopic investigation of s-(+)-ketamine hydrochloride and vibrational assignment by Density Functional Theory. *The Journal of Physical Chemistry A*, 114(12):4364–4374, 2010.

[89] Patrick M. Hakey, Damian G. Allis, Wayne Ouellette, and Timothy M. Korter. Cryogenic terahertz spectrum of (+)-methamphetamine hydrochloride and assignment using solid-state density functional theory. *The Journal of Physical Chemistry A*, 113(17):5119–5127, 2009.

[90] F Pascale, CM Zicovich-Wilson, FL Gejo, B Civalleri, R Orlando, and R Dovesi. CRYSTAL09 User's Manual. *http://www.crystal.unito.it*, 2009.

[91] F Pascale, CM Zicovich-Wilson, FL Gejo, B Civalleri, R Orlando, and R Dovesi. The calculation of the vibrational frequencies of crystalline compounds and its implementation in the CRYSTAL code. *Journal Of Computational Chemistry*, 25(6):888–897, Apr 30 2004.

[92] Karen L. Schuchardt, Brett T. Didier, Todd Elsethagen, Lisong Sun, Vidhya Gurumoorthi, Jared Chase, Jun Li, and Theresa L. Windus. Basis set exchange:

A community database for computational sciences. *Journal Of Chemical Information And Modeling*, 47(3):1045–1052, May-Jun 2007.

[93] Stefan Grimme. Semiempirical GGA-type density functional constructed with a long-range dispersion correction. *Journal Of Computational Chemistry*, 27(15):1787–1799, Nov 30 2006.

[94] M. C. Payne, M. P. Teter, D. C. Allan, T. A. Arias, and J. D. Joannopoulos. Iterative minimization techniques for ab initio total-energy calculations: molecular dynamics and conjugate gradients. *Rev. Mod. Phys.*, 64:1045–1097, Oct 1992.

[95] D. R. Hamann, M. Schluter, and C. Chiang. Norm-conserving pseudopotentials. *Phys. Rev. Lett.*, 43:1494–1497, Nov 1979.

[96] Dirk Porezag and Mark R. Pederson. Infrared intensities and Raman-scattering activities within density-functional theory. *Phys. Rev. B*, 54:7830–7836, Sep 1996.

[97] Michael J. Frisch, Yukio Yamaguchi, Jeffrey F. Gaw, Henry F. Schaefer, and J. Stephen Binkley. Analytic Raman intensities from molecular electronic wave functions. *The Journal of Chemical Physics*, 84(1):531–532, 1986.

[98] Chaudhari Sachin, Griffin John, Broch Katharina, Lesage Anne, Lemau Vincent, Dudenko Dmytro, Olivier Yoann, Sirringhaus Henning, Emsley Lyndon, and Grey Clare. Donor-acceptor stacking arrangements in bulk and thin-film high-mobility conjugated polymers characterized using molecular modelling and MAS and surface-enhanced solid-state NMR spectroscopy. *Chemical Science*, Submitted.

[99] Jui-Fen Chang, Tomo Sakanoue, Yoann Olivier, Takafumi Uemura, Marie-Beatrice Dufourg-Madec, Stephen G. Yeates, Jerome Cornil, Jun Takeya, Alessandro Troisi, and Henning Sirringhaus. Hall-effect measurements probing the degree of charge-carrier delocalization in solution-processed crystalline molecular semiconductors. *Physical Review Letters*, 107(6), AUG 2 2011.

[100] Michael Gross and Rainer Jaenicke. Growth inhibition of lysozyme crystals at high hydrostatic pressure. *FEBS Letters*, 284(1):87–90, 1991.

[101] Phil M. Oger, Isabelle Daniel, and Aude Picard. Development of a low-pressure diamond anvil cell and analytical tools to monitor microbial activities in situ

under controlled P and T. *Biochimica et Biophysica Acta (BBA) - Proteins and Proteomics*, 1764(3):434 – 442, 2006.

[102] Van Valkenburg A Bunting EN Weir CE, Lippincott ER. Infrared studies in the 1- to 15- micron region to 30,000 atmospheres. *Journal of research of the national bureau of standards section a-physics and chemistry*, 63(1):55–62, 1959.

[103] Prakapenka VB Abakumov AM Dubrovinsky L, Dubrovinskaia N. Implementation of micro-ball nanodiamond anvils for high-pressure studies above 6 Mbar. *Nature Communications*, 3(1163), 2012.

[104] A. Jayaraman. Diamond anvil cell and high-pressure physical investigations. *Rev. Mod. Phys.*, 55:65–108, Jan 1983.

[105] W. B. Holzapfel and N. I. Isaacs. *High-Pressure Techniques in Chemistry and Physics*. Oxford University Press, 1997.

[106] I. R. Walker. Nonmagnetic piston cylinder pressure cell for use at 35 kbar and above. *Review of Scientific Instruments*, 70(8):3402–3412, 1999.

[107] Y. Okada, K. Sakai, T. Uemura, Y. Nakazawa, and J. Takeya. Charge transport and Hall effect in rubrene single-crystal transistors under high pressure. *Phys. Rev. B*, 84:245308, Dec 2011.

[108] Stephen A. Moggach, David R. Allan, Simon Parsons, and John E. Warren. Incorporation of a new design of backing seat and anvil in a Merrill-Bassett diamond anvil cell. *Journal of Applied Crystallography*, 41(2):249–251, Apr 2008.

[109] Leo Merrill and William A. Bassett. Miniature diamond anvil pressure cell for single crystal xray diffraction studies. *Review of Scientific Instruments*, 45(2):290–294, 1974.

[110] H. K. Mao, J. Xu, and P. M. Bell. Calibration of the ruby pressure gauge to 800 kbar under quasi-hydrostatic conditions. *Journal of Geophysical Research: Solid Earth*, 91(B5):4673–4676, 1986.

[111] Agnes Dewaele, Marc Torrent, Paul Loubeyre, and Mohamed Mezouar. Compression curves of transition metals in the Mbar range: Experiments and projector augmented-wave calculations. *Phys. Rev. B*, 78:104102, 2008.

[112] S. Guha, W. Graupner, R. Resel, M. Chandrasekhar, H.R. Chandrasekhar, R. Glaser, and G. Leising. High pressure studies on the planarity of para-hexaphenyl. *Synthetic Metals*, 101(1):180 –181, 1999.

[113] J R Weinberg-Wolf, L E McNeil, Shubin Liu, and Christian Kloc. Evidence of low intermolecular coupling in rubrene single crystals by Raman scattering. *Journal of Physics: Condensed Matter*, 19(27):276204, 2007.

[114] M.J. Winokur, D. Spiegel, Y. Kim, S. Hotta, and A.J. Heeger. Structural and absorption studies of the thermochromic transition in poly(3-hexylthiophene). *Synthetic Metals*, 28(1-2):419 – 426, 1989.

[115] M. Hanfland, H. Beister, and K. Syassen. Graphite under pressure: Equation of state and first-order Raman modes. *Phys. Rev. B*, 39:12598–12603, 1989.

[116] Q.G. Zeng, Z.J. Ding, X.D. Tang, and Z.M. Zhang. Pressure effect on photoluminescence and Raman spectra of PPV. *Journal of Luminescence*, 115(1):32 – 38, 2005.

[117] Shao M etï¿œal. The isotopic effects of deuteration on optoelectronic properties of conducting polymers. *Nature Communications*, 5(3180), 2014.

[118] Wing C. Tsoi, David T. James, Ester Buchaca Domingo, Jong Soo Kim, Mohammed Al-Hashimi, Craig E. Murphy, Natalie Stingelin, Martin Heeney, and Ji-Seon Kim. Effects of a heavy atom on molecular order and morphology in conjugated polymer:fullerene photovoltaic blend thin films and devices. *ACS Nano*, 6(11):9646–9656, 2012.

[119] Wing C. Tsoi, David T. James, Jong Soo Kim, Patrick G. Nicholson, Craig E. Murphy, Donal D. C. Bradley, Jenny Nelson, and Ji-Seon Kim. The nature of in-plane skeleton Raman modes of P3HT and their correlation to the degree of molecular order in P3HT:PCBM blend thin films. *Journal of the American Chemical Society*, 133(25):9834–9843, 2011.

[120] Horng-Long Cheng, Xin-Wei Liang, Wei-Yang Chou, Yu-Shen Mai, Chou-Yu Yang, Li-Ren Chang, and Fu-Ching Tang. Raman spectroscopy applied to reveal polycrystalline grain structures and carrier transport properties of organic semiconductor films: Application to pentacene-based organic transistors. *Organic Electronics*, 10(2):289 – 298, 2009.

[121] Takafumi Uemura, Yuri Hirose, Mayumi Uno, Kazuo Takimiya, and Jun Takeya. Very high mobility in solution-processed organic thin-film transistors of highly ordered [1]benzothieno[3,2-b]benzothiophene derivatives. *Applied Physics Express*, 2(11):111501, 2009.

[122] Hiromi Minemawari, Toshikazu Yamada, Hiroyuki Matsui, Jun'ya Tsutsumi, Simon Haas, Ryosuke Chiba, Reiji Kumai, and Tatsuo Hasegawa. Inkjet printing of single-crystal films. *Nature*, 475(7356):364–367, Jul 21 2011.

[123] Hideaki Ebata, Takafumi Izawa, Eigo Miyazaki, Kazuo Takimiya, Masaaki Ikeda, Hirokazu Kuwabara, and Tatsuto Yui. Highly soluble [1]benzothieno[3,2-b]benzothiophene (BTBT) derivatives for high-performance, solution-processed organic field-effect transistors. *Journal of the American Chemical Society*, 129(51):15732–15733, 2007.

[124] Chang-Hyun Kim and Ioannis Kymissis. Graphene-organic hybrid electronics. *J. Mater. Chem. C*, 5:4598–4613, 2017.

[125] Sung Kyu Park, Devin A. Mourey, Sankar Subramanian, John E. Anthony, and Thomas N. Jackson. High-mobility spin-cast organic thin film transistors. *Applied Physics Letters*, 93(4):043301, 2008.

[126] Aaron B. Naden, Joachim Loos, and Donald A. MacLaren. Structure-function relations in diF-TES-ADT blend organic field effect transistors studied by scanning probe microscopy. *J. Mater. Chem. C*, 2:245–255, 2014.

[127] Iain McCulloch, Martin Heeney, Michael L. Chabinyc, Dean DeLongchamp, R. Joseph Kline, Michael Coelle, Warren Duffy, Daniel Fischer, David Gundlach, Behrong Hamadani, Rick Hamilton, Lee Richter, Alberto Salleo, Maxim Shkunov, David Sporrowe, Steven Tierney, and Weimin Zhong. Semiconducting Thienothiophene Copolymers: Design, Synthesis, Morphology, and Performance in Thin-Film Organic Transistors. *Advanced Materials*, 21(10-11):1091–1109, MAR 20 2009.

[128] Kirkpatrick James, Nielsen Christian B., Zhang Weimin, Bronstein Hugo, Ashraf R. Shahid, Heeney Martin, and McCulloch Iain. A systematic approach to the design optimization of light-absorbing indenofluorene polymers for organic photovoltaics. *Advanced Energy Materials*, 2(2):260–265.

[129] Gao Liang, Zhang Zhi-Guo, Xue Lingwei, Min Jie, Zhang Jianqi, Wei Zhixiang, and Li Yongfang. All-polymer solar cells based on absorption-complementary polymer donor and acceptor with high power conversion efficiency of 8.27%. *Advanced Materials*, 28(9):1884–1890.

[130] Jonathan Rivnay, Michael F. Toney, Yan Zheng, Isaac V. Kauvar, Zhihua Chen, Veit Wagner, Antonio Facchetti, and Alberto Salleo. Unconventional face-on texture and exceptional in-plane order of a high mobility n-type polymer. *Advanced Materials*, 22(39):4359–4363, 2010.

[131] Jonathan Rivnay, Robert Steyrleuthner, Leslie H. Jimison, Alberto Casadei, Zhihua Chen, Michael F. Toney, Antonio Facchetti, Dieter Neher, and Alberto Salleo. Drastic control of texture in a high performance n-type polymeric semiconductor and implications for charge transport. *Macromolecules*, 44(13):5246–5255, 2011.

[132] Alessandro Troisi and Giorgio Orlandi. Dynamics of the intermolecular transfer integral in crystalline organic semiconductors. *The Journal of Physical Chemistry A*, 110(11):4065–4070, 2006.

[133] Alessandro Troisi, Giorgio Orlandi, and John E. Anthony. Electronic interactions and thermal disorder in molecular crystals containing cofacial pentacene units. *Chemistry of Materials*, 17(20):5024–5031, 2005.

[134] S. Ciuchi and S. Fratini. Electronic transport and quantum localization effects in organic semiconductors. *Phys. Rev. B*, 86:245201, Dec 2012.

[135] Simone Fratini, Didier Mayou, and Sergio Ciuchi. The transient localization scenario for charge transport in crystalline organic materials. *Advanced Functional Materials*, 26(14):2292–2315, 2016.

[136] Alexander S. Eggeman, Steffen Illig, Alessandro Troisi, Henning Sirringhaus, and Paul A. Midgley. Measurement of molecular motion in organic semiconductors by thermal diffuse electron scattering. *Nature Materials*, (12, 1045-1049), 2013.

[137] M. P. Lightfoot C. R. Groom, I. J. Bruno and S. C. Ward. The cambridge structural database. *Acta Cryst.*, B72:171–179, 2016.

[138] Pankaj Sinha, Scott E. Boesch, Changming Gu, Ralph A. Wheeler, and Angela K. Wilson. Harmonic vibrational frequencies: Scaling factors for HF,

B3LYP, and MP2 methods in combination with correlation consistent basis sets. *The Journal of Physical Chemistry A*, 108(42):9213–9217, 2004.

[139] Rodrigo Noriega, Jonathan Rivnay, Koen Vandewal, Felix P. V. Koch, Natalie Stingelin, Paul Smith, Michael F. Toney, and Alberto Salleo. A general relationship between disorder, aggregation and charge transport in conjugated polymers. *Nature Materials*, 12(11):1038–1044, Nov 2013.

[140] Zhuoying Chen, Mi Jung Lee, Raja Shahid Ashraf, Yun Gu, Sebastian Albert-Seifried, Martin Meedom Nielsen, Bob Schroeder, Thomas D. Anthopoulos, Martin Heeney, Iain McCulloch, and Henning Sirringhaus. High-performance ambipolar diketopyrrolopyrrole-thieno[3,2-b]thiophene copolymer field-effect transistors with balanced hole and electron mobilities. *Advanced Materials*, 24(5):647–652, 2012.

[141] Huajie Chen, Yunlong Guo, Gui Yu, Yan Zhao, Ji Zhang, Dong Gao, Hongtao Liu, and Yunqi Liu. Highly pi-extended copolymers with diketopyrrolopyrrole moieties for high-performance field-effect transistors. *Advanced Materials*, 24(34):4618–4622, 2012.

[142] Xinran Zhang, Lee J. Richter, Dean M. DeLongchamp, R. Joseph Kline, Matthew R. Hammond, Iain McCulloch, Martin Heeney, Raja S. Ashraf, Jeremy N. Smith, Thomas D. Anthopoulos, Bob Schroeder, Yves H. Geerts, Daniel A. Fischer, and Michael F. Toney. Molecular packing of high-mobility diketo pyrrolo-pyrrole polymer semiconductors with branched alkyl side chains. *Journal of the American Chemical Society*, 133(38):15073–15084, 2011.

[143] Richard D. McCullough, Renae D. Lowe, Manikandan Jayaraman, and Deborah L. Anderson. Design, synthesis, and control of conducting polymer architectures: structurally homogeneous poly(3-alkylthiophenes). *The Journal of Organic Chemistry*, 58(4):904–912, 1993.

[144] Yuning Li, Prashant Sonar, Leanne Murphy, and Wei Hong. High mobility diketopyrrolopyrrole (DPP) based organic semiconductor materials for organic thin film transistors and photovoltaics. *Energy and Environmental Science*, 6:1684, 06 2013.

[145] Kim Tremel, Florian S. U. Fischer, Navaphun Kayunkid, Riccardo Di Pietro, Roman Tkachov, Anton Kiriy, Dieter Neher, Sabine Ludwigs, and Martin

Brinkmann. Charge transport anisotropy in highly oriented thin films of the acceptor polymer P(NDI2OD-T2). *Advanced Energy Materials*, 4(10):1301659, 2014.

[146] Auke J. Kronemeijer, Vincenzo Pecunia, Deepak Venkateshvaran, Mark Nikolka, Aditya Sadhanala, John Moriarty, Monika Szumilo, and Henning Sirringhaus. Two-dimensional carrier distribution in top-gate polymer field-effect transistors: Correlation between width of density of localized states and urbach energy. *Advanced Materials*, 26(5):728–733, 2014.

[147] He Yan, Zhihua Chen, Yan Zheng, Christopher Newman, Jordan R. Quinn, Florian Dotz, Marcel Kastler, and Antonio Facchetti. A high-mobility electron-transporting polymer for printed transistors. *Nature*, 457(7230):679–U1, Feb 5 2009.

[148] Robert Steyrleuthner, Riccardo Di Pietro, Brian A. Collins, Frank Polzer, Scott Himmelberger, Marcel Schubert, Zhihua Chen, Shiming Zhang, Alberto Salleo, Harald Ade, Antonio Facchetti, and Dieter Neher. The role of regioregularity, crystallinity, and chain orientation on electron transport in a high-mobility n-type copolymer. *Journal of the American Chemical Society*, 136(11):4245–4256, 2014.

[149] Martin Brinkmann, Eric Gonthier, Stefan Bogen, Kim Tremel, Sabine Ludwigs, Martin Hufnagel, and Michael Sommer. Segregated versus mixed interchain stacking in highly oriented films of naphthalene diimide bithiophene copolymers. *ACS Nano*, 6(11):10319–10326, 2012.

# Appendix A

# Publications and Presentations

[1] D. Venkateshvaran, M. Nikolka, A. Sadhanala, V. Lemaur, **M. Zelazny**, M. Kepa, M. Hurhangee, A. J. Kronemeijer, V. Pecunia, I. Nasrallah, I. Romanov, K. Broch, I. McCulloch, D. Emin, Y. Olivier, J. Cornil, D. Beljonne, H. Sirringhaus, Approaching disorder-free transport in high-mobility conjugated polymers, *Nature*, 515, 384-388 (2014)

[2] K. Broch, D. Venkateshvaran, V. Lemaur, Y. Olivier, D. Beljonne, **M. Zelazny**, I. Nasrallah, D. J. Harkin, M. Statz, R. Di Pietro, A. J. Kronemeijer, H. Sirringhaus, Measurements of Ambipolar Seebeck Coefficients in High-Mobility Diketopyrrolopyrrole Donor–Acceptor Copolymers, *Advanced Electronic Mater*ials, 2017, 3, 1700225.

[3] **M. Zelazny**, M. Kepa, V. Leamur, Y. Olivier, H. Sirringhaus, High Pressure Studies of Conjugated Polymers, IMRS-S ICEM 2016, Singapore

# Appendix B

# Sample CRYSTAL09 input file.

```
init. geom. from expt. YOKBIK set to standard setting, H atoms normalised,
B3LYP-D*/6-31Gdp opt
CRYSTAL
0 0 0
14
29.5272 7.88 5.927 99.126
36
16 0.53071 0.1127 0.80681
6 0.5758 0.0511 0.6642
6 0.6213 0.0776 0.7342
6 0.6541 0.0207 0.6030
6 0.6368 -0.0648 0.3961
6 0.5914 -0.0909 0.3222
6 0.5580 -0.0312 0.4495
6 0.4898 0.0367 0.5863
6 0.7035 0.0563 0.6718
6 0.7276 -0.0243 0.8899
6 0.7766 0.0302 0.9596
6 0.8017 -0.0365 1.1767
6 0.8499 0.0276 1.2449
6 0.8770 -0.036 1.4610
6 0.9246 0.027 1.5216
6 0.9518 -0.032 1.7338
1 0.632606 0.143939 0.894418
1 0.661231 -0.111866 0.291296
1 0.580575 -0.158747 0.162693
1 0.707315 0.193212 0.691336
1 0.720976 0.0135194 0.533507
1 0.727091 -0.161383 0.866339
1 0.708697 0.00854091 1.0273
1 0.776788 0.168069 0.972383
1 0.795395 -0.00854046 0.824254
1 0.803238 -0.17406 1.16198
1 0.782322 -0.00305902 1.31204
1 0.847944 0.165079 1.25941
1 0.868815 -0.00495276 1.10743
1 0.878602 -0.173684 1.44853
1 0.858605 -0.00133384 1.59959
1 0.92284 0.16478 1.53155
1 0.94291 -0.00888117 1.38319
1 0.955024 -0.169569 1.72893
1 0.985754 0.0253764 1.75378
1 0.934953 0.00409218 1.8773
OPTGEOM
FULLOPTG
TOLDEG
0.00003
TOLDEX
0.00012
TOLDEE
10
```

## Sample CRYSTAL09 input file.

```
MAXCYCLE
500
FINALRUN
4
ENDOPT
END
16 5 0 0 6 2.0 1.0
.2191710000D+05    .1869000000D-02
.3301490000D+04    .1423000000D-01
.7541460000D+03    .6969600000D-01
.2127110000D+03    .2384870000D+00
.6798960000D+02    .4833070000D+00
.2305150000D+02    .3380740000D+00
0 1 6 8.0 1.0
.4237350000D+03   -.2376700000D-02    .4061000000D-02
.1007100000D+03   -.3169300000D-01    .3068100000D-01
.3215990000D+02   -.1133170000D-00    .1304520000D-00
.1180790000D+02    .5609000000D-01    .3272050000D-00
.4631100000D+01    .5922550000D-00    .4521851000D-00
.1870250000D+01    .4550060000D-00    .2560420000D-00
0 1 3 6.0 1.0
.2615840000D+01   -.2503740000D+00   -.1451100000D-01
.9221670000D-01    .6695700000D-01    .3102630000D+00
.3412870000D+00    .1054510000D+01    .7544830000D+00
0 1 1 0.0 1.0
.1171670000D+00    .1000000000D+01    .1000000000D+01
0 3 1 0.0 1.0
.6500000000D+00    .1000000000D+01
6 4
0 0 6 2.0 1.0
.3047524880D+04    .1834737130D-02
.4573695180D+03    .1403732280D-01
.1039486850D+03    .6884262220D-01
.2921015530D+02    .2321844430D+00
.9286662960D+01    .4679413480D+00
.3163926960D+01    .3623119850D+00
0 1 3 4.0 1.0
.7868272350D+01   -.1193324200D+00    .6899906660D-01
.1881288540D+01   -.1608541520D+00    .3164239610D+00
.5442492580D+00    .1143456440D+01    .7443082910D+00
0 1 1 0.0 1.0
.1687144782D+00    .1000000000D+01    .1000000000D+01
0 3 1 0.0 1.0
.8000000000D+00    .1000000000D+01
1 3 0 0 3 1.0 1.0
.1873113696D+02    .3349460434D-01
.2825394365D+01    .2347269535D+00
.6401216923D+00    .8137573262D+00
0 0 1 0.0 1.0
.1612777588D+00    .1000000000D+01
0 2 1 0.0 1.0
.1100000000D+01    .1000000000D+01
99    0
END
DFT
B3LYP
XLGRID
ENDDFT
GRIMME
1.00 20. 25.
3
1 0.14 1.3013
6 1.75 1.5246
16 5.57 1.76715
MPP
TOLINTEG
7 7 7 7 16
NOBIPOLAR
MAXCYCLE
500
FMIXING
40
LEVSHIFT
6 1
SHRINK
```

```
6  6
CMPLXFAC
2
DCDIAG
END
```

# Appendix C

# Sample CASTEP .param input file.

```
comment          = pbe, 1100eV, 0.04A-1, H-normalised
iprint           = 1
cut_off_energy   = 1100 eV
finite_basis_corr = auto
xc_functional    = pbe
sedc_apply       = true
sedc_scheme      = TS
fix_occupancy    = true
elec_energy_tol = 1e-12 ! eV
elec_convergence_win = 3
calculate_stress = true
backup_interval = 3600
task             = GeometryOptimization
opt_strategy = speed
geom_method      = DampedMD
MD_OPT_DAMPED_DELTA_T = TRUE
geom_max_iter    = 150
geom_energy_tol = 0.5e-6     ! eV/atom
geom_force_tol   = 0.5e-4     ! eV/Ang
geom_disp_tol    = 0.1e-3     ! Ang
geom_stress_tol = 0.02        ! GPa
```

# Appendix D

# Sample CASTEP .cell input file.

```
%block LATTICE_ABC
 29.5272  7.88  5.927
 90  99.126  90 %endblock LATTICE_ABC

%block SPECIES_POT
C     /fs3/e05/e05/mz319/DiF-TESADT/c-optgga2.recpot
H     /fs3/e05/e05/mz319/DiF-TESADT/h_optgga3.recpot
S     /fs3/e05/e05/mz319/DiF-TESADT/s-optgga1.recpot
%endblock SPECIES_POT

%BLOCK positions_frac
H        0.633626          0.144382          0.891662
H        0.661897          -0.10781          0.281564
H        0.579541          -0.155405         0.15324
H        0.708026          0.201644          0.688524
H        0.721933          0.034021          0.514942
H        0.728411          -0.165708         0.84399
H        0.708721          -0.008288         1.015916
H        0.776812          0.175515          0.968077
H        0.797541          0.013411          0.807374
H        0.805255          -0.18163          1.146317
H        0.782348          -0.023845         1.306508
H        0.84799  0.170206          1.261837
H        0.870953          0.014111          1.099784
H        0.880422          -0.18365          1.438166
H        0.857444          -0.027668         1.600807
H        0.92196  0.169953          1.552445
H        0.944755          0.017108          1.385346
H        0.95731  -0.183798         1.724118
H        0.986427          0.011623          1.787442
H        0.934516          -0.028845         1.892379
H        0.366374          -0.144382         0.108338
H        0.338103          0.10781  0.718436
H        0.420459          0.155405          0.84676
H        0.278067          -0.034021         0.485058
H        0.291974          -0.201644         0.311476
H        0.291279          0.008288          -0.015916
H        0.271589          0.165708          0.15601
H        0.202459          -0.013411         0.192626
H        0.223188          -0.175515         0.031923
H        0.217652          0.023845          -0.306508
H        0.194745          0.18163  -0.146317
H        0.129047          -0.014111         -0.099784
H        0.15201  -0.170206         -0.261837
H        0.142556          0.027668          -0.600807
H        0.119578          0.18365  -0.438166
H        0.055245          -0.017108         -0.385346
H        0.07804  -0.169953         -0.552445
H        0.065484          0.028845          -0.892379
H        0.013573          -0.011623         -0.787442
H        0.420459          0.344595          0.34676
```

```
H       0.291974        0.701644        -0.188524
H       0.278067        0.534021        -0.014942
H       0.271589        0.334292        -0.34399
H       0.291279        0.491712        -0.515916
H       0.223188        0.675515        -0.468077
H       0.202459        0.513411        -0.307374
H       0.194745        0.31837 -0.646317
H       0.217652        0.476155        -0.806508
H       0.15201 0.670206        -0.761837
H       0.129047        0.514111        -0.599784
H       0.119578        0.31635 -0.938166
H       0.142556        0.472332        -1.100807
H       0.07804 0.669953        -1.052445
H       0.055245        0.517108        -0.885346
H       0.04269 0.316202        -1.224118
H       0.013573        0.511623        -1.287442
H       0.065484        0.471155        -1.392379
H       0.633626        0.355618        0.391662
H       0.661897        0.60781 -0.218436
H       0.579541        0.655405        -0.34676
H       0.721933        0.465979        0.014942
H       0.708026        0.298356        0.188524
H       0.708721        0.508288        0.515916
H       0.728411        0.665708        0.34399
H       0.797541        0.486589        0.307374
H       0.776812        0.324485        0.468077
H       0.782348        0.523845        0.806508
H       0.805255        0.68163 0.646317
H       0.870953        0.485889        0.599784
H       0.84799 0.329794        0.761837
H       0.857444        0.527668        1.100807
H       0.880422        0.68365 0.938166
H       0.944755        0.482892        0.885346
H       0.92196 0.330047        1.052445
H       0.934516        0.528845        1.392379
H       0.986427        0.488377        1.287442
H       0.95731 0.683798        1.224118
C       0.575422        0.048516        0.660761
C       0.622167        0.07712 0.732051
C       0.653647        0.023295        0.593648
C       0.637407        -0.063081       0.388018
C       0.590906        -0.090517       0.314323
C       0.55882 -0.032297       0.448299
C       0.490246        0.035918        0.58808
C       0.704075        0.063612        0.659873
C       0.728446        -0.027713       0.87491
C       0.777587        0.036325        0.947079
C       0.802792        -0.042974       1.167831
C       0.850847        0.031601        1.240157
C       0.877337        -0.045165       1.459622
C       0.925227        0.031912        1.528126
C       0.952359        -0.04654        1.744508
C       0.424578        -0.048516       0.339239
C       0.377833        -0.07712        0.267949
C       0.346353        -0.023295       0.406352
C       0.362593        0.063081        0.611982
C       0.409094        0.090517        0.685677
C       0.44118 0.032297        0.551701
C       0.509754        -0.035918       0.41192
C       0.295925        -0.063612       0.340127
C       0.271554        0.027713        0.12509
C       0.222413        -0.036325       0.052921
C       0.197208        0.042974        -0.167831
C       0.149153        -0.031601       -0.240157
C       0.122663        0.045165        -0.459622
C       0.074773        -0.031912       -0.528126
C       0.047641        0.04654 -0.744508
C       0.424578        0.548516        -0.160761
C       0.377833        0.57712 -0.232051
C       0.346353        0.523295        -0.093648
C       0.362593        0.436919        0.111982
C       0.409094        0.409483        0.185677
C       0.44118 0.467703        0.051701
C       0.509754        0.535918        -0.08808
C       0.295925        0.563612        -0.159873
```

```
C       0.271554        0.472287        -0.37491
C       0.222413        0.536325        -0.447079
C       0.197208        0.457026        -0.667831
C       0.149153        0.531601        -0.740157
C       0.122663        0.454835        -0.959622
C       0.074773        0.531912        -1.028126
C       0.047641        0.45346 -1.244508
C       0.575422        0.451484        0.160761
C       0.622167        0.42288 0.232051
C       0.653647        0.476705        0.093648
C       0.637407        0.563081        -0.111982
C       0.590906        0.590517        -0.185677
C       0.55882 0.532297        -0.051701
C       0.490246        0.464082        0.08808
C       0.704075        0.436388        0.159873
C       0.728446        0.527713        0.37491
C       0.777587        0.463675        0.447079
C       0.802792        0.542974        0.667831
C       0.850847        0.468399        0.740157
C       0.877337        0.545165        0.959622
C       0.925227        0.468088        1.028126
C       0.952359        0.54654 1.244508
S       0.531339        0.109122        0.808563
S       0.468661        -0.109122       0.191437
S       0.468661        0.609122        -0.308563
S       0.531339        0.390878        0.308563
%ENDBLOCK positions_frac

%BLOCK PHONON_KPOINT_LIST
 0.0000000000     0.0000000000     0.0000000000
%ENDBLOCK PHONON_KPOINT_LIST

SYMMETRY_GENERATE
 fix_all_cell     true
 fix_all_ions     false

SNAP_TO_SYMMETRY

KPOINTS_MP_SPACING  0.04     ! inverse Angs
```